SEISMIC SOIL-STRUCTURE INTERACTION IN THE TIME DOMAIN

A Thesis
Submitted in partial fulfilment
of the requirement of the degree
of
Doctor of Philosophy in Civil Engineering
at the
University of Canterbury

by

Zhang Jian Jing
June, 2000

DEPARTMENT OF CIVIL ENGINEERING
UNIVERSITY OF CANTERBURY
CHRISTCHURCH, NEW ZEALAND

ABSTRACT

A time domain analysis procedure and method for seismic soil-structure interaction analysis are introduced in this work. This includes the selection of the soil model, the far field model, the structural model and the soil-structure interaction analysis method.

The bounding surface plasticity model is implemented to model the near field. The boundary element method in the time domain is used as the far field model. A coupling method between the boundary elements and finite elements has been proposed, its main advantages being: equilibrium and compatibility conditions are used directly and the present boundary element and finite element packages only need a small modification before they are used in this coupled procedure.

Nonlinear local site analyses have been carried out. The comparisons of the effects of strong and weak input motions, different soft clay sites and different input motions on local site amplification show the effect of soil yielding on local site response.

A primary investigation of the effect of soil-structure interaction on structural response is carried out using the linear and nonlinear soil models. When the linear elastic model is used to represent the soil behaviour, the effects of different sites, frames and input motions from the basement rock on the soil-structure interaction are investigated. The results show that the natural vibration periods of the site and structure can represent the effect of the site and structure on the soil-structure interaction and the predominant period of the input motion can represent the effect of the input motion on soil-structure interaction. Acceleration response at the foundation, displacement at the top floor, inter-storey shear force and the rocking of the foundation are used to show the effect of the natural periods on the soil-structure interaction. When the nonlinear soil model is used to represent the soil behaviour, a comparison of the results of the linear and nonlinear analyses shows that the soil yielding has a great influence on vibration frequency and vibration amplitude of both the acceleration and the displacement at the foundation and at the top floor of the structures. The permanent settlement of the foundation shows its accumulative characteristics.

ACKNOWLEDGEMENT

The research work on the seismic soil-structure interaction in the time domain was carried out at the Department of Civil Engineering, University of Canterbury.

I wish to express my deepest gratitude to Dr. Athol J. Carr, the main supervisor of the research project, and Dr. Peter J. Moss, the co-supervisor of the research project, for their enduring patience, invaluable advice and encouragement which have been of fundamental importance in completing this work.

Thanks are due to Dr. John Berrill for his invaluable discussion and his seismology course.

Special thanks are due to Dr. John X. Zhao of the Institute of Geological and Nuclear Science for his invaluable discussion, help, enthusiasm and encouragement.

My thanks are also extended to the technical staff of the department, especially for Mr. B. Hutchison and Mr. P. Coursey for their assistance with the computer facilities. The friendly service of the Engineering Library Staff is also appreciated. Thanks also are due to fellow students for their support and friendship especially Dr. Amar Rahman, Dr. Iman Satyarno, Dr. Charng Peng Xong and Brian Adams.

Finally, I wish to express my deepest gratitude to my parents and my brothers for their support, to my wife Chen Qi for her special support and feeling, to my daughter Kathy Zhang who provides me much happiness.

TABLE OF CONTENTS

Chapter Seven Investigation of Seismic Soil-Structure Interaction Using a Linear Soil Model

Chapter Eight Investigation of Seismic Soil-Structure Interaction by Using a Bounding Surface Soil Model

Chapter Nine Conclusions and Recommendations for Further Research

Notations

{ }	=	column vector
[ ]	=	matrix or submatrix
<>	=	step function operator
σ	=	normal stress
σij	=	stress tensor
σ_{ij}^{b}	=	stress on the bounding surface
$\{\Delta\sigma_0\}$	=	an unbalanced stress vector
ε	=	axial strain or given tolerance
εij	=	strain tensor
εvd	=	volumetric strain
Δεvd	=	volumetric strain increment
$d\varepsilon_{ij}^{e}$	=	elastic strain increment
$d\varepsilon_{ij}^{p}$	=	plastic strain increment
ε_{v}^{p}	=	plastic volumetric strain
τ	=	shear stress
τmax	=	maximum shear stress
γ	=	shear strain or bi-linear model factor or parameter in the α method
εmax	=	highest natural vibration frequency
α	=	parameter in the Newmark implicit integration method or parameter in the α method or stress lode angle
δ	=	parameter in the Newmark implicit integration method
θ	=	parameter in the Wilson-θ method
β	=	parameter in the α method
δij	=	Kronecker delta symbol
δ( )	=	Dirac delta function
λ	=	Lame elastic constant or the slope of the normal consolidation line of soils
κ	=	the slope of the swelling line of soils
μ	=	Lame elastic constant or Poisson's ratio or Poisson's ratio

ρ	=	mass density
ξ	=	the source point in the boundary element or damping ratio
γij	=	jump term
δij	=	Kronecker delta
θ	=	parameter in the Wilson-θ method
c	=	damping coefficient or tolerance error for refined element
cv	=	vertical damping coefficient
ch	=	horizontal damping coefficient
cr	=	rocking damping coefficient
ce	=	damping value for the spring representing the small strain behaviour
ce	=	damping for the spring
cp	=	dilatational wave velocity
cs	=	shear wave velocity
cn	=	damping coefficient in the normal direction in dashpot
ct	=	damping coefficient in the tangential direction in dashpot
e	=	void ratio
fj	=	body force per unit mass
Ic	=	isotropic back-stress
kn	=	stiffness for the nonlinear spring in the Pender model or wave number
ke	=	stiffness for the spring in the Pender model
k	=	hardening parameter in the bounding surface model or stiffness coefficient
κv	=	vertical stiffness coefficient
κh	=	horizotal stiffness coefficient
κr	=	rocking stiffness coefficient
κe	=	stiffness value of the spring representing the small strain behaviour
nij	=	loading direction
$\left\{p_{eff}^{(m)}\right\}$	=	effective load vector in the finite element
p'	=	average stress
q	=	difference between $\sigma 1$ and $\sigma 3$
r0	=	radius of the footing
rmax	=	minimum distance between element and field points in the boundary element

$\{s\}$	=	force vector in the boundary element
s	=	parameter for controlling the size of the elastic nucleus
Δt	=	time increment
tij	=	traction tensor
u	=	displacement
$\dot{u}$	=	velocity
$\ddot{u}$	=	acceleration
x	=	the receiver point in the boundary element
Ω^b	=	the boundary element domain
Ω^f	=	the finite element domain
Γ_I^B	=	interface between the finite elements and boundary elements in the boundary element domain
Γ_0^B	=	non-interface boundary in the boundary element domain
Γ_I^F	=	interface between the finite elements and boundary elements in the finite element domain
Γ_0^B	=	non-interface boundary in the finite element domain
$[A]$	=	transformation matrix from nodal force to traction
[C]	=	damping matrix
$[I]$	=	unit matrix
$[K_p]$	=	global stiffness matrix of the foundation plate
$[K_{eff}]$	=	effective stiffness matrix in the finite element
[K]	=	stiffness matrix
[M]	=	mass matrix
$\{R\}$	=	interactive force tensor between the foundation plate and the soil or load vector
$[T]$	=	displacement influence matrix in the boundary element
$[U]$	=	force influence matrix in the boundary element
$\{W_f\}$	=	vertical displacement tensor of the surface of the foundation
B	=	surface region
Bt	=	tangent bulk moduli

Ct	=	tangent shear moduli
BS	=	bounding surface model
CSL	=	critical state line
$Dijkl$	=	two order stress tensor
E	=	elastic modulus
Er	=	rebound modulus
FF	=	free field
F	=	yield function
Fij	=	second order traction tensor in the boundary element
Gij	=	the fundamental singular solution of the elastodynamic equation
$Gmax$	=	maximum shear modulus
$[Gij]$	=	second order displacement tensor in the boundary element
H	=	plastic modulus
H^b	=	plastic modulus of the bounding surface
Hi	=	plastic hinge length
H(z)	=	Heaviside function
$I\phi$	=	moment of inertial of footing with respect to a horizontal axis
$J1$	=	the first stress invariant
$J2$	=	the deviatoric stress invariant
K	=	bulk modulus
K	=	Gaussian integration points
$K0$	=	static earth pressure coefficient
L	=	Gaussian integration points
L	=	loading index
LL	=	linear elastic model
R	=	volume
SSI	=	soil-structure interaction
T	=	predominant period or natural vibration period
U	=	pore pressure
ΔU	=	pore pressure increment

Chapter One

Introduction

1.1 General

Seismic soil-structure interaction is an important element in the understanding of seismic structural failure, yet is very complex to analyse. Several recent earthquakes have provided us with many examples of soil-structure interaction (Daniel and Velesos, 1987, EERC report, 1995), improving the understanding of the phenomena and providing stimulation for research. The first earthquake is the Mexico City earthquake of 19th September 1985. One of its main characteristics was soft soil amplification that resulted in much structural failure in Mexico City and significant inspiration for research into the local soil effect on structures (Quaas and Mena, 1987, Seed etc, 1987). The second earthquake is the Loma Prieta earthquake of 17th October 1989 which confirmed the soft clay amplification observed in the Mexico City earthquake and produced much data on soil-structure interaction and showed nonlinear seismic soil responses (EERC report, 1990). Data recorded in this earthquake also showed the effect of buildings on the input motion around the building and confirmed that the input motion to the building is different from the free field response. The third earthquake is the Kobe earthquake of 17th January 1995, in which a number of records displayed nonlinear soft soil amplification (Takaji Kokusho and Masalli Matsumoto, 1995). Their results are consistent with those recorded in previous earthquakes such as the Loma Prieta earthquake and the 1986 earthquake in Taiwan (Chang, etc, 1990). The data recorded in these earthquakes illustrate the importance of soil-structure interaction on structural behaviour and show that the consideration of soft soil amplification and nonlinear soil properties is an alternative to soil-structure interaction analysis (Romo, 1995).

Usually, a soil-structure interaction analysis involves combining an input motion with the far field, the local site (near field) and the structure. The far field, the near field

and the structure have to be simulated by different models so that the solution becomes very complex. In order to simplify the solution, many assumptions have been introduced. At present, two methods widely used in soil-structure interaction analysis are the discrete element method and the finite element method (Wolf, 1985). Generally, the discrete element method assumes a linear soil response to the seismic excitation and replaces the half space with a spring and dashpot boundary. This method is simple and easily implemented, yet has several disadvantages. One disadvantage being that the soil must be idealised as a linear elastic material, and the other being that the free field response is used directly as input motion (Wolf, 1985). The finite element method, however, is suitable for the analysis of nonlinear materials and complex geometry (Zienkiewicz, 1977). When considering the recorded data from the above earthquakes, the finite element method is almost certainly a better alternative for representing the near field foundation.

The finite element method has been very popular in studying soil-structure interaction, yet the soil model most commonly used to simulate seismic soil behaviour is still a linear soil model or an equivalent linear soil model. Although several simplified models in recent years have been used for investigating seismic behaviour, they can not directly calculate pore pressure, which is a very important parameter in geotechnology.

On the other hand, when the finite element method is used for studying soil-structure interaction, the far field has to be considered. For meeting the far field conditions, a transmitting boundary is usually enforced as the near field boundary condition. At present, the Lysmer dashpot boundary (Lysmer and Richard, 1969) is one of the most widely used transmitting boundaries in the time domain analysis (Wolf, 1987), while many transmitting boundaries are available in the frequency domain. In recent years, rigorous boundary elements have been widely used for studying soil-foundation interaction. However, most of the boundary element methods employed in studying soil-foundation interaction work in the frequency domain and when they are used in the time domain it is necessary to use a fast Fourier transform (FFT). If the near field is nonlinear, an iterative solution has to be used. If an FFT procedure is employed again, the computation cost becomes huge. Fortunately, a boundary element method in the time domain has been proposed and successfully used for soil-foundation

interaction (Karabalis and Beskos, 1985) and dynamic dam analysis (Abouseeda and Dakoulas, 1998). This boundary element method in the time domain can be used directly in the nonlinear analyses.

When finite elements are used to represent the near field and the structure and boundary elements are used for the transmitting boundary, the coupled finite element and boundary element method becomes very important. In recent years, this coupled method in elastodynamics has attracted many researchers (Estorff and Prabucki, 1990). Two important aspects of this research are: firstly, what is the best coupling method, and secondly, how can existing finite element packages and boundary element packages be used to complete this coupling in such a way as to reduce the considerable implementation work required.

Nonlinear local site amplification and its effects on the structural response have been given attention in recent years. However, in most of the research, only simplified soil models and certain earthquake motions were used to investigate the nonlinear local site amplification and its effects on the structural response. Thus, to obtain better analysis results the use of advanced elasto-plasticity models will be helpful.

The effect of soil-structure interaction on structural response has been investigated for many years. In the use of linear soil model, most of the investigations concentrate on the effect of a layered soil and flexible or rigid foundation on the structural response. Generally the effect of soil-structure interaction on the structural response depends on the soil conditions, structures, and input motions from the basement rock. Investigating the effects of the soil conditions, structures and input motions on soil-structure interaction are helpful for visualising the effects of soil-structure interaction on the structural response in the structural design. In the use of a nonlinear soil model to analyses soil-structure interaction, the Mohr-Coulomb and cap models have been used widely while the bounding surface model was used to analyse a one-storey frame. It is necessary to use advanced elastoplastic soil model, the bounding surface soil model, for further investigating the effect of soil-structure interaction on the response of multi-storey frames to improve the accuracy of the prediction of the structural response.

1.2 Objectives of the Research

The objectives of the research were to

- generate a computer program using a bounding surface soil model to simulate the nonlinear local site amplification and nonlinear seismic soil-structure interaction.

- generate a computer program for boundary element analyses in the time domain. The boundary element is used as a transmitting boundary in the nonlinear local site amplification and nonlinear seismic soil-structure interaction analyses.

- develop a coupled finite element and boundary element method that can be implemented easily using existing finite element and boundary element packages.

- investigate three nonlinear local site amplifications and their effects on the structural response by using the bounding surface soil model.

- investigate the effects of soil conditions, structures, and input motions from the basement rock on the soil-structure interaction by using the linear elastic soil models.

- investigate the effect of soil-structure interaction on the structural response by using the bounding surface soil model.

1.3 Scope and Outline of the Thesis

Before evaluating the time history analyses in the soil-structure interaction analyses, a literature review is described in Chapter Two by investigating the published materials in this subject. The advantages and disadvantages of different soil models, methods of analysis for soil-structure interaction and transmitting boundaries are also compared.

In Chapter Three the bounding surface soil model that is used for the research is discussed. An explicit stress matrix for the computer code is also obtained. The methods to obtain tested parameters for the model are described. The implementation algorithm used for the computer program is then illustrated in detail. Different numerical integration methods are introduced. The results are calculated by using the generated computer program and the nonlinear time history analysis program RUAUMOKO (Carr, 1998) are compared in this Chapter.

In Chapter Four, a boundary element method in the time domain is derived in detail. The three dimensional and two dimensional singular integration solutions and numerical treatments are introduced. Finally, a benchmark problem is solved by using the generated computer program.

A coupling procedure for the finite element and boundary element is proposed in Chapter Five. The procedure is described by a flowchart and can be used for the linear or nonlinear analyses.

Nonlinear free field responses and their effects on structural response are introduced in Chapter Six. Three soft soil sites are used to investigate the site effects. The Loma Prieta (1989), the Parkfield (1966) and the El-Centro (1940) earthquakes are used to investigate the effect of these different input motions. The effects of intensity on ground response are investigated by using both strong and weak motions. In the analysis, the calculated soil domain used in the analyses is 100m wide by 30m deep and assumes that the rigid boundary consists of rock material at the bottom and flexible soil extended infinitely along in the horizontal directions.

In Chapter Seven, soil-structure interactions are investigated for 6- and 12-storey moment-resistant frames by using a linear elastic soil model with five sets of linear elastic soil parameters; the records from the Loma Prieta and the Mexico City earthquakes are used as the input motions from the basement rock. This investigation include the ground response at the foundation, the maximum displacement at the top floor, the inter-storey shear force and the rocking of foundations.

In Chapter Eight, soil-structure interactions are investigated for 6- and 12-storey moment-resistant frames by using the nonlinear soil model and the records from the Loma Prieta and the Mexico City earthquakes as input motions from the basement rock. The ground response at the foundation and the maximum acceleration and displacement at the top floor are used as the measurement indicators for the structural responses.

Contributions and conclusions from the research based on the results from the analyses are presented in Chapter Nine. Recommendations for further research are also discussed in this chapter.

Chapter Two

The Literature Review of Seismic Soil-Structure Interaction

2.1 Introduction

In recent decades, soil-structure interaction has been given much attention in both research and practice. The main reason is its important effect on the response of buildings in earthquakes. The second is its complexity. These characteristics were revealed by both the Mexico City Earthquake of 1985 and the Loma Prieta Earthquake of 17th October 1989.

Mexico City Earthquakes

From a geotechnical point of view, Mexico City has been divided into three regions (Fig.2.1):

a) The lake zone, consisting of a 20m to more than 100m deep deposit of highly compressible, high water content clay, underlain by the so-called deep deposits formed by very stiff layers of cemented silty sand.
b) The hill zone, formed by volcanic tuffs and lava flows.
c) The transition zone, composed of erratic stratifications of alluvial sand and silt layers interlaced with clay layers.

Local effects on ground motions at Mexico City recorded during the 1985 event are shown in Fig.2.2 with response spectra of the motions at different sites (Seed, etc, 1987). Motions on the firm ground (CU site) were amplified about 13 times by the clay deposit (SCT site) for natural periods of free vibration of around 2.0 seconds. Investigation showed that the worst damage occurred in the lake zone. It was consistent with the response spectra of the motions recorded at these sites.

In the investigation, it was found that certain types of structures, such as reinforced concrete framed systems with deep beam and slabs, were most affected by the

earthquake because their periods of free vibration, in many cases, were close to those of the ground motion. The effects of the natural period of free vibration is correlated with the height of the collapsed buildings: over 100 buildings less than 5 storeys, almost 140 buildings between 6 and 10 storeys, 27 between 11 and 15 storeys, and 3 greater than 15 storeys were destroyed (Daniel and Velesos, 1987).

Further investigation showed that because of Mexico City's special geological and geographical conditions, the damping of the clay is small so that the earthquake acceleration was amplified at the ground surface as shown in Fig.2.3.

As mentioned above, soil-structure interaction was very important during the 1985 Mexico City earthquake. There were, however, not enough data recorded in this event. In a 1990 earthquake, the motions at various depths below the Bernardo Quintana, an eight-storey concrete structure supported by a rigid box foundation embedded eight metres into the soil deposit and located in the lake zone of Mexico City, were recorded (Romo, 1995). The acceleration response spectra of the motions recorded at three different depths are shown in Fig.2.4. It may be seen that the spectral ordinates are amplified over depths from 40m to 20m, while over depths from 20m to the ground surface the motions are significantly attenuated.

According to the above observation, several simple conclusions can be made: a) soft clay will amplify input earthquake acceleration in the linear material range; b) the presence of structures will attenuate the ground surface motion.

The Loma Prieta Earthquake

A significant part of the USGS (United States Geology Survey) data set clearly demonstrates the effect of local site geology on the travelling seismic wave during the 1989 Loma Prieta event. In stiff site conditions the peak accelerations followed attenuation relationships, while on softer sites north of the epicentral region, motions recorded were significantly amplified. Some data recorded in this event showed peak horizontal accelerations of 0.12g, from the Crystal Springs Reservoir (epicentral distance 62km), 0.28g from Redwood Shores (soft site, epicentral distance 65km), 0.12g from Foster City (epicentral distance 66km) and 0.26g from Emeryville (soft

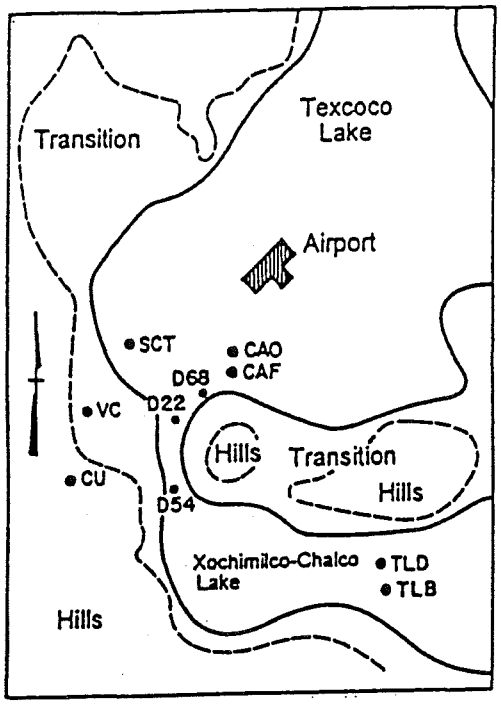

Fig. 2.1 Mexico City geotechnical zoning

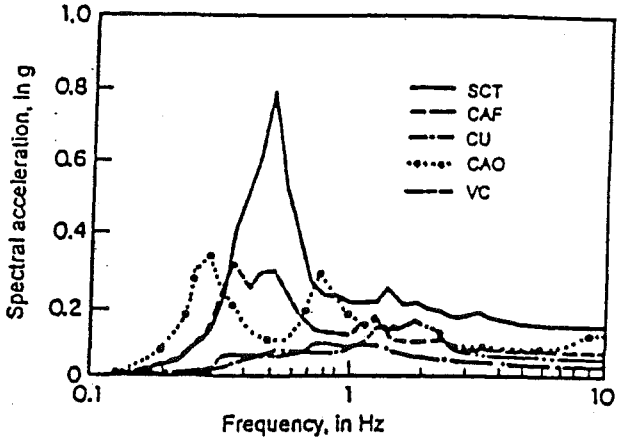

Fig. 2.2 Mexico City ground motion variations

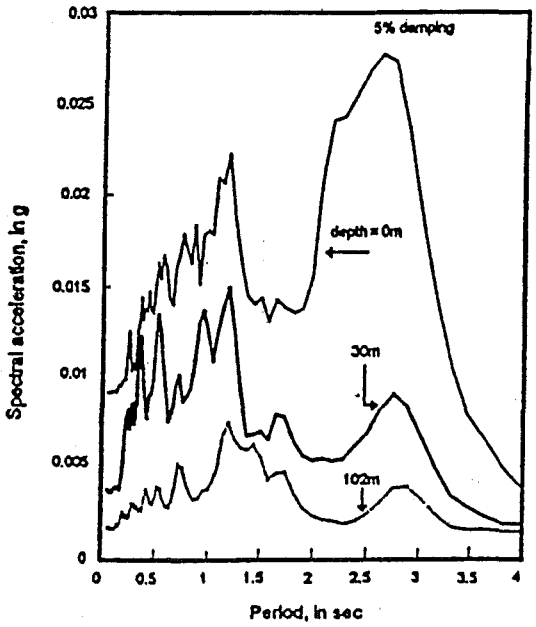

Fig. 2.3 Mexico City ground motion variation

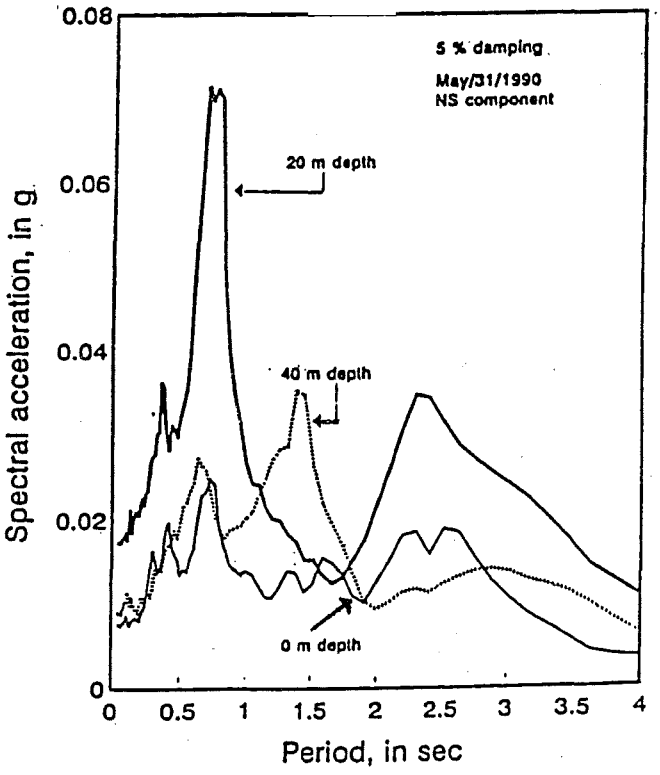

Fig. 2.4 Ground motion at Bernardo Quintana building

site, epicentral distance 97km). Recorded strong motions in instrumented structures also illustrate soil-structure interaction as given in Table 2.1.

Table 2.1 Recorded Data in the 1989 Loma Prieta Earthquake

1.	Pacific Park Plaza, 30-storey, symmetrical three-winged Reinforced concrete building (on bay mud)	FF(0.26g) Ground(0.22g) Roof Wing (0.39g)
2.	Hayward City Hall, 11-storey, reinforced concrete, Framed structure (on consolidated alluvium)	FF(0.10g) Ground(0.07g) 12^{th} floor (0.13g)

FF: Free field response

Ground: Ground floor response

Based on the above data, some conclusions can be made: a) the acceleration response of the free field is greater than that at the ground floor; b) the acceleration response at the building base are amplified at the top of the building.

Recently, similar conclusions were obtained by Zhao (1995) concerning the Gisborne Post Office Building. These recorded data reflect the concept of effective acceleration proposed by Newmark and Hall (1982). It can be stated in the following manner:

"It is that acceleration which is most closely related to structural response and to damage potential of an earthquake. It differs from, and is less than, the peak free-field ground acceleration. It is a function of the size of loaded area, the frequency content of the excitation, which in turn depends on the closeness to the source of the earthquake, and to the weight, embedment, damping characteristic, and stiffness of the structure and its foundation."

This concept illustrates the structural effect on site response and clarifies that the field response is different from the practical input motion of a building.

Usually the analysis of soil-structure interaction involves an input motion (bedrock motion), the local site and the structure. In most cases, the seismic response of the structure during an earthquake is affected not only by its own characteristics and the nature of the bedrock motion, but also by the characteristics of the building foundation and the deformability of the soil deposit. Generally, the influence of soil and foundation can be separated into the following parts:

(1) Local site effect (bedrock-soil interaction): this kind of interaction often results in the amplification of ground surface response to the earthquake input motion in the underlying bedrock. The intensity of amplification depends on the depth to bedrock, the local ground water table level, the local soil properties and the intensity of earthquake shaking (Seed etc, 1987). For example, in the Mexico City earthquake of 1985, the uniform soft clay amplified the intensity of the earthquake shaking.

(2) Interaction effect (soil-structure interaction): this kind of interaction results in a change in the response of the building and in the soil surrounding the building foundation due to the deformability of the soils. The effective acceleration mentioned in the above is one of the results of this kind of interaction.

The first kind of soil effect can be considered as the difference between the response of the ground surface and the bedrock motion in the free field (Fig.2.5a). The second kind of soil effect on the building can be considered as the difference between the response of the building on a fixed foundation (Fig.2.5b) and on the deformable soil (Fig.2.5c). The effect of the soil can be considered as the difference between the response of the ground surface in the free field and the building on the ground surface. In these cases, modelling the soil is a key to the soil-structure interaction model.

Different soil models have been proposed for modelling the seismic soil behaviour. With regard to simplified and complex analysis methods for soil-structure interaction, they can be usually classified into the discrete element method (spring and dashpot) and the finite element method. The following sections will introduce soil models and the analysis methods of soil-structure interaction.

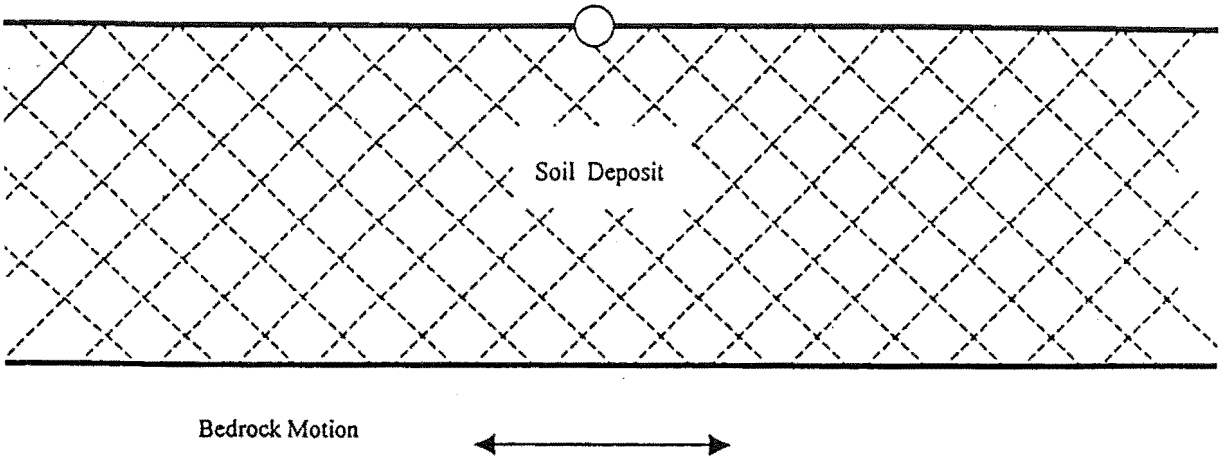

Fig. 2.5a Free Field Response

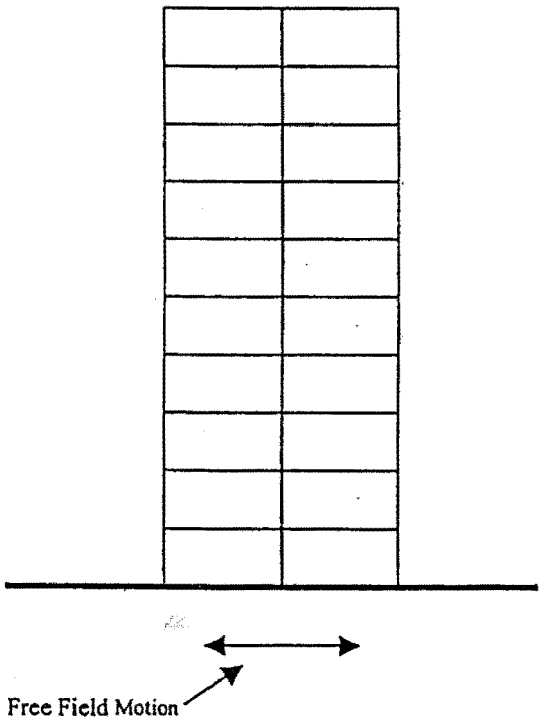

Fig. 2.5b Fixed Foundation

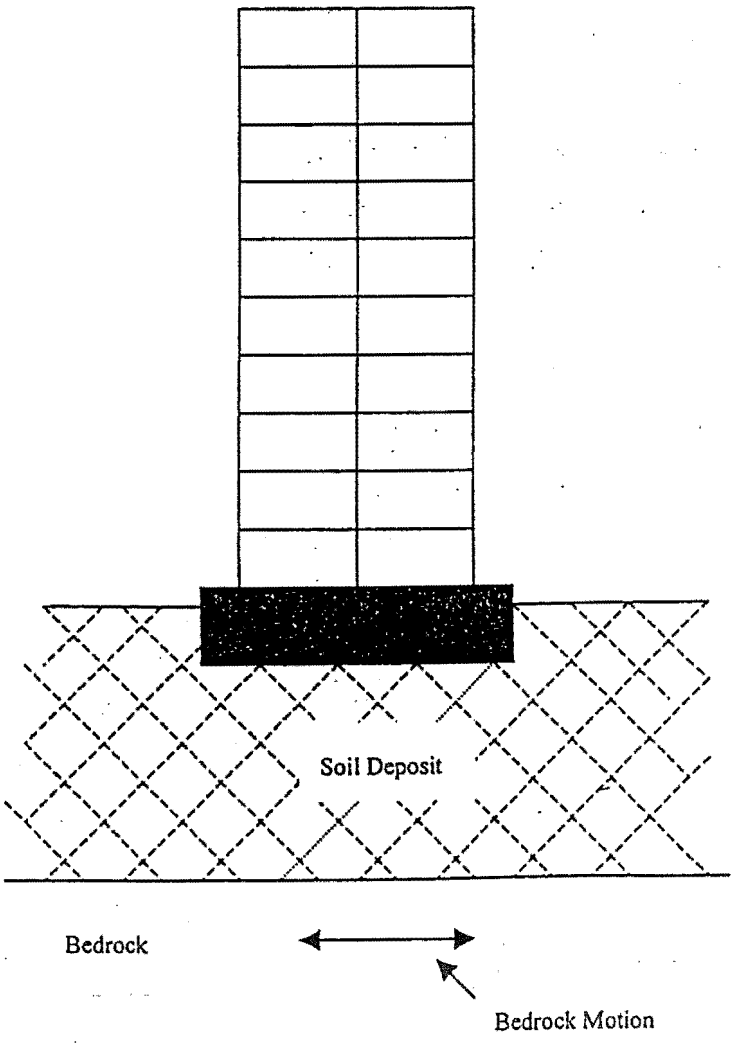

Fig. 2.5c Coupling Structure and Soil

2.2 Soil Models

It is known that a correct and precise soil model is a key to the analysis of seismic soil response. In previous decades, geotechnical researchers and engineers have carried out tests and hoped to obtain an accurate and simple soil model to represent soil properties. Many soil models have been proposed and verified by shaking table tests, centrifuge tests and from earthquake response records. In this section, only the linear elastic model, the Finn et al nonlinear soil model, and the bounding surface model will be discussed. These three models basically outline the development of the dynamic soil model. The advantages and disadvantages of each can be shown by comparing features of the three models.

2.2.1 The Linear Elastic Model

If the soil strain is less than 10^{-4}, the relationship between stress and strain can be represented by a linear elastic model. Usually, Hooke's law (Eq.2.1) can be used directly.

$$\{\sigma\} = [D]\{\varepsilon\} \tag{2.1}$$

where $[D]$ is the elastic matrix.

The linear elastic model has only two parameters, the elastic modulus E and Poisson's ratio μ, so it is very simple. However, it is only suitable if the shear strain is small. When the shear strain increases above about 10^{-4}, the linear elastic model can not reflect the change of soil properties.

2.2.2 Finn et al's (1976,1984,1985) Nonlinear Soil Model

Finn (1985) found the equivalent linear method works well for stable soils when high pore pressure and strong nonlinearity do not develop during the seismic excitation. If

these effects do develop, the equivalent linear procedures become less satisfactory because they do not allow the direct computation of pore pressure or permanent deformations. Therefore, Finn et. al. proposed a nonlinear effective stress soil model considering the volume strain and the pore pressure.

The relationship between shear stress τ and shear strain γ for the initial loading phase under drained or undrained loading conditions is described by a hyperbolic equation

$$\tau = \frac{G_{\max}\gamma}{1+(G_{\max}/\tau_{\max})|\gamma|} \tag{2.2}$$

where G_{max} and τ_{max} are the maximum shear modulus and the maximum shear stress.

The unloading-reloading has been modelled using the Masing rule (Masing, 1926), where the assumed unloading curve from (γ_r, τ_r) in Fig.2.6 is given by

$$\frac{\tau-\tau_r}{2} = \frac{G_{\max}(\gamma-\gamma_r)/2}{1+(G_{\max}/\tau_{\max})|\gamma-\gamma_r|/2} \tag{2.3}$$

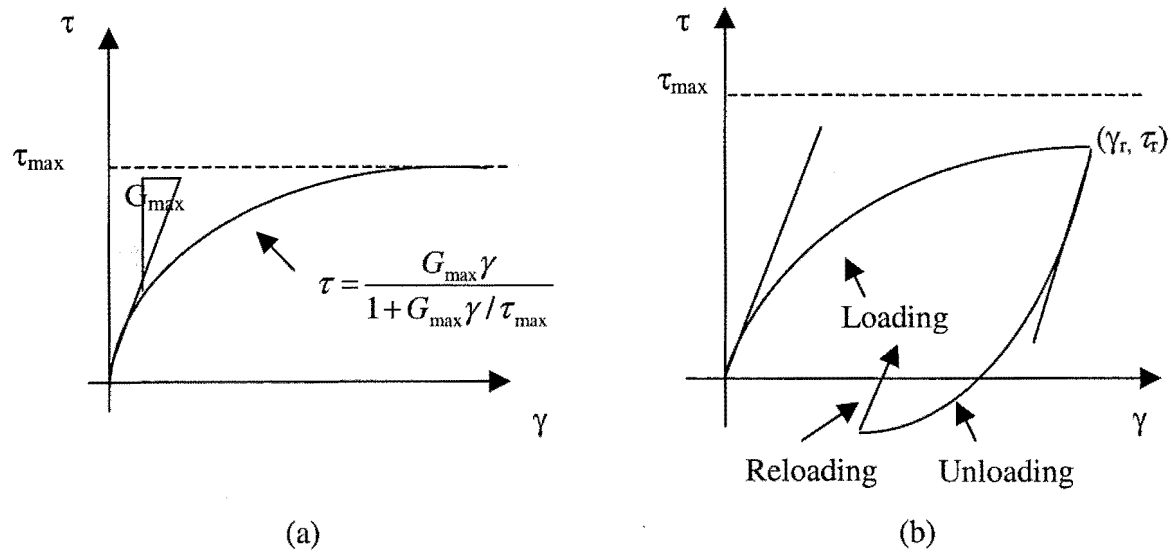

Figure 2.6 (a) Initial Loading Curve; (b) Masing Stress Strain Curve for Unloading and Reloading

Finn et. al. (1976) proposed rules for extending the Masing rule to irregular loading. They suggested that unloading and reloading curves follow the skeleton loading curve when the magnitude of the previous maximum shear strain is exceeded. Fig.2.6 shows the general rules.

The pore pressure model proposed by Martin et. al. (1975) was used in the soil model to represent the change of pore pressure U. The pore pressure model is described as

$$\Delta U = \bar{E}_r \bullet \Delta \varepsilon_{vd} \tag{2.4}$$

in which $\bar{E}_r$ is the rebound modulus and $\Delta\varepsilon_{vd}$ is the volumetric strain increment and are given by

$$\Delta \varepsilon_{vd} = c_1(\gamma - c_2 \varepsilon_{vd}) + \frac{c_3 \varepsilon_{vd}^2}{\gamma + c_4 \varepsilon_{vd}} \tag{2.5}$$

$$\bar{E}_r = \frac{d\sigma_v'}{d\varepsilon_{vr}} = \frac{(\sigma_v')^{1-m}}{\{mK_2(\sigma_{v0}')^{n-m}\}} \tag{2.6}$$

where c_1, c_2, c_3, and c_4 are volume change constants and ε_{vd} is the total accumulated volumetric strain; σ_{v0}' is the initial value of the effective stress and K_2, m and n are experimental constants.

Finally, $[D]$, in the finite element formulation is given by

$$[D] = B_t[Q_1] + C_t[Q_2] \tag{2.7}$$

where B_t and C_t are the tangent bulk moduli and the tangent shear moduli respectively and dependent on the level of mean effective stress $\sigma_m' = \sigma_m - u$, in which σ_m is the total mean normal stress and u the current induced porewater pressure, and $[Q_1]$ and $[Q_2]$ are constant matrices.

The Finn et. al. non-linear model is conceptually simple. A very well known hyperbolic equation was used to represent the basic shear stress strain curve. A modified Masing rule was used to represent irregular loading. In this model, however, pore pressure and volume strain can not be expressed. Martin's pore pressure model was employed to overcome this problem. Using the shear strain, the hyperbolic model and Martin's model were connected together to form Finn's model which has been verified by centrifuge tests and from examination of recorded earthquake response (Finn, 1985).

2.2.3 The Bounding Surface Model

The bounding surface model is an advanced soil model based on classic plasticity such as the nested surface model (Provest, 1977) or the Desai model (Desai, 1984). In terms of classical theory, at a plastic state the loading direction L_{ij} must be along the gradient of a loading surface $f = 0$ passing through the point σ_{ij} in stress space, i.e.

$$f(\sigma_{ij}, q_n) = 0; \qquad L_{ij} = m\frac{\partial f}{\partial \sigma} \tag{2.8a}$$

In the bounding surface model, a bounding surface F in stress space and its stress gradient direction are defined by

$$F\left(\bar{\sigma}, q_n\right) = 0; \qquad \bar{L}_{ij} = \bar{m}\frac{\partial F}{\partial \bar{\sigma}_{ij}} \tag{2.8b}$$

where a bar over stress quantities includes their association with $F = 0$, which always enclose the loading surface $f = 0$ or it may contact it at a point tangentially or even become identical with it but never intersect with it. In terms of this concept, the plastic response depends on how "far" the current stress state σ_{ij} on $f = 0$ is from a corresponding bounding or "image" stress state $\bar{\sigma}_{ij}$ on $F = 0$. The actual plastic modulus and the bounding plastic modulus can be determined:

$$\bar{K}_p = -\bar{m}\frac{\partial F}{\partial q_n} r_n \qquad K_p = \hat{K}(\bar{K}_p, \delta, \sigma_{ij}, q_n) \qquad (2.9)$$

where $\delta = \left[\left(\bar{\sigma}_{ij} - \sigma_{ij}\right)\left(\bar{\sigma}_{ij} - \sigma_{ij}\right)\right]^{1/2}$, r_n is the "direction" of $\dot{q}_n$. A more detailed procedure will be given in Chapter three.

2.3 Analysis Methods for Soil-Structure Interaction

As was mentioned above, in soil-structure interaction analyses the discrete element method and the finite element method have been used widely. Their advantages and disadvantages were introduced by Seed et. al. (1975) and Hadjian et. al.(1974). In the application of both methods, however, there is the same question: how to represent the half-space or far field behaviour. This question has resulted in much research in recent years. The following section will discuss the analysis methods for soil-structure interaction and the representation of the far field.

2.3.1 The Discrete Element Method in Soil-Structure Interaction

The discrete element method for solving soil-structure interaction problems is mostly limited to elastic or viscoelastic representation of the soil. The problem can usually be solved in three steps (Luco and Wong, 1979; Wolf, 1985): (1) the determination of the input motion to the foundation; (2) the evaluation of the force and displacement relationship for the foundation, and (3) the solution of the equations of motion including the superstructure. In most applications it is assumed that the input motion at the level of the foundation is the same as the surface free field motion which is easily determined from free field analysis. Many methods for solving the equation of motion have been proposed, for example the Newmark step by step method. Therefore, the evaluation of the force and displacement for the foundation is a key step. Because the force-displacement relationship is affected by many factors, different models show different characteristics. Here, only the fundamental lumped-parameter model and the Pender model and methods for determining their parameters

will be discussed. The reason for choosing these two models is that the fundamental lumped-parameter model is a fundamental model used as the basis of many of the improved models. The Pender model reflects nonlinear soil characteristics.

2.3.1.1 The Fundamental Lumped-Parameter Model

When compared with the solution of the elastic half space method, the fundamental lumped-parameter model shows its advantage: simple formulation and clear physical meaning. Fig.2.7 displays a mathematical representation of the fundamental lumped-parameter model. If a rigid surface foundation is loaded by a vertical steady state force $Q(\omega)$, the equation of motion can be expressed as

$$m\frac{d^2z}{dt^2}+c\frac{dz}{dt}+kz=Q(\omega) \qquad (2.10)$$

where c is the damping coefficient, k is the stiffness coefficient and z is displacement.

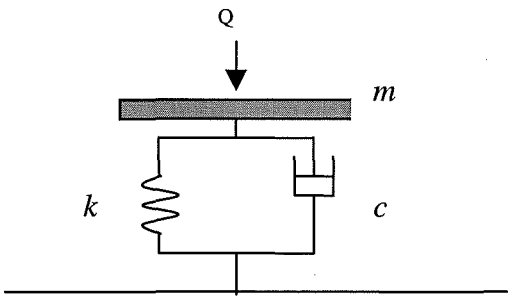

Fig. 2.7 Fundamental Lumped-Parameter Model

The foundation response can be obtained easily by solving Eq.2.10. For different vibration modes, the differential equation of motion of the foundation is the same as Eq.2.10. The difference is that the corresponding damping coefficient c, stiffness coefficient k and loading mode are used. In this procedure, the damping and the stiffness coefficients have to be determined. However, they are affected by many factors, such as soil properties, the size and mass of the foundation and the frequency of the excitation.

If a constant frequency excitation is applied in Eq.2.10, in this situation frequency-independent coefficients can be used. They are also called static damping and stiffness coefficients. Whitman and Richard (1967) investigated the static damping and stiffness coefficients of a rigid circular surface foundation and obtained the following expressions for vertical, horizontal and rocking vibration modes

$$k_v = \frac{4Gr_0}{1-\nu} \quad , \qquad c_v = \frac{3.4r_0}{1-\nu}\sqrt{G\rho} \tag{2.11a}$$

$$k_h = \frac{8Gr_0}{2-\nu} \quad , \qquad c_h = \frac{2.6r_0^2}{2-\nu}\sqrt{G\rho} \tag{2.11b}$$

$$k_r = 8G\frac{r_0^3}{3(1-\nu)} \quad , \qquad c_r = \frac{0.84r_0^4}{(1-\nu)(1+B_\phi)}\sqrt{G\rho} \tag{2.11c}$$

where

$$B_\varphi = \frac{3(1-\nu)I_\phi}{8\rho r_0^5} \quad ,$$

k_v, k_h, k_r, c_v, c_h and c_r are spring stiffness and damping coefficients for vertical, horizontal and rocking modes, respectively, ν is the soil Poisson's ratio, r_0 is the radius of the footing, G is the soil shear modulus, ρ is the soil density and I_ϕ is the mass moment of inertia of the footing with respect to a horizontal axis.

For a rectangular footing, with a length to width ratio of less than 3, the equivalent radius for vertical, horizontal and rocking modes, respectively, can be computed as

$$r_{e,v} = r_{e,h} = \left[\frac{LB}{\pi}\right]^{0.5} \quad \text{and} \quad r_{e,r} = \left[\frac{BL^3}{3\pi}\right]^{0.25} \tag{2.11d}$$

where L and B are the half length and half width of the footing respectively.

In considering a general case, the solution of these equations describes the frequency-dependent relationship between the applied force $P_i(t)$ and the corresponding displacement amplitude $u_i(t)$ in compact form

$$P_i(t) = Q_i u_i(t) \tag{2.12a}$$

where Q_i is the complex stiffness given by

$$Q_i = K_{s,i}(k_i + ia_0 c_i) \tag{2.12b}$$

the real part of which represents the spring coefficient, and the imaginary part represents the damping coefficient.

Velesos and Verbil (1973) investigated the dynamic response of a rigid surface footing resting on an elastic half space. The relationship between force and displacement can be written as

$$P = K_{s,i}[k_i(a_0, v) + ia_0 c_i(a_0, v)]u_0 \tag{2.13a}$$

where $K_{s,i}$ is the stiffness constant in the vibration mode i, and k_i and c_i are the dynamic stiffness and damping coefficients respectively of vibration mode i. Based on the results of the shear cone analysis (Wolf, 1994), the coefficients k_i and c_i for the vertical, horizontal and rocking modes of a rigid circular surface foundation were approximated by

$$k_v = 1 - b_1 \frac{(b_2 a_0)^2}{1 + (b_2 a_0)^2} - b_3 a_0^2 \tag{2.13b}$$

$$k_h = 1 \tag{2.13c}$$

$$k_r = 1 - d_1 \frac{(d_2 a_0)^2}{1 + (d_2 a_0)^2} - d_3 a_0^2 \tag{2.13d}$$

$$c_v = b_4 + b_1 b_2 \frac{(b_2 a_0)^2}{(1 + b_2 a_0)^2} \tag{2.13e}$$

$$c_h = a_1 \tag{2.13f}$$

$$c_r = d_1 d_2 \frac{(d_2 a_0)^2}{1+(d_2 a_0)^2} \tag{2.13g}$$

The values of a, b and d for any value of soil Poisson's ratio, ν, were tabulated in Velesos and Verbic (1973, 1974). After these values are obtained, the fundamental lumped-mass model can be used to predict the response of the structure on the surface foundation.

2.3.1.2 The Pender Model (1983)

According to the test results, the energy dissipated per loading and unloading cycle of soil is independent of the frequency of loading (at least over the range of frequencies of interest in earthquake engineering) (Larkin, 1976), and the stiffness and hysteretic damping of soil have a nonlinear relationship with strain. Pender (1983) proposed a two layered model shown in Fig.2.8. The first layer spring represents the zone of soil immediately beneath the footing which will deform nonlinearly. The second layer Winkler-Voigt model represents the small strain elastic behaviour of the soil remote from the footing that will deform elastically. The depth of the nonlinear zone is approximately one footing diameter. Pender also recommended a method to determine the coefficients for the model. Firstly, the two springs in series are reduced to an equivalent viscously damped spring, the parameters of which are given by

$$K = k_e /(k_e + k_n) \tag{2.14a}$$

$$C = k_c c_e /(k_e + k_n) \tag{2.14b}$$

where k_e and c_e are the stiffness and damping values for the spring representing the small strain behaviour of the soil and k_n is the stiffness of the nonlinear spring which incorporates the hysteretic damping.

The stiffness of the nonlinear spring k_n can be determined by a finite element analysis. However, this is too expensive for meeting earthquake loading studies. A numerical version of the stress path method to k_n is recommended by Pender (1983). The procedure can be described as:

(a.) Select a characteristic point beneath the centre of the footing where the nonlinear strain increments are the maximum.

(b.) By using a pseudo Poisson's ratio the stress increments, which are caused by load increments, are calculated

(c.) Strain increments are calculated by a soil model proposed by Graham (1982) and modified by an averaging factor to get the average strain for the soil.

(d.) Calculate the incremental nonlinear stiffness.

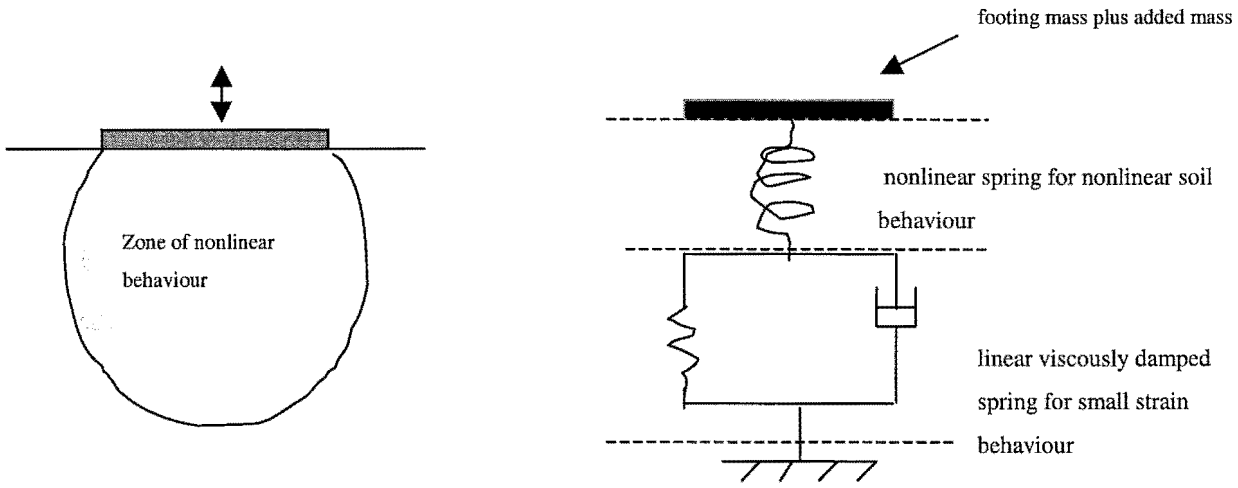

Fig. 2.8 Modelling of Nonlinear Soil Behaviour Beneath a Footing
(a) Physical Situation; (b) Representation with Equivalent System

2.3.2 Finite Element Method in the Soil-Structure Interaction

The finite element method has been widely used in earthquake engineering. However, when the finite element is used in soil-structure interaction analysis, the simulation of a far field domain has to be considered. A general method is to enforce an artificial boundary at the contact interface between the structure and ground. The artificial boundary can not consist of elementary boundary conditions because it is given prescribed displacements or stresses when the load is applied directly to the structure so that they can not transmit waves into the infinite domain. Therefore, in seismic soil-structure interaction analysis, three aspects need to be considered. They are the structural model, the soil model and the far field model. Some soil models have been discussed in section 2.3 and structural models will be discussed in Chapter three. The following section will discuss only the far field models, the viscous dashpot transmitting boundary (Lysmer and Richard, 1969), the Zhao, Carr and Moss discrete wave number indirect boundary element method (Zhao et al, 1997) and the boundary element method in the time domain (Manolis and Beskos, 1989).

2.3.2.1 The Viscous Dashpot Transmitting Boundary

The viscous dashpot transmitting boundary is shown in Fig.2.9. In the two dimensional case where the waves impinge perpendicular to the artificial boundary, the exact transmitting boundary condition is formulated as in Eqs. 2.15a and 2.15b. Here, $\sigma(s)$ and $\tau(s)$ are the normal and shear stresses on the boundary, $u(s)$ and $v(s)$ are the normal and tangential displacements, c_p represents the dilatational-wave velocity and s denotes the coordinate on the artificial boundary. In a discretised form it is customary to lump the distributed dampers described by the above equations, which results in dashpots with coefficients c_n and c_t in the normal and the tangential direction at each node in the boundary.

$$\sigma(s) + \rho c_p \dot{u}(s) = 0 \qquad (2.15a)$$

$$\tau(s) + \rho c_s \dot{v}(s) = 0 \qquad (2.15b)$$

$$c_n = A\rho c_p \qquad (2.16a)$$

$$c_t = A\rho c_s \qquad (2.16b)$$

A - area; ρ - soil density

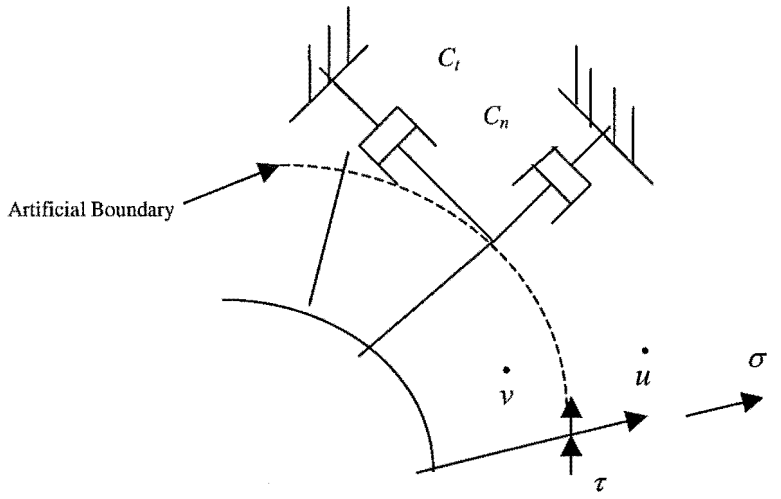

Fig. 2.9 Viscous Dashpot Transmitting Boundary

where $\dot{u}$ and $\dot{v}$ are normal and tangent velocity. These local viscous dashpots represent the exact solution for P- and S-waves which impinge perpendicular to the artificial boundary. They are an approximation for an inclined P-wave, where the reflected energy is only a small part of the total energy (Lymser and Richard, 1969). In many cases, the further the artificial boundary is from a source which radiates waves, the more the angle of incidence with respect to the artificial boundary will approach 90^0 and thus the better the viscous dashpot model will perform.

Although a certain caution is appropriate for surface waves, the viscous dashpots represent a suitable transmitting boundary for many applications involving both dilatational and shear waves. The accuracy is generally acceptable and the procedure is simple and easily implemented in most analyses.

2.3.2.2 The Zhao, Carr and Moss Discrete Wave Number Indirect Boundary Element Method

Zhao, Carr and Moss (1997) proposed a discrete wave number indirect boundary element method. It can be employed as a transmitting boundary to calculate both

surface and embedded foundations. When compared with other special methods, the method can solve the problem of a foundation resting on a multi-layered half space and can directly couple with the finite element method to solve the nonlinear problem of the near field.

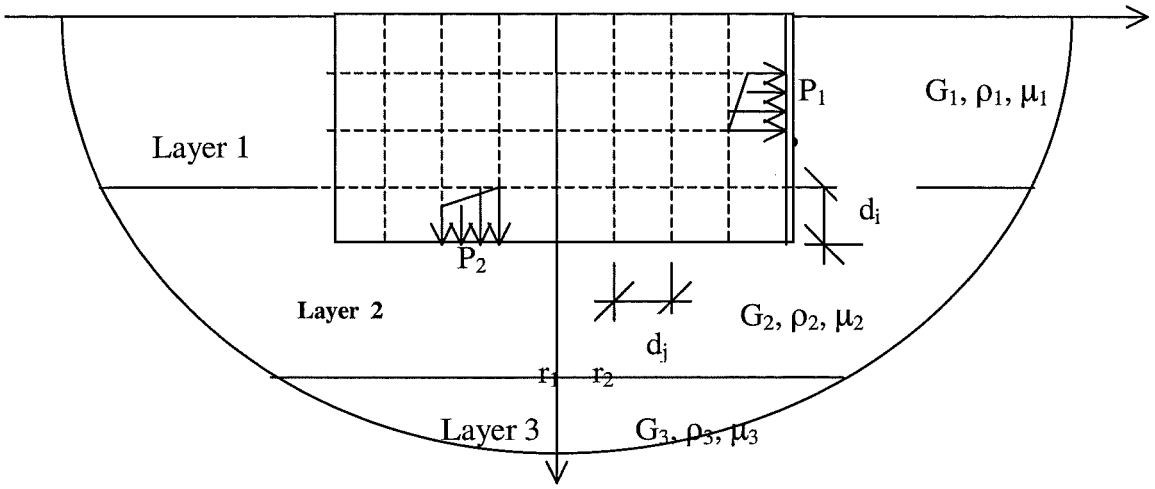

Figure 2.10 Mathematic model of discrete wave number indirect boundary element method

The mathematical model is shown in Fig.2.10. Firstly, the method divides the boundaries into a vertical boundary and a horizontal boundary. When load acts on the vertical boundary, its Green's function can be calculated on the vertical and the horizontal boundaries. Then when load acts on the horizontal boundary, its Green's function can be calculated on the vertical and the horizontal boundaries. The total effects will be the summation from both components.

Based on the above, the displacement of element i caused by the piece-wise linearly distributed loads on element j of a vertical boundary in a layered half space can be written in the wave number domain in matrix form as

$$\{u_{vv}(k,z)\}_{ij} = \left[g^{u}_{vv}(k,z)\right]_{ij}\left\{\bar{p}_N(k)\right\}_j \tag{2.17a}$$

where

$$\{u_{vv}(k,z)\}^T = [u(k,z) \quad iw(k,z)] \tag{2.17b}$$

and $$\left\{\bar{p}_N(k)\right\}^T = [p_1(k) \quad ir_1(k) \quad p_2(k) \quad ir_2(k)] \tag{2.17c}$$

where k represents the wave number. The displacement Green's function is

$$\left[g^u_{vv}(k,z)\right]_{ij} = [G_u(z)]_i \left[G^A\right]_i^{-1} \left[F^s_{vv}\right]_{ij} \left[G^E\right]_j \tag{2.18}$$

$[F^s_{vv}]_{ij}$ is a sub-matrix of the system flexibility matrix for the layered half space and has been given by Wolf (1985). $[G_u(z)]_i$, $\left[G^A\right]_i^{-1}$ and $\left[G^E\right]_j$ have been given by Zhao, Carr and Moss (1997).

For the Green's functions of element i due to the loads on itself, the total response is given by

$$\left[g^u_{vv}(k,z)\right]_{ii} = [G_u(z)]_i \left[G^A\right]_i^{-1} \left\{\left[F^s_{vv}\right]_{ii} \left[G^E\right]_i - \left[F^p\right]_i\right\} + \left[\bar{g}^p_u(k,z)\right]_i \tag{2.19}$$

where matrix $[\bar{g}^p_u(k,z)]$ is the displacement Green's function from the particular solution given by Zhao (1989). $[F^p]$ is the nodal displacement matrix from the particular solution given by Wolf (1985).

For the horizontal boundary, the displacements due to the loads on element j of the vertical boundary are given by

$$\left\{u_{hv}(k)\right\}_j = \left[g^u_{hv}\right]_j \left\{\bar{p}_N(k)\right\}_j \tag{2.20a}$$

where the Green's function is given by

$$\left[g^{u}_{hv}(k)\right]_j = \left[F^{s}_{hv}\right]_j \left[G^{E}\right]_j \tag{2.20b}$$

Matrix $[F^{s}_{hv}]_j$ is defined as for $[F^{s}_{vv}]_{ij}$ but corresponds to the displacement of the horizontal boundary and the loads on element j of the vertical boundary.

The displacements of the horizontal boundary due to the linearly distributed loads on element j of the same boundary are given by

$$\left\{u_{hh}(k)\right\}_j = \left[g^{u}_{hh}\right]_j \left\{\bar{p}_N\right\}_j \tag{2.21a}$$

where $$\left[g^{u}_{hh}(k)\right]_j = \left[F^{s}_{hh}\right]_j \left[L(k)\right]_j \tag{2.21b}$$

Matrix $[F^{s}_{hh}]_j$ corresponds to both the displacements and the loads of the horizontal boundary. $[L(k)]_j$ is the Fourier transform of the load interpolation function.

In Eqs. 2.18 to 2.21, the Green's functions have to be transformed into the spatial domain. The displacements in the spatial domain can be written following Bouchon and Aki (1987) as

$$F(x,z) = \int_{-\infty}^{+\infty} f(k,z) e^{-ikx} dk \tag{2.22}$$

and can be approximated by

$$F(x,z) = \frac{2\pi}{L_I} \sum_{n=-N}^{N} f(k_n, z) e^{-ik_n x} \tag{2.23a}$$

$$k_n = \frac{2\pi}{L_I} n \tag{2.23b}$$

In the above, all displacement Green's functions have been obtained and can be transformed into the spatial domain from the wave number domain. Now following

the indirect boundary element method proposed by Wolf (1985) and Wolf and Darbre (1984a,b), the dynamic stiffness matrix of a foundation can be written generally as

$$[S_{bb}] = [T]^T [G]^{-1} [T] \tag{2.24}$$

For surface foundations, these matrices are given by

$$[G] = \int_s [L(s)]^T [g^u(s)] ds \tag{2.25a}$$

$$[T] = \int_s [L(s)]^T [N(s)] ds \tag{2.25b}$$

For embedded foundations these matrices are given by

$$[G] = \int_s [g^t(s)]^T [g^u(s)] ds \tag{2.26a}$$

$$[T] = \int_s [g^t(s)]^T [N(s)] ds \tag{2.26b}$$

where $[g^t(s)]$ is the Green's functions for a surface traction at the boundary in the spatial domain.

At low frequencies the stiffness matrix of embedded foundations can be separated into the free field and the excavated parts (Wolf 1985)

$$[S_{bb}^g] = [S_{bb}^f] - [S_{bb}^e] \tag{2.27}$$

The dynamic stiffness matrix of the free-field $[S_{bb}^f]$ can be calculated by Eqs.2.24 as for a surface foundation. That of the excavated part can be modelled by the finite element method. The main advantage of this separation is that the surface traction Green's functions are not required.

The numerical results calculated by the method were compared with the published results to confirm the advantages and accuracy of this method (Zhao et. al, 1997).

2.3.2.3 Integration Direct Boundary Element Method in the Time Domain

As described above, the Zhao, Carr and Moss discrete wave number indirect boundary method can express the far field very well, but it works in the wave number domain. If the near field is nonlinear and the far field is linear, finite elements can be used to model the near field and the above methods can be used to model the far field. However, they work in different domains so that a FFT has to be used to transform them from the frequency domain to the time domain. It is clear that the boundary element method in the frequency domain is computationally expensive when nonlinear and large calculations are carried out. To overcome this difficulty, the general integration direct boundary element methods in the time domain were proposed by Niwa et al (1980), Manolis (1983) and Karabalis & Beskos (1984), This method will be discussed in detail in Chapter five.

2.4 The Coupling Methods for the Boundary Element and the Finite Element Methods in Soil-Structure Interaction Analysis

In the boundary element method, known fundamental solutions of the governing differential equations can be used to obtain solutions for the boundary value problem and meet the radiation condition automatically. This means that only the boundary of the domain to be analysed has to be discretised, in contrast with the finite element method, which requires a subdivision of the whole domain. The finite element method however, is suitable for the solution of nonlinear and irregular geometric problems. Therefore, the coupling of the boundary element and the finite element is to use the advantages of the both numerical methods.

Zienkiewicz, Kelly and Bettes (1977) were among the first authors to propose the coupling of the boundary element and the finite element methods. In recent years,

several researchers have focused their attention on the development of coupling procedures for elastodynamic problems. Kobayashi and Mori (1986) have used a combination of the boundary element with the finite element methods for the solution of soil-structure interaction problems in the frequency domain. Spyrakos and Beskos (1986) and Karabalis and Beskos (1985), respectively, considered plane and three-dimensional soil-foundation interaction problems in the time domain using boundary elements for the soil and finite elements for the foundation. Esttorff and Prabucki (1990) applied the coupling of the boundary element method and the finite element method to dynamic analysis of elastic bodies. Feng and Owen (1997) proposed a general iteration coupling procedure. In this section, only Esttorff and Probucki's coupling method and Feng and Owen's method will be discussed in detail.

2.4.1 Esttorff and Prabucki's Method of Coupling Boundary Elements and Finite Elements

According to Antes (1985) and Estorff (1986), the system of algebraic equations for the boundary element domain can be expressed as

$$\left(\frac{1}{2}[I]+[T]\right)\{\bar{u}\}=\left[\bar{T}\right]\{\bar{u}\}=[U]\{s\} \tag{2.28}$$

where $\bar{u}$ and s are vectors of all nodal displacements and tractions, respectively, $[U]$ and $[T]$ represent influence matrices which contain integral terms evaluated over each boundary element and over each time step. According to causality conditions, these matrices are lower triangular and composed of block submatrices.

Considering the above properties of the matrices, a relation between $\{u\}$ and $\{s\}$ can be given as

$$[U^{(1)}]\{s^{(m)}\}+\sum_{p=1}^{m-1}[U^{m-p+1}]\{s^{(p)}\}=[T^{(1)}]\{u^{m}\}+\sum_{p=1}^{m-1}[T^{(m-p+1)}]\{u^{(p)}\} \tag{2.29}$$

which is valid for each time step m. Rearranging gives

$$\{s^{(m)}\}=[Q^{(1)}]\{u^{(m)}\}+\sum_{p=1}^{m-1}[Q^{(m-p+1)}]\{u^{(p)}\}-\sum_{p=1}^{m-1}[H^{(m-p+1)}]\{u^{(p)}\} \tag{2.30}$$

where

$$[Q^{(m)}]=[U^{(1)}]^{-1}\{T^{(m)}\} \quad \text{, and} \quad [H^{(m)}]=[U^{(1)}]^{-1}\{U^{(m)}\} \tag{2.31}$$

For the finite element domain, a dynamic equilibrium equation is obtained. If an integration method is used, the effective dynamic equilibrium equation can be expressed as

$$[K_{eff}]\{u^{(m)}\}=\{p_{eff}^{(m)}\} \tag{2.32}$$

Fig.2.11 shows the finite element and boundary element domains. It is easy to distinguish between the nodes on the non-interface and those on the interface of the boundary element domain and the finite element domain. Then the boundary element equilibrium equation can be expressed in terms of the non-interface and interface nodes as

$$\begin{Bmatrix}\{s_i^{B(m)}\}\\ \{s_o^{B(m)}\}\end{Bmatrix}=\begin{bmatrix}[Q_{ii}^{(1)}] & [Q_{io}^{(1)}]\\ [Q_{oi}^{(1)}] & [Q_{oo}^{(1)}]\end{bmatrix}\times\begin{Bmatrix}\{u_i^{B(m)}\}\\ \{u_o^{B(m)}\}\end{Bmatrix}$$

$$+\sum\left\{\begin{bmatrix}[Q_{ii}^{(m-p+1)}] & [Q_{io}^{(m-p+1)}]\\ [Q_{oi}^{(m-p+1)}] & [Q_{oo}^{(m-p+1)}]\end{bmatrix}\times\begin{Bmatrix}\{u_i^{B(p)}\}\\ \{u_o^{B(p)}\}\end{Bmatrix}-\begin{bmatrix}[H_{ii}^{(m-p+1)}] & [H_{io}^{(m-p+1)}]\\ [H_{oi}^{(m-p+1)}] & [H_{oo}^{(m-p+1)}]\end{bmatrix}\times\begin{Bmatrix}\{s_i^{B(p)}\}\\ \{s_o^{B(p)}\}\end{Bmatrix}\right\} \tag{2.33}$$

where subscript *i* and *0* represent interface and non-interface boundaries respectively.

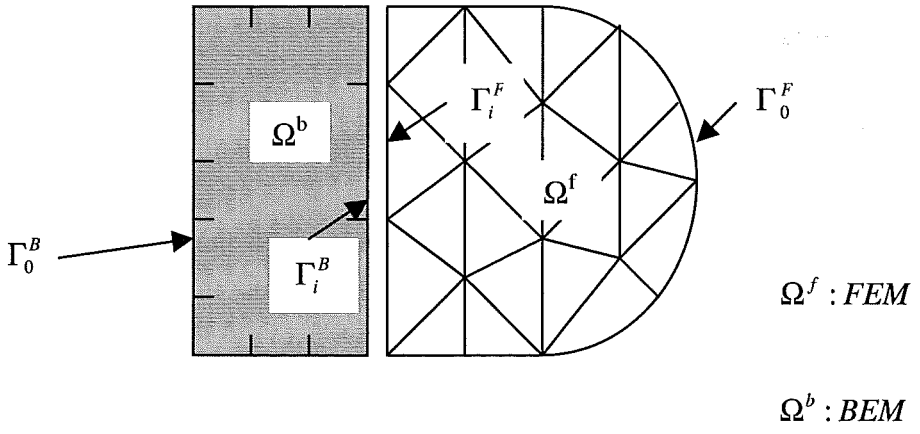

Fig. 2.11 BE and FE Subdomains of an Elastic Domain

By separating $\{u_0^{B(m)}\}$ from the lower part and substituting it into the upper part, one obtains

$$\begin{aligned}\{s_i^{B(m)}\} &= [K_{ii}^B]\{u_i^{B(m)}\} + [G]\{s_o^{B(m)}\} + \sum_{p=1}^{m-1}\{[Q_I^{(m-p+1)}]\{u_i^{B(p)}\} + [Q_{II}^{(m-p+1)}]\{u_o^{B(p)}\} - [H_I^{(m-p+1)}]\{s_i^{B(p)}\} \\ &\quad - [H_{II}^{(m-p+1)}]\{s_o^{B(p)}\} \\ &= [K_{ii}^B]\{u_i^{B(m)}\} + \{P_i^{B(m)}\} \end{aligned} \tag{2.34}$$

Assuming the tractions $\{s\}$ along the outer boundary are given, only $\{s_i^{B(m)}\}$ and $\{u_i^{B(m)}\}$ at the interface are unknown. The matrix $[K_{ii}^B]$ physically denotes the resistance developed by the boundary element sub-domain at the interface of the boundary element and finite element domain.

The same procedure can be applied to the finite element domain. Interface nodes connected with the boundary element domain and non-interface nodes are separated as for the boundary element domain.

To obtain consistency between the finite element and boundary element formulations, the interface tractions $\{s\}$ in the boundary element domain have to be transformed to resultant nodal forces according to Eq.2.35.

$$\{s_i^B\} = [A]\left\{\bar{s}_i^B\right\} \tag{2.35}$$

$\left\{\bar{s}_i^B\right\}$ - nodal force vector

Based on compatibility conditions, the assemblage of the relationship yields an expanded system of equations

$$\begin{bmatrix} [K_{oo}^F] & [K_{oi}^F] & [0] \\ [K_{oi}^F]^T & [K_{ii}^F] & [A] \\ [0] & [K_{ii}^B] & [I] \end{bmatrix} \begin{Bmatrix} \{u_o^{F(m)}\} \\ \{u_i^m\} \\ \{s_i^{(m)}\} \end{Bmatrix} = \begin{Bmatrix} \{P_o^{F(m)}\} \\ \{P_i^{F(m)}\} \\ \{P_i^{B(m)}\} \end{Bmatrix} \tag{2.36}$$

which gives the unknown displacements $\{u_0^F\}$, $\{u_i\}$ and the interface nodal forces $\{s_i\}$ in each time step m. Once these values are known, it is straight-forward step to determine the displacements of the outer boundary by using the lower partition of Eq.2.33.

2.4.2 Feng and Owen's Coupled Boundary Element and Finite Element Method

Feng and Owen (1997) reviewed the present coupling methods for boundary elements and finite elements. They found that the programs for finite elements and boundary elements are quite different in terms of data structures, program organisation and numerical techniques. Thus, merging two different kinds of programs together to form an integrated finite element and boundary element environment would require considerable effort. Therefore, they proposed a method in which the boundary element equations are not explicitly assembled into the finite element equations, but instead used an iterative scheme to obtain the final solution. This procedure will be discussed in detail in this section.

Usually, the finite element analysis of the foundation plate yields the following linear equation:

$$[K_p]\{U\}=\{F\}-\{R\} \tag{2.37}$$

where $[K_p]$ is the global stiffness matrix of the foundation plate, $\{F\}$ is the external loading, $\{U\}$ is the nodal unknown of the foundation plate and $\{R\}$ is the interactive force between the foundation plate and the soil, which is also unknown.

In general, the boundary element equation of the elastic foundation takes the form

$$[H]\{U\}=[G]\{P\} \tag{2.38}$$

where $[H]$, $[G]$ are coefficient matrices, usually fully populated and unsymmetric, $\{U\}$ are the nodal unknowns of the foundation plate and $\{P\}$ are the nodal tractions. For an elastic half-space, the BE formulation can be greatly simplified if we adopt the Boussinesq solution as the fundamental solution. Therefore the vertical displacement of the foundation surface is

$$\{W_f\}=[G]\{P\} \tag{2.39}$$

in which $\{W_f\}$ represents the vertical displacements of the surface of the foundation.

In order to couple Eqs. 2.37 and 2.39 to form the final equations, displacement compatibility and force equilibrium need to be imposed. The displacement condition can be written as

$$\{W_f\}=[E]^T\{U\} \tag{2.40}$$

where $[E]=[\,I_m,\ 0,\ 0]^T$ is a matrix which extracts the unknown vector from $\{U\}$. The equilibrium condition requires

$$\{R_f\}=\{R_p\} \tag{2.41}$$

where $\{R\}=[E]\{R_p\}$. Since the boundary element method uses nodal tractions instead of nodal point forces, a relationship between tractions and nodal forces on the boundary element should be established. Usually, this relationship takes the form

$$\{R_f\}=[T']\{P\} \tag{2.42}$$

where $[T]$ is the conversion matrix. Therefore, the equilibrium condition can be expressed as

$$\{R\}=[E][T']\{P\} \tag{2.43}$$

Using Eq.2.42, we can rewrite Eq.2.40 as

$$[K_f]\{W_f\}=\{R_f\} \tag{2.44}$$

in which $[K_f]$ is the equivalent stiffness matrix of the boundary element region with

$$[K_f]=[T']^{-1} \tag{2.45}$$

Combining Eqs. 2.37 and 2.44 gives the following final coupled equations

$$([K_p]+[E][K_f][E]^T)\{U\}=\{F\} \tag{2.46}$$

Hence, the final solution will be

$$\{U\}=([K_p]+[E][K_f][E])^{-1}\{F\} \tag{2.47}$$

The above procedure is a direct solution scheme. However, calculation of $[G]^{-1}$ is computationally very expensive. An iterative solution scheme is proposed. Firstly, Eq.2.46 is rewritten in iterative fashion as

$$[K_p]\{U_{n+1}\}=\{F\}-[E][M][G]^{-1}[E]^T\{U_n\} \tag{2.48}$$

where the scheme of iteration is as follows

(1) Given the initial guess $\{R_0\}$

(2) For n = 0, 1, 2, ……,

Solve $[K_p]\{U_{n+1}\}=\{F\}-\{R_n\}$

Extract $\{W_{n+1}\}=[E]^T\{U_{n+1}\}$

Solve $[G]\{P_{n+1}\}=\{W_{n+1}\}$

Convert $\{R_{n+1}\}=[E][M]\{P_{n+1}\}$

Until

$$\frac{\|\{U_{n+1}\}-\{U_n\}\|}{\|\{U_{n+1}\}\|}<\varepsilon \qquad \text{(given tolerance)}$$

The above method was successfully used to analyse foundation plate and soil interaction.

2.5 Summary

As mentioned above, many earthquake records have shown the effect of soil-structure interaction on the structural response to be very important in seismic structural analysis. In this Chapter, the Mexico City earthquake of 1985 and the Loma Prieta earthquake of 17th October 1989 were used to illustrate the significant importance of the soil-structure interaction.

Even though the linear soil model is widely used for soil-structure interaction analysis and is helpful in seismic structural analysis, an advanced elasto-plastic soil model is a better alternative. In more recent years, the advanced elasto-plastic soil models, especially the bounding surface models, have been used to analyse local site response. It is therefore worthwhile to investigate their application in soil-structure interaction.

When comparing the discrete element method with the finite element method, if nonlinear soil response caused by earthquake excitation is considered in the calculation, the finite element method is the most suitable approach. If only linear soil response and regular sites are considered, the discrete element method is more suitable than the finite element method. The selected calculation method, therefore, is mainly determined by the objective of the analysis.

In the finite element method, the far field expression is a very important aspect as mentioned above. Usually, transmitting boundaries such as Lysmer's dashpot boundary are used to represent the far field. The boundary element method is, however, a better alternative. Boundary elements in the frequency domain are usually used in linear analyses. When the boundary element method is used for a nonlinear analysis and a FFT has to be used, this procedure will be very expensive. In this situation, the boundary element method in the time domain shows its advantages. At

present, although the boundary element in the time domain has disadvantages, such as it can be only used with a homogenous half space or a layered homogenous material, it is very convenient when coupled with finite elements in a nonlinear analysis.

In order to get benefit from the boundary element and finite element methods, they should be coupled. In more recent years, many different techniques have been proposed. In this Chapter, only two methods have been introduced in detail. The purpose is to use their advantages, such as directly coupling the boundary elements and finite elements to reduce programming effort.

In this thesis, the bounding surface model proposed by Dafalias and Herrmann (1986) will be used as a soil model and implemented into a soil-structure interaction analysis program called SSINAP2D. The boundary element method in the time domain will be implemented into the boundary element code. A coupled boundary element and finite element method will be proposed. Its main advantage is to use existing boundary element and finite element packages. In the coupling procedure, only a small revision is required. The code SSINAP2D is firstly used to analyse the nonlinear local site amplification of soft clay, then its results are used to calculate the structural responses which are compared with linear analysis results. Finally, linear soil-structure interaction and nonlinear soil-structure interaction are investigated. In these calculations, the calculated soil domain is 100m wide ×30m deep. Some conclusions are given in Chapter Nine.

Chapter Three

Near Field Modelling, Structural Modelling, Numerical Integration Methods and Numerical Implementations

3.1 Introduction

As mentioned in Chapter two, in soil-structure interaction analysis the soil is one of the important factors and displays strong nonlinear behaviour. Generally, the nonlinear behaviour of the soil can be represented by a simplified elastoplastic model or an advanced elastoplastic model. Some simplified models have been introduced. In this Chapter, only the advanced models will be discussed in detail. They will then be implemented a computer code.

Soil displays complicated properties that can be shown by test results. Several typical stress-strain curves for soils in triaxial tests are shown in Fig.3.1a. For normally consolidated clay in a drained test, the relationship between the deviatoric stress σ_1-σ_3 and the axial strain ε_3 is characterised by a nonlinear response curve, which rises at a lower rate after reaching a certain stress level. Straining is always associated with an increase in stress, namely strain-hardening. For overconsolidated clay in a drained test, the phenomena of strain-softening occurs. Sand, however, shows different properties from clay. In Fig.3.1b, loose sand in a drained test shows strain-hardening. Both loose sand in an undrained test and dense sand in a drained test show strain-softening. From the above test results, it can be concluded that a soil has strong nonlinear and strain-dependent characteristics and is affected by many factors such as consolidation, drained conditions, etc.

Because of this inherent complexity, many soil models have been proposed to describe soil behaviour ranging from very simple models to very complicated models. These can be summarised as linear elastic models, hyperbolic-elasticity models and elasto-

plasticity models. Usually, an elasto-plasticity model is the best practical model. This elasto-plasticity model can be further separated into two parts; one being the simple elasto-plasticity model that is expressed by loading and unloading curves, but can not directly calculate pore pressure, the other being the advanced elasto-plasticity model that can directly calculate pore pressure and permanent deformation. More recently, advanced elasto-plasticity models have been used to study seismic soil-structure interaction (Lacy and Provest, 1986, Anandarajah et al., 1995, Li et al. 1997).

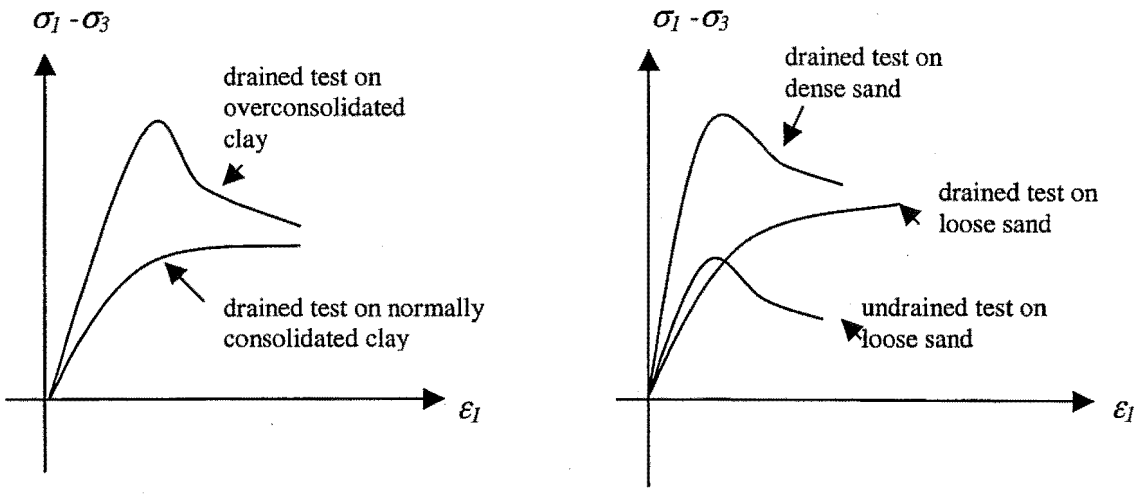

a. Normal Consolidation Clay b. Sand

Figure 3.1 Relation between Deviatoric Stress and Strain

Usually, an advanced elasto-plasticity model originates from classical plasticity and is developed to reflect the main dynamic soil properties. The critical state concept is one of the most important developments and has been widely accepted in soil mechanics. Many sophisticated soil models have been proposed under this theoretical framework. A brief introduction to the theory is given below.

In the following section, the stress parameters in the triaxial space are defined as

$$p = (\sigma_1 + 2\sigma_3)/3 \tag{3.1}$$

$$q = \sigma_1 - \sigma_3 \tag{3.2}$$

where σ_1 and σ_3 are the axial and radial effective stresses and $\sigma_2 = \sigma_3$.

In the triaxial test of a virgin soil sample under a drained condition, the mean effective normal stress p and the void ratio e are related by a simple function when the deviatoric

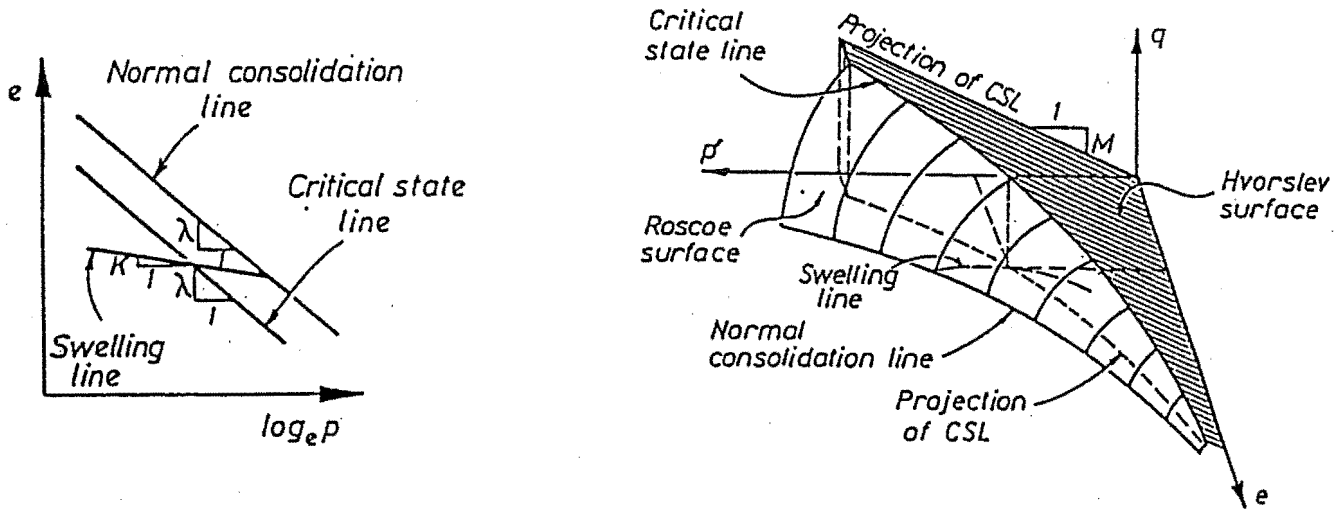

a b

Figure 3.2 Critical State Line and its Projection

stress q is absent. On the plot of void ratio e versus the logarithm of the mean effective normal stress p, the test result can be approximated by a straight line with a slope λ for loading and κ for unloading as shown in Fig.3.2a. They are referred to as the normal consolidation line (NCL) and the swelling line respectively. If q is not zero, at failure, p, q and e are related by a unique function referred to as the critical state line (CSL) in $p - q - e$ space as shown in Fig.3.2b. The projection of CSL on the $p - q$ plane is a straight line with a slope M while on the $e - Log_e p$ plane it is a straight line parallel to the normal consolidation line as shown in Fig.3.2a. These relationships for all normally consolidated soils are valid under both drained and undrained tests and λ, κ and M are constants for the same soil condition. In the $p - q - e$ space, the continuous surface connecting NCL and CSL is referred to as a Roscoe surface under which over-consolidated states are defined and above which are impossible states. The soil states under the Roscoe surface are described as 'wet' because the soil has higher water content than at the critical state. On the other side of the CSL, a surface which intersects with the Roscos surface along the CSL is called a Hvorslev surface along which the

heavily over-consolidated clay sample reaches the critical state. Soil states under the Hvorslev surface are described as 'dry'. These surfaces are shown in Fig.3.2a.

Based on the critical state concept, various plasticity models for soils have been developed. For example: in the Cap Model, the projection of the CSL in the $p - q$ plane is adopted as a fixed yield surface and the cap is adopted as a moving yield surface to implement the hardening behaviour of the soil. It has been recognised that these models can represent most of the important aspects of the soil under monotonic loading and are relatively simple to implement in the finite element method. For cyclic loading, these models usually fail to satisfactorily predict some of the important aspects of soil behaviour. Because only an isotropic hardening rule is adopted, when the loading is reversed plastic strain can not be induced before the previously applied load is removed completely and the stress state point touches the yield surface again at the opposite side of the stress space. Soil usually does not behave elastically under cyclic loading within the yield surface defined in these models. In recent years, more sophisticated models have been developed for soil under cyclic loading. They are usually very complex mathematically and involve more parameters. A critical review on these models has been given by Chen and Mizuno (1990).

In 1967, Moroz introduced the nested surface model into the theory of plasticity. Since then this model has been developed to predict soil behaviour, and some modifications have been introduced by Prevost (1977), and Moroz, Norris and Zienkiewicz (1979) to model the important aspects of soil under cyclic loading. This model introduces a series of yield surfaces which can translate with no rotation and change their sizes in the stress space during the loading and unloading procedure as illustrated in Fig. 3.3, and kinematic and isotropic hardening rules are used. In this model, both origin anisotropy and plastic strain induced anisotropy behaviour can be described adequately and accuracy to a required level can be achieved by introducing the necessary number of yield surfaces. The disadvantage of the model is the extensive memory requirement in a numerical implementation.

To overcome the shortcomings of the model, a bounding surface model was proposed by Dafalias and Popov (1976) and Krieg (1975) and introduced into soil mechanics by

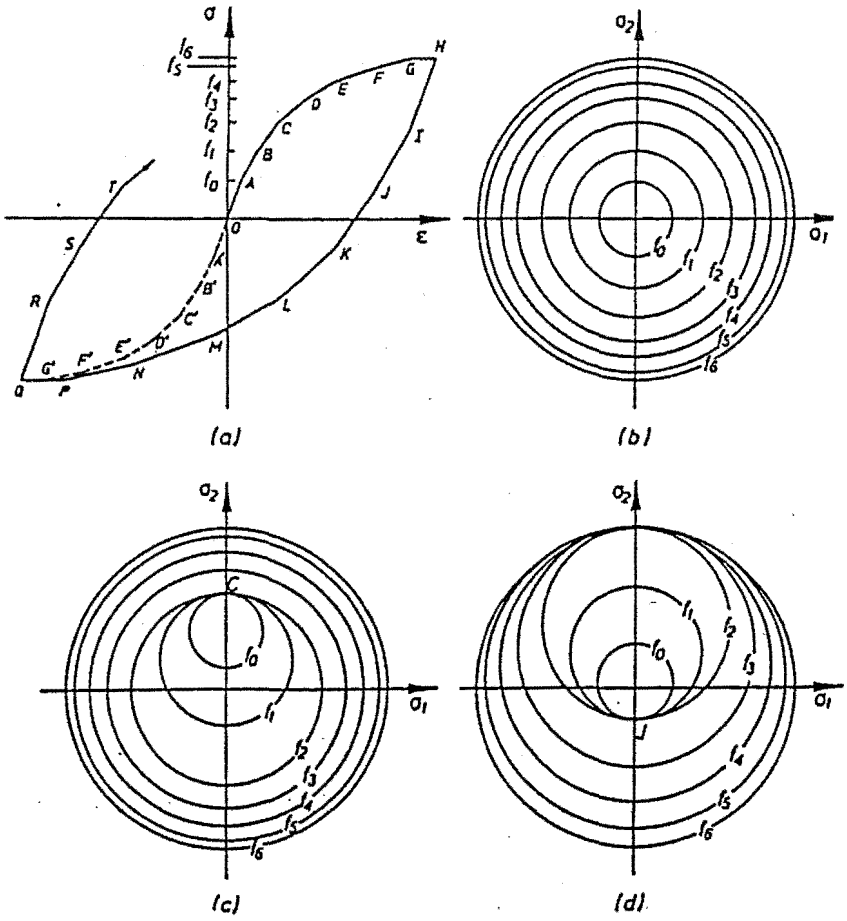

Figure 3.3 Nested Surface Model (a) Stress-Strain Curve (b) Before Loading
(c) Loading Behaviour (d) Unloading Behaviour

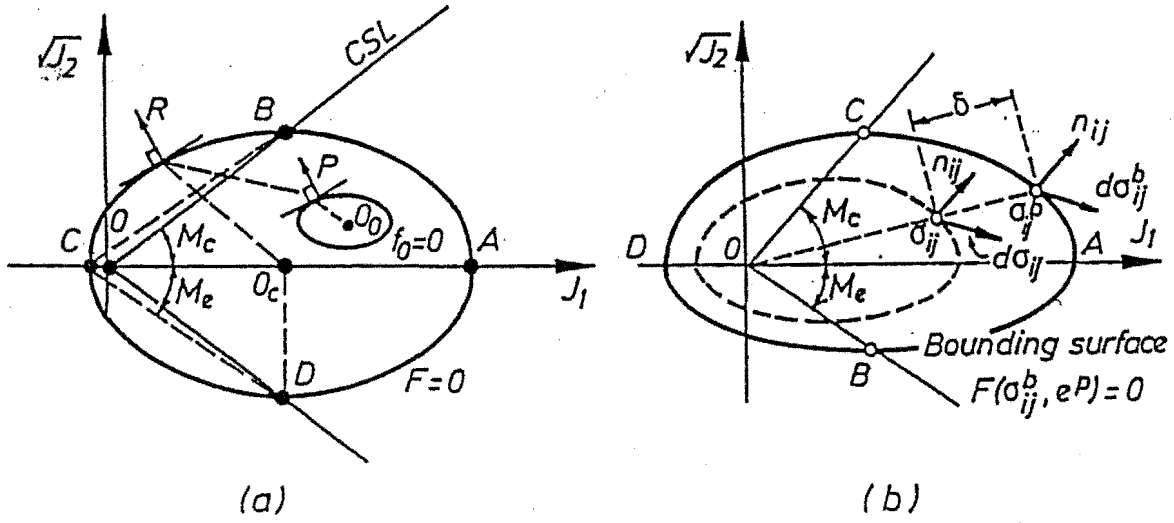

Figure 3.4 Bounding Surface model: Definition of Stress Direction

Dafalias and Herrmann (1982). Instead of individually defining a series of yield surfaces, a bounding surface and a yield surface are introduced to define the direction of plastic strain increment. The yield surface defines the elastic region and translates without rotation within the bounding surface from the current stress state to an image point on the bounding surface, at which the outward normal vector has the same direction as that of the current stress state on the yield surface, as illustrated in Fig.3.4. Both surfaces can expand or contract simultaneously under the isotropic hardening rule. The amplitude of the plastic strain increment due to a stress increment is computed by defining a plastic modulus interpolation function in terms of the position of current stress state and the yield surface relative to the bounding surface. As a result, the model is considerably simplified and much less storage is required when compared to the nested surface model.

In order to better understand these models and implement them into a finite element analysis, the theory of classical plasticity will be introduced in the following section.

3.2 Basic Formulation of the Theory of Classical Plasticity

For completeness, some basic formulae of the theory of classical plasticity are given here (Chen and Mizuno, 1990). It is usually assumed that a strain increment can be subdivided into an elastic strain increment and a plastic strain increment.

$$d\varepsilon_{ij} = d\varepsilon_{ij}^{e} + d\varepsilon_{ij}^{p} \tag{3.1}$$

where the superscripts e and p represent elastic and plastic strains, respectively. The stress increment is related to the elastic strain by the generalised Hook's law

$$d\sigma_{ij} = D_{ijkl} d\varepsilon_{kl}^{e} \tag{3.2a}$$

$$D_{ijkl} = (K\text{-}2G/3\,\delta_{ij}\delta_{kl}) + G(\delta_{ik}\delta_{jl} + \delta_{il}\delta_{jk}) \tag{3.2b}$$

where K is the bulk modulus and G is the shear modulus. δ_{ij} is the Kronecker delta symbol. When $i = j$, $\delta_{ij} = 1$. Otherwise $\delta_{ij} = 0$. The yield condition specifying the stress state at which plastic flow occurs is defined as

$$F(\sigma_{ij}, k(\varepsilon_v^p)) = 0 \tag{3.3a}$$

where k is a hardening parameter defining the isotropic hardening rule and ε_v^p is the plastic volumetric strain. The flow rule relating the plastic strain increment vector with the stress and stress increment vector is defined as

$$S(\sigma_{ij}, k) = 0 \tag{3.3b}$$

When an associated flow rule is specified, then $F = S$. If an anisotropic hardening rule is introduced, σ_{ij} in the function F and S can be replaced with $\sigma_{ij} - \alpha_{ij}$ where α_{ij} denotes the translation of the surface centre in the stress space. When plastic flow takes place, the plastic strain increment for the associated flow rule may be given as

$$d\varepsilon_{ij}^p = \langle L \rangle n_{ij} \tag{3.4a}$$

where $$L = \frac{1}{H} d\sigma_{kl} n_{kl} \tag{3.4b}$$

$$n_{ij} = \frac{\partial F}{\partial \sigma_{ij}} \frac{1}{f} \quad , \quad f = \left[\frac{\partial F}{\partial \sigma_{ij}} \frac{\partial F}{\partial \sigma_{ij}} \right]^{1/2} \tag{3.4c}$$

and $\langle\ \rangle$ is an operator defined as

$$\langle L \rangle = L \quad \text{if} \quad L > 0 \quad \text{(Loading)} \tag{3.4d}$$

$$\langle L \rangle = L \quad \text{if} \quad L = 0 \quad \text{(Neutral loading)} \tag{3.4e}$$

$$\langle L \rangle = 0 \quad \text{if} \quad L < 0 \quad \text{(Unloading)} \tag{3.4f}$$

H is the plastic modulus and can be obtained from the consistency condition that the stress state must always lie within or on the yield surface, ie. , $F = 0$ and $dF = 0$ and then

$$H = -\frac{n_{ij}}{f}\frac{\partial F}{\partial k}\frac{\partial k}{\partial \varepsilon_v^p} \tag{3.4g}$$

Substituting Eq.3.4a into Eqs. 3.1 and 3.2, it follows that

$$d\sigma_{ij} = D_{ijkl}(d\varepsilon_{kl} - \langle L \rangle n_{kl}) \tag{3.5a}$$

$$L = \frac{D_{rspq} n_{rs} d\varepsilon_{pq}}{H + D_{abcd} n_{ab} n_{cd}} \tag{3.5b}$$

Substituting Eq.3.2b into Eq.3.5a, then

$$d\sigma_{ij} = 2Gd\varepsilon_{ij} + (K - 2G/3)\delta_{ij} d\varepsilon_{kk} - \left[2Gn_{ij} + (K - 2G/3)n_{kk}\delta_{ij}\right]\langle L \rangle \tag{3.6a}$$

$$L = \frac{2Gn_{kl} d\varepsilon_{kl} + (K - 2G/3)n_{ss} d\varepsilon_{kk}}{H + (K - 2G/3)n_{rr} + 2G} \tag{3.6b}$$

For the undrained case, $d\varepsilon_{kk} = 0$ and for an ideal elastic material, H is zero.

In the above, the elasto-plastic constitutive equation has been obtained by using classical plasticity, and the elasto-plastic stress matrix has been given in an explicit form. The following section will introduce an elasto-plastic soil model, the bounding surface model, that has been accepted widely by researchers and engineers because it has been verified by different tests.

3. 3 Bounding Surface Model Formulation and Implementation

As discussed in section 3.2, the bounding surface model can capture the main soil behaviour. In this section, the formulation of the bounding surface model proposed by Dafalias and Herrmann (1986) and its implementation will be discussed in detail.

3.3.1 Formulation of the Bounding Surface Model to Isotropic Cohesive Soils

The formulation outlined in section 3.2 is applied to the bounding surface model except that the bounding surface is defined by

$$F(\sigma_{ij}^{b}, J_0(\varepsilon_v^p)) = 0 \tag{3.7a}$$

where the superscript b stands for the bounding surface.

$$L = \frac{1}{H} d\sigma_{ij} n_{ij} = \frac{1}{H^b} d\sigma_{ij}^{b} n_{ij}^{b} \tag{3.7b}$$

where H is the plastic modulus and H^b is the plastic modulus of the bounding surface.

$$n_{ij} = \frac{\partial F}{\partial \sigma_{ij}^{b}} \frac{1}{f} \qquad \text{and} \qquad f = \left[\frac{\partial F}{\partial \sigma_{ij}^{b}} \frac{\partial F}{\partial \sigma_{ij}^{b}} \right]^{1/2} \tag{3.7c,d}$$

A simple radial mapping rule is applied

$$\bar{I} = b(I - I_C) + I_C \tag{3.8a}$$

$$\bar{s}_{ij} = b s_{ij} \Rightarrow \bar{J} = bJ; \quad \bar{S} = bS; \quad \bar{\alpha} = \alpha \tag{3.8b}$$

where the superscript bar denotes the value on the bounding surface. I_c may be thought of as an isotropic back-stress. If the bounding surface intersects the positive I-axis at I_o,

one can assume $I_c=CI_o$ with $0\leq C<1$, the C being constant or variable with void ratio e. Therefore, The above equation becomes

$$\bar{I} = b(I - CI_O) + CI_O \tag{3.8c}$$

the bounding plastic modulus and the elastic bulk modulus may be chosen as

$$\bar{K} = \frac{1+e_{in}}{\lambda-\kappa}\left(\left\langle 1-\frac{I_l}{I_o}\right\rangle + \frac{I_l}{I_o}\right)3F_{,\bar{I}}(F_{,\bar{I}}\bar{I} + F_{,\bar{J}}) \tag{3.9a}$$

$$K = \frac{1+e_{in}}{3\kappa}\left(\langle I - I_l\rangle + I_l\right) \tag{3.9b}$$

These stress invariants and their stress gradients used by the above equations are defined by

$$I = \sigma_{kk}; \qquad \frac{\partial I}{\partial \sigma_{ij}} = \delta_{ij}$$

$$J = \left(\frac{1}{2}s_{ij}s_{ij}\right)^{1/2}; \qquad \frac{\partial J}{\partial \sigma_{ij}} = \frac{s_{ij}}{2J}$$

$$S = \left(\frac{1}{3}s_{ij}s_{jk}s_{ki}\right)^{1/3}; \quad -\frac{\pi}{6} \leq \alpha = \frac{1}{3}\sin^{-1}\left[\frac{3\sqrt{3}}{2}\left(\frac{S}{J}\right)^3\right] \leq \frac{\pi}{6}$$

$$\frac{\partial \alpha}{\partial \sigma_{ij}} = \frac{\sqrt{3}}{2J\cos 3\alpha}\left[\frac{s_{ik}s_{kj}}{J} - 3\left(\frac{S}{J}\right)^3\frac{s_{ij}}{2J} - \frac{2}{3}\delta_{ij}\right]$$

where α is the stress Lode angle; s_{ij} the deviatoric stress; I, J and S are stress invariants. Dafalias and Herrmann (1986) chose the bounding surface described below and shown in Fig.3.5. The bounding surface consists of ellipse 1, hyperbola and ellipse 2.

For ellipse 1:

$$F = (\bar{I} - I_o)(\bar{I} + \frac{R-2}{R} I_o) + (R-1)^2 (\frac{\bar{J}}{N})^2 = 0 \tag{3.10}$$

For the hyperbola:

$$F = (\bar{I} - \frac{I_o}{r})^2 - (\frac{\bar{J}}{N} - \frac{I_o}{R}) \left[\frac{\bar{J}}{N} - \frac{I_o}{R}(1 + 2\frac{RA}{N}) \right] = 0 \tag{3.11}$$

For ellipse 2:

$$F = (\bar{I} - TI_o) \left[\bar{I} - (T + 2\zeta) I_o \right] + \rho \bar{J}^2 = 0 \tag{3.12}$$

$$\zeta = -\frac{T(Z + TF')}{Z + 2TF'}; \qquad \rho = \frac{T^2}{Z(Z + 2TF')}$$

$$y = \frac{RA}{N}; \qquad F' = \frac{N}{\sqrt{1 + y^2}}; \qquad Z = \frac{N}{R}(1 + y - \sqrt{1 + y^2})$$

The dependence on e occurs through $I(e)$, and the dependence on α through the parameters $N(\alpha)$, $R(\alpha)$, and $A(\alpha)$ according to

$$Q(\alpha) = g(\alpha, c) Q_c \qquad c = \frac{Q_e}{Q_c} \tag{3.13a,b,c}$$

$$g(\alpha, c) = \frac{2c}{1 + c - (1 - c)\sin 3\alpha}$$

where Q stands for any one of N, R, or A. Q_c is its value at $\alpha = \pi/6$ and Q_e its value at $\alpha = -\pi/6$. These equations define a possible interpolation law between Q_c and Q_e.

Matching this bounding surface, a shape-hardening function and a practical plastic modulus are proposed:

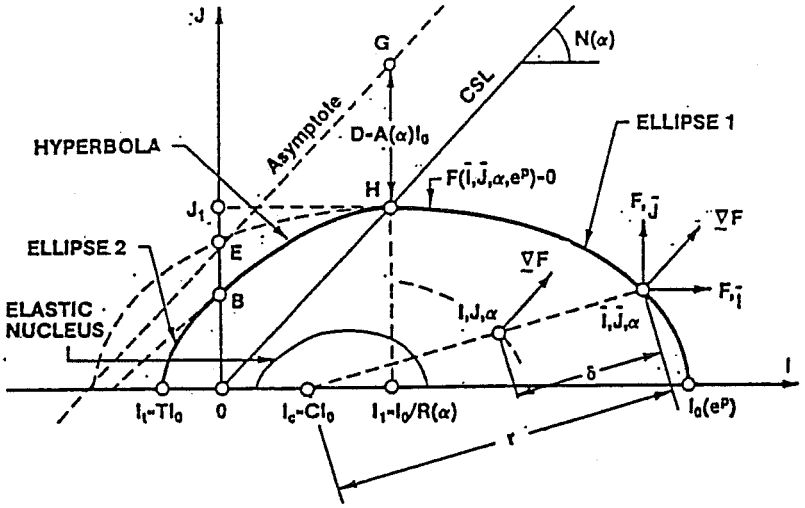

Figure 3.5 Schematic illustration of bounding surface and radial mapping rule in stress invariant space

$$\hat{H} = \frac{1+e_{in}}{\lambda-\kappa} g^{*2} p_a \left[z^{m} h(\alpha) + (1+z^{m}) h_o \right] \tag{3.14a}$$

$$K_p = \bar{K}_p + \hat{H} \left\langle \frac{b}{b-1} - s \right\rangle^{-1} \tag{3.14b}$$

where

$$g^{*} = \left(9F^2{}_{,\bar{I}} + \frac{1}{3} F^2{}_{,\bar{J}} \right)^{1/2}$$

Finally, the explicit form of the D_{ijkl} tensor is determined by using the associated flow rule giving the following form

$$D_{ijkl} = G(\delta_{ki}\delta_{lj} + \delta_{kj}\delta_{li}) + (K - \frac{2}{3}G)\delta_{ij}\delta_{kl}$$
$$-\frac{h(L)}{B}\left[3KF_{,\bar{I}}\delta_{ij} + \frac{G}{J}F_{,\bar{J}}\delta_{ij} + \frac{\sqrt{3}G}{\cos(3\alpha)}\frac{F_{,\alpha}}{bJ}\left(\frac{s_{in}s_{nj}}{J^2} - \frac{3S^3 s_{ij}}{2J^4} - \frac{2\delta_{ij}}{3}\right)\right] \quad (3.15a)$$
$$\left[3KF_{,\bar{I}}\delta_{kl} + \frac{G}{J}F_{,\bar{J}}s_{kl} + \frac{\sqrt{3}G}{\cos(3\alpha)}\frac{F_{,\alpha}}{bJ}\left(\frac{s_{kn}s_{nl}}{J^2} - \frac{3S^3 s_{kl}}{2J^4} - \frac{2\delta_{kl}}{3}\right)\right]$$

in which

$$L = \frac{1}{B}\left\{3KF_{,\bar{I}}\varepsilon_{kk} + \frac{G}{J}F_{,\bar{J}}s_{ij}\dot{\varepsilon}_{ij} + \frac{\sqrt{3}G}{\cos(3\alpha)}\frac{F_{,\alpha}}{bJ}\left[\left(\frac{s_{ik}s_{kj}}{J^2} - \frac{3S^3 s_{ij}}{2J^4}\right)\dot{\varepsilon}_{ij} - \frac{2\dot{\varepsilon}_{kk}}{3}\right]\right\} \quad (3.15b)$$

$$B = K_p + 9K(F_{,\bar{I}})^2 + G(F_{,\bar{J}})^2 + G(\frac{F_{,\alpha}}{bJ}) \quad (3.15c)$$

$$K = \frac{1+e_{in}}{3\kappa}(\langle I - I_1\rangle + I_1) \quad (3.15d)$$

$$\bar{K}_p = \frac{1+e_{in}}{\lambda-\kappa}\left(\left\langle 1 - \frac{I_1}{I_o}\right\rangle + \frac{I_1}{I_o}\right)3F_{,\bar{I}}(F_{,\bar{I}}\bar{I} + F_{,\bar{J}}) \quad (3.15e)$$

$$z = \frac{3JR\sqrt{3}}{MI_o}$$

where $\dot{\varepsilon}_{ij}$ is the rate of strain, $h()$ is the heavyside function, $\hat{H}$ and K_p are expressed in Eqs. 3.14a and 3.14b.

In the bounding surface model, a total of 14 constants are required. They are listed in Table 3.1 in that subscripts *e* and *c* represent extension and compression respectively.

Recapitulating the meaning of these constants, κ, λ, G or ν, and $N_c=M_c/(3\sqrt{3})$, $N_e=M_e/(3\sqrt{3})$ represent the slope of the critical state line (CSL) for a given α at stress invariant, J and I, space and M_c and M_e are the slope of the critical state line (CSL) at stress space p and q. The κ and λ can be determined by consolidation and swelling of triaxial specimens, G from the initial slope of deviatoric stress/strain curves, or by

assuming a constant Poisson ratio v and obtaining $G=3K(1-2v)/(2(1+v)$. N_c and N_e are determined by the friction angle at failure in compression and extension. The R_c, R_e, A_c, A_e, and T determine the shape of the bounding surface in compression and extension as shown in Fig.3.5, the first two for ellipse 1, the second two for the hyperbola, and the T for ellipse 2. The C, s, and h_c, h_e are related to the response for overconsolidated states, the first determining the projection centre I_c, the second the size of the elastic nucleus, the last two are the values of the shape hardening-factor h in compression and extension. All these constants can be determined by triaxial experiments. Usually I_l and m can be fixed, I_l=10 kP_a and m=0.02, hence they are not included in the set of model constants. All parameters are shown in Eqs. 3.10 to 3.15.

Table 3.1 Parameters of the Bounding Surface Model

Parameter No.	1	2	3	4	5	6	7	8	9	10	11	12	13	14
Parameter	κ	G	λ	N_c	N_e	R_c	R_e	A_c	A_e	T	C	s	h_c	H_e

As mentioned above, s controls the size of the elastic nucleus. For s=1, the elastic nucleus shrinks to a point coinciding with the projection centre, and for $s > 1$, it has a finite size but smaller than that of the bounding surface. Although the introduction of the elastic nucleus improved the predictions, certain aspects of observed behaviour of clay can not still be predicted. For example: Sangrey et al (1969) observed that upon continuation of the cyclic loading, the total pore pressure builds up with increasing amplitude of loading. Anandarajah et al (1995) modified the method by employing a progressively vanishing elastic nucleus instead of a permanent elastic nucleus. This is achieved by allowing s to change as

$$s = 1 + \langle s_0 - \alpha \eta_m \rangle \tag{3.16}$$

where η_m is the previous maximum value $\eta=RJ/NI_0$, and s_0 and α are fixed model parameters. Depending on the value of s_0 and α, s may become unity for large

amplitude loading, thus making the elastic nucleus shrink to a point and eliminating the existence of the elastic domain within the bounding surface.

3.3.2 Numerical Implementation of the Bounding Surface Model for Cohesive Soil

Many numerical implementation methods of the plasticity model have been proposed (Desai, et al. 1984, Geradin, et al. 1981, Herrmann, et al. 1987, Owen, et al. 1980). In this section, only the numerical implementation of the bounding surface model for cohesive soil will be discussed (Herrmann, et al. 1987).

For a nonlinear analysis, an incremental iteration procedure is called global iteration. The bounding surface model will provide only an estimate of the stiffness matrix so as to calculate an estimate of the present stress vector.

Usually, the stress vector in the nonlinear analysis is expressed as:

$$\{\Delta\sigma\}_{N,K} = [\bar{D}]_{N,K-1}\{\Delta\varepsilon\}_{N,K} + \{\Delta\sigma_0\}_{N,K-1} \tag{3.17}$$

where $\{\Delta\sigma_0\}$ is an unbalanced stress vector at the *k-th* iteration, and $[\bar{D}]$ is a stress matrix at the *k-th* iteration. *N* denotes the *n-th* solution time step at the global solution. *K* denotes the *k-th* iteration at the *n-th* solution time step. For simplicity, the above equation can be expressed as the following:

$$\{\Delta\sigma\} = [\bar{D}]\{\Delta\varepsilon\} + \{\Delta\sigma_0\} \tag{3.18}$$

In elasto-plasticity, the relationship between stress and strain tensors is often expressed by the rate vector. This can be given as

$$\left\{\dot{\sigma}\right\} = [D]\left\{\dot{\varepsilon}\right\} \tag{3.19}$$

For a given solution time step, the desired relationship between stress and strain increments can be obtained by integrating over the step

$$t_{N-1} \rightarrow t_N : \quad \int_{t_{N-1}}^{t_N} \left\{\dot{\sigma}\right\} dt = \int_{t_{N-1}}^{t_N} [D] \left\{\dot{\varepsilon}\right\} dt \tag{3.20}$$

For increment N, the strain rate is approximated by the finite difference expression:

$$\left\{\dot{\varepsilon}\right\} = \frac{\{\Delta\varepsilon\}}{\Delta t_N} \tag{3.21}$$

For a given solution time step, the special conditions of all the strain components being proportional should occur. For a rate-independent model, if there is no water movement within the soil, the input history for the interval could be selected so that the rate of all components of $\{\varepsilon\}$ are constant and are given by the above expression without approximation. Now an incremental relationship between stress and strain can be given:

$$\{\Delta\sigma\} = \frac{\{\Delta\varepsilon\}}{\Delta t_N} \int_{t_{N-1}}^{t_N} [D]\, dt \tag{3.22a}$$

letting $$\left[\overline{D}\right] = \frac{1}{\Delta t_N} \int_{t_{N-1}}^{t_N} [D] dt \tag{3.22b}$$

yields $$\{\Delta\sigma\} = \left[\overline{D}\right]\{\Delta\varepsilon\} \tag{3.22c}$$

The next step is an accurate evaluation of the average value of $[D]$ over the solution increment. The multi-step trapezoidal rule is adopted here.

M substeps in the global solution time step will be used to generate the following evaluation:

$$\left[\overline{D}\right]=\sum_{m=1}^{M}\left[\overline{D}\right]_m \tag{3.23a}$$

in which

$$\left[\overline{D}\right]_m \approx \frac{1}{2\Delta t_m}\left\{[D]_{m-1}+[D]_m\right\} \tag{3.23b}$$

$[D]_{m-1}$and $[D]_m$ represent the values of $[D]$ corresponding to the stress and strain states at the beginning and end of a substep, respectively. If the substep of equal length is used, the strain is given at time t_m:

$$\{\varepsilon\}_m \approx \{\varepsilon\}_{N-1}+\frac{m}{M}\{\Delta\varepsilon_N\} \tag{3.24}$$

The stress estimate at the corresponding time is initially (in the first local iteration) taken to be:

$$\{\sigma\}_m \approx \{\sigma\}_{m-1}+\{\Delta\sigma\}_{m-1}=\{\sigma\}_{N-1}+\sum_{k=1}^{m-1}\{\Delta\sigma\}_k+\{\Delta\sigma\}_{m-1} \tag{3.25}$$

That is, an estimate, equal to the value found in the previous substep, is initially used for $\{\Delta\sigma\}_m$. In the local iteration process, the value is successively modified by replacing $\{\Delta\sigma\}_{m-1}$ with improved estimates (using $\{\Delta\varepsilon\}_m$ and $\left[\overline{D}\right]_m$ from the previous local iteration).

To avoid inaccurate integration and a stress state outside of the bounding surface, an internal parameter b can be used as a monitor. According to the theory of the bounding surface model, if b is less than 1, the stress state is outside of the surface. In general, b is set up as 0.999 (Herrmann, et al. 1987). For a nearly neutral loading path where inaccurate integration may predict "loading" when "unloading" should occur or vice versa, the second criterion is imposed as follows: $\left|L_0^n-L_0^n\right|/L_0^n$ is required to be less than 0.01, where L_0^n and L_0^n represent the sum of the absolute values of the calculated

incremental stress components at the end of the increment with different numbers of substeps.

Classical radial return has been adopted to bring a point back to the bounding surface when the stress state is outside of it. This scaled stress state is then used to calculate the plastic modulus, but it is not used to update the size of the bounding surface as determined by the value of I_0. The importance of using the unscaled stress for this operation stems from the fact that the size of the bounding surface is really controlled by strain considerations and the strains are not scaled.

The scaling of the invariants of the stress yields:

$$I_{scaled} = b(I - cI_0) + cI_0; \quad J_{scaled} = bJ; \quad S_{scaled} = bS \tag{3.26}$$

When the stress state at the beginning of the step $\{\sigma\}_{N-1}$ is outside of the bounding surface, the individual stress components are scaled back to the bounding surface as follows:

$$\{\sigma\}_{N-1_{scaled}} = b\{\sigma\}_{N-1} + \frac{1}{3}(1-b)cI_0\{1\} \tag{3.27}$$

and a stress correction vector $\{\Delta\sigma_0\}$ is calculated:

$$\{\Delta\sigma_0\} = -(1-b)(\{\sigma\} - \frac{1}{3}cI_0\{1\} \tag{3.28}$$

where the quantity $\{1\}$ represents the column vector equivalent of the Kronecker delta, i.e., the first three terms are unity and the last three are zero. This stress correction is incorporated into the global analysis by treating it as a strain-independent stress.

The bounding surface model relates effective soil stress with strain. However, in a finite element analysis, only the total stress boundary condition can be considered. Several possibilities exist for modelling the pore-water pressure in soil: ideal drained conditions (where the excess pore-water pressure is identically zero), ideal undrained conditions (where the soil is completely saturated and no flow of water occurs) and the more

realistic situation where there is a global flow of water (the soil may be fully or partially saturated). The first case requires that loading should be very slow. The second case is suitable for loading rapidly, short loading duration and low permeability of the soil. The last case is close to the site condition but it is very complex. For an earthquake loading and clay site in this thesis, only the ideal undrained condition is considered.

The total stress increment $\{\Delta\sigma\}$ is the sum of the effective stress and the pore-water pressure increments

$$\{\Delta\sigma\}^t = \{\Delta\sigma\} + \Delta u\{1\} \tag{3.29a}$$

$$\Delta u = \Gamma \Delta\varepsilon_{kk} \tag{3.29b}$$

For the undrained conditions, the value of Γ is very large compared to the terms in $[D]$ and thus the soil is like a nearly incompressible solid. For nearly incompressible conditions care must be exercised to avoid numerical round-off and problems of excessive constraint. As recommended by Naylor (1974), the reduced integration scheme is preferred and averaging the calculated stresses from integration points is taken as the element stress to reduce the stress error.

Finally, the total stress can be represented by

$$\{\Delta\sigma\}^t = ([D] + [d])\{\Delta\varepsilon\} + \{\Delta\sigma_0\} \tag{3.30}$$

The nine terms in the upper left 3×3 submatrix of $[d]$ are each equal to Γ while the remaining terms are all zero.

For showing characteristics of the bounding surface model, a sample mesh of four 8-node elements shown in Fig.3.6 is used for the numerical testing. The nonlinear two-dimensional analysis code written by the author is used for the analysis.

For the sample, only the x and y directions at the bottom of the sample are constrained. Other surfaces are free. The monotonic loading and unloading acts at the top of the sample and the loading step is small enough to avoid great deformation. The lateral pressure is $50kp_a$. The calculated relationship between the shear stress and shear strain at the centre of the sample is shown in Fig. 3.7. This curve is similar to most of the test results.

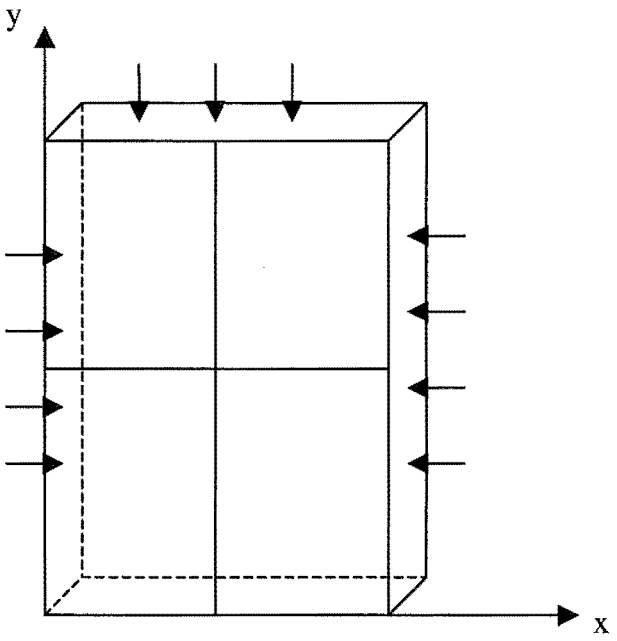

Figure 3.6 The Sample divided into four elements

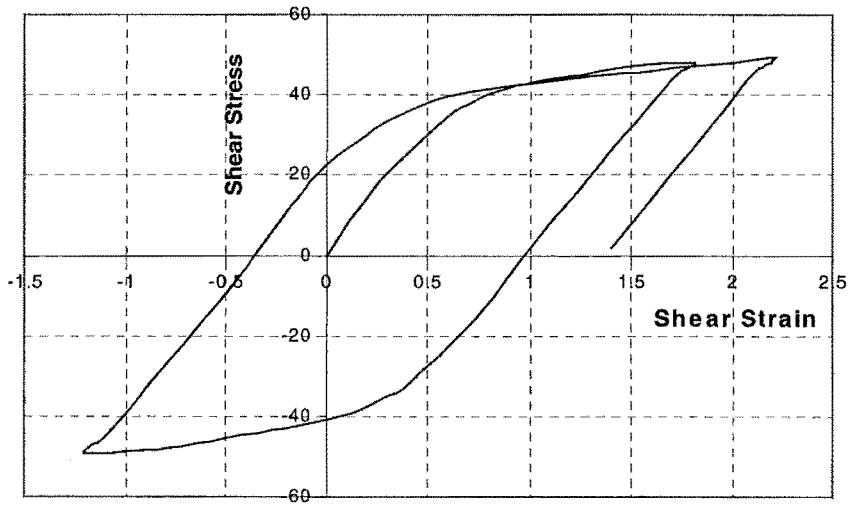

Figure 3.7 Calculated Relationship between Shear Stress and Shear Strain

3.4 Structural Modelling

Like soil modelling, many structural models have been proposed from simple models to complex models. However, simple models are preferred by some researchers and engineers because they have been confirmed by many test results (Paulay and Priestley, 1992). The bi-linear model shown in Fig.3.8 is one of these hysteretic models.

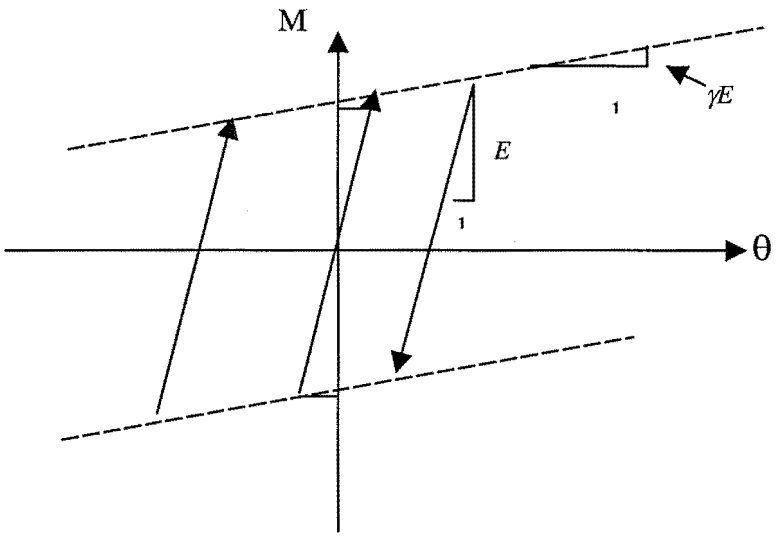

Figure 3.8 Sketch of Bilinear Model

The one-component model in Fig.3.9 is employed to represent a structural beam or column. The relationship between moment and curvature can be expressed as:

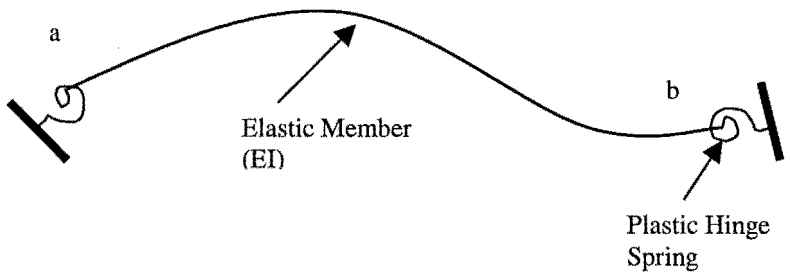

Figure 3.9 One Component Beam Model

$$\begin{Bmatrix}\Delta\theta_a\\ \Delta\theta_b\end{Bmatrix}=\begin{bmatrix}\frac{L}{3EI} & \frac{L}{6EI}\\ \frac{L}{6EI} & \frac{L}{3EI}\end{bmatrix}\begin{Bmatrix}\Delta M_a\\ \Delta M_b\end{Bmatrix}+\frac{1}{GA_S}\begin{bmatrix}1 & 1\\ 1 & 1\end{bmatrix}\begin{Bmatrix}\Delta M_a\\ \Delta M_b\end{Bmatrix}+ \begin{bmatrix}\frac{1}{k_a} & 0\\ 0 & \frac{1}{k_b}\end{bmatrix}\begin{Bmatrix}\Delta M_a\\ \Delta M_b\end{Bmatrix} \tag{3.31}$$

EI is the elastic stiffness, L is the member length, GA_s is shear stiffness, k_i is the stiffness of plastic hinge, where i represents a or b. If the perfect plasticity is used at plastic hinge a or b, the numerical difficulties occur as infinite rotational flexibility exists. Therefore three cases will be solved respectively:

a) only $k_a = 0$

b) only $k_b = 0$

c) $k_a = 0$ and $k_b = 0$.

For the three cases, some certain methods must be taken (Carr, 1998).

This bi-linear model and the one-component model are directly used in the structural analysis.

3.5 Numerical Integration of the Dynamic Equilibrium Equations

For seismic soil-structure interaction analysis, the dynamic equilibrium equation can be easily obtained from the virtual work principle or other similar methods. (Zienkiewicz, 1977, Cook, 1990). Usually the dynamic equilibrium equation is a second-order ordinary differential equation so that a numerical integration method has to be used (Bathe and Wilson, 1976). Generally the numerical integration methods can be separated into two types; one being an explicit numerical integration method, for example, the central difference method, the other being an implicit numerical integration method, for example, the Newmark method, the Wilson-θ method and the α

method. For different cases, different methods are preferred. In this section, several numerical methods will be introduced, after which their advantages and disadvantages will be discussed.

Equations for the dynamic response of a structure can be derived easily by requiring the work of the external forces to be absorbed by the work of internal, inertial, and viscous damping forces for any small kinematically admissible motion. Using the finite element concept, dynamic equilibrium equations can be written as

$$[M]\{\ddot{u}\}+[C]\{\dot{u}\}+[K]\{u\}=\{R\} \tag{3.32}$$

where $\{\ddot{u}\}$, $\{\dot{u}\}$ and $\{u\}$ are the acceleration, the velocity and the displacement; $[M]$, $[C]$ and $[K]$ are the mass matrix, the damping matrix and the stiffness matrix. Eq.3.32 is a system of coupled, second-order, ordinary differential equations in the time domain and is called a finite element semi-discretization. Many numerical integration techniques have been used to solve it. The popular methods are the central-difference method, the Newmark method and the Wilson-θ method. In recent years, the α-method has been given special attention.

3.5.1 Explicit Direct Integration Method - the Central-Difference Method

A popular method (Cook et al, 1990) which is characteristic of explicit methods in general is the central-difference method. It approximates the velocity and acceleration by the equations

$$\{\dot{u}\}_n=\frac{1}{2\Delta t}(\{u\}_{n+1}-\{u\}_{n-1}) \tag{3.33a}$$

$$\{\ddot{u}\}_n=\frac{1}{\Delta t^2}(\{u\}_{n+1}-2\{u\}_n+\{u\}_{n-1}) \tag{3.33b}$$

Combining Eqs. 3.33a and 3.33b with Eq.3.32 provides

$$\left[\frac{1}{\Delta t^2}[M]+\frac{1}{2\Delta t}[C]\right]\{u\}_{n+1}=\{R\}_n-[K]\{u\}_n+$$

$$\frac{1}{\Delta t^2}[M](2\{u\}_n-\{u\}_{n-1})+\frac{1}{2\Delta t}[C]\{u\}_{n-1} \qquad (3.34)$$

Eq.3.34 is conditionally stable and requires Δt such that

$$\Delta t \le 2/\omega_{max} \qquad (3.35)$$

where ϖ_{max} is the highest natural frequency of free vibration and its accuracy is markedly time-step size-dependent. The central difference method is suitable for solving nonlinear material cases because the stiffness matrix does not need to be assembled at each time step. If the mass matrix is a diagonal matrix and the damping matrix [*C*] is a function of the mass matrix [*M*], Eq.3.34 can be solved very easily. If the damping matrix [*C*] is not diagonal, special numerical procedures must be considered so that [*C*] is at the left of Eq.3.34.

3.5.2 The Newmark Implicit Integration Method

The Newmark integration scheme can also be understood to be an extension of the linear acceleration method. It approximates velocity and displacement by

$$\left\{\dot{u}\right\}_{n+1}=\left\{\dot{u}\right\}_n+\left[(1-\delta)\left\{\ddot{u}\right\}_n+\delta\left\{\ddot{u}\right\}_{n+1}\right]\Delta t \qquad (3.36a)$$

$$\{u\}_{n+1}=\{u\}_n+\left\{\dot{u}\right\}_n\Delta t+\left[\left(\frac{1}{2}-\alpha\right)\left\{\ddot{u}\right\}_n+\alpha\left\{\ddot{u}\right\}_{n+1}\right]\Delta t^2 \qquad (3.36b)$$

In addition to Eqs. 3.36a and 3.36b, the equilibrium Eq.3.32 at time (n+1)Δt is considered:

$$[M]\{\ddot{u}\}_{n+1} + [C]\{\dot{u}\}_{n+1} + [K]\{u\}_{n+1} = \{R\}_{n+1} \tag{3.37}$$

where α and δ are parameters that can be determined to obtain integration accuracy and stability. When $\delta=1/2$ and $\alpha=1/6$, the relations in Eqs. 3.36a and 3.36b correspond to the linear acceleration method which is only conditionally stable. When $\delta=1/2$ and $\alpha=1/4$, the relations are the constant-average-acceleration method and it is unconditionally stable. Because of this property, its time-step size can be large. Accuracy, however, is very important in solving the dynamic equation, especially for nonlinear dynamic problems, hence the time-step size is limited by this factor. Another property of the Newmark method is that there is no artificial damping in the algorithm if $\delta=\frac{1}{2}$.

3.5.3 The Wilson-θ Method

The Wilson-θ method is an extension of the linear acceleration method. In the Wilson-θ method, the acceleration is assumed to be linear from time t to time t+θΔt, where $\theta \geq 1.0$. It approximates the velocity and acceleration as

$$\{\dot{u}\}_{t+\theta\Delta t} = \frac{3}{\theta\Delta t}(\{u\}_{n+\theta\Delta t} - \{u\}_n) - 2\{\dot{u}\}_n - \frac{\theta\Delta t}{2}\{\ddot{u}\}_n \tag{3.38a}$$

$$\{\ddot{u}\}_{n+\theta\Delta t} = \frac{6}{\theta^2\Delta t^2}(\{u\}_{n+\theta\Delta t} - \{u\}_n - \frac{6}{\theta\Delta t}\{\dot{u}\}_n - 2\{\ddot{u}\}_t \tag{3.38b}$$

To obtain the solution for the displacements, velocities, and accelerations at time t+Δt, the equilibrium Eq.3.32 is considered at time t+θΔt

$$[M]\{\ddot{u}\}_{t+\theta\Delta t} + [C]\{\dot{u}\}_{t+\theta\Delta t} + [K]\{u\}_{t+\theta\Delta t} = \{\overline{R}\}_{t+\theta\Delta t} \tag{3.39}$$

where

$$\{\bar{R}\}_{t+\theta\Delta t} = \{R\}_t + \theta(\{R\}_{t+\Delta t} - \{R\}_t) \tag{3.40}$$

When $\theta \geq 1.37$, the Wilson-θ method is unconditionally stable. Another property of the method is artificial damping provided by the algorithm. However, this artificial damping seriously affects the low-frequency part of the response. When only the low-frequency part of the response is concerned, such as the analysis of the seismic free field that is controlled by low-frequency response of the response, the method will have serious effects on the results.

3.5.4 The α Method

Since a disadvantage of the Newmark method is that the algorithmic damping cannot be obtained, or only obtained at the expense of reduced accuracy, and the Wilson-θ algorithmic damping affects the low-frequency part of the response, many researchers in more recent years have implemented the α method into their dynamic analysis softwares. The α method proposed by Hilber, Hughes and Taylor (1977) overcomes the weaknesses of the Newmark method and the Wilson-θ method. It provides effective high-frequency dissipation and retains second-order accuracy for the linear dynamic analysis when the parameters are selected appropriately. In order to illustrate this method, the linear undamped dynamic equilibrium equations are considered:

$$[M]\{\ddot{u}\} + [K]\{u\} = \{R\} \tag{3.41}$$

Approximate solutions of Eq.3.41 can be obtained by one-step difference methods. To this end consider the family of algorithms defined by the following relations:

$$[M]\{\ddot{u}\}_{n+1} + (1+\alpha)[K_{n+1}]\{u\}_{n+1} - \alpha[K_n]\{u\}_n = \{R\}_{n+1} \tag{3.42}$$

Displacement and velocity at the n+1 time step are expressed as follows

$$\{u\}_{n+1} = \{u\}_n + \Delta t\left\{\dot{u}\right\}_n + \Delta t^2\left[\left(\frac{1}{2}-\beta\right)\left\{\ddot{u}\right\}_n + \beta\left\{\ddot{u}\right\}_{n+1}\right] \tag{3.43a}$$

$$\left\{\dot{u}\right\}_{n+1} = \left\{\dot{u}\right\}_n + \Delta t\left[(1-\gamma)\left\{\ddot{u}\right\}_n + \gamma\left\{\ddot{u}\right\}_{n+1}\right] \tag{3.43b}$$

In the above equations, α, β and γ are free parameters which govern the stability and numerical dissipation of the algorithm. If $\alpha = 0$ this family of algorithms reduces to the Newmark family. In this case, if $\gamma = 1/2$ the algorithms possess no numerical dissipation, whereas if $\gamma > 1/2$ numerical dissipation is present (Cook, 1990). If $\beta \geq \frac{1}{4}\left(\gamma+\frac{1}{2}\right)^2$, the algorithm in question is unconditionally stable.

It is noteworthy that the parameter α controls the amount of damping in the numerical algorithm. As the α decreases, the amount of damping increases. In order to assure an unconditionally stable, second-order convergent scheme for the linear dynamic problem results the equation that the three parameters should be chosen such that $-\frac{1}{3} \leq \alpha \leq 0$, $\gamma = \frac{1}{2}(1-2\alpha)$, and $\beta = \frac{1}{4}(1-\alpha)^2$. When only low mode response is of interest the α method is often advantageous to possess some numerical dissipation to damp out any spurious participation of the higher modes. However for a multi-storey framed structure, the higher modes often have the strong effect on the structural response (Carr, 1998) or when Rayleigh damping which is controlled by critical damping ratio is used, the Newmark unconditional stable algorithm is preferred.

3.6 SSINAP2D Program Explanation and Testing

SSINAP2D program is a two-dimensional seismic soil-structure interaction analysis program. The original static elastic program is from a book edited by Hinton and Owen (1977). In this program, a frontal equation solver was used. In order to save memory and increase calculation speed, a sky-line equation solver was used here to replace the

frontal equation solver, but most of the independent subroutines remain. Furthermore, the program was developed to carry out solid and structural dynamic analyses. In the dynamic analysis, the α integration method was used (Newmark integration method is a special case). For a nonlinear analysis, Newton-Raphson's predictor–corrector method was used. The analysis and iteration procedure follows the steps:

Step 1: Initialise iteration counter i to zero

$$d_{n+1}^{(i)} = \bar{d}_{n+1} = d_n + v_n \Delta t + (\frac{1}{2} - \beta) a_n \Delta t^2$$

Step 2: Predictor $v_{n+1}^{(i)} = \bar{v}_{n+1} = v_n + (1-\gamma) a_n \Delta t$

$$a_{n+1}^{(i)} = 0$$

Step 3:

$$\psi^{(i)} = (1+\alpha) f_{n+1} - \alpha f_n - M a_{n+1}^{(i)} - (1+\alpha) C_{n+1}^{i} v_{n+1}^{(i)} + \alpha C_n v_n - (1+\alpha) K_{n+1}^{i} d_{n+1}^{i} + \alpha K_n d_n$$

Step 4: $M_{eff}^{(i)} = M + (1+\alpha)\gamma \Delta t C_T + (1+\alpha)\beta \Delta t^2 K_T^{(i)}$

where K_T is the global tangent stiffness matrix

Step 5: Solve $M_{eff}^{(i)} \Delta a^{(i+1)} = \psi^{(i)}$

Step 6: Corrector $a_{n+1}^{(i+1)} = a_{n+1}^{(i)} + \Delta a^{(i+1)}$

$$v_{n+1}^{(i+1)} = \bar{v}_{n+1} + \gamma a_{n+1}^{(i+1)} \Delta t$$

$$d_{n+1}^{(i+1)} = \bar{d}_{n+1} + \beta a_{n+1}^{(i+1)} \Delta t^2$$

Step 7:

$$\psi^{(i+1)} = (1+\alpha) f_{n+1} - \alpha f_n - M a_{n+1}^{(i+1)} - (1+\alpha) C v_{n+1}^{(i+1)} + \alpha C_n v_n - (1+\alpha) K_{n+1}^{i+1} d_{n+1}^{i+1} + \alpha K_n d_n$$

Step 8: Convergence check if $\frac{\|\psi^{(i+1)}\|}{\|\psi^{(0)}\|} \le \varepsilon_1$ and $\frac{\|\Delta a^{(i+1)}\|}{\|a_{n+1}^{(i+1)}\|} \le \varepsilon_2$

Then go to next time step; else set i=i+1 and go to Step 4

Where α, β, γ are parameters in the α method.

In order to verify SSINAP2D accuracy, two tests were carried out. One is a linear fixed-base 6-storey frame that was designed by Jury (Jury, 1978); the other is a soil-structure interaction problem that consists of the linear 6-storey frame, the foundation and the soil. They are shown in Fig.3.10.

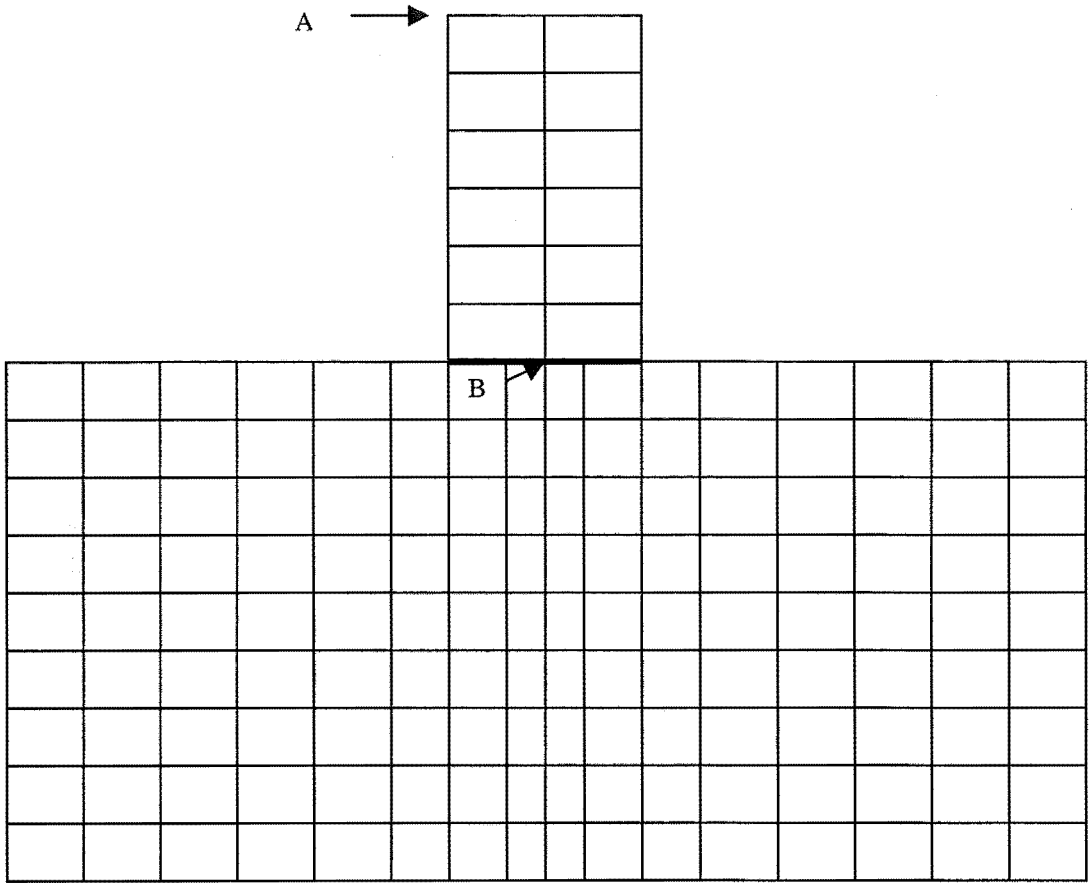

Figure 3.10 Sketch of the 6-Storey Frame, the Foundation and the Soil

The input earthquake record at SANTA CRUZ during the 1989 Loma Prieta earthquake is shown in Fig.3.11. The horizontal displacement time histories at point A calculated by SSINAP2D and RUAUMOKO (Carr, 1998) are shown in Fig.3.12 (in this example,

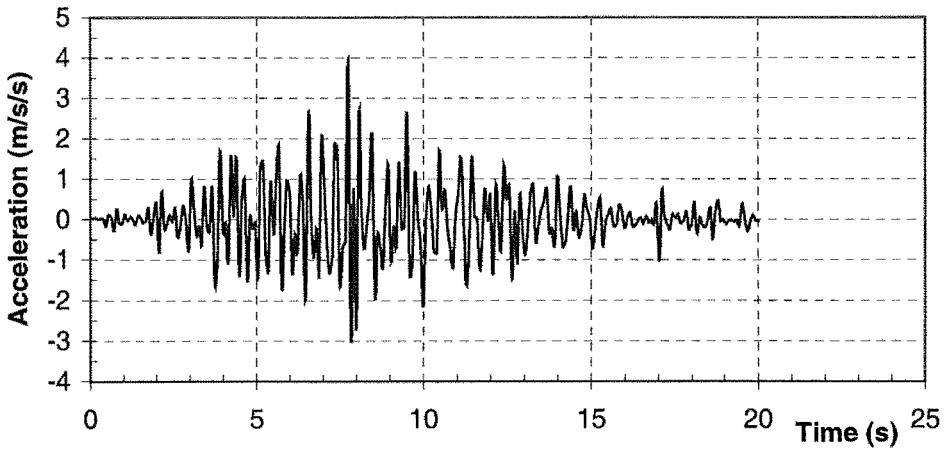

Figure 3.11 the Loma-Prieta Earthquake

only the Newmark method is used because it is a special case). These two results are

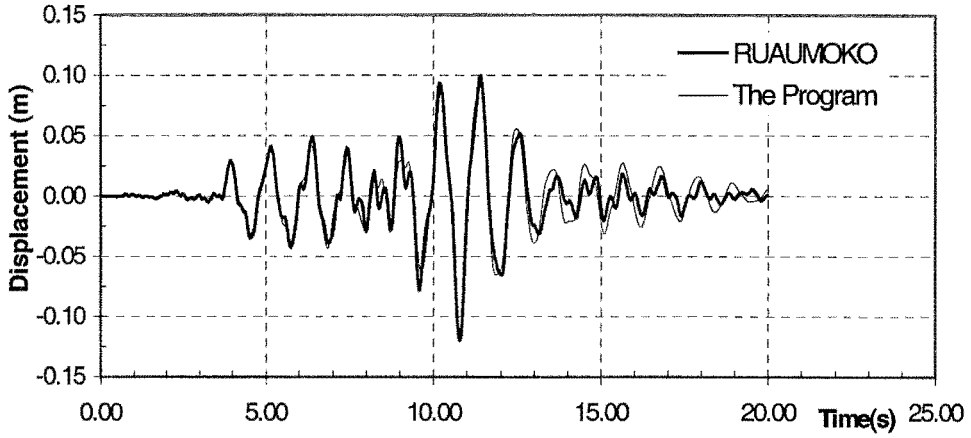

Figure 3.12 Comparison of Displacement at Node A

very close. A slight difference is observed after 14 seconds of the excitation.

The system consisting of the 6-storey frame, the foundation and the soil shown in Fig.3.10 is used to carry out a soil-structure interaction analysis. The results calculated at point A by RUAUMOKO and SSINAP2D are shown in Fig.3.13. It can be seen that the maximum displacement and frequency from both programs are nearly the same at point A.

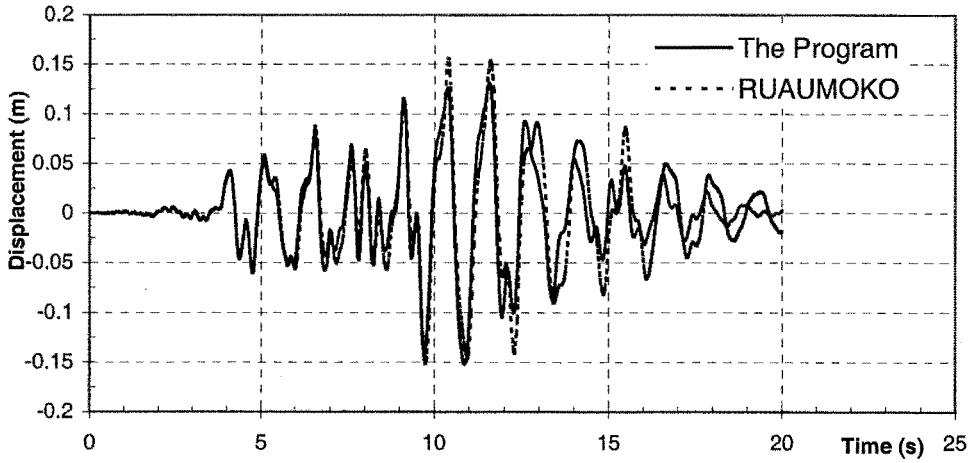

Figure 3.13 Comparison of Displacement at Node A

3.7 Summary

The soil is a very important part of any soil-structure interaction analysis and its behaviour is very complex. Many models have been proposed to describe the soil

properties. When compared with simple elastic models or simplified elastoplastic models, advanced elasto-plastic models show their advantages: one is that pore pressure and permanent deformation can be directly calculated; the second is that the kinematic-hardening can be considered. In this Chapter, the bounding surface model has been discussed. Its advantages are that it needs less memory than the nested surface model and is easily implemented in software applications because of the simple radial mapping employed.

In order to investigate seismic soil-structure interaction in this thesis, the bounding surface model has been implemented into the computer code. The result in Fig.3.7 shows that the nonlinear analysis code can adequately predict the soil response.

For the structure, the bi-linear model is used as the material model and the one-component model is used as the numerical analysis model of the beam and column. The applications of the above model will be discussed in chapter 7.

As the dynamic equilibrium equation is a second-order differential equation, a numerical integration technique has to be employed to solve it. In this Chapter, the advantages and disadvantages of four numerical integration methods were reviewed. When compared with the Newmark method and the Wilson-θ method, the α method shows second-order accuracy and artificial damping, with the Newmark method being a special case.

In order to implement the theories in this Chapter, a special purpose computer program, SSINAP2D, was designed. In the SSINAP2D program, the α method is used for the numerical integration, the Newton-Raphson method is used for carrying out the nonlinear iteration, and Rayleigh damping is employed to represent damping in the soil and the structure. Finally, the results calculated by SSINAP2D are compared with those calculated by RUAUMOKO. The program will be used in Chapters Six, Seven and Eight.

Chapter Four

Transmitting Boundary – Boundary Element Method in the Time Domain

4.1 Introduction

As mentioned in Chapter 2, the far field simulation in soil-structure interaction has been a topic of considerable interest over the past twenty years. Two main methods, a general transmitting boundary method and a boundary element method, have been used to simulate the far field. When compared with the general transmitting boundary method, the boundary element method (BEM) is more rigorous. Usually the boundary element method is divided in modelled either the frequency domain or the time domain. When both the soil and structure in the soil-structure interaction analysis are considered as linear elastic materials, the boundary element method in the frequency domain shows its simplicity and is easily implemented. However if the structure is considered as a nonlinear material, the boundary element method in the time domain is to be preferred. In this Chapter, the boundary element method in the time domain will be discussed in detail, then it will be used in Chapter 6.

In the following, a brief description of the necessary analytical formulation of the problem is given on the basis of the book by Eringen and Suhubi (1975). Betti's reciprocal theorem will be used to deduce an integral representation. A solution procedure will be discussed in detail. Finally, a benchmark problem will be solved by the boundary element computer code and the results will be compared with published data.

4.2 Governing Equations

The standard index notation has been adopted as in Chapter Two where summation is implied for repeated indices, commas and dots indicate spatial and time differentiation,

and Latin subscripts assume the values 1 to 3 for three dimensional analyses and 1 to 2 for two dimensional analyses.

The elastodynamic state of a three dimensional linear, isotropic region with volume R and surface B can be expressed as the Navier-Cauchy equations of motion

$$(c_1^2 - c_2^2)u_{i,ij} + c_2^2 u_{j,ii} + f_j = \ddot{u}_j \tag{4.1}$$

where $u_j = u_j(x, t)$ is the displacement vector at the point x and at time t, f_j is the body force per unit mass and c_1 and c_2 are the velocities of the dilatational and shear waves respectively, which can be expressed in terms of the Lame elastic constants λ and μ and mass density ρ as

$$c_1^2 = (\lambda + 2\mu)/\rho \tag{4.2a}$$

$$c_2^2 = \mu/\rho \tag{4.2b}$$

The traction tensor t_{ij} and the displacement gradients are related by Hook' s law

$$t_{ij} = \rho(c_1^2 - 2c_2^2)u_{m,m}\delta_{ij} + \rho c_2^2(u_{i,j} + u_{j,i}) \tag{4.3}$$

where δ_{ij} is the Kronecker delta that has been introduced in Chapter 3. In addition, the following conditions should be satisfied along the boundary B,

$$t_{(n)i} = t_{ij}n_j \qquad x \in B_t \tag{4.4a}$$

$$u_i = u_i(x,t) \qquad x \in B_n \tag{4.4b}$$

where $t_{(n)i}$ is the traction vector, n is the unit normal vector of a differential element on surface B, and $B_t \cup B_n = B$. For soil-structure interaction problems, quiescent conditions are usually assumed, i. e .,

$$u_i(x,t) = \dot{u}_i(x,t) = 0, \tag{4.5}$$

if $t \le 0, \quad x \in R \cup B$

4.3 The Integral Representation

To generate the general form of integral equations replacing Eq.4.1, it is first necessary to specify the required fundamental solution that will be applied in this work. For this purpose, the fundamental singular solution of Eq.4.1 in an infinite solid medium due to a concentrated body force is employed. Such a body force can be expressed as

$$\rho f(x,t) = f(t)\delta(x-\xi)e \tag{4.6}$$

where x and ξ are points in the infinite medium, $\delta(z)$ is the Dirac delta function (if z is greater than or equal to zero, it equals z, otherwise it equals zero), e is the direction in which the above force is applied, and $f(t)$ is its time variation. Substitution of Eq.4.6 as a body force in Eq.4.1 will derive the equation of the response in the infinite soil medium in the form

$$u_i = G_{ij}(x,t;\xi)e_j \tag{4.7}$$

where G_{ij} is the second order displacement tensor. Usually, G_{ij} is called the fundamental singular solution of the elastodynamic equations or the Stokes' displacement tensor and given by

$$G_{ik}(x,\, t;\, \xi \,|f) = \frac{1}{4\pi\rho}\{(\frac{3r_i r_k}{r^3} - \frac{\delta_{ik}}{r})\int_{c_2^{-1}}^{c_1^{-1}} \lambda f(t-\lambda r)d\lambda +$$

$$\frac{r_i r_k}{r^3}[\frac{1}{c_1^2} f(t-\frac{r}{c_1}) - \frac{1}{c_2^2} f(t-\frac{r}{c_2})] +$$

$$\frac{\delta_{ij}}{rc_2^2} f(t-\frac{r}{c_2})\} \tag{4.8}$$

where

$$r_i = x_i - \xi_i, \quad r^2 = (x_i - \xi_i)(x_i - \xi_i),$$

and

$$f(t-s) \neq 0, \quad \text{if} \quad t-s > 0. \tag{4.9}$$

With the time retard function $f(t-s)$ used in Eq.4.8 and the substitution of u_i of Eq.4.7 into Eq.4.3, the traction tensor t_{ij} can be expressed as

$$t_{ij} = F_{ij} n_k \tag{4.10}$$

where

$$F_{ij}(x,t;\xi) = \frac{1}{4\pi}\{(-6c_2^2)(\frac{5r_i r_j r_k}{r^5} -$$

$$\frac{\delta_{ij}r_k + \delta_{ik}r_j + \delta_{jk}r_i}{r^3}) \int_{c_1^{-1}}^{c_2^{-1}} \lambda f(t-\lambda r) d\lambda +$$

$$2(\frac{6r_i r_j r_k}{r^5} - \frac{\delta_{ij}r_k + \delta_{ik}r_j + \delta_{jk}r_i}{r^3}).\ [f(t-\frac{r}{c_2}) - \frac{c_2^2}{c_1^2} f(t-\frac{r}{c_1})] +$$

$$2\frac{r_i r_j r_k}{r^4 c_2}[\dot{f}(t-\frac{r}{c_2}) - \frac{c_2^3}{c_1^2}\dot{f}(t-\frac{r}{c_1})] +$$

$$\frac{r_k \delta_{ij}}{r^3}(1-2\frac{c_2^2}{c_1^2})[f(t-\frac{r}{c_1}) - \frac{r}{c_1}\dot{f}(t-\frac{r}{c_1})] +$$

$$\frac{\delta_{ik}r_j + \delta_{jk}r_i}{r^3}[f(t-\frac{r}{c_2}) - \frac{r}{c_2}\dot{f}(t-\frac{r}{c_2})]\} \tag{4.11}$$

Eq.4.8 stands for the displacement component at time t in the i-direction at the point x due to a concentrated force of magnitude $f(t)$ acting at the point ξ in the k-direction. A

similar physical meaning is also attached to the tensor F_{ij}. The pair of fundamental singular solutions $[G_{ij}, F_{ij}]$ is called the "Stokes" state of the quiescent past.

The above fundamental singular solutions obey the causality condition

$$G_{ij}(x,t;\xi,\tau)=0 \qquad \text{if} \qquad c_1(t-\tau)<r \tag{4.12a}$$

and have the following time translation property:

$$G_{ij}(x,t+t_0;\xi,\tau+t_0)=G_{ij}(x,t;\xi,\tau) \tag{4.12b}$$

The integral equation can be obtained by using Betti's reciprocal theorem. The obvious choice for one of the two elastodynamic states is the unknown state which is being sought. A judicious choice for the other state is the appropriate fundamental singular solution that satisfies the governing equations of motion in the region. The singular integral equations are of the form

$$c_{ij}u_i(\xi,t)=\int_S \{G_{ij}(x,t;\xi)*t_i(x,t)-F_{ij}(x,t;\xi)*u_i(x,t)\}dS(x) \tag{4.13}$$

where ξ is the source point and x is the receiver point.

$$c_{ij}=\delta_{ij}-\gamma_{ij} \tag{4.14}$$

γ_{ij} is a discontinuity or jump term such that: (a) for ξ inside the region it is equal to zero; (b) for ξ exterior to the region it is equal to δ_{ij}; (c) for ξ on the boundary of the region it is defined by the local tangent plane.

Now that the three dimensional foundational singular solutions and integral representation have been obtained in Eqs. 4.8, 4.11 and 4.13, the two dimensional singular solutions can be obtained in two ways.

First, the three dimensional tensors G_{ij} and F_{ij} can be transformed into the case of plane strain (Manolis 1983). Consider a cylindrical body of infinite extent along the Z direction, as shown in Fig.4.1. At a time t a wave that emanated from source point ξ envelops a spherical region of radius R=ct, where c is the propagation velocity. Notice that ξ is taken to lie on the XY plane for convenience, since both displacement and velocity vectors are now independent of the Z coordinate. Therefore, at time t the first of the two integrals appearing in Eq.4.13 becomes

$$\sum_{K=1}^{N}\int_{S}\int_{Z_{K-1}}^{Z_K} G_{ij}(x,K\Delta t;\xi)t_i(x,(N-K+1)\Delta t)dzdS(x) \qquad (4.15)$$

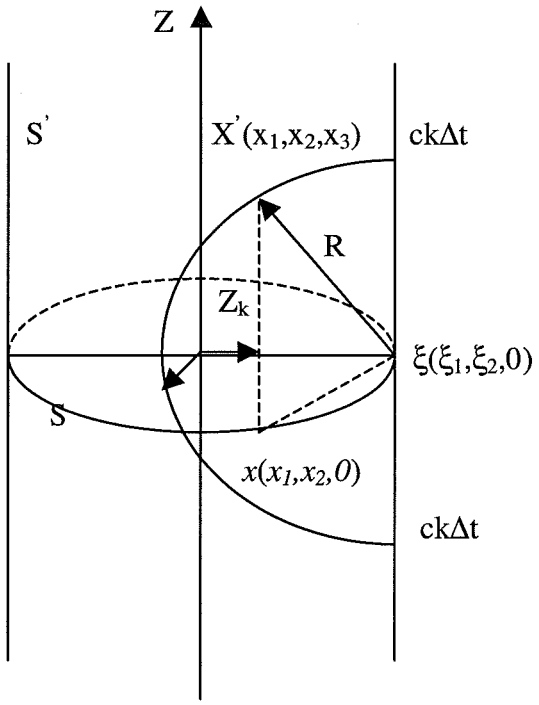

Figure 4.1 Circular cylindrical cavity of infinite length-region affected by wave propagating from point ξ

In the above equation, the current time $t=N\Delta t$ with Δt being an appropriate time increment and x is the projection of X' on the XY plane. Furthermore, Z_k is the vertical distance x_3 between X' and x at time $K\Delta t$, that is

$$Z_K = \sqrt{[(cK\Delta t)^2 - (x-\xi)^2]}$$

If constant traction is assumed during the time interval $[K\Delta t, (K-1)\Delta t]$, the above equation becomes

$$\sum_{K=1}^{N}\int_S G_{ij}^{"}(x, K\Delta t;\xi)t_i(x,(N-K+1)\Delta t)dS(x) \tag{4.16a}$$

where

$$G_{ij}^{"} = (2/4\pi\rho)[\int\frac{dc}{c^3}\int\frac{1}{r}(3r_{,i}r_{,j}-\delta_{ij})dz$$

$$+\frac{1}{c_1^2}\int\frac{r_{,i}r_{,j}}{r}dz+\frac{1}{c_2^2}\int\frac{1}{r}(\delta_{ij}-r_{,i}r_{,j})dz] \tag{4.16b}$$

where r is the distance between x and ξ and that i and j assume the values 1 and 2 only. Similarly, the second integral of Eq.4.13 can be written as

$$\sum_{K=1}^{N}\int_S n_m\left\{T_{ijm}(x, K\Delta t;\xi)u_i(x,(N-K+1)\Delta t)+Q_{ijm}(x, K\Delta t;\xi)\dot{u}_i(x,(N-K+1)\Delta t)\right\}dS(x) \tag{4.17a}$$

where

$$T_{ijm} = \frac{2}{4\pi}[-6c_2^2\int_{c_2}^{c_1}\frac{dc}{c^3}\int_{z_{K-1,C}}^{Z_{K,C}}\frac{1}{r^2}\{5r_{,i}r_{,j}r_{,m}-(\delta_{im}r_{,j}+\delta_{ij}r_{,m}+\delta_{jm}r_{,i})\}dz$$

$$-\int_{Z_{K-1,C_1}}^{Z_{K,C_1}}\frac{1}{r^2}\left\{2\left(\frac{c_2}{c_1}\right)^2[6r_{,i}r_{,j}r_{,m}-(\delta_{im}r_{,j}+\delta_{ij}r_{,m}+\delta_{jm}r_{,i}]+\left[1-2\left(\frac{c_2}{c_1}\right)^2\delta_{im}r_{,j}\right]\right\}dz$$

$$+\int_{Z_{K-1,C_2}}^{Z_{K,C_2}}\frac{1}{r^2}\{12r_{,i}r_{,j}r_{,m}-(2\delta_{im}r_{,j}+\delta_{ij}r_{,m}+\delta_{jm}r_{,i})\}dz] \tag{4.17b}$$

and

$$Q_{ijm} = \frac{2}{4\pi}[-\frac{1}{c_1}\int\frac{1}{r}\left\{2\left(\frac{c_2}{c_1}\right)^2 r_{,i}r_{,j}r_{,m} + \left[1-2\left(\frac{c_2}{c_1}\right)^2\right],\delta_{ij}r_{,j}\right\}dz$$

$$+\int\frac{1}{r}\{2r_{,i}r_{,j}r_{,m} - (\delta_{ij}r_{,m} + \delta_{jm}r_{,i})\}dz] \qquad (4.17c)$$

Furthermore, the velocity $\dot{u}_i$ in Eq.4.17a can be replaced by a backward finite difference in time

$$\dot{u}_i(x,(N-K+1)\Delta t) \cong \{u_i(x,(N-K+1)\Delta t) - u_i(x,(N-K)\Delta t))\}/\Delta t \qquad (4.17d)$$

Another approach is to use a corresponding solution for two dimensions which can be directly obtained from the three dimensional solution via the method of descent (Eringen and Suhubi 1975), i.e. the fundamental displacement singular solution in two dimensions for a unit impulse uniformly distributed along the z-axis is

$$G_{ij}^{2D} = \int_{-\infty}^{\infty} G_{ij}^{3D}\,dz \qquad (4.18)$$

The desired 2 dimensional fundamental singular solution is

$$G_{ij}^{"} = \frac{1}{2\pi\rho}\{(\frac{\left[2t^2-\frac{r^2}{c_1^2}\right]}{\left[t^2-\frac{r^2}{c_1^2}\right]^{1/2}}H(t-\frac{r}{c_1}) - \frac{\left[2t^2-\frac{r^2}{c_2^2}\right]}{\left[t^2-\frac{r^2}{c_2^2}\right]^{1/2}}H(t-\frac{r}{c_2}))\frac{r_i r_j}{r^4}$$

$$-[(t^2-\frac{r^2}{c_1^2})^{1/2}H(t-\frac{r}{c_1}) - (t^2-\frac{r^2}{c_2^2})^{1/2}H(t-\frac{r}{c_2})]\frac{\delta_{ij}}{r^2}$$

$$+\frac{1}{c_2^2\left[t^2-\frac{r^2}{c_2^2}\right]^{1/2}}H(t-\frac{r}{c_2})\delta_{ij}\} \qquad (4.19)$$

where subscripts i, j range from 1 to 2 and H is the Heaviside function

$$H(t-\tau)=\begin{cases}1 & if \quad t-\tau>0\\ 0 & if \quad t-\tau<0\end{cases} \tag{4.20a,b}$$

The Heaviside function ensures causality. In view of this, the fundamental displacement solution can be alternately written as

$$G_{ij}^{"}=\frac{1}{2\pi\rho}\left\{\frac{1}{c_1}g_1-\frac{1}{c_2}g_2\right\} \tag{4.21a}$$

where

$$g_1=\begin{cases}\dfrac{2\left(\dfrac{c_1t}{r}\right)^2-1}{\sqrt{\left(\dfrac{c_1t}{r}\right)^2-1}}\left(\dfrac{r_{,i}r_{,j}}{r}\right)-\dfrac{\delta_{ij}}{r}\sqrt{\left(\dfrac{c_1t}{r}\right)^2-1} & \text{when} \quad \dfrac{c_1t}{r}>1\\ 0 & \dfrac{c_1t}{r}<1\end{cases} \tag{4.21b}$$

$$g_2=\begin{cases}\dfrac{2\left(\dfrac{c_2t}{r}\right)^2-1}{\sqrt{\left(\dfrac{c_2t}{r}\right)^2-1}}\left(\dfrac{r_{,i}r_{,j}}{r}\right)-\dfrac{\delta_{ij}}{r}\dfrac{\left(\dfrac{c_2t}{r}\right)}{\sqrt{\left(\dfrac{c_2t}{r}\right)-1}} & \text{when} \quad \dfrac{c_2t}{r}>1\\ 0 & \dfrac{c_2t}{r}<1\end{cases} \tag{4.21c}$$

The fundamental traction solution is derived by using the expression in Eq.4.3 and finally the Heaviside function is introduced to assure the causality condition. It takes the

$$\text{form } F_{ij}^{''} = \frac{\mu}{2\pi\rho r}\left\{\frac{1}{c_1}H\left(\frac{c_2 t}{r}-1\right)\left[\frac{1}{\left\{\left(\frac{c_1 t}{r}\right)^2-1\right\}^{3/2}}\left(\frac{A_1}{r}\right)+\frac{2\left(\frac{c_1 t}{r}\right)-1}{\sqrt{\left(\frac{c_1 t}{r}\right)-1}}\left(\frac{2A_2}{r}\right)\right]\right\}$$

$$-\left\{\frac{1}{c_2}H\left(\frac{c_2 t}{r}-1\right)\left[\frac{1}{\left\{\left(\frac{c_2 t}{r}\right)^2-1\right\}^{3/2}}\left(\frac{A_3}{r}\right)+\frac{2\left(\frac{c_2 t}{r}\right)^2-1}{\sqrt{\left(\frac{c_2 t}{r}\right)-1}}\left(\frac{2A_2}{r}\right)\right]\right\} \tag{4.22}$$

where

$$A_1 = (\lambda/\mu)n_i r_{,j} + 2r_{,i}r_{,j}\frac{\partial r}{\partial n}$$

$$A_2 = n_i r_{,j} + n_j r_{,i} + \frac{\partial r}{\partial n}(\delta_{ij} - 4r_{,i}r_{,j})$$

$$A_3 = \frac{\partial r}{\partial n}(2r_{,i}r_{,j} - \delta_{ij}) - n_j r_{,i}$$

The above integral representation can be suitable for three-dimensional or two-dimensional problems and produces the radiation condition, where only an outward flow of energy is allowed at infinity. Thus, reflections from infinite boundaries are eliminated.

4.4 Numerical Treatment

Since it is difficult to mathematically resolve Eq.4.13 while dealing with arbitrary boundary geometry and complicated time variation of the related functions, a numerical approach is usually sought as in the finite element method. In the time domain, the method consists of two levels of discretisation, namely time and space, as shown in Fig.4.2. With regard to time discretisation, the real time axis is divided into a number of equally spaced time intervals in which displacements and tractions are assumed to have either a constant or a linear variation. With regard to spatial discretisation, the boundary B of the domain of interest is discretised into a number of linear elements for two

dimensional analysis and rectangular elements for three dimensional analysis where the variation of the field variables is described according to the same shape functions. In order to develop accurate boundary element method algorithms, it is essential that isoparametric representations of the geometry based on polynomial shape functions are similar to those used in the finite element method. In this section, only time integration will be discussed in detail. Firstly, the three dimensional solution will be discussed, then the two dimensional solution will follow.

In order to integrate the time convolutions analytically, the time interval of interest t_N is discretised into N time steps of duration Δt, so that $t_n = n\Delta t$, where $n=1, 2, \ldots, N$. The current time is denoted as t. A linear time variation is assumed for both displacements and tractions at a given station x_i as shown in Fig.4.2b. The displacement can be written as

$$u_i(x,t) = \sum_{n=1}^{N}\left[\left(\frac{t_n - t}{\Delta t}\right)u_i^{n-1}(x) + \left(\frac{t - t_{n-1}}{\Delta t}\right)u_i^{n}(x)\right]\Phi_n(t) \qquad (4.23)$$

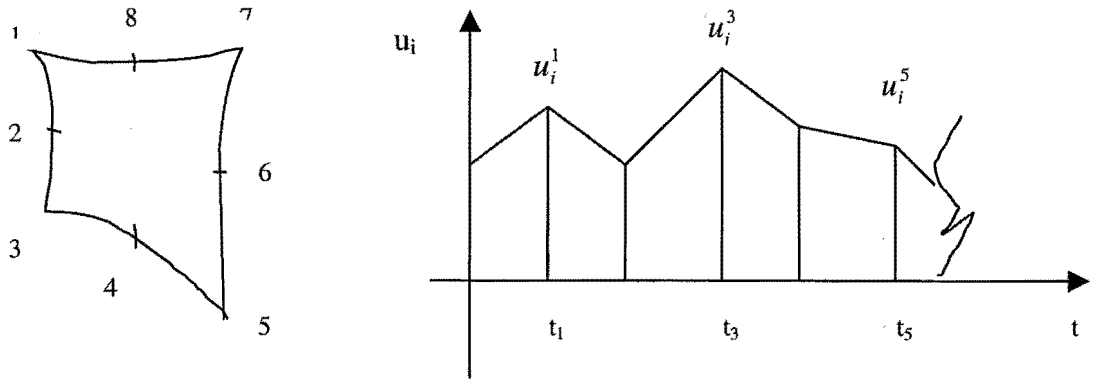

(a) Eight-node quadrilateral element (b) Linear variation of displacement vector u with respect to time

Figure 4.2 Sketch of Spatial and Time Discretisation

where u_i^n contains the spatial variation of the displacements at time t_n. A similar formula can be written for the tractions. Furthermore,

$$\Phi_n(t) = H(t-(n-1)\Delta t) - H(t-n\Delta t) \tag{4.24}$$

where H is the Heaviside function.

Now consideration is focused on the second term of the integral representation of Eq.4.13. One has

$$\begin{aligned}\int_S F_{ij} * u_i dS = \int_S \{ & d_{ij}(r)\delta(t-\frac{r}{c_1}) + e_{ij}(r)\delta(t-\frac{r}{c_2}) \\ & + f_{ij}(r)\int \delta(t-\lambda r)\lambda d\lambda + g_{ij}\dot{\delta}(t-\frac{r}{c_1}) \\ & + h_{ij}(r)\dot{\delta}(t-\frac{r}{c_2})\} * u_i dS\end{aligned} \tag{4.25a}$$

where d_{ij}, e_{ij}, f_{ij}, g_{ij}, h_{ij} are shown in Manolis and Beskos (1989). Substituting Eq.4.23 for u_i in the above and considering each term, one obtains

$$\begin{aligned}&\int_S \int_0^t d_{ij}\delta(t-\tau-\frac{r}{c_1})u_i(x,\tau)d\tau dS(x) \\ &= \sum_n \int_s d_{ij}\left\{\left(\frac{t-t_{n-1}-r/c_1}{\Delta t}\right)u_i^n - \left(\frac{t-t_n-r/c_1}{\Delta t}\right)u_i^{n-1}\right\}\phi(t-r/c_1)dS\end{aligned} \tag{4.25b}$$

Then

$$\begin{aligned}&\int_S \int_{c_1^{-1}}^{c_2^{-1}} \int_0^t \delta(t-\lambda r-\tau)u_i(x,\tau)d\tau\lambda d\lambda dS(x) \\ &= \sum_n \int_S f_{ij}\{(\frac{(t-t_{n-1})\psi_n - r\chi_n}{\Delta t})u_i^n + (\frac{(t_n-t)\psi_n + r\chi_n}{\Delta t})u_i^{n-1}\}dS\end{aligned} \tag{4.25c}$$

and finally

$$\begin{aligned}&\int_S \int_0^t g_{ij}\dot{\delta}(t-\tau-\frac{r}{c_1})u_i(x,\tau)d\tau dS(x) \\ &= \sum_n \int_S g_{ij}\{\frac{1}{\Delta t}u_i^n - \frac{1}{\Delta t}u_i^{n-1}\}\phi_n(t-\frac{r}{c_1})dS\end{aligned} \tag{4.25d}$$

In the above,

$$\psi_n = I_{n-1} - I_n, \qquad \chi_n = J_{n-1} - J_n \tag{4.25e}$$

where

$$I_n = \begin{cases} 0 & t - \dfrac{r}{c_2} < n\Delta t \\ \dfrac{1}{2}\left(\dfrac{1}{c^2} - \dfrac{1}{c_1^2}\right) & \text{if} \quad t - \dfrac{r}{c_2} \le n\Delta t \le t - \dfrac{r}{c_1} \\ \dfrac{1}{2}\left(\dfrac{1}{c_2^2} - \dfrac{1}{c_1^2}\right) & t - \dfrac{r}{c_2} > n\Delta t \end{cases} \tag{4.25f}$$

with $1/c = (t - n\Delta t)/r$. The definition for J_n is following

$$J_n = \begin{cases} 0 & t - \dfrac{r}{c_2} < n\Delta t \\ \dfrac{1}{3}\left(\dfrac{1}{c^3} - \dfrac{1}{c_1^3}\right) & \text{if} \quad t - \dfrac{r}{c_2} \le n\Delta t \le t - \dfrac{r}{c_1} \\ \dfrac{1}{3}\left(\dfrac{1}{c_2^3} - \dfrac{1}{c_1^3}\right) & t - \dfrac{r}{c_2} > n\Delta t \end{cases} \tag{4.25g}$$

The remaining terms e_{ij} and h_{ij} in Eq.4.25a are evaluated by replacing c_1 with c_2 in Eqs. 4.25b and 4.25c. The contribution of the $G_{ij}*t_i$ kernel can also be derived by substituting a_{ij}, b_{ij}, and c_{ij} for d_{ij}, e_{ij}, and f_{ij}, respectively, in the expressions for the $F_{ij}*u_j$ kernel. Thus, all time integrations are evaluated by closed-form expressions and only the surface integrations need to be done numerically.

Under the above discretisation, the boundary integral equation in Eq.4.13 is written for a number of M boundary elements with a total of Q nodal points (if constant elements are used $M=Q$) is transformed into a system of $3Q$ linear algebraic equations for each time step N. In a matrix summation form it can be expressed as

$$\frac{1}{2}\{u^{N,q}\} = \sum_{n=1}^{N}\sum_{s=1}^{Q}[G^{n,s}]\{t^{(N-n+1),s}\} - [F^{n,s}]\{u^{(N-n+1),s}\} \tag{4.26}$$

where $\{u^{p,q}\}$ or $\{u^{p,s}\}$ is the displacement vector of the receiver point $q=1, \ldots, Q$ or the source point $s=1, \ldots, Q$ at time step p, and $\{t^{p,s}\}$ is, similarly, the traction vector. The displacement tensor $[G^{n,s}]$ and the traction tensor $[F^{n,s}]$ represent the time- and space-discretised equivalents of fundamental solutions in the time domain. Physically, the 3×3 displacement tensor $G_{ik}^{n,s}$ represents the displacement component in the direction i at the nodal point q (receiver) and time step n due to a rectangular impulse traction component in the direction k acting at nodal point s (source) during the time step. A similarly physical meaning is attached to the 3×3 traction tensor.

For the two dimensional temporal integration, constant and linear temporal variations can be used. As in the three dimensional case, time integration is treated by analysis and spatial integration has to be done numerically.

Constant time variation

The displacements and tractions are assumed to be constant during a time step. Therefore, they can be taken out of the integration. Thus the time integration can be expressed as

$$G_{ij}^{N-n+1} = \int_{(n-1)\Delta T}^{n\Delta T} G_{ij}(x,T;\xi,\tau)d\tau \tag{4.27}$$

A similar expression for the traction kernel can be used to yield

$$c_{ij}(\xi)u_i^N(\xi,T) = \sum_{n=1}^{N}\int_S \left[G_{ij}^{N-n+1}t_i^n(x) - F_{ij}^{N-n+1}u_i^n(x)\right]dS(x) \tag{4.28a}$$

where the convolution is given in the explicit form, as

$$G_{ij}^{N-n+1} = \int_0^{\Delta T} G_{ij}(x,T;\xi,\tau)d\tau$$

$$= \frac{1}{2\pi\rho}\left[\frac{H(\alpha_1-1)}{c_1^2}\left\{\frac{\delta_{ij}}{2}\left[\cosh^{-1}(\alpha_1)-\alpha_1\beta_1\right]+r_{,i}r_{,j}\alpha_1\beta_1\right\}\right]$$

$$+\left[\frac{H(\alpha_2-1)}{c_2^2}\left\{\frac{\delta_{ij}}{2}\left[\cosh^{-1}(\alpha_2)+\alpha_2\beta_2\right]-r_{,i}r_{,j}\alpha_2\beta_2\right\}\right]_{z=(N-n)\Delta T}^{z=(N-n+1)\Delta T} \quad (4.28b)$$

and

$$F_{ij}^{N-n+1} = \frac{\mu}{2\pi\rho r}\left[\frac{H(\alpha_1-1)}{c_1^2}\left\{-\frac{\alpha_1}{\beta_1}(A_1)+2\alpha_1\beta_1(A_2)\right\}\right]$$

$$+\left[\frac{H(\alpha_2-1)}{c_2^2}\left\{\frac{\alpha_2}{\beta_2}(A_3)-2\alpha_2\beta_2(A_2)\right\}\right]_{z=(N-n)\Delta T}^{z=(N-n+1)\Delta T} \quad (4.28c)$$

where

$$\alpha_i = \frac{c_i z}{r}; \qquad \beta_i = \sqrt{\alpha_i^2-1} \quad (4.28d)$$

and A_1, A_2 and A_3 have been defined earlier.

Linear time variation

The displacements and tractions are expressed by

$$u_i(x,\tau) = M_1(\tau)u_i^n(x) + M_2(\tau)u_i^{n-1}(x) \quad (4.29a)$$

and

$$t_i(x,\tau) = M_1(\tau)t_i^n(x) + M_2(\tau)t_i^{n-1}(x) \quad (4.29b)$$

where $M_1(\tau)$ and $M_2(\tau)$ are linear temporal shape functions, given by

$$M_1(\tau) = \frac{\tau - T_{n-1}}{\Delta T}; \qquad M_2(\tau) = \frac{T_n - \tau}{\Delta T}; \quad T_{n-1} \le \tau \le T_n \quad (4.29c)$$

Subscripts 1 and 2 refer to the forward and backward local time nodes respectively. These linear temporal shape functions are shown graphically in Fig.4.3

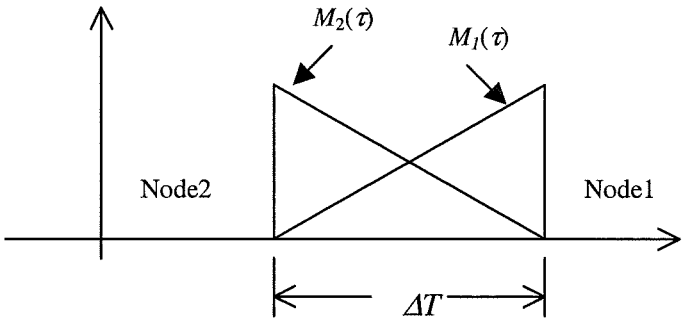

Figure 4.3 Linear temporal shape functions

The convoluted boundary element equation for linear temporal variation is

$$c_{ij}(\xi)u_i^N(\xi) = \sum_{n=1}^{N}\int\left(\left[G_{ij_1}^{N-n+1}t_i^n(x) + G_{ij_2}^{N-n+1}t_i^{n-1}(x)\right]\right.$$
$$\left. - \left[F_{ij_1}^{N-n+1}u_i^n(x) + F_{ij_2}^{N-n+1}u_i^{n-1}(x)\right]\right)dS(x) \qquad (4.29d)$$

The explicit expressions of $G_{ij_1}^{N-n+1}, G_{ij_2}^{N-n+1}, F_{ij_1}^{N-n+1}, F_{ij_2}^{N-n+1}$ are listed in Appendix One.

In the above, time discretisation in three dimensional and two dimensional analyses have been introduced. The spatial discretisation method is the same as in the finite element method.

4.5 Numerical Integration Schemes

Due to the singular characteristics of the fundamental solutions in carrying out the integrations indicated in Eq.4.13 (when r becomes zero in G_{ij}), two cases are distinguished:

Nonsingular Case

When the distance r between the receiver node q and the source node s remains finite, the integration in Eq.4.13 can be performed by a standard Gauss quadrature scheme. For improved accuracy, an element can be divided into subelements. This depends on the minimum distance r_{min} between element and field points and on the minimum L_{min} and maximum L_{max} element side lengths. The subdivision is determined by an intrinsic coordinate system, Gaussian integration scheme K3L and tolerance error c. Lachat and Watson (1976) gave an approximate relationship between these parameters.

$$(2K+1)(\frac{a}{4r_{min}})^{2K} \leq cab \tag{4.30a}$$

$$(2L+1)(\frac{b}{4r_{min}})^{2L} \leq cab \tag{4.30b}$$

where a and b are the dimensions of a subelement. For a line element, the criterion of subdivision is given as

$$(\frac{a}{4r_{min}})^{2K} \leq ca \tag{4.30c}$$

Singular Case

When the receiver node q belongs to the source element, a singularity will occur. Due to the nature of wave propagation, such a case will be encountered only during the first time step. The singularity of the discretised fundamental solution $G_{ik}^{n,s}$ is of order $1/r$, while that of $F_{ik}^{n,s}$ of order $1/r^2$

As far as the displacement singular solution $G_{ik}^{n,s}$ is considered, the singularity $1/r$ can be removed by transforming the local Cartesian coordinate system to a polar coordinate system. For the first time step, the "active" area surrounding a source point $\boldsymbol{a}$ is a full

circle centred at ***a***. Hence, during the first time interval Δt, the displacement tensor of Eq.4.8 can be expressed in terms of polar coordinates as

$$G_{ik}^{1,s} = \frac{1}{4\pi\rho}\left(\frac{1}{2}\left(\frac{1}{c_2^2}-\frac{1}{c_1^2}\right)\int_{\beta}^{\alpha}\int_{0}^{R_2}\left(\frac{3r_i r_k}{r^2}-\delta_{ik}\right)N^s dr d\vartheta\right.$$

$$+\frac{1}{2}\int\int\frac{1}{r^2}\left[(\Delta t)^2-\left(\frac{r}{c_1}\right)^2\right]\left(\frac{3r_i r_k}{r^2}-\delta_{ik}\right)N^s dr d\vartheta$$

$$+\frac{1}{c_1^2}\int_{\beta}^{\alpha}\int_{0}^{R_1}\frac{r_i r_k}{r^2}N^s dr d\vartheta \qquad (4.31)$$

$$\left.+\frac{1}{c_2^2}\int_{\beta}^{\alpha}\int_{0}^{R_2}\left(\delta_{ik}-\frac{r_i r_k}{r^2}\right)N^s dr d\vartheta\right)$$

where $r_1 = r\cos\vartheta$, $r_2 = r\sin\vartheta$, $r_3 = 0$ for a plane, R_1 and R_2 are the distance travelled by the dilatation and shear waves within the first time step Δt, and $[\beta, \alpha]$ is the range of integration as shown in Fig.4.4. In view of the above equation, it is clear that the singularity has been eliminated.

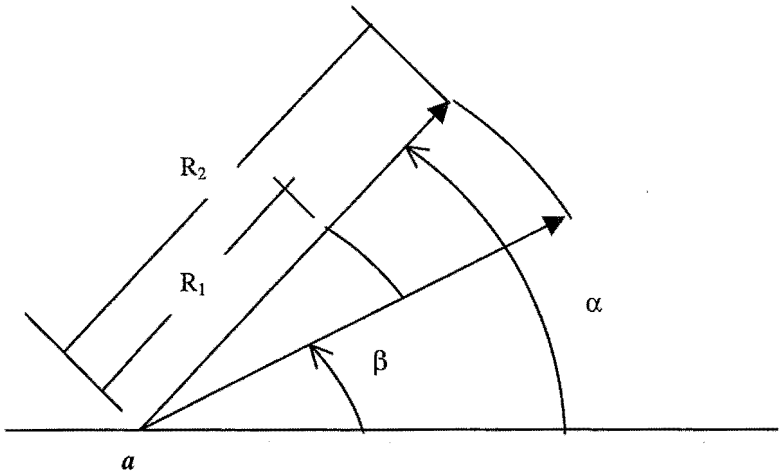

Figure 4.4 Notation for Spatial Integration over Singular Area

In two dimensions, it is necessary to divide the element into subelements only if the singular node lies inside the element. Numerical integration in all cases is carried out using the Gaussian quadrature formula with a weighting function $\log(1/\eta)$ (Stroud and Secrest 1966).

As far as the traction kernel integrand $F_{ik}^{1,s}$ is concerned, for plane elements, it has the same type and order of singularity as the corresponding elastostatic kernel. The singular integral is evaluated in the following way:

$$\int_S F_{ij}^{trans} dS = \int_S F_{ij}^{static} dS + \int_S (F_{ij}^{trans} - F_{ij}^{static}) dS \tag{4.32}$$

The first integral on the right hand side of the equation is singular and its evaluation using the technique of rigid body motions is well known. However, for this technique the body must have a closed boundary. Thus for half-plane problems, the region of interest must be enclosed with a fictitious boundary. For detailed discussions of the procedure refer to the papers by Ahmad and Banerjee (1988) and Henry and Banerjee (1988). A similar numerical integration can be used in two dimensions.

4.6 Solution Procedure

After the temporal and spatial discretisation, a system of algebraic equations can be developed. For each boundary node, the equation can be put into matrix form as

$$\sum \left([G^{N-n+1}] \{t^n\} - [F^{N-n+1}] \{u^n\} \right) = \{0\} \tag{4.33}$$

where $\{t\}$ and $\{u\}$ are global vectors of the nodal tractions and displacements respectively with the superscript referring to the time-step index.

At time T, only part of the boundary variables are unknown, the rest are known and so is the past history of the response. The above equation then can be rearranged to give

$$[A^1]\{X^N\}=[B^1]\{Y^N\}-\sum_{n=1}^{N-1}([G^{N-n+1}]\{t^n\}-[F^{N-n+1}]\{u^n\}) \tag{4.34a}$$

or $$[A^1]\{X^N\}=[B^1]\{Y^N\}+\{R^N\} \tag{4.34b}$$

in which $\{X\}$ is a vector of the unknown quantities and $\{Y\}$ is a vector of known quantities at time T and $\{R\}$ represents the effect of past dynamic history on the current time step. The above equation can be solved for the unknown boundary values using any standard matrix equation solver.

4.7 Numerical Example

The method presented in the above section is implemented into a computer code. A numerical example will be introduced here. An elastic half-plane Γ under discontinuous boundary stress distribution is shown in Fig.4.5. A half-plane is initially at rest with uniform compressive tractions T on Γ applied as a step function in time, as given by T(x,0,t)= -p(x,0)δH(t-0) where p = qh(x+b){1-H(x-b)}, where H() is heaviside function.

The vertical impulse force of intensity q = 6.896×10 kN/m acts on a strip of 2b = 146.4m width. The supporting homogenous, linear elastic soil medium is characterised by a modulus of elasticity E = 1.724×10 kN/m, mass density ρ = 3.151t/m and Poisson's ratio ν = 0.25. Thus, the propagation velocities of the dilatational and distortional waves are c_1 = 8.306×10 m/s and c_2 = 4.724×10 m/s. Points A, B and C are measured points.

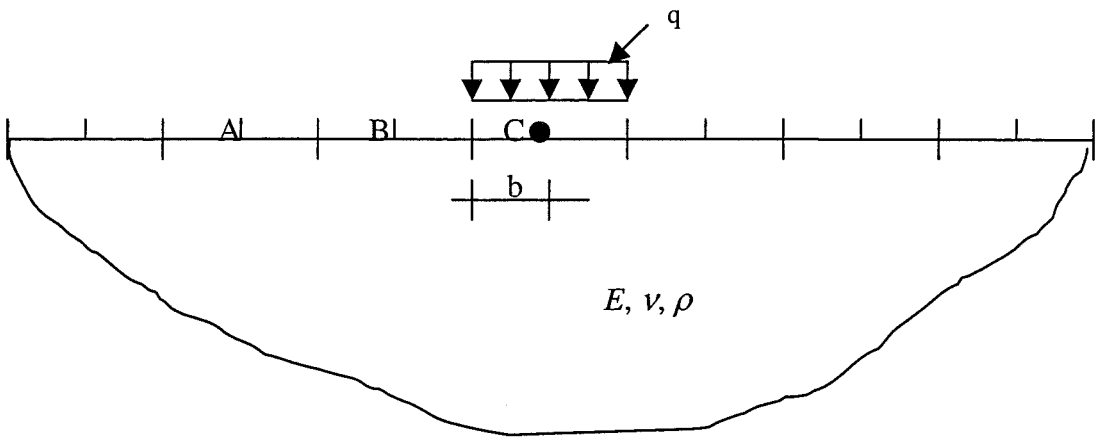

Figure 4.5 Spatial discretisation of the half-plane under discontinuous boundary stress Distribution

The calculated displacements at points A, B and C under the above load are shown in Fig.4.6. When compared with published data (Antes, 1986), the results are comparable.

4.8 Summary

In this Chapter, the boundary element method in the time domain is presented in detail. The three dimensional displacement and traction singular solutions have been given. Its integration representation is obtained by Betti's reciprocal theorem. The two dimensional displacement and traction singular solutions can be obtained by directly integrating the three dimensional singular solution or alternately by using Manolis's method. Numerical integration schemes and the solution procedure are introduced in detail. An implemented computer code is used to calculate a benchmark problem. The results show the method can be used to simulate an elastic half-plane deformation characteristics under dynamic loading.

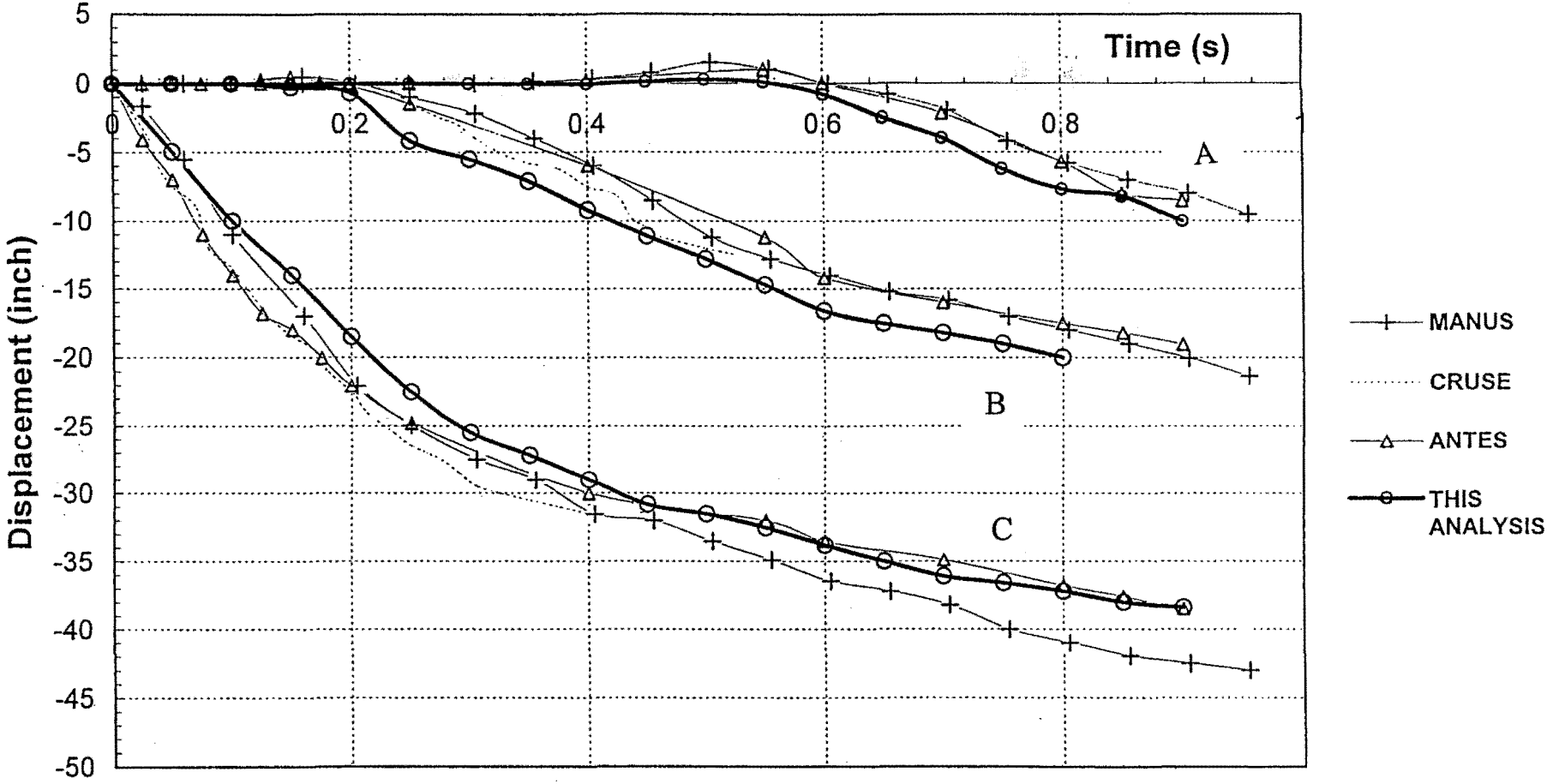

Figure 4.6 Comparisons between MANUS Data, CRUSE Data, ANTES Data and This Analysis

Chapter Five

Coupling Boundary Elements and Finite Elements in the Time Domain

5.1 Introduction

In the boundary element method, known fundamental solutions of the governing differential equations can be used to obtain solutions for boundary value problems. This means that only the boundary of the domain to be analysed has to be discretised and this is in contrast with the finite element method that requires a subdivision of the whole domain. The discretisation effort is, therefore, greatly reduced for problems analysed by the boundary element method because only the surface has to be divided into elements, hence coordinate and connectivity data are specified on the boundary only. But the boundary element method also exposes its disadvantage that the fundamental solutions are only available for a linear elastic and homogeneous domain. It also leads to coefficient matrices that are fully populated and non-symmetric and this contrasts with the sparsely populated and symmetric matrices obtained for the finite element method. This means that, for the same number of equations, substantially more computer time is spent in establishing and solving the equations for the boundary element method. In most cases, however, the number of boundary element equations will be considerably less than the number of finite element equations.

The finite element method, because of the volume discretisation, is ideally suited to problems involving non-homogeneous, anisotropic and nonlinear domains, but it is not suitable for modelling the far-field influence for problems in soil-structure interaction. Here the boundary element method is much better suited because the boundary conditions at infinity can be satisfied exactly by the fundamental solution.

In order to profit from the advantages of each of the two basic approaches, while avoiding their disadvantages, it seemed to be quite promising to develop combined

formulae. Zienkiewicz, Kelly and Bettes (1977) were among the first authors to propose a coupling of finite elements and boundary elements. Since then, there have been several papers suggesting coupling techniques; a summary with references and further details were given by Brebbia, Telles and Wrobel(1984) and Vallabhan (1987).

The early publications mostly considered potential and fluid-structure interaction problems. Fundamental works in this field have been carried out by Brebbia and Georgiou (1979); Beer and Meek (1981); Li, Han, Mang and Torzicky (1986); Swoboda, Mertz and Beer (1987).

In recent years, some researchers have focused their attention on the development of coupling procedures for elastodynamic problems. Amongst others, Kobayashi and Mori (1986) have used a combination of the boundary element method with the finite element method for the solution of soil-structure interaction problems, when their model was formulated in the frequency domain. Spyrakos and Beskos (1986), and Karabalis and Beskos (1985), respectively, considered plane and three-dimensional soil-foundation problems in the time domain using boundary elements for the soil and finite elements for the foundation. Estorff and Prabucki (1990) considered soil-elastic block interaction by coupling the boundary element method and the finite element method and used this coupled method to solve nonlinear problems.

In this Chapter, a differently deduced procedure will be employed to obtain similar coupled formula to those of Estorff and Prabucki's, but avoiding the transform and inversion calculations in Estorff and Prabucki's approach, and will be shown to be more easily implemented into a computer code. Finally, the method will be extended into seismic soil-structure interaction analysis.

5.2 Formulation

In this section, the basic governing equation, the assumptions, the boundary element, finite element formulations and the coupling procedure will be discussed. Finally a flow chart is given that shows how the method can be directly implemented into a computer code.

5.2.1 Governing Equation and Assumptions

For a homogeneous, isotropic and linear region, the mechanical behaviour can be expressed by the Navier-Cauchy equations of motion (Eq.4.1)

$$(c_1^2 - c_2^2)u_{i,ij} + c_2^2 u_{j,ii} + f_j = u_j \tag{5.1}$$

where c_1 and c_2 are the velocities of the dilatational and shear waves, respectively, which can be expressed by elastic coefficients (in Chapter 4, they are expressed by Lame constants). To use the same elastic constants as in the finite element method, the elastic coefficients are used).

$$c_1^2 = \frac{E(1-\upsilon)}{\rho(1+\upsilon)(1-2\upsilon)}; \qquad c_2^2 = \frac{E}{2\rho(1+\upsilon)} \tag{5.2}$$

where E indicates Young's modulus and ν is Poisson's ratio. ρ stands for the mass density of the elastic medium.

The boundary conditions and initial conditions are summarised as follows:

a) boundary conditions (specified along $\Gamma = \Gamma_1 \cup \Gamma_2$)

$u_i(x,t) = \bar{u}_i(x,t)$ for $t > t_0$ on Γ_1

$t_i(x,t) = \sigma_{ij} n_j = \bar{t}_i(x,t)$ for $t > t_0$ on Γ_2

b) initial conditions

$u_i(x,t) = \bar{u}_{i0}(x)$ for $t = t_0$ on Γ and in Ω

$\dot{u}(x,t) = \dot{\bar{u}}_{i0}(x)$

where overbars indicate prescribed values and n_j are the direction cosines of the outward normal to the boundary Γ. The traction components $\sigma_{ij}(x,t)$ can be expressed as functions of displacement derivations according to Eq.4.3

5.2.2 Boundary Element Formulation

Following Chapter 4, Collocation at each boundary node and at all time steps finally leads to a system of algebraic equations (Eq.4.17)

$$(\frac{1}{2}[I]+\left[\bar{F}\right])\{u\}=[F]\{u\}=[G]\{t\} \tag{5.3}$$

where $\{u\}$ and $\{t\}$ are vectors of all nodal displacements and tractions, respectively. $[G]$ and $[F]$ represent influence matrices which contain integral terms evaluated over each boundary element (numerically) and over each time step (analytically).

Considering the properties of the influence matrices one obtains from Eq.5.3, a relation between $\{u\}$and $\{t\}$ that can be given as:

$$[G^1]\{t^n\}+\sum_{p=1}^{n-1}[G^{(n-p+1)}]\{t^{(p)}\}=[F^1]\{u^n\}+\sum_{p=1}^{n-1}[F^{(n-p+1)}]\{u^{(p)}\} \tag{5.4a}$$

or

$$[G^1]\{t^n\}=[F^1]\{u^n\}-\sum_{p=1}^{n-1}([G^{(n-p+1)}]\{t^{(p)}\}-[F^{(n-p+1)}]\{u^{(p)}\}) \tag{5.4b}$$

Furthermore, Eq.5.4b can be expressed as

$$\{t^n\}=[G^1]^{-1}[F^1]\{u^n\}-[G^1]^{-1}(\sum_{p=1}^{n-1}([G^{(n-p+1)}]\{t^{(p)}\}-[F^{(n-p+1)}]\{u^{(p)}\}) \tag{5.4c}$$

Assuming

$$\left[\vec{K}\right]=[G^1]^{-1}[F^1] \tag{5.4d}$$

$$\left\{\vec{f}\right\}=\left[G^1\right]^{-1}\left(\sum_{p=1}^{n-1}\left(\left[G^{(n-p+1)}\right]\left\{t^{(p)}\right\}-\left[F^{(n-p+1)}\right]\left\{u^{(p)}\right\}\right.\right. \tag{5.4e}$$

substituting Eq.5.4d and Eq.5.4e into Eq.5.4c gives

$$\left\{t^n\right\}=\left[\vec{K}\right]\left\{u^n\right\}+\left\{\vec{f}\right\} \tag{5.4f}$$

According to Eq.5.4f, $\left[\vec{K}\right]$ can be considered as the stiffness matrix of a boundary element. $\left\{\vec{f}\right\}$ can be considered as a load that is produced by the time history.

5.2.3 Finite Element Formulation

The dynamic equilibrium equation in the finite element domain has been obtained in Chapter 3. In order to simplify the procedure, viscous damping is neglected here. If viscous damping is to be considered, it can be very easily incorporated. The dynamic equilibrium can be expressed as

$$[M]\left\{\ddot{u}\right\}+[K]\{u\}=\{p\} \tag{5.5}$$

where $[M]$ is the mass matrix, either a lumped mass matrix or a consistent mass matrix (Clough and Penzien, 1993), $[K]$ is the stiffness matrix in the finite element domain and $\{p\}$ is the external load vector. Because Eq.5.5 is a second-order differential equation, numerical integration must be employed. Here the Newmark constant-average acceleration method is used. At $t_m = n\Delta t$, velocity and acceleration can be expressed as

$$\left\{\dot{u}\right\}^n=h_1\left[\{u\}^n-\{u\}^{n-1}\right]+h_2\left\{\dot{u}\right\}^{n-1}+h_3\left\{\ddot{u}\right\}^{n-1} \tag{5.6a}$$

$$\left\{\ddot{u}\right\}^n = h_4\left[\{u\}^n - \{u\}^{n-1}\right] + h_5\left\{\dot{u}\right\}^{n-1} + h_6\left\{\ddot{u}\right\}^{n-1} \tag{5.6b}$$

where

$$h_1 = \frac{1}{\Delta t^2}\frac{\delta}{\alpha}, \qquad h_2 = (1-\frac{\delta}{\alpha}), \qquad h_3 = (1-\frac{\delta}{2\alpha})\Delta t$$

$$h_4 = \frac{1}{\Delta t^2}\frac{1}{\alpha}, \qquad h_5 = \frac{1}{\Delta t}\alpha, \qquad h_6 = (1-\frac{1}{2\alpha})$$

$\delta = 0.5$; $\alpha = 0.25(0.5+\delta)$

The integration process can be realised either at an element level or, after assembling the local matrices, at a system level. Both approaches lead to a so-called effective stiffness matrix $[K_{eff}]$ and an effective load vector $\{P_{eff}\}$.

$$[K_{eff}]\{u\}^n = \{P_{eff}\}. \tag{5.7a}$$

where

$$[K_{eff}] = h_4[M] + [K] \tag{5.7b}$$

and

$$\{P_{eff}\}^n = \{p\}^n - [M](h_6\left\{\ddot{u}\right\}^{n-1} + h_5\left\{\dot{u}\right\}^{n-1} - h_4\{u\}^{n-1} \tag{5.7c}$$

5.2.4 Coupling Procedure between Boundary Elements and Finite Elements

In order to exploit the advantages of the boundary and finite element methods, all domains can be subdivided into a boundary element domain that represents an infinite domain and a finite element domain that represents the near field and the structure. Fig.5.1 shows the two different domains, where subscript *i* represents a contact boundary between the boundary element domain and the finite element domain and 0

represents a non-contact boundary; superscripts b and f denote the boundary element domain and the finite element domain, respectively.

The coupling of the boundary element and the finite element is performed by imposing compatibility and equilibrium conditions along a contact boundary between the two domains and an assumed weld condition along the contact boundary. Compatibility and equilibrium conditions can be expressed as

$$u_i^{f(n)} = u_i^{b(n)} \; ; \qquad p_i^{f(n)} + p_i^{b(n)} = 0 \tag{5.8}$$

To meet Eq.5.8, the equilibrium equations, Eq.5.7a in the finite element domain and Eq.5.4e in the boundary element domain, will be rearranged according to the contact and non-contact boundaries.

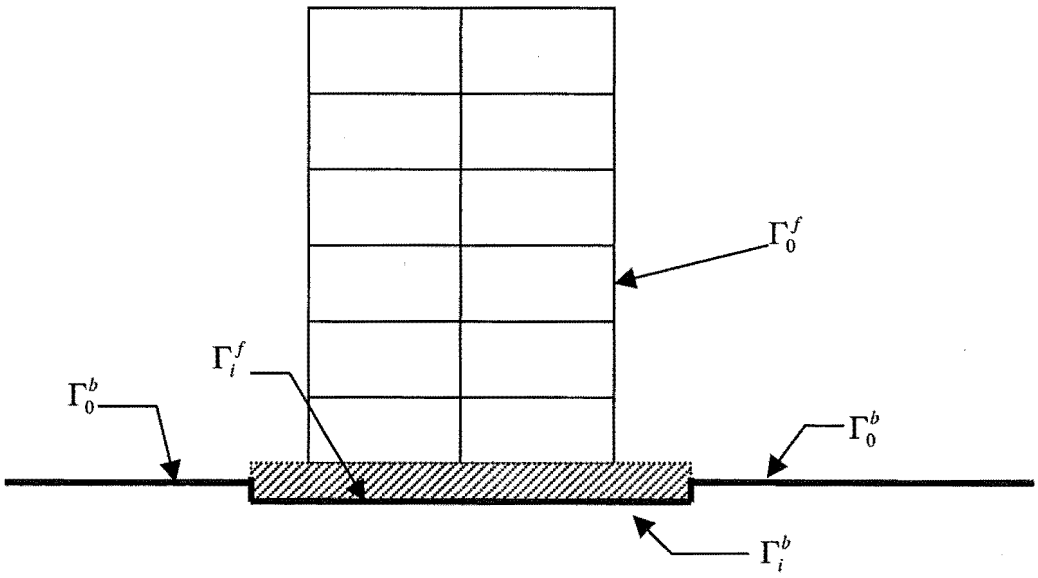

Figure 5.1 Sketch of boundary element and finite element domains

Rewriting Eq.5.7a for the contact and non-contact boundaries

$$\begin{bmatrix} [K_{00}]^f & [K_{0i}]^f \\ [K_{i0}]^f & [K_{ii}]^f \end{bmatrix} \begin{Bmatrix} \{u_0\}^{f(n)} \\ \{u_i\}^{f(n)} \end{Bmatrix} = \begin{Bmatrix} \{p_0\}^{f(n)} \\ \{p_i\}^{f(n)} \end{Bmatrix} = \begin{Bmatrix} \{p_0\}^{f(n)} \\ \{0\} \end{Bmatrix} + \begin{Bmatrix} \{0\} \\ \{p_i\}^{f(n)} \end{Bmatrix} \tag{5.9a}$$

Therefore, the node load vector at the contact domain can be expressed as

$$\begin{Bmatrix} \{0\} \\ \{p_i\}^{f(n)} \end{Bmatrix} = \begin{bmatrix} [K_{00}]^f & [K_{0i}]^f \\ [K_{i0}]^f & [K_{ii}]^f \end{bmatrix} \begin{Bmatrix} \{u_0\}^{f(n)} \\ \{u_i\}^{f(n)} \end{Bmatrix} - \begin{Bmatrix} \{p_0\}^{f(n)} \\ \{0\} \end{Bmatrix} \tag{5.9b}$$

In Eq.5.4e, the solution is a traction, but in Eq.5.9b, the solution is the nodal load. Therefore, the traction has to be converted into a nodal load. For any one element, the relation between the traction and the nodal load can be expressed as

$$\{p\}^n = [D]\{t\}^n \tag{5.10}$$

where $[D]$ is expressed as

$$[D] = \begin{bmatrix} N_{11}^e[I] & N_{12}^e[I] & N_{13}^e[I] \\ N_{21}^e[I] & N_{22}^e[I] & N_{23}^e[I] \\ N_{31}^e[I] & N_{32}^e[I] & N_{33}^e[I] \end{bmatrix}$$

for a 3-node quadratic element, and

$$[D] = \begin{bmatrix} N_{11}^e[I] & N_{12}^e[I] \\ N_{21}^e[I] & N_{22}^e[I] \end{bmatrix}$$

for a 2-node line element.

In the above, $N_{ij}^e = \int_{S_e} N_i N_j ds$ and $[I]$ is a 2×2 unit vector.

In the boundary element domain, the nodal load can be expressed as

$$\begin{aligned} \{p^n\} &= [D]\{t^{b(n)}\} = [D]\left[\vec{K}\right]\{u^{b(n)}\} - [D]\left\{\vec{f}\right\}^{b(n)} \\ &= \left[\overleftrightarrow{K}\right]\{u^{b(n)}\} - \left\{\overleftrightarrow{f}\right\}^{b(n)} \end{aligned} \tag{5.11a}$$

Rewriting Eq.5.11a for a contact and non-contact boundaries gives:

$$\begin{Bmatrix} \{p_0^{b(n)}\} \\ \{p_i^{b(n)}\} \end{Bmatrix} = \begin{bmatrix} \left[\overleftrightarrow{K}_{00}\right]^b & \left[\overleftrightarrow{K}_{0i}\right]^b \\ \left[\overleftrightarrow{K}_{i0}\right]^b & \left[\overleftrightarrow{K}_{ii}\right]^b \end{bmatrix} \begin{Bmatrix} \{u_0^{b(n)}\} \\ \{u_i^{b(n)}\} \end{Bmatrix} - \begin{Bmatrix} \left\{\overleftrightarrow{f}_0\right\}^{b(n)} \\ \left\{\overleftrightarrow{f}_i\right\}^{b(n)} \end{Bmatrix} \tag{5.11b}$$

Separating Eq.5.11b into

$$\{p_0^{b(n)}\} = \left[\overleftrightarrow{K}_{00}\right]^b \{u_0^{b(n)}\} + \left[\overleftrightarrow{K}_{0i}\right]^b \{u_i^{b(n)}\} - \left\{\overleftrightarrow{f}_0\right\}^{b(n)} \tag{5.11c}$$

$$\{p_i^{b(n)}\} = \left[\overleftrightarrow{K}_{i0}\right]^b \{u_0^{b(n)}\} + \left[\overleftrightarrow{K}_{ii}\right]^b \{u_i^{b(n)}\} - \left\{\overleftrightarrow{f}_i\right\}^{b(n)} \tag{5.11d}$$

From Eq.5.11c

$$\{u_0^{b(n)}\} = \left[\overleftrightarrow{K}_{00}\right]^{b^{-1}} (\{p_0^{b(n)}\} - \left[\overleftrightarrow{K}_{oi}\right]^b \{u_i^{b(n)}\} + \left\{\overleftrightarrow{f}_0\right\}^{b(n)}) \tag{5.11e}$$

Substituting Eq.5.11e into Eq.5.11d

$$\{p_i^{b(n)}\} = \left[\overleftrightarrow{K}_{i0}\right]^b \left[\overleftrightarrow{K}_{00}\right]^{b^{-1}} (\{p_0^{b(n)}\} - \left[\overleftrightarrow{K}_{0i}\right]^b \{u_i^{b(n)}\} + \left\{\overleftrightarrow{f}_0\right\}^{b(n)}) + \left[\overleftrightarrow{K}_{ii}\right]^b \{u_i^{b(n)}\} - \left\{\overleftrightarrow{f}_i\right\}^{b(n)}$$

$$= (\left[\overleftrightarrow{K}_{ii}\right]^b - \left[\overleftrightarrow{K}_{i0}\right]^b \left[\overleftrightarrow{K}_{00}\right]^{b^{-1}} \left[\overleftrightarrow{K}_{oi}\right]^b) \{u_i^{b(n)}\} + \left[\overleftrightarrow{K}_{i0}\right]^b \left[\overleftrightarrow{K}_{00}\right]^{b^{-1}} \{p_i^{b(n)}\}$$

$$+ \left[\overleftrightarrow{K}_{i0}\right]^b \left[\overleftrightarrow{K}_{00}\right]^{b^{-1}} \left\{\overleftrightarrow{f}_0\right\}^{b(n)} - \left\{\overleftrightarrow{f}_i\right\}^{b(n)} \tag{5.11}$$

Let $$[K]_{BB} = \left[\overleftrightarrow{K}_{ii}\right]^b - \left[\overleftrightarrow{K}_{i0}\right]^b \left[\overleftrightarrow{K}_{00}\right]^{b^{-1}} \left[\overleftrightarrow{K}_{0i}\right]^b$$

$$\{\underline{f}\}=\left[\overleftrightarrow{K}_{i0}\right]^{b}\left[\overleftrightarrow{K}_{00}\right]^{b^{-1}}(\{p_o^{b(n)}\}+\left\{\overleftrightarrow{f}_0\right\}^{b(n)})-\left\{\overleftrightarrow{f}_i\right\}^{b(n)}$$

Therefore

$$\{p_i^{b(n)}\}=[K]_{BB}\{u_i^{b(n)}\}+\{\underline{f}\} \tag{5.11g}$$

Eq.5.11g is multiplied by the matrix $[E]$, where the $[E]$ matrix is given by

$$[E]=\begin{bmatrix}[0]_{00} & [0]_{0b}\\ [0]_{b0} & [I]_{bb}\end{bmatrix}$$

$$[E]\{p_i^{b(n)}\}=[E][K]_{BB}[E]^T[E]\{u_i^{b(n)}\}+[E]\{\underline{f}\} \tag{5.11h}$$

Therefore Eq.5.11h can be written as

$$\begin{Bmatrix}\{0\}\\ \{p_i^{b(n)}\}\end{Bmatrix}=\begin{bmatrix}[0] & [0]\\ [0] & [K]_{BB}\end{bmatrix}\begin{Bmatrix}\{0\}\\ \{u_i^{b(n)}\}\end{Bmatrix}+\begin{Bmatrix}\{0\}\\ \{f\}\end{Bmatrix} \tag{5.11i}$$

where the subscript *BB* denotes the degree of freedom for the contact part between the boundary element and the finite element.

Combining Eq.5.8, Eq.5.9b and Eq.5.11i gives

$$\begin{bmatrix}[K_{00}]^f & [K_{0i}]^f\\ [K_{i0}]^f & [K_{ii}]^f+[K]_{BB}\end{bmatrix}\begin{Bmatrix}\{u_0\}^f\\ \{u_i\}\end{Bmatrix}=\begin{Bmatrix}\{p_1\}^f\\ -\{f\}\end{Bmatrix} \tag{5.12}$$

(5.12)Eq.5.12 is the coupling equation of the boundary element and the finite element. After $\{u_i\}$ is formed, it is substituted into Eq.5.11e to solve for the displacements of the non-contact nodes in the boundary element domain.

From this coupling procedure, it is seen that a finite element package and a boundary element package only need to be slightly modified, for example; by directly inserting

the boundary element into the finite element procedure. The following flow chart illustrates the procedure.

Flow Chart of coupling boundary element and finite element

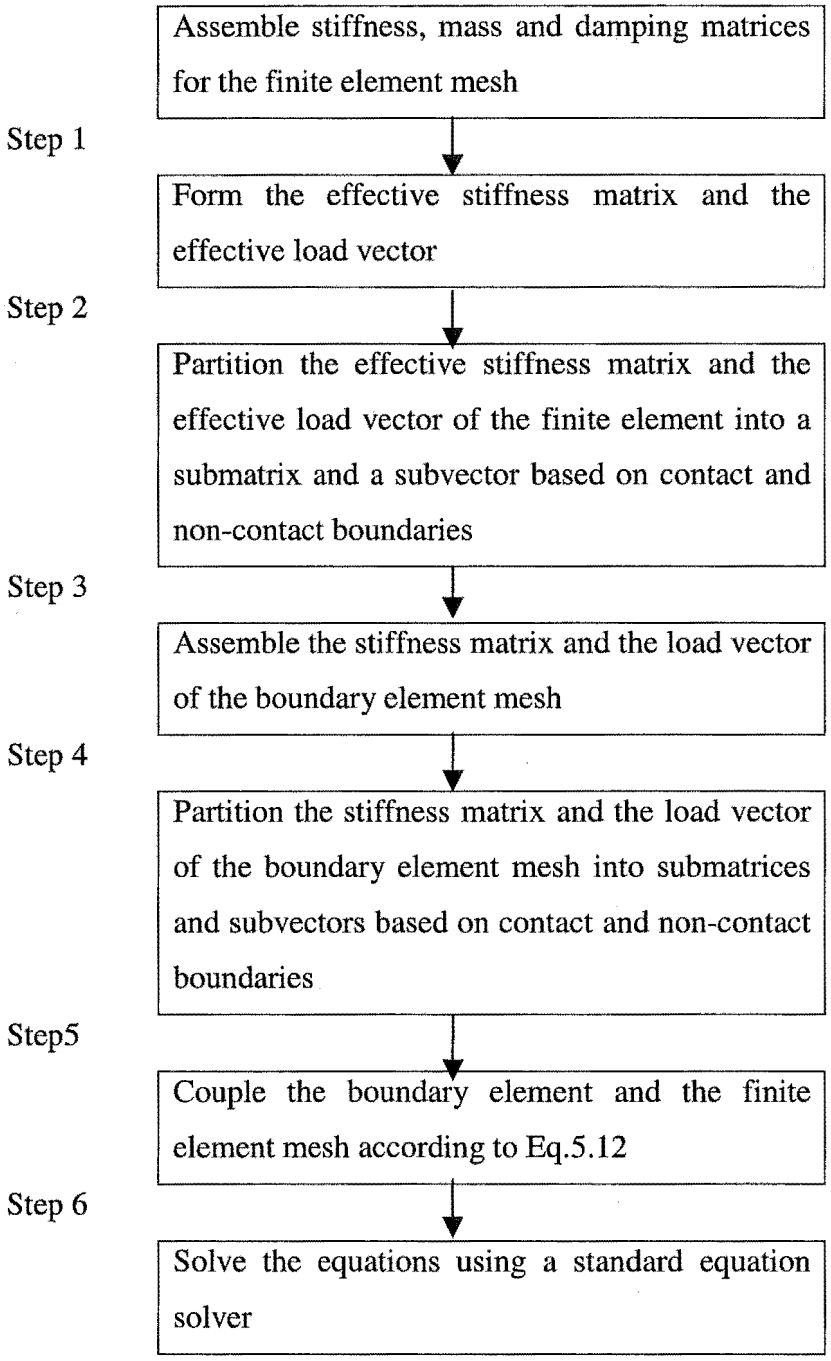

Figure 5.2 Flowchart for coupling boundary element and finite element

The above procedure can be directly assembled into a linear or a nonlinear dynamic analysis procedure. In most cases, additional steps are very simple and are easily implemented.

5.3 Summary

In this section, a coupling procedure has been proposed and the resulting procedure has been introduced. Its advantage is that the coupling is preceded by a direct method and current finite element packages and boundary element packages can be used. Changes to the programs are simple and easy to achieve. The coupling procedure is illustrated in a flow chart that can be utilised in a linear analysis or a nonlinear analysis. The procedure will be implemented and used in Chapters Six and Eight.

Chapter Six

Investigation of the Effect of Nonlinear Site Amplification on Structural Response

6.1 Introduction

It has long been recognised that the passage of seismic waves through near surface layers can produce free ground motions that are amplified and of different frequencies. A typical example is the 19 September 1985 Mexico City earthquake. Although attributed to special geological conditions, many researchers have demonstrated the phenomenon called local site amplification using numerical methods.

Among the numerical methods for local site amplification, SHAKE (Schnable, et. al. 1972) is well known. It is, however, only one-dimensional and an equivalent linear analysis method. Lysmer et. al. (1974) developed a two dimensional program LUSH which utilised the same frequency domain analysis method as in SHAKE. Joyner (1975) developed a nonlinear analysis method and extended the method to model a two-dimensional analysis. Taylor and Larkin (1978) suggested a nonlinear analysis method and Larkin (1978) extended the method to a two-dimensional analysis. Larkin's method has similar characteristics to Joyner's, in that a simplified soil model was used. Arulanandan et. al. (1997) utilised a bounding surface model to analyse the local site responses and compared these responses with results from SHAKE. Their conclusion was that the bounding surface model could effectively capture the nonlinear response of the soil and its pore pressure characteristics.

If the ground response is given, the effect of a local site on the structural response can be easily shown by comparing the results with those from a fixed-base structural response. When a linear or nonlinear site analysis method is used, the difference between responses for the fixed-base structure will show the effect of the site analysis

method. The method will be used to illustrate the effect of local site amplification on a structural response.

In order to show the effect of local site amplification on structural response, several cases will be considered. Firstly, the Loma Prieta earthquake record (17 October 1989) which was an accelerogram at SANTA CRUZ is scaled to a strong shaking motion and a weak shaking motion, having maximum accelerations of 0.433g and 0.0433g, respectively and the strong shaking motion is shown in Fig.6.1. Then linear and nonlinear soil models are used to investigate the local site amplification of the free field motion when subjected to the input motions. The structural responses will be calculated using the ground response of the free field. Secondly, three different sites will be investigated by the nonlinear analysis in order to further display characteristics of the nonlinear local site responses and demonstrate their effects on the structural response. Finally, the Loma Prieta (17 October 1989), the El-Centro (1940) and the Parkfield (1966) earthquake records are used to show the effects of different acceleration time histories on the nonlinear local site responses. Then the structural response is calculated using the above ground responses of the free field

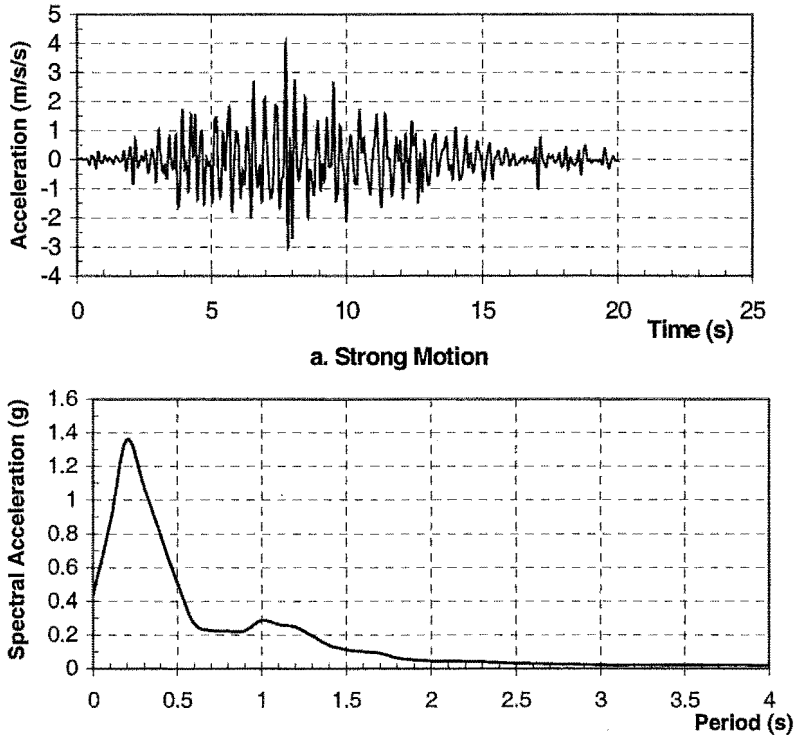

a. Strong Motion

b. Acceleration Spectrum of the Strong Motion

Figure 6.1 Acceleration Time Histories and Acceleration Spectrum of the Input Motion

6.2 Comparison between the Two-Dimensional Linear and Nonlinear Local Site Responses and Their Effects on Structural Response

In this section, the local site response calculated by the linear and nonlinear analyses and their corresponding effects on the structural response will be investigated. The finite element method will be employed as the numerical model and the bounding surface model introduced in Chapter 3 will be employed as the material model, whose parameters are listed in Table 6.1. The natural vibration period of the site is 0.82s. The far field modelled by the boundary element will be assumed to be linear and homogenous.

The scaled input acceleration time histories shown in Fig.6.1 are used in the calculation. They have a duration of 20 seconds.

Table 6.1 Parameters in the bounding surface model

Void ratio(e)	K_o	λ	κ	M_c	M_e/M_c	R_c	A_c	C	h_c	h_e/h_c
1.18	0.5	0.21	0.02	1.35	0.8	2.0	0.4	0.3	6.0	1.0

The calculated domain shown in Fig.6.2 is 100m wide by 30m deep. Below 30m is linear elastic rock.

Rock and soil properties are:

Rock	Soil
ρ =2700kg/m^3	ρ =1800kg/m^3
c_s =2000m/s	c_s =146m/s
c_p=3750m/s	c_p =273m/s

Three output points A, B and C shown in Fig.6.2 are chosen at the centre of the mesh and at depths of 0m, 15m and 27m below the surface. The acceleration time history and

the acceleration response spectra will be calculated at each of these points. Here only vertically propagating SH waves are considered.

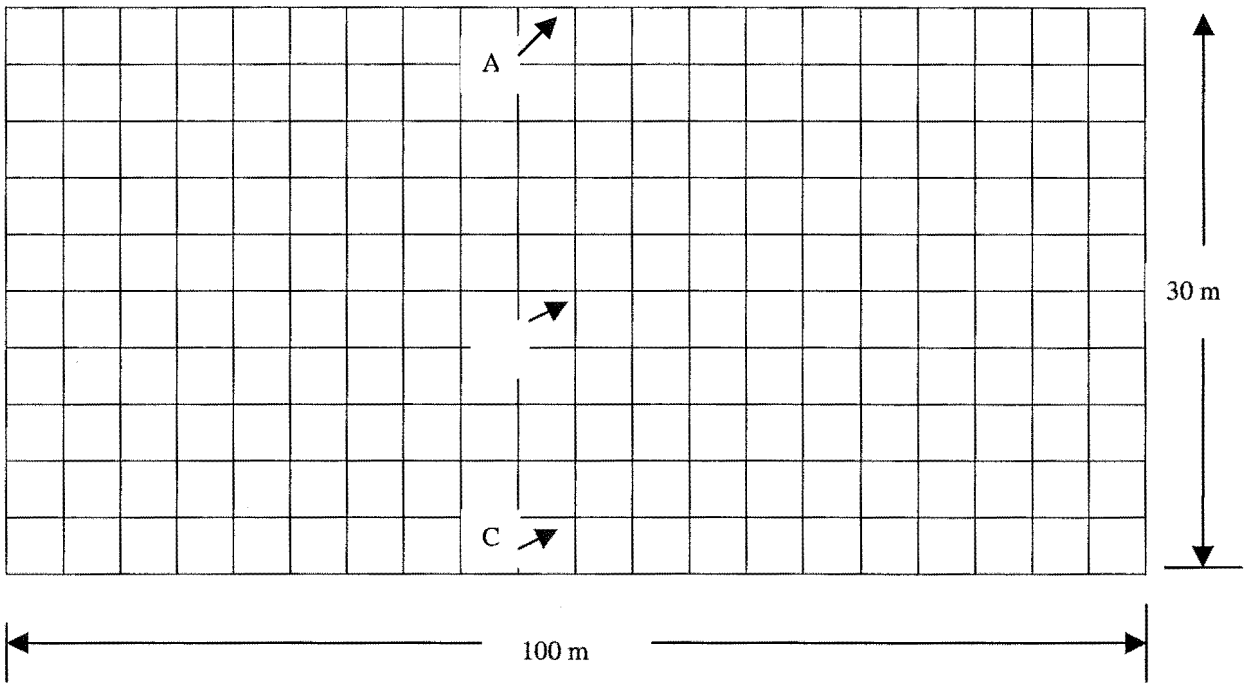

Figure 6.2 Mesh of Analysis Domain

6.2.1. The Strong Input Motion

The acceleration time history in Fig.6.1a represents the input motion from the basement. It will be used to compare the local site responses from the linear and nonlinear analyses. The responses on the ground surface will then be used as input motions to calculate the responses of the fixed-base 6-storey frame designed by Jury (Jury, 1978), which is shown in Fig.3.11.

The linear elastic model, the simplest model, has only two parameters, the shear modulus and Poisson's ratio. The shear modulus is usually assumed to be constant or else to have a linear distribution with depth. In order to simplify the calculation, only the constant distribution is used in these analyses. To remain consistent with the nonlinear analysis and to be representative of a typical soil, Poisson's ratio is set at 0.3. In the nonlinear analysis, the bounding surface in the bounding surface model will be affected by the initial stress state, stress history and stress path.

6.2.1.1 The Local Site Response When Subjected to the Strong Input Motion

The acceleration time histories calculated from the both linear and nonlinear analyses at three points A, B and C are shown in Figs. 6.3 and 6.4. For point A, the acceleration time histories calculated from the linear and nonlinear analyses show a great difference in acceleration amplitude, frequency content and duration. The linear analysis amplifies the maximum acceleration of the input motion by a factor of approximately 1.8 and its maximum acceleration is about twice that observed in the nonlinear analysis. On the other hand, the nonlinear analysis lengthens the duration of the strong shaking of the input motion and changes its frequency content. The maximum peak ground acceleration from the nonlinear analysis is slightly less than that of the input motion. For point B, the results from both linear and nonlinear analyses are similar, but the frequency contents show a slight difference. For point C, the results from both analyses are approximately the same. The aforementioned differences at points A and B can be explained as following: when a stress state reaches the yielding state, the shear strain will rapidly increase so that the shear modulus and shear wave velocity reduce and the soil damping increases. These factors result in the maximum acceleration amplitude from the nonlinear analysis being less than that from the linear analysis. On the change of duration of the strong shaking, Marsh (1992) gave the following explanation: This variation of the shear modulus results in a general dispersion of the waveform in the nonlinear solution, where waves with a low shear wave velocity travel slowly, and waves with a high velocity travel more quickly, and therefore the waveform is stretched out in time.

From Fig.6.4, it is seen that acceleration amplitudes and frequency contents at points A and C display a great difference. The reason is that due to the different initial stress states of the soil at different depths, the bounding surface at different points in the domain will be at different places in the stress space. When subjected to the same loading, the point with a low consolidated pressure will yield first. Therefore, point A shows strong nonlinear characteristics, whereas point C displays a linear response. Chang et. al. (1990) analysed downhole ground motion data from Taiwan and found that the shear modulus and shear wave velocity in a surface layer decreased as the level

of shaking increased. The same reason can be used to explain how the maximum peak ground acceleration from the nonlinear analysis is slightly lower than that of the input motion. This result is also supported by Idriss (1990) who suggested that if the maximum input acceleration is greater than about 0.4g, the maximum ground acceleration at a clay site will be de-amplified.

When comparing the acceleration time history at the ground surface from the nonlinear analysis with that from the linear analysis, the linear analysis overpredicts the peak ground acceleration. It can be seen that the difference of the results between the linear and the nonlinear analyses decreases as the depth increases. When the depth reaches point C, the results from the linear and nonlinear analyses are nearly the same. This will be discussed again in the following sections.

In a seismic structural response analysis, the acceleration spectrum is often used to express the design earthquake force. In order to compare the effect of different analysis methods on the structural response, the acceleration spectra calculated from the linear and nonlinear analyses at the ground surface are shown in Fig.6.5.

At points A, B and C, the three acceleration spectra show different characteristics. At the predominant period of the input motion, the spectral peak acceleration from the linear analysis at point A amplifies that of the input motion by a factor of approximately 2 and its predominant period undergoes a slight change. The shapes of both the acceleration spectra are nearly the same, which illustrates that the frequency content is not greatly changed. The acceleration spectrum from the nonlinear analysis, however, is different from that of the linear analysis. The maximum spectral acceleration at point A is nearly the same as that of the input motion, but its predominant period is longer than that of the input motion. Therefore, the input acceleration spectrum is amplified by the soil at the predominant period from the nonlinear analysis. This feature may be explained as follows: because of soil yielding, the soil shear modulus reduces so that the natural vibration period is lengthened. In order to show this feature, the displacement spectra from the linear and the nonlinear analyses at points A, B and C are drawn in Fig.6.6.

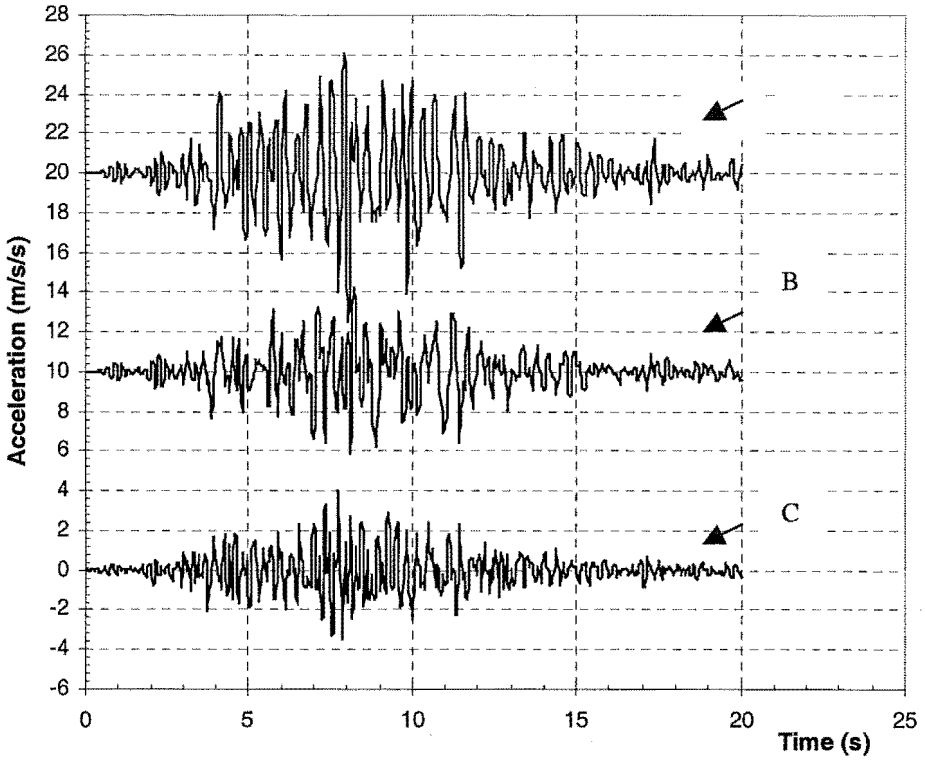

Figure 6.3 Linear Free Field Analysis Results for the Strong Motion

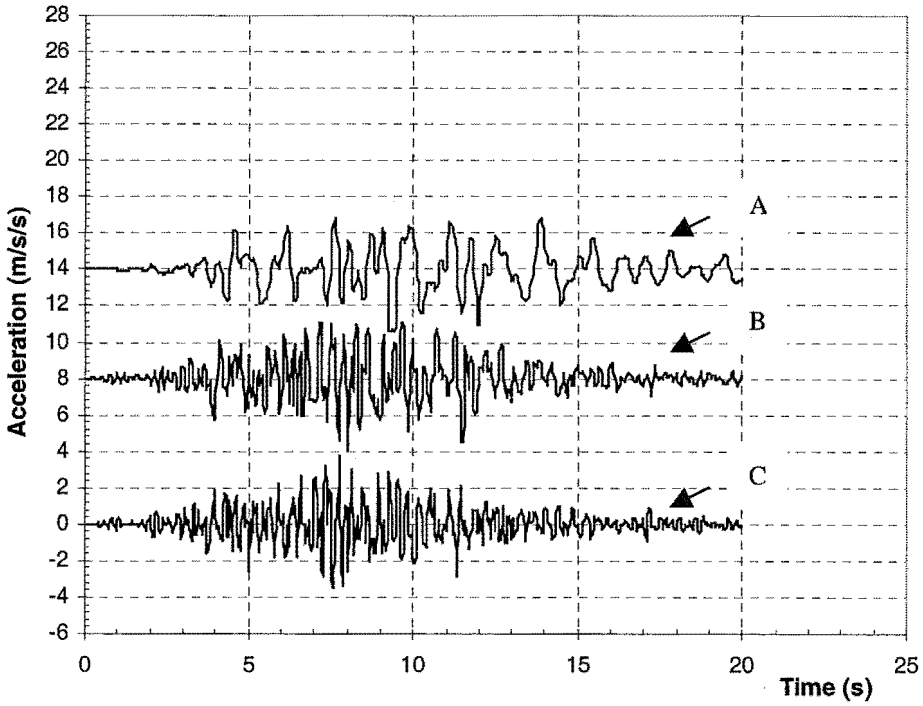

Figure 6.4 Nonlinear Free Field Analysis Results for the Strong Motion

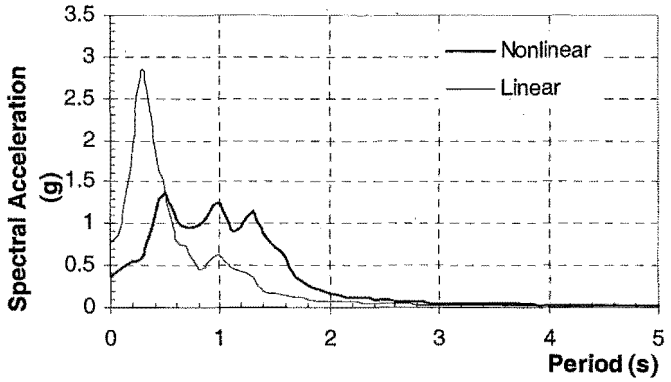

a. Acceleration Spectra at Point A

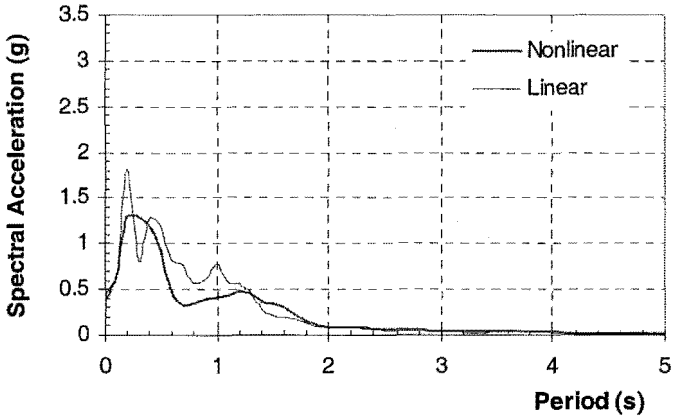

b.Acceleration Spectra at Point B

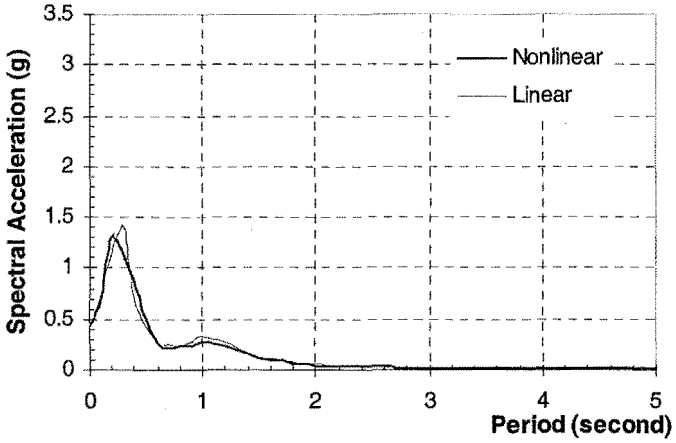

c. Acceleration Spectra at Point C

Figure 6.5 Comparison of the Acceleration Spectra for the Linear and Nonlinear Analyses at Points A, B and C under the Strong Motion

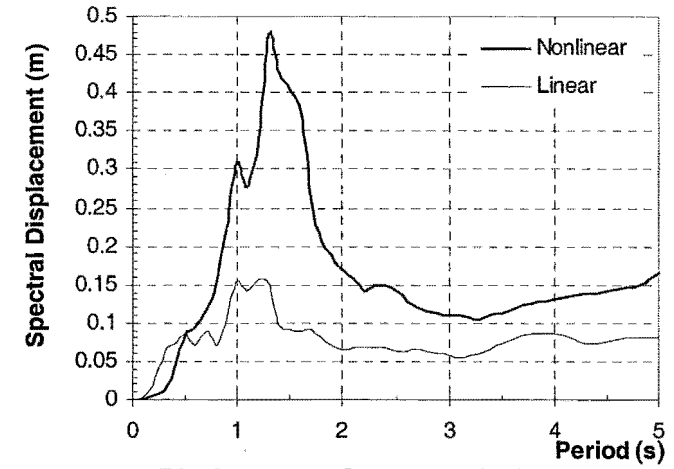

a. Displacement Spectra at Point A

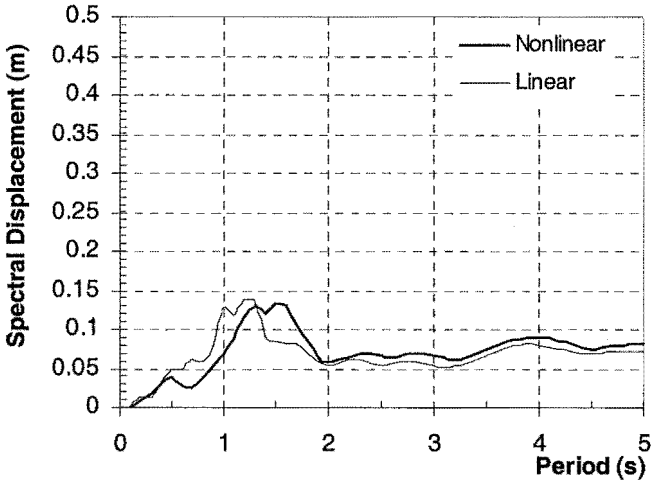

b. Displacement Spectra at Point B

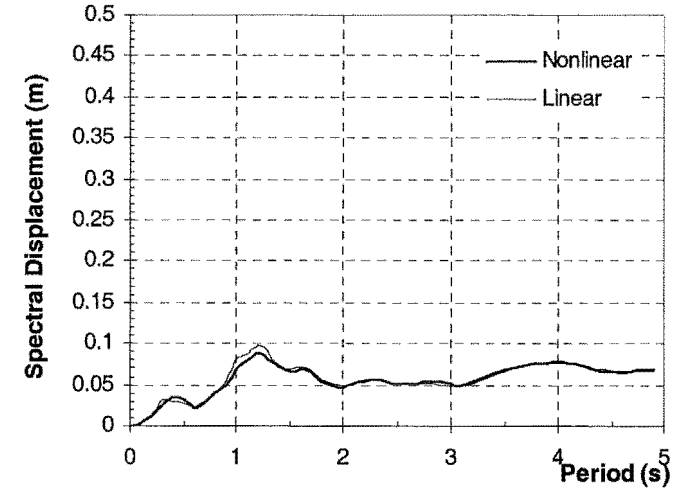

c. Displacement Spectra at Point C

Figure 6.6 Comparison of the Displacement Spectra for the Linear and Nonlinear Analyses at Points A, B and C under the Strong Motion

The spectral displacement from the nonlinear analysis at point A is about 3 times that from the linear analysis. This also confirms that the stiffness of the soil reduces and the displacement increases on the ground surface with the nonlinear analysis. The spectral accelerations from the linear and the nonlinear analyses at point B only show a slight difference.

The above comments are mainly concerned with the differences between the linear and the nonlinear analyses. The following observation can be made. When subjected to a strong input motion from the basement rock, a linear analysis amplifies the input motion and overpredicts the response at a surface layer. The frequency content of the response at the ground surface is similar to that from the input motion. For a nonlinear analysis, the yielding of soil lies at a surface layer. In the investigation, the maximum peak ground acceleration and spectral peak acceleration from the nonlinear analysis at the ground surface is close to those from the input motion. When compared with the results from the linear analysis, the predominant period from the nonlinear analysis at the ground surface is lengthened and its frequency content is changed. At the predominant period of the ground response from the nonlinear analysis, the spectral acceleration of the input motion is amplified. As the depth increases, the results from the nonlinear analysis become closer to those from the linear analysis.

6.2.1.2 The Effect of Local Site Response on the Structural Response

In order to compare the effect of the acceleration time histories from the linear and nonlinear analyses on structural response, acceleration time histories at the ground surface (in following sections, they are called linear input motion and nonlinear input motion) are used directly as input motions to calculate the responses of the Jury fixed-base 6-storey frame.

Displacement time histories and the maximum displacement envelopes at nodes 7, 13 and 19 in Fig.6.7 generated by the linear and the nonlinear input motions are shown in Figs. 6.8 and 6.9. It is seen that the maximum displacements generated by the nonlinear input motion are greater than those generated by the linear input motion. However, from

Figs. 6.4 and 6.5, the maximum peak acceleration and spectral acceleration from the linear analysis are greater than those from the nonlinear analysis. This result can be explained by the predominant period of the ground response as follows:

The predominant period of the ground response from the linear analysis is about 0.3s and the spectral peak periods of ground response from the nonlinear analysis are 0.5s, 1.0s and 1.3s. The natural vibration period of the Jury fixed-base 6-storey frame is 1.142s. With the nonlinear input motion, because the peak period is very close to the natural vibration period of the frame, resonant response occurs and this results in a greater displacement than that given with the linear input motion.

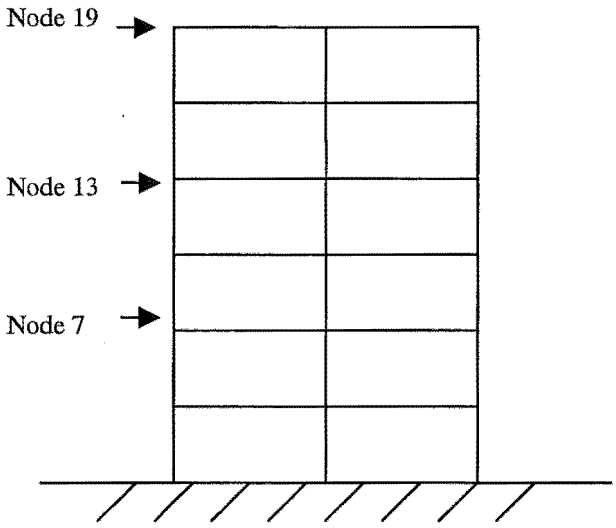

Figure 6.7 Sketch of Jury 6-storey frame

As mentioned above, when a site is subjected to a strong shaking motion, the soft clay site will produce a response with a longer predominant period at the ground surface which is different from that at the rock. When compared with the structural responses generated by the linear input motion in this case, the displacement at the top floor generated by the nonlinear input motion is greater than that caused by the linear input motion.

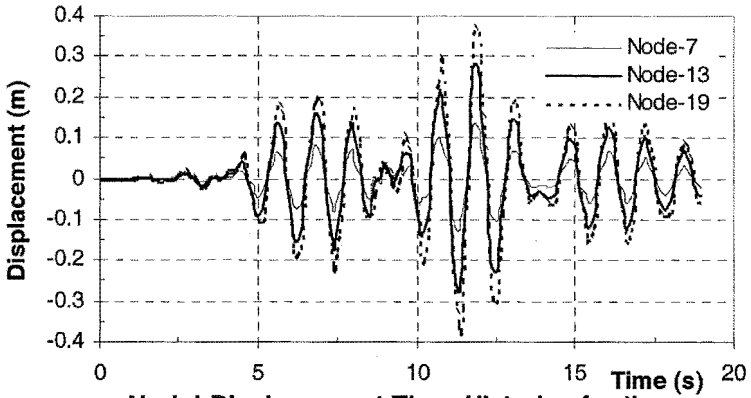

a. Nodal Displacement Time Histories for the Nonlinear Analysis

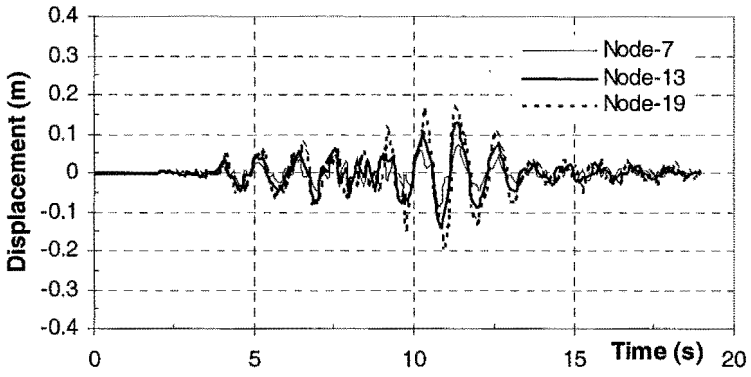

b. Nodal Displacement Time Histories for the Linear Analysis

Figure 6.8 The Nodal Displacement Time Histories for the Linear and Nonlinear Analyses

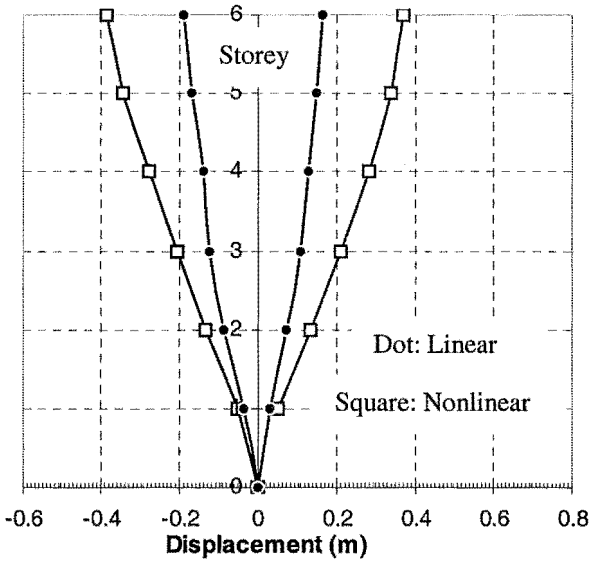

Figure 6.9 The Maximum Displacement Envelopes for the Linear and Nonlinear Analyses

6.2.2 The Weak Input Motion

In the previous section, the local site responses from the linear and nonlinear analyses have been discussed when a site is subjected to a strong input motion. A substantial difference has been seen between the linear and the nonlinear analyses. In this section, the local site responses and the structural responses will be discussed when the site is subjected to a weak input motion from the basement rock.

6.2.2.1 The Local Site Response When Subjected to the Weak Input Motion

The acceleration time history of the weak shaking motion whose maximum acceleration is 0.0433g is displayed in Fig.6.1b. The acceleration time histories from the linear and the nonlinear analyses at points A, B and C are displayed in Figs. 6.10 and 6.11.

From Figs. 6.10 and 6.11, it can be seen that the acceleration histories at points B and C are similar. The comparison at point A, however, shows some differences which indicate the yielding of soil in the nonlinear analysis, but when compared with the calculated results subjected to the strong input motion in Fig.6.4, both analyses at point A show very close each other. When comparing the peak ground acceleration from the linear analysis with the maximum input acceleration, the difference is a factor of approximately 1.5. It is very clear that the soil amplifies the input motion when subjected to the weak input motion. This result has also been found by many researchers using a range of different models (Marsh, 1992).

The acceleration spectra from the linear and the nonlinear analyses are displayed in Fig.6.12. This figure shows that spectral acceleration amplification not only occurs from the linear analysis, but also from the nonlinear analysis and that the amplification from the linear analysis is slightly larger than that from the nonlinear analysis. This result illustrates nonlinear local site amplification. On the other hand, the nonlinear analysis clearly amplifies the spectral peak acceleration at 1.0 second at point A. When compared with the results from the linear analysis in this case, the nonlinear analysis will affect the structural response over a wide range of natural periods of free vibration.

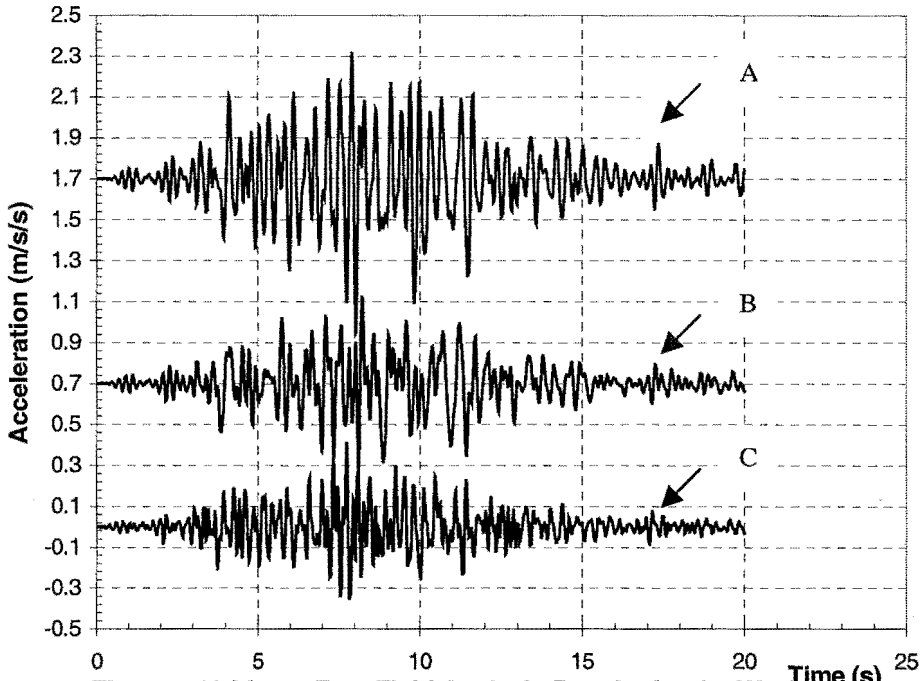

Figure 6.10 Linear Free Field Analysis Results for the Weak Motion

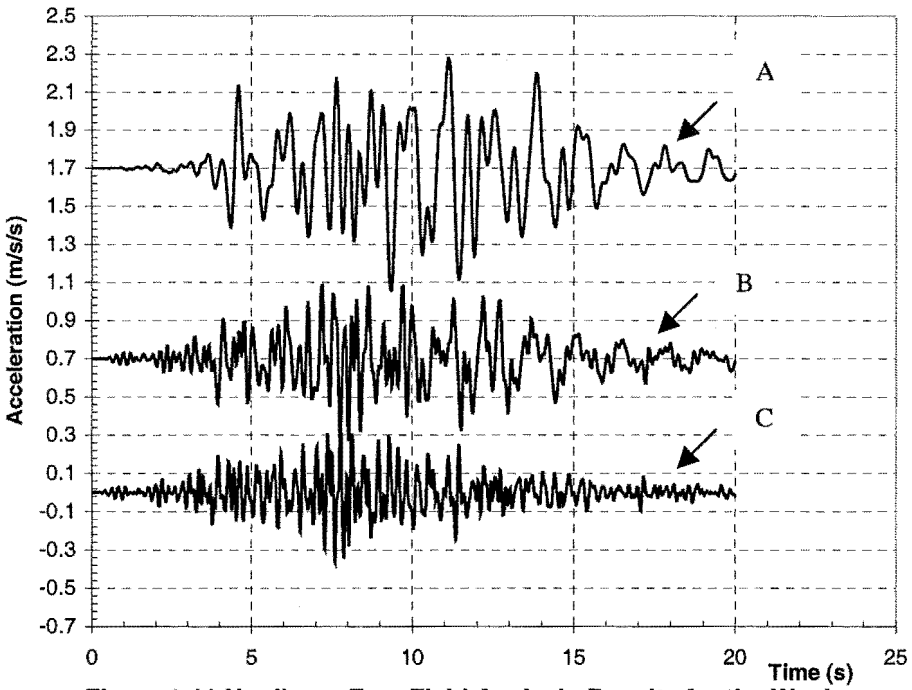

Figure 6.11 Nonlinear Free Field Analysis Results for the Weak Motion

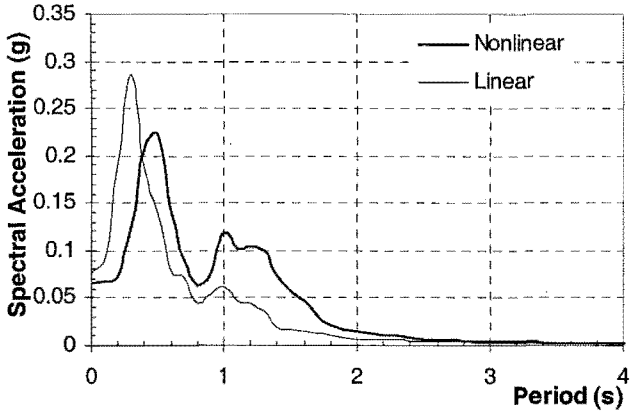

a. Acceleration Spectra at Point A

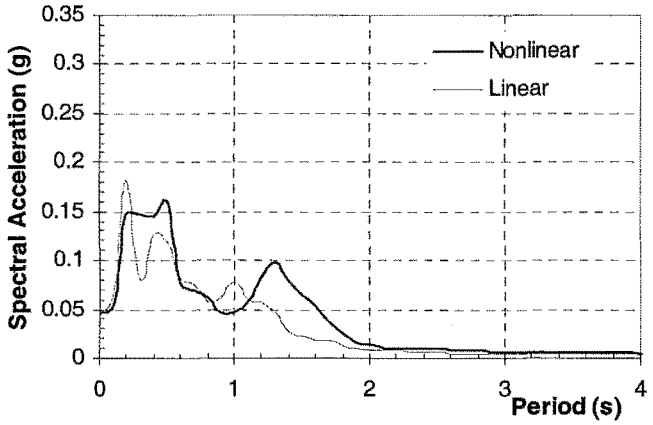

b. Acceleration Spectra at Point B

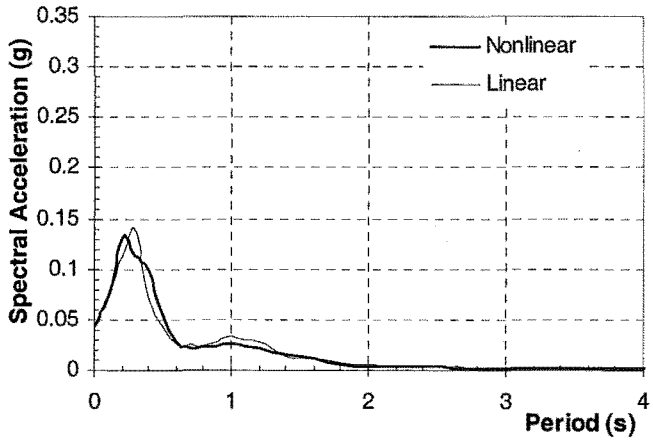

c. Acceleration Spectra at Point C

Figure 6.12 Comparison of the Acceleration Spectra for the Linear and Nonlinear Analyses at Points A, B and C under the Weak Motion

From the above comparisons, it is seen that the results from the linear and nonlinear analysis show acceleration amplification at the ground surface when the site is subjected to the weak input motion from the basement rock.

6.2.2.2 The Effect of the Local Site Responses on the Structural Response

The acceleration time histories at the ground surface from linear and nonlinear analyses shown in Figs. 6.10 and 6.11 will be used as input motions to calculate the response of the Jury fixed-base 6-storey frame.

The displacement time histories at Nodes 7, 13 and 19 and the maximum displacement envelopes generated by the linear and the nonlinear input motions are shown in Figs. 6.13 and 6.14. Although the input acceleration time histories from the basement rock for both analyses are same, in the site response analysis, the spectral peak acceleration at 1.0 seconds at the ground surface is greatly amplified in the nonlinear analysis. Hence the maximum structural displacement calculated by the nonlinear input motion is greater than that due to the linear input motion by about 20 percent. The reason is the same as that from the strong input motion, namely the peak period at 1.0 seconds is close to the natural vibration period of the structure.

6.3 Comparison among Different Site Responses from the Nonlinear Analyses

In the above sections, the local site amplification and structural responses subjected to strong and weak input motions have been discussed. Different soils, however, show different characteristics of strength and deformation. Therefore evaluating different site responses and their effects on structural response will have some significance. In order to compare the differences among different sites, three sets of soils are selected (Arulanandan, et. al, 1997) and they will be subjected to the strong input motion. The parameters of the soils are listed in Table 6.2 and their natural vibration periods are 0.68s, 0.82s and 0.44s.

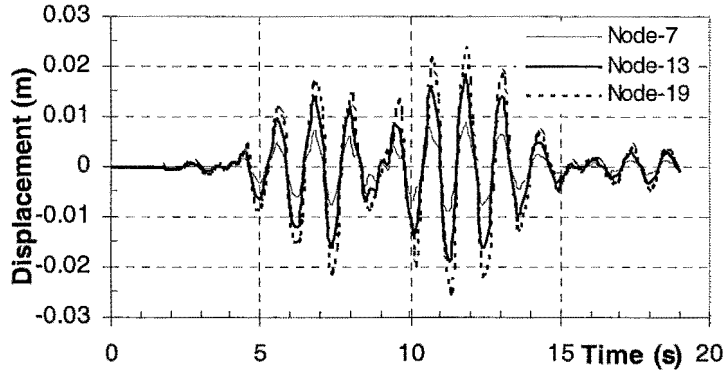

a. Nodal Displacement Time Histories for the Nonlinear Analysis

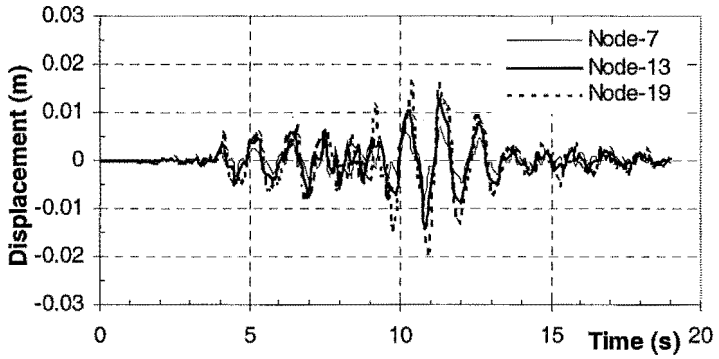

b. Nodal Displacement Time Histories for the Linear Analysis

Figure 6.13 The Nodal Displacement Time Histories for the Linear and Nonlinear Analyses

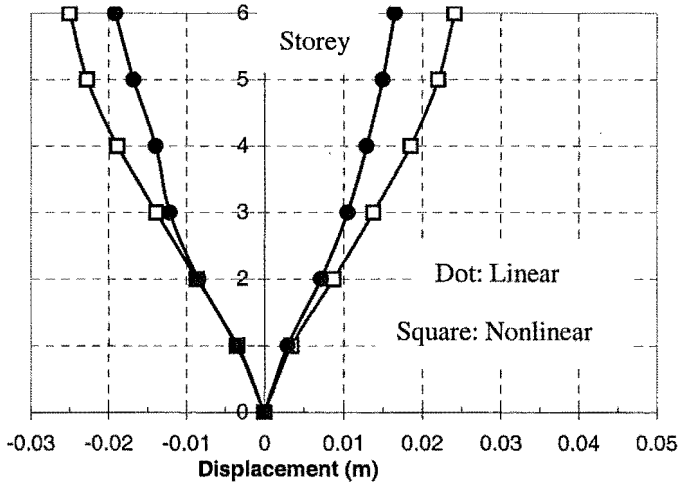

Figure 6.14 The Displacement Envelopes for the Linear and Nonlinear Analyses

Site	Void Ratio	K_o	λ	κ	M_c	M_e/M_c	R_c	A_c	T	C	h_c	h_e/h_c
1	1.10*	0.5	0.167	0.007	1.36	0.8	2.0	0.2	0.01	0.1	3.0	1.0
2	1.18	0.5	0.21	0.02	1.35	0.8	2.0	0.4	0.01*	0.3	6.0	1.0
3	1.04	0.5	0.29	0.04	1.35	0.8	2.0	0.4	0.01*	0.3	6.0	1.0

'*' represents an assumed value.

The acceleration time histories at points A, B and C for the three sites are shown in Fig.6.15. The results at point A for the three sites all show soil yielding so that the maximum ground accelerations are less than or equal to the maximum acceleration of the input motion from the basement rock, frequency content of the ground response is different from that of the input motion, and the duration of strong shaking of the input motion is lengthened at the ground surface. When comparing Figs. 6.15a and 6.15b with Fig.6.15c, it is clear that their frequency contents are different. This illustrates that soft clay shows yielding at a surface layer.

The acceleration spectra for the three sites are plotted in Fig.6.16. In this figure, it is notable that the spectral peak acceleration at the predominant period of the input motion gradually reduces from point C to A for sites 1 and 3. The reason is that the natural vibration period of the soil site shifts as the soil yields.

Following the method in section 6.2, the acceleration time histories at the ground are used as input motions to calculate the fixed-base 6-storey frame response. The displacement time histories at nodes 13 and 19 for sites 1, 2 and 3 and the maximum displacement envelopes are displayed in Figs. 6.17 and 6.18. All analyses show large structural displacements. The maximum displacement difference over these sites is of the order of 25% to 30%.

The following observations can be drawn. Soft clay sites display nonlinear properties when the site is subjected to strong input motion from the basement rock. Because of

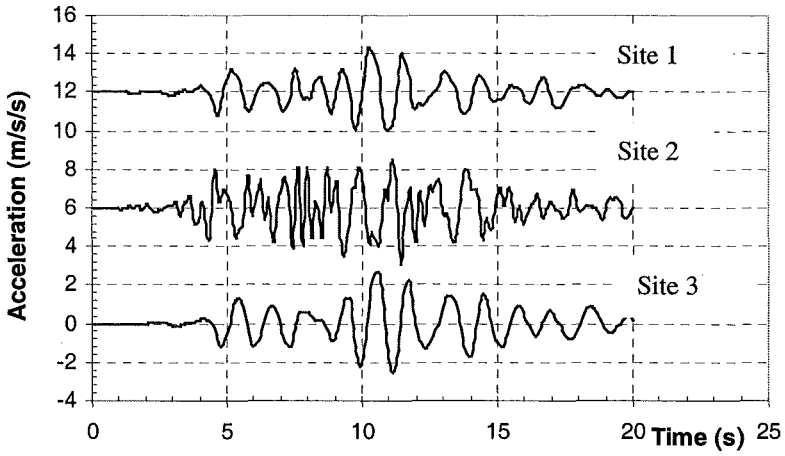

a. Acceleration Time Histories at Point A

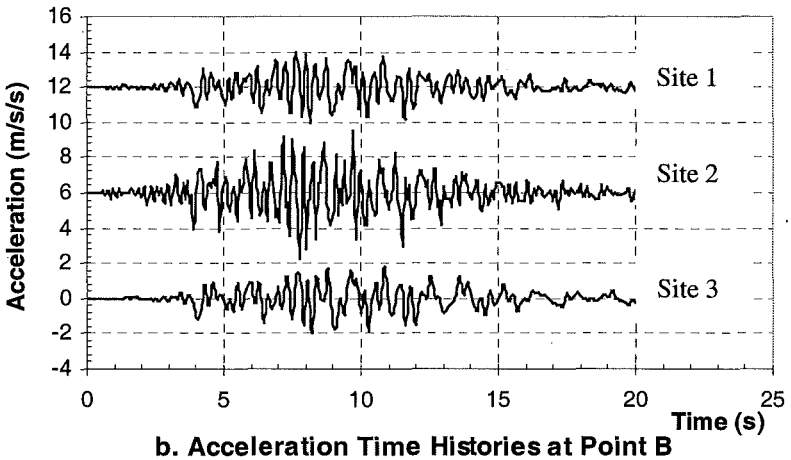

b. Acceleration Time Histories at Point B

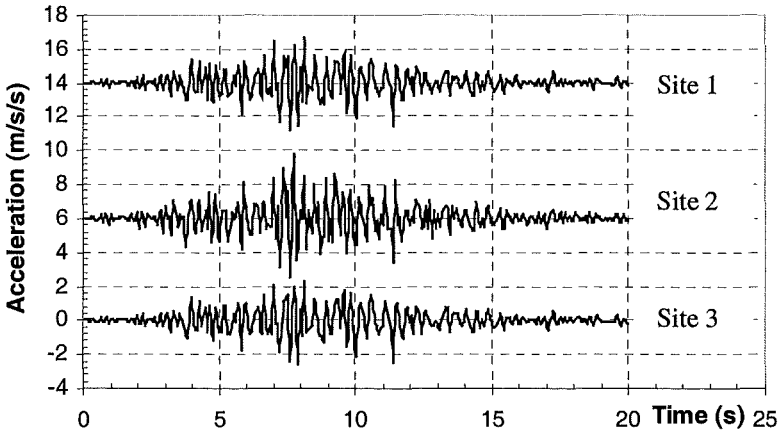

c. Acceleration Time Histories at Point C

Figure 6.15 The Acceleration Time Histories at Different Points for the Different Sites

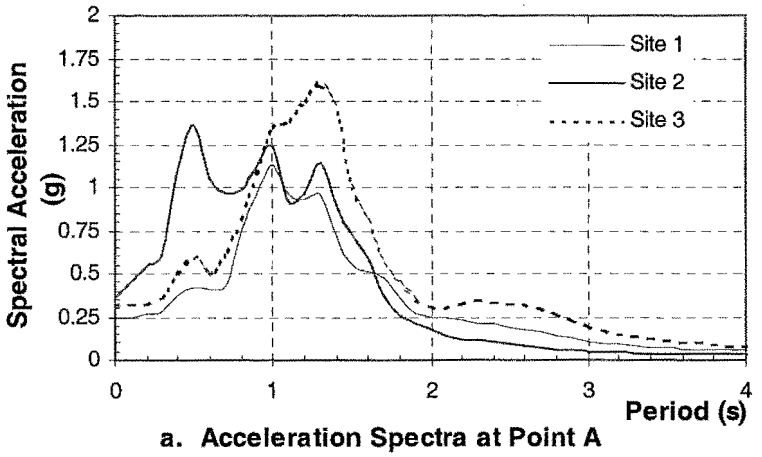

a. Acceleration Spectra at Point A

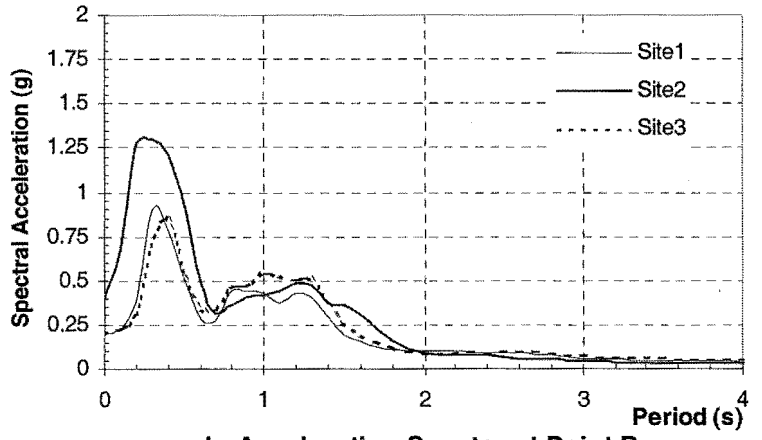

b. Acceleration Spectra at Point B

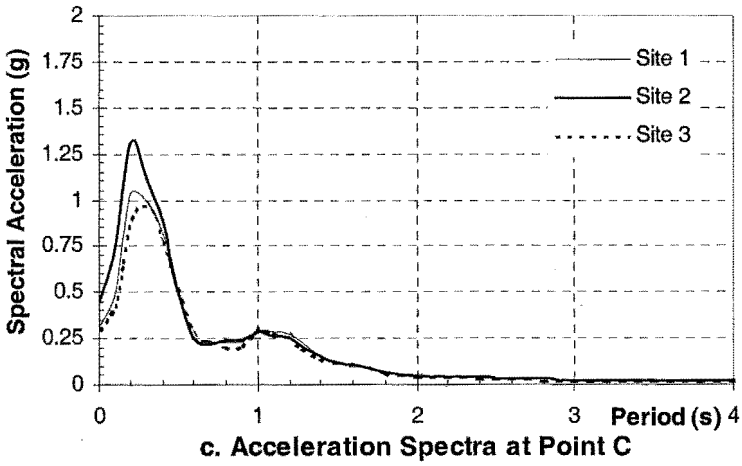

c. Acceleration Spectra at Point C

Figure 6.16 The Acceleration Spectra at Different Points for the Different Sites

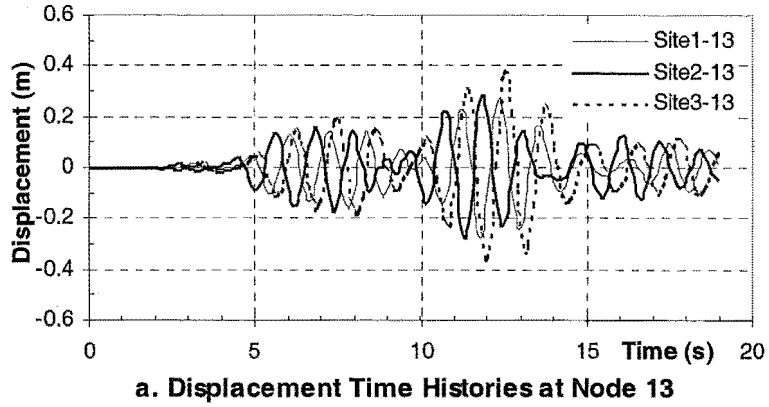

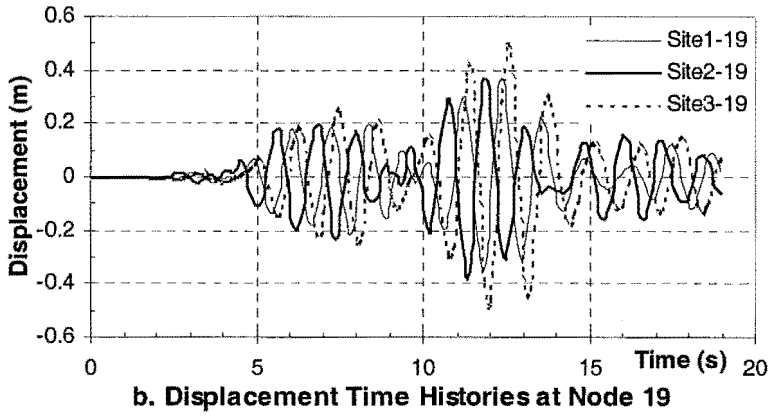

Figure 6.17 The Displacement Time Histories at Nodes 13 and 19 for the Different Sites

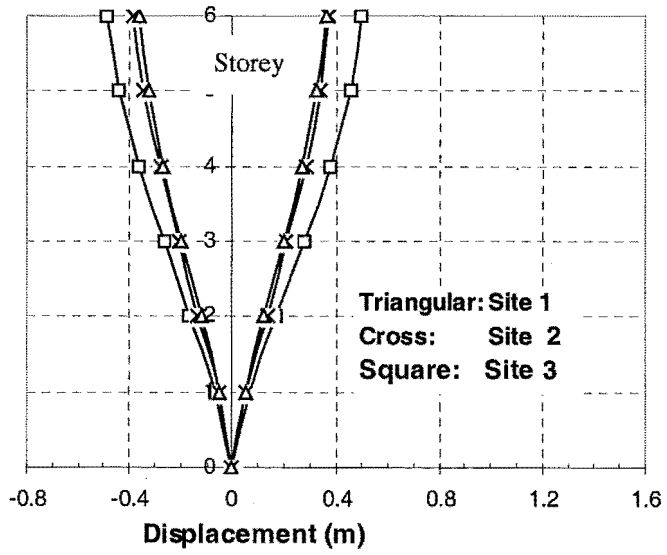

Figure 6.18 The Displacement Envelopes for the Different Sites

Soil yielding, the seismic responses at a surface layer show differences from those obtained from the input motion in both frequency content and duration and the natural vibration period of the soil at the ground surface is lengthened. For different sites, different acceleration time histories at the ground surface are obtained and they generate different structural responses.

6.3 Comparison of the Ground Response When Subjected to Different Input Motions

In order to compare ground response subjected to different input motions, the Loma Prieta (1989), the Parkfield (1966) and the El-Centro (1940) accelerograms are selected as input earthquake records. These are shown in Fig.6.19a. Their acceleration spectra are presented in Fig.6.19b.

The acceleration time histories from both the linear and nonlinear analyses at different points are shown in Fig.6.20 for the Parkfield and Fig.6.21 for the El-Centro earthquakes. In comparing the ground responses from both the linear and the nonlinear analyses for the Parkfield earthquake in Fig.6.20, it is clear that the waveforms are nearly the same at points B and C. This means that their frequency contents are nearly the same. When comparing the acceleration time histories at points A, B and C for the Parkfield and the Loma Prieta earthquakes, the yielding layer for the Parkfield earthquake is not as deep as for the Loma Prieta earthquake.

The acceleration time histories from both the linear and nonlinear analyses at points A, B and C under the El-Centro earthquake are shown in Fig.6.21. The acceleration amplitudes, frequency contents and strong shaking durations from the two analyses at point C are nearly the same. Although frequency contents at point B have a slight difference in the first 10 seconds, they are still similar. Yielding occurs on the ground surface such that the acceleration amplitudes, frequency contents and strong shaking

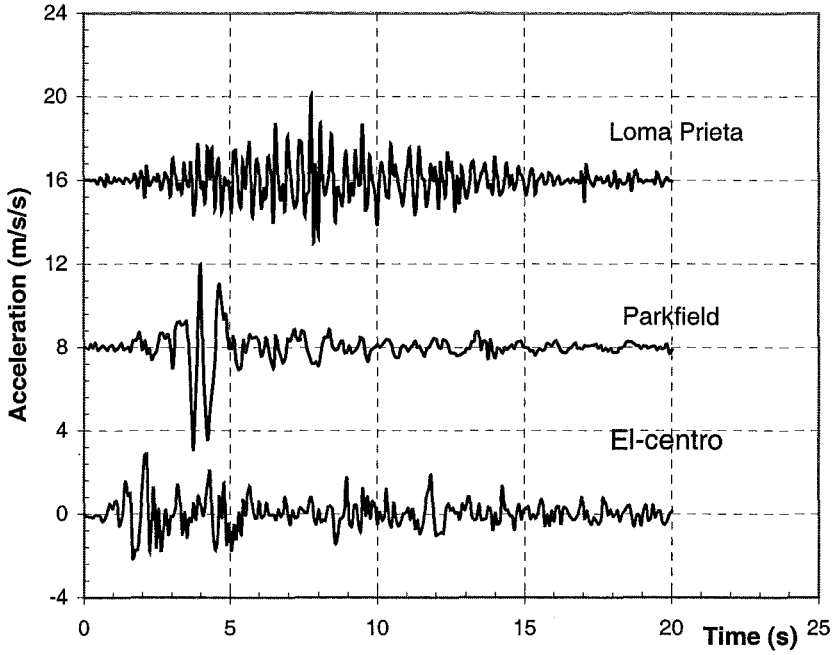

a. Acceleration Time Histories for the Three Earthquakes

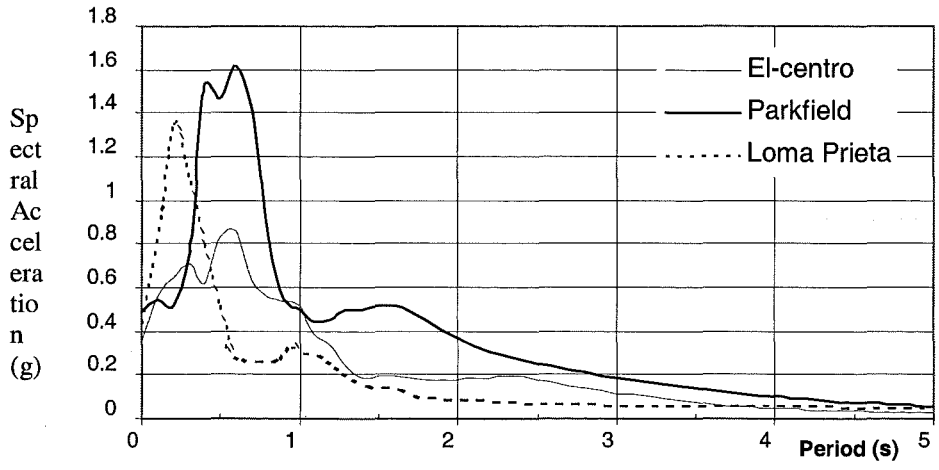

b. Acceleration Spectra for the Three Earthquakes

Figure 6.19 Acceleration Time Histories and Their Spectra for Three Earthquake Records

durations from both the linear and the nonlinear analyses are different.

Both ground surface accelerations for the Parkfield and the El-Centro earthquakes, however, show a great difference with regard to acceleration amplitude and frequency content. These results can be explained from the viewpoint of soil strength. When the soil is subjected to repeated loading, soil strength will reduce when compared to its static strength. However, when subjected to impulse loading, soil strength will increase. Although the soil displays yielding in the nonlinear analysis for the Parkfield earthquake, its peak ground acceleration still is about 1.7 times greater than the maximum acceleration of the input motion.

The acceleration spectra from the linear and the nonlinear analyses at points A, B and C for the El-Centro and the Parkfield earthquakes are shown in Figs. 6.22 and 6.23. It is seen from Fig.6.22 that the predominant periods at points B and C are nearly the same, but at point A the spectral acceleration from the nonlinear analysis is greatly amplified in the range of period from 1.0 to 2.2 seconds when compared with that from the linear analysis. The spectral accelerations at points B and C for the Parkfield earthquake have the same characteristics as those for the El-Centro earthquake, but at the ground surface for the El-Centro earthquake, more spectral peaks occur.

When comparing the results from the linear and nonlinear analyses under the El-Centro and the Parkfield earthquakes, it is found that the different earthquake acceleration time histories generate different linear and nonlinear acceleration spectra, but they all show that nonlinear behaviour amplifies the spectral accelerations of the input motion. On the other hand, the ground response is greatly affected by the input acceleration time history.

For the El-Centro and the Parkfield earthquakes, the fixed-base 6-storey frame responses are again calculated by using the ground surface responses as input motions. Their displacement time histories and displacement envelopes are shown in Figs. 6.24, 6.25, 6.26 and 6.27. The input motion from the nonlinear analysis results in a greater structural displacement.

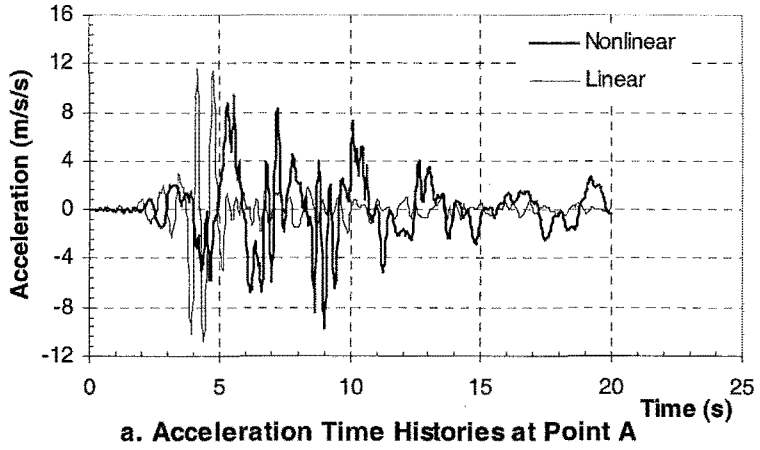

a. Acceleration Time Histories at Point A

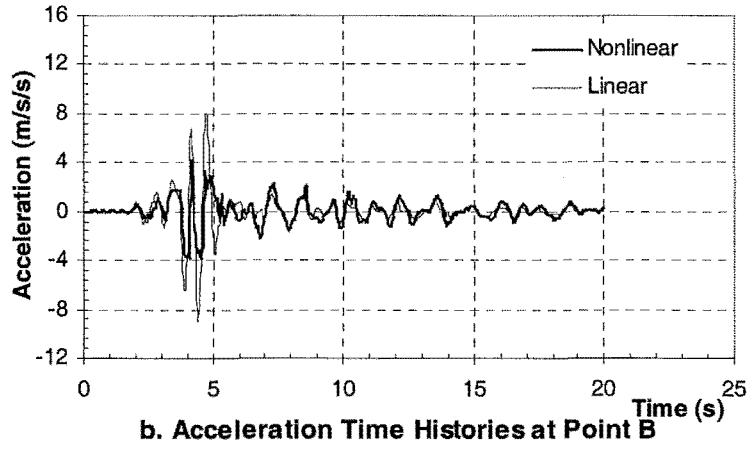

b. Acceleration Time Histories at Point B

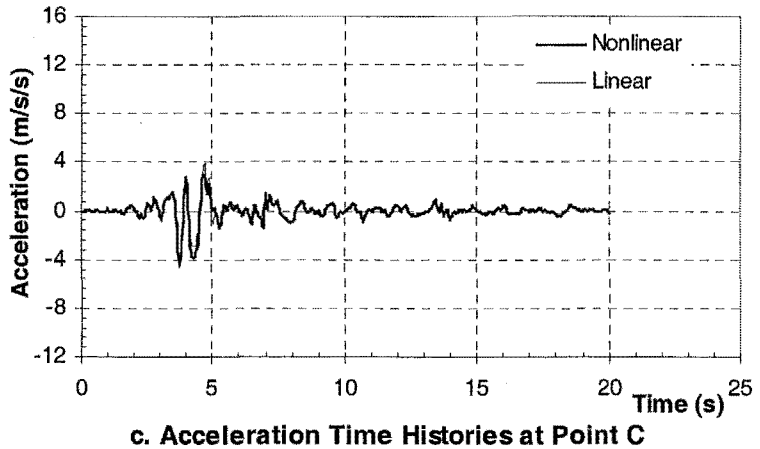

c. Acceleration Time Histories at Point C

Figure 7.20 Comparison of the Acceleration Time Histories for the Linear and Nonlinear Analyses at Points A, B and C under the Parkfield Earthquake

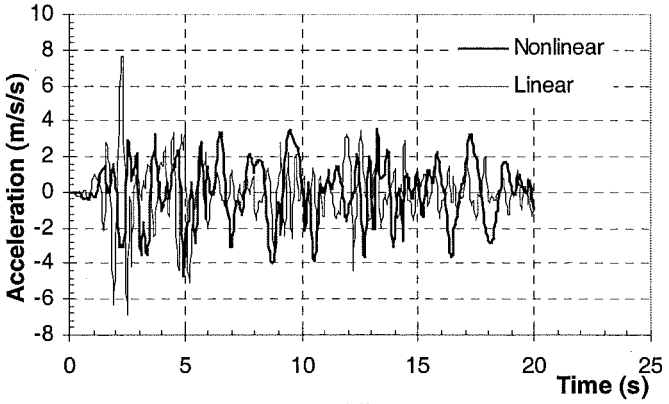

a. Acceleration Time Histories at Point A

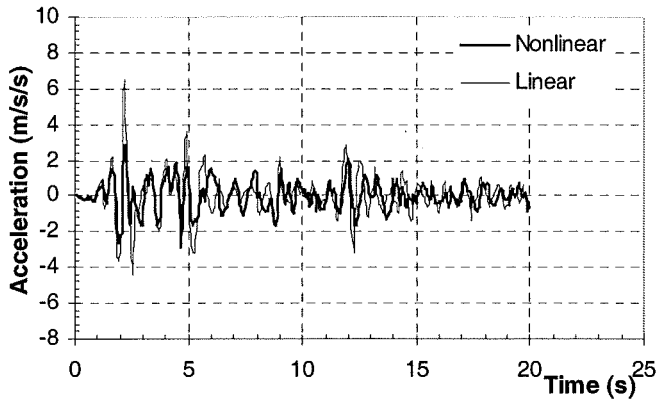

b. Acceleration Time Histories at Point B

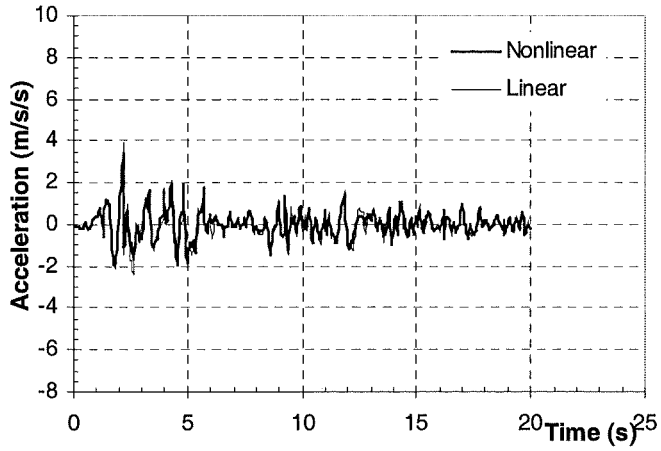

c. Acceleration Time Histories at Point C

Figure 6.21 Comparison of the Acceleration Time Histories for the Linear and Nonlinear Analyses at Points A, B and C under the El-Centro Earthquake

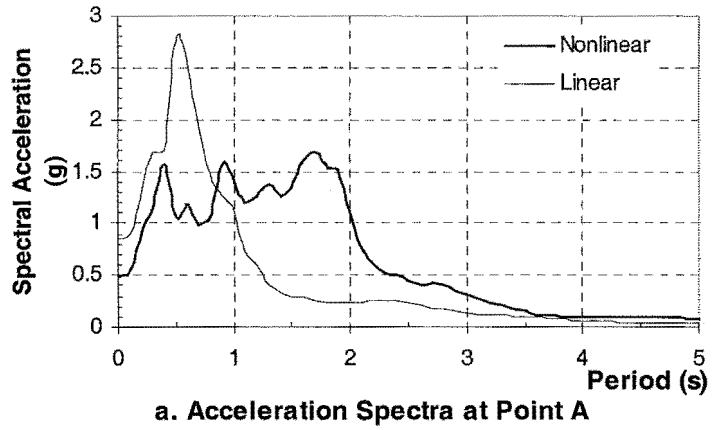

a. Acceleration Spectra at Point A

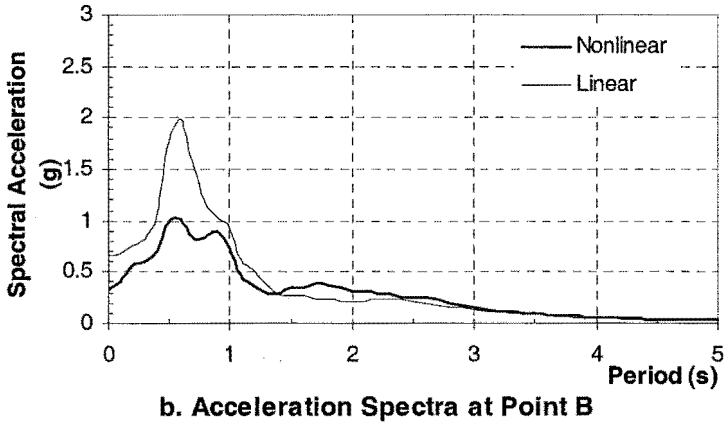

b. Acceleration Spectra at Point B

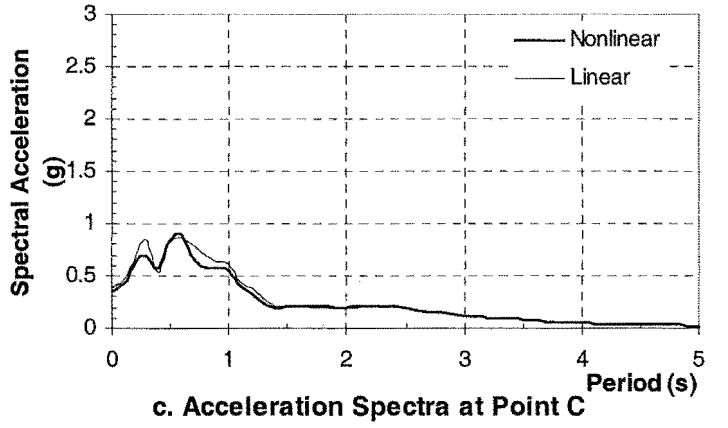

c. Acceleration Spectra at Point C

Figure 6.22 Comparison of the Acceleration Spectra for the Linear and Nonlinear Analyses at Points A, B and C under the El-Centro Earthquake

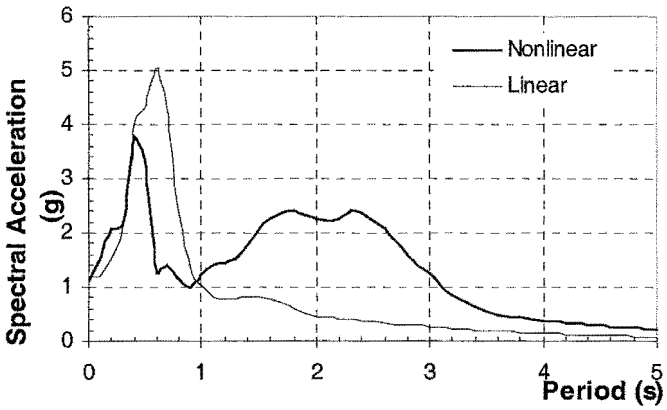

a. Acceleration Spectra at Point A

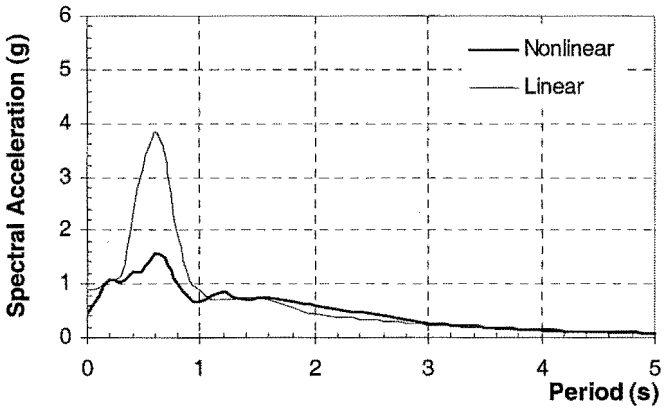

b. Acceleration Spectra at Point B

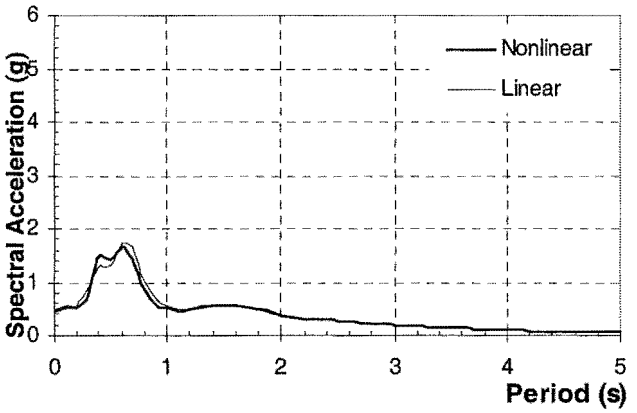

c. Acceleration Spectra at Point C

Figure 6.23 Comparison of the Acceleration Spectra for the Linear and Nomnlinear Analyses at Points A, B and C under the Parkfield Earthquake

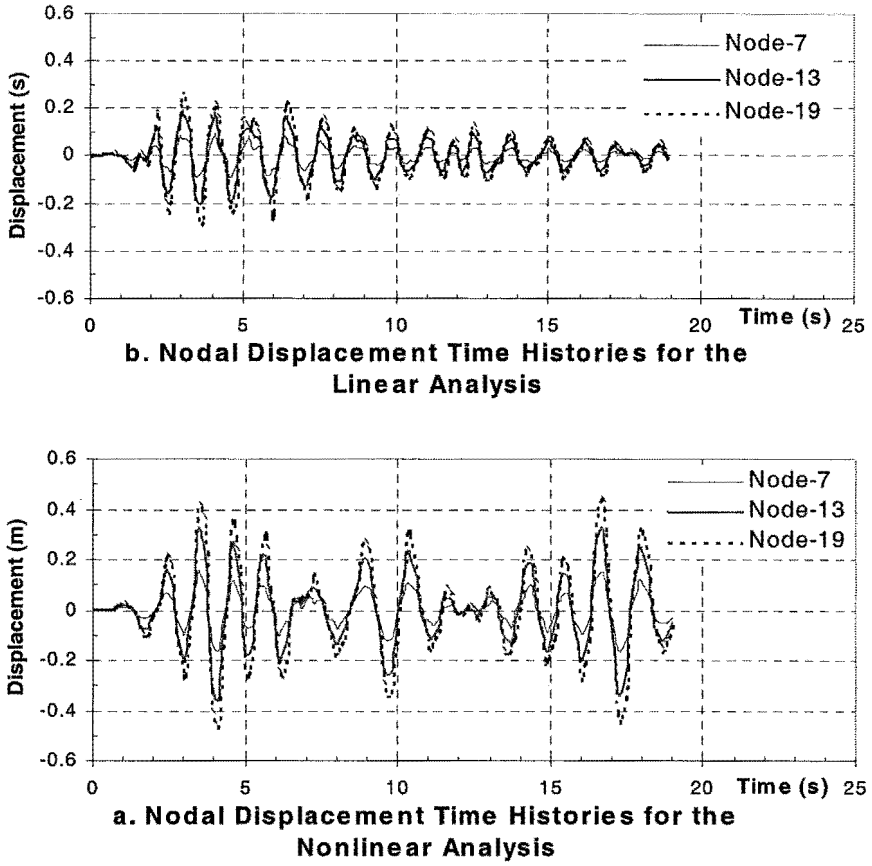

Figure 6.24 The Nodal Displacement Time Histories for the Linear and Nonlinear Analyses under the El-Centro Earthquake

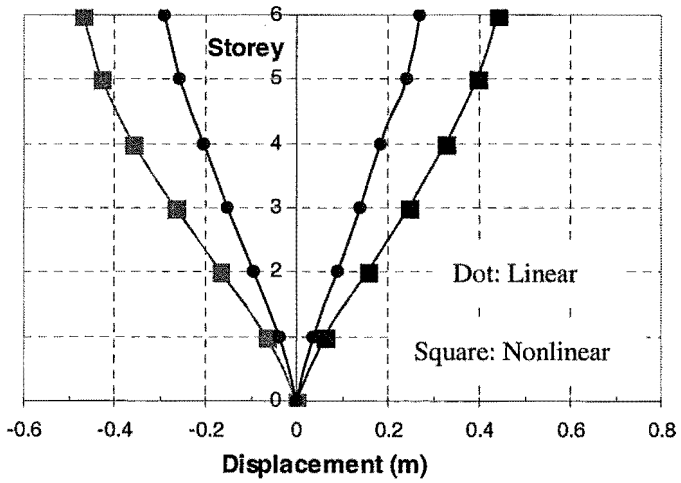

Figure 6.25 The Maximum Displacement Envelopes for the Linear and Nonlinear Analyses Under the El-Centro Earthquake

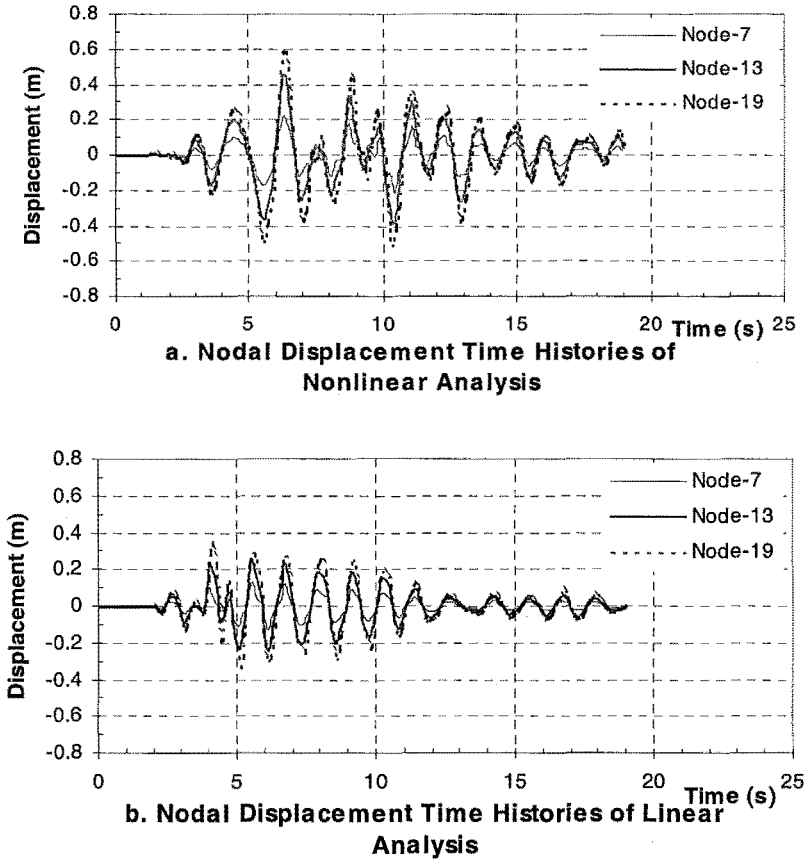

Figure 6.26 The Nodal Displacement Time Histories for the Linear and Nonlinear Analyses under the Parkfield Earthquake

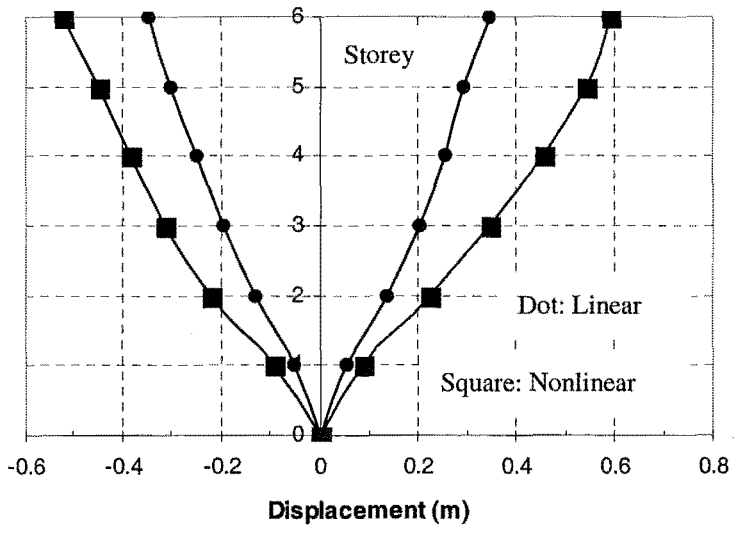

Figure 6.27 The Maximum Displacement Envelopes for the Linear and Nonlinear Analyses under the Parkfield Earthquake

As mentioned above, different earthquake acceleration time histories will generate different responses at the ground surface. When subjected to the El-Centro earthquake, the peak ground acceleration is close to the maximum acceleration of the input motion. When subjected to the Parkfield earthquake, however, the peak ground acceleration is greater than the maximum acceleration of the input motion. The reason is that the Parkfield earthquake is similar to an impulse loading. In this case, the soil strength is higher than the static strength. Because of yielding near the ground surface for these earthquakes, their acceleration amplitudes, frequency contents and strong shaking durations display a great difference between the linear and nonlinear analyses. The spectral accelerations from the nonlinear analysis are amplified at the predominant period of ground response. The results from the linear and nonlinear analyses gradually become more alike as the depth increases. This reflects that the preconsolidated pressure of the soil directly influences the soil response.

6.5 Summary

In this Chapter, the local site amplification and their effects on the structural response of a frame have been discussed when the site is subjected to strong and weak input motions from the basement rock. Some conclusions can be drawn. When subjected to strong input motion, soft clay will yield in a surface layer. The peak ground acceleration from the nonlinear analysis is less than that from the linear analysis, the frequency content of the ground response is different from that of the input motion, and the duration of strong shaking of the input motion is lengthened at the ground surface. As the depth increases, the results from the linear and nonlinear analyses become similar to each other. The frequency contents of the ground response from the linear and nonlinear analyses show a great difference so that the structural responses calculated by both surface motions show a great difference.

When a site is subjected to weak input motion, the results from the linear and nonlinear analyses show similarity at different depths and the acceleration of the input motion from the basement rock is amplified on the ground surface. Although the structural

responses generated by the nonlinear surface motion are greater than those from the linear surface motion, the difference is slight.

Nonlinear site amplification is determined by many factors. The input motion from the basement rock is one of the important factors. For example, although the maximum acceleration for the Parkfield earthquake is larger than that for the El-Centro earthquake, the peak acceleration of the ground response under the El-Centro earthquake is nearly the same as the maximum acceleration of the El-Centro earthquake, however the peak acceleration of the ground response under the Parkfield earthquake is greater than the maximum acceleration of the Parkfield earthquake. Therefore, the maximum acceleration of the input motion at the basement rock is not only important to assess ground surface response of the site, the acceleration time history of the input motion is also important.

The fixed-base structural response is influenced directly by the ground response from the linear and nonlinear analyses. By comparing the effects on the structural response between the acceleration amplitude and predominant period of the ground response, the predominant period of the ground response is more important. The reason is that when the predominant period of the site and the natural vibration period of the structure are close, resonance will occur.

Chapter Seven

Investigation of Seismic Soil-Structure Interaction Using a Linear Soil Model

7.1 Introduction

The behaviour of structures subjected to an earthquake is affected by the foundation and its surrounding soil. Until the advent of nuclear power stations or offshore platforms with their heavy and stiff structures, soil-structure interaction had not been given any special attention (Wolf, 1985). Many experiments and site measurements (Mita, et al 1989, Meli, et al 1998) have been carried out to show the importance of the soil-structure interaction. Many numerical methods have been proposed. Common examples are the lumped-mass method, the substructure method, the finite element method and the boundary element method. Advantages and disadvantages of both the lumped-mass method and the finite element method have been illustrated by Seed, el. at. (1975) and Hadjian, el. at. (1974).

The above researches have shown that the effect of soil-structure interaction on structural response depends on site conditions, structural properties, foundation types and input motions. Normally the natural free-vibration period can describe the characteristics of the site conditions and the structure, and the predominant period can describe characteristics of the input motion from the basement rock. Therefore these parameters can be used to investigate the effect of soil-structure interaction on the structural response. In order to realise this objective, five sites, two multi-storey frames and two earthquake motions are chosen for the study and soil-structure interaction and fixed-base cases will be discussed in this Chapter. In one case, both the soil model and the structural model are linear. The second case is where the soil model is linear when the structural model is bilinear. In each case, the effect of the structure on the ground acceleration response is investigated, then the effects of soil properties, structural properties and soil-structure interaction on the structural

response are investigated. The program, RUAUMOKO (Carr, 1998), will be used to analyse both cases.

To illustrate the effect of the soil behaviour on structural response, five different sites have been chosen and are shown in Table 7.1 each having a different natural vibration period.

The shear modulus and Poisson's ratio of the soil are very important parameters in soil-structure interaction analysis. The shear modulus usually changes with depth, for example in a linear fashion, but for the sake of simplicity, a uniform soil modulus is used in this research. In order to compare the calculated results in these cases, the Poisson's ratio is assumed to remain constant and is taken as equal to 0.3.

Table 7.1 Five Different Sites and Their Properties

No	Site 1	Site 2	Site 3	Site 4	Site 5
T (sec.)	0.7	0.9	1.1	1.25	1.5
G (MP_a)	52.6	32.3	21.4	16.6	11.5

T: Natural vibration period

G: Shear modulus

Two structural systems are investigated in this study: A twelve storey two-bay Jury frame (abbreviated J12) and a six storey two-bay Jury frame (abbreviated J6) (Jury, 1978). Both structures are reinforced concrete moment-resistant frames and were designed in accordance with the New Zealand design code (NZ4203, 1978 and NZ4203, 1982). The floor height and span of J12 is 3.65 by 9.2 metres, the total height of the frame is 43.8 metres and its fixed-base natural vibration period is 2.24 second. The floor height and span of J6 is 3.35 by 5.50 metres, the total height of the frame is 20.1 metres and its fixed-base natural vibration period is 1.142 second.

When the structural model is bilinear, the post-yield stiffness was taken as 2.5% of the elastic stiffness and only the beams and ground floor columns were allowed to be

inelastic assuming that the frame was designed following a "capacity design" approach (Paulay and Priestley, 1992).

The first strong earthquake motion employed is one from the Loma Prieta earthquake of 17th October 1989. The initial twenty seconds containing the main part of the earthquake (maximum acceleration=0.433g) are used as the input motion from the basement rock. Its acceleration time history and its acceleration spectrum are shown in Figs. 6.1a and 6.1b. The second is a motion from the Mexico City earthquake of 19th September 1985. The initial sixty seconds containing the main part of the earthquake are used as the input motion from the basement rock. The acceleration time history and acceleration spectrum are shown in Figs 7.1a and 7.1b. The reason for selecting these two motions is that they have different predominant periods, 0.25s and 2.0s respectively.

In above models, the near field and structure are simulated by the finite element and the far field is represented by the dashpot boundary (Lysmer and Richard, 1969). An assumption is therefore introduced into the calculation, that far field domain is linear. In this study, only a vertically propagated SH wave and a surface foundation are considered. The coupled (soil-structure interaction) and uncoupled (fixed-base) cases discussed in Chapter Two are shown in Figs. 7.2a and 7.2b

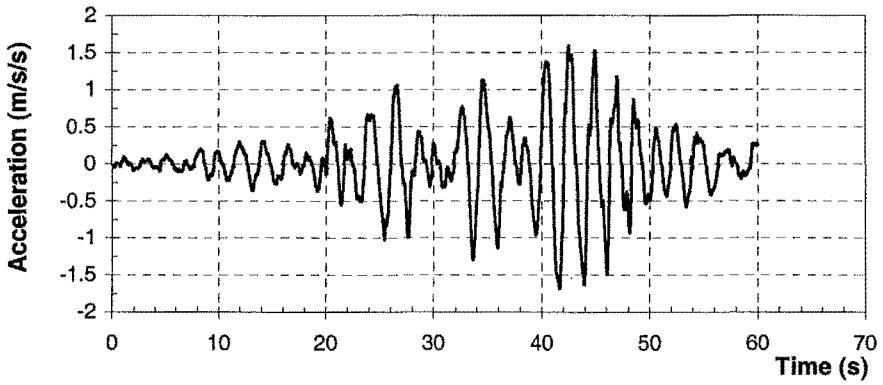

7.1a Acceleration Time History of Mexico City Earthquake

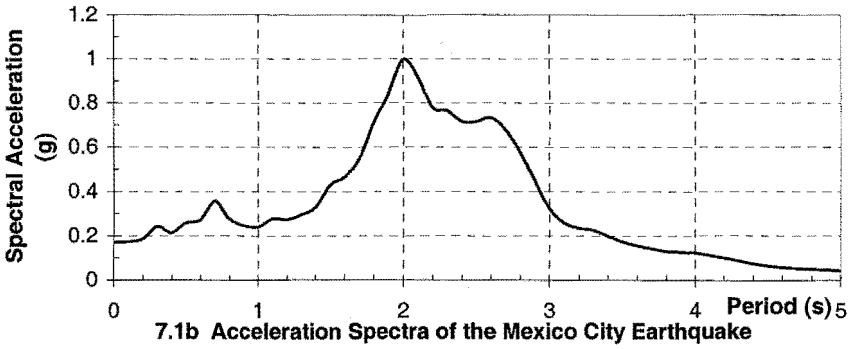

Figure 7.1 Acceleration Time History and Acceleration Spectrum of the Mexico City Earthquake

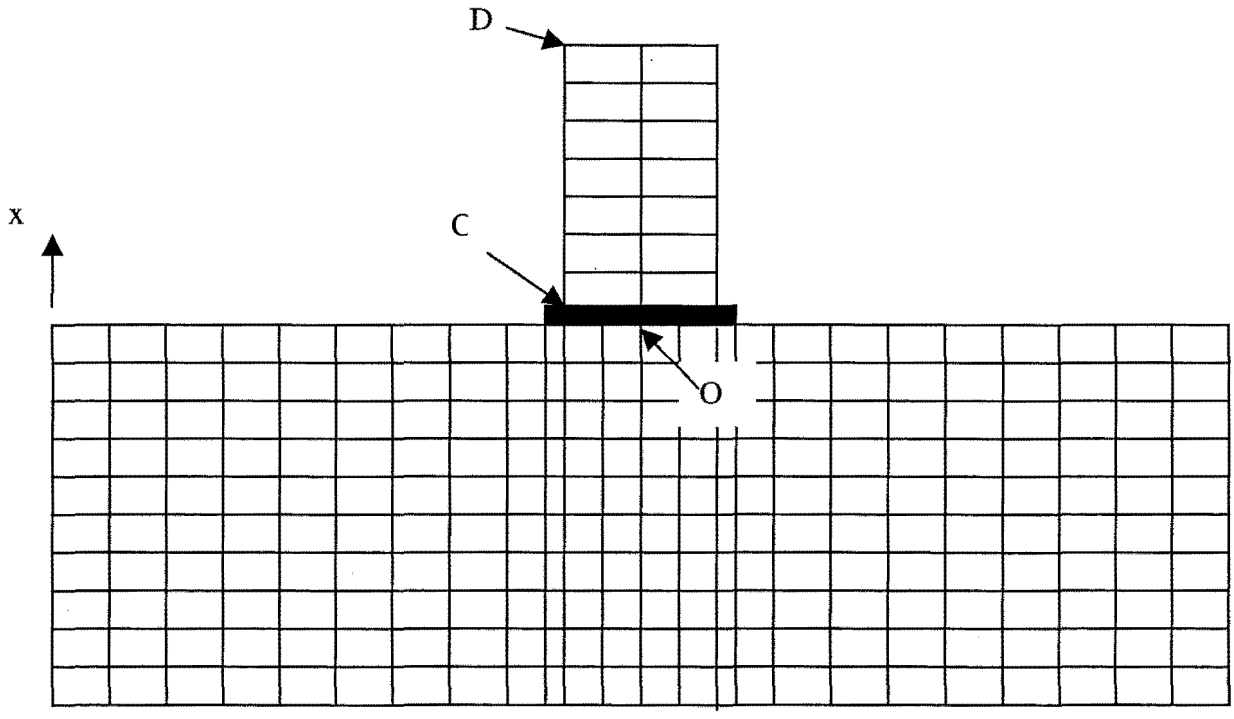

Figure 7.2a Coupled Case (Soil-Structure Interaction)

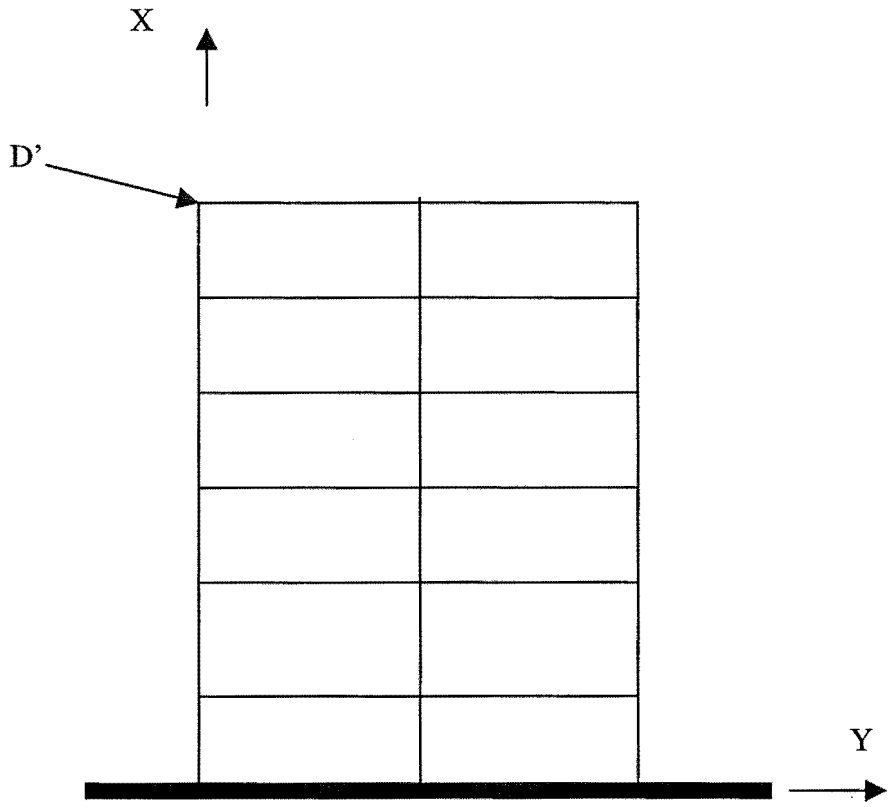

7.2b Uncoupled Case (Fixed-Base)

7.2 The Loma Prieta Earthquake

The Loma Prieta earthquake of 17th October 1989 has been discussed in the last Chapter. Here its effect on the structural response will be investigated and in the calculation, soil-structure interaction and fixed-base cases will be considered. The 6-storey frame will be discussed first, then the 12-storey frame.

7.2.1 The 6-Storey Frame

For the five different sites, the effect of soil-structure interaction on the structural response is investigated using the linear and nonlinear structural models. The first is to evaluate the effect of the structure to the ground acceleration response. The method used is to compare the acceleration time histories and acceleration spectra between the free field and soil-structure interaction at point O in Fig.7.2a. Then the structural response is evaluated by considering the effect of soil-structure interaction. The displacement at the top floor, the maximum inter-storey shear force and the rocking of the structural foundation are calculated and compared with those in the fixed-base case when the acceleration time history from soil-structure interaction analysis at point O shown in Fig.7.2a is used as input motion.

7.2.1.1 The Effect of the Structure on the Ground Acceleration Response

An acceleration time history can show the acceleration amplitude, frequency content and acceleration phase. Comparison of the acceleration time histories between the free field and the soil-structure interaction cases at point O are shown in Fig.7.3. The soil modulus has a great impact on the acceleration time history at point O regardless of the free field or soil-structure interaction case. As the soil modulus reduces, the natural vibration period of the site increases, but the acceleration amplitude at point O reduces.

Although comparison of the acceleration time histories is one way to illustrate the effect of the structure on the ground acceleration response, the acceleration spectrum clearly show the difference at point O using the free field and soil-structure interaction analyses. Comparison of the acceleration spectra at point O between the free field and soil-structure interaction cases is given in Fig.7.4. This figure shows some important characteristics. When the predominant period of the input motion is not equal to the natural vibration period of the site, the acceleration spectrum at point O will contain two peaks whose periods are nearly equal to the predominant period of the input motion and the natural vibration period of the site. When the two periods are close to each other, the spectral peak acceleration whose period is equal to the

predominant period of the input motion will be amplified. Fig.7.4 also shows that the spectral acceleration from the free field case is greater than that from the soil-structure interaction case at point O. The effect of the structure on the ground acceleration response at point O is clear.

In order to reflect the effect of the site on the ground acceleration response, the difference of amplitudes of the spectral peak accelerations between the free field and soil-structure interaction cases is shown in Fig.7.4f. When the natural vibration periods of the site and structure are close to each other, the difference is large.

When the bilinear model is used to model the structural behaviour, comparison of the spectral accelerations at point O for the linear and nonlinear structural models is shown in Fig.7.5. The structural material behaviour has little influence on the acceleration response of the ground at point O.

7.2.1.2 Evaluation of the Structural Response

In order to show the structural response by considering soil-structure interaction, a reference case with a fixed-base structure is proposed and shown in Fig.7.2b. The displacements at the top floor for the fixed-base and soil-structure interaction cases from the linear analyses are shown in Fig.7.6. The displacements at the top floor for the fixed-base case are greater than that for the soil-structure interaction case when the natural vibration periods of the site and structure are close to each other. In the soil-structure interaction case, the maximum displacements at the top floor in the five sites show only a slight difference.

In order to further analyse the above results for the soil-structure interaction case, the natural vibration period of the soil-structure systems are listed in Table 7.2. The natural vibration period of the soil-structure system is greater than that of the structure or the site, which illustrates that the natural vibration period of the structure is lengthened. Therefore, the effect of the input motion on the structural response for the soil-structure interaction case is small.

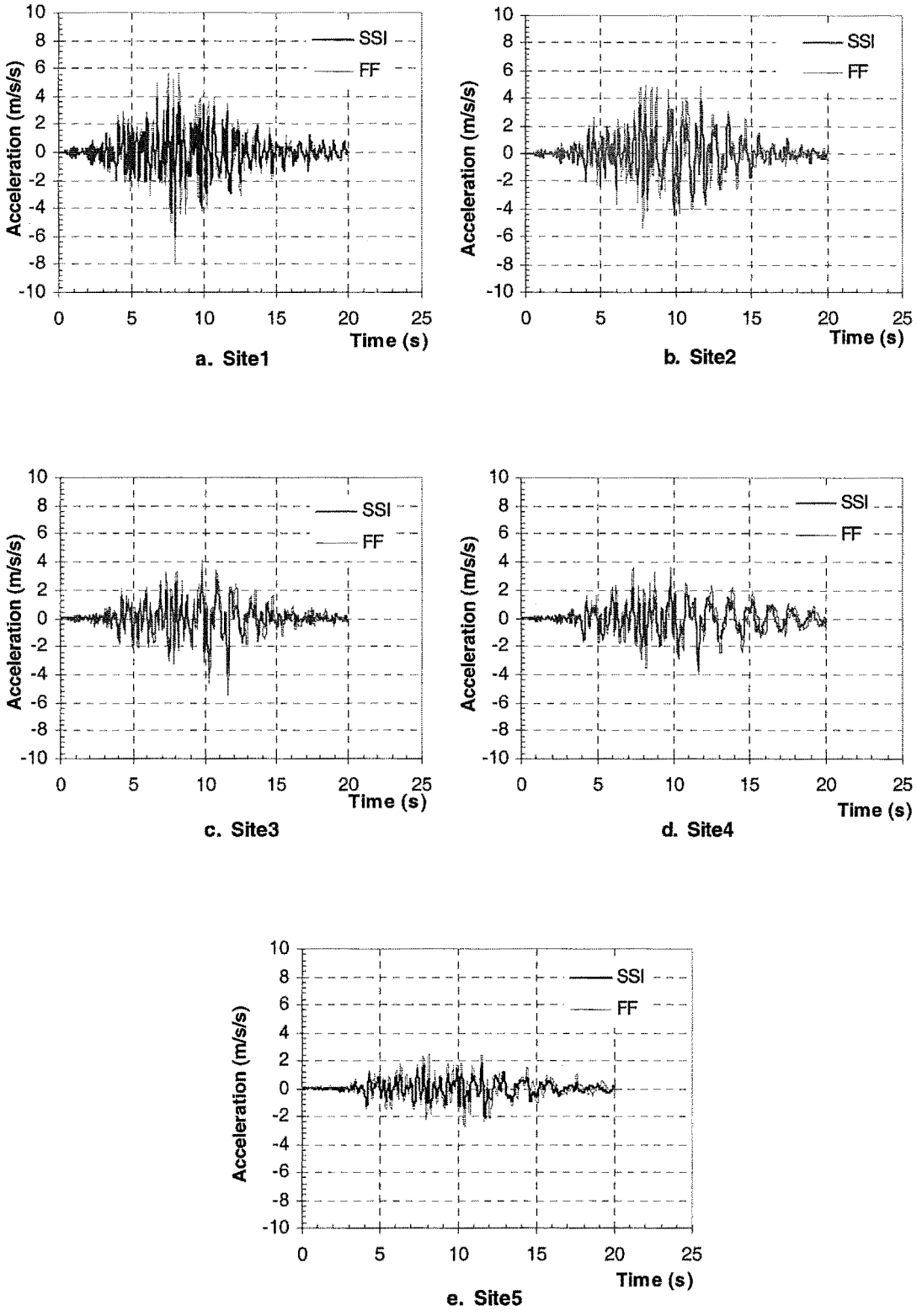

Figure 7.3 Comparison of the Acceleration Time Histories for the Free Field and Soil-Structure Interaction at Point O from Site1 to Site5 for the Linear Analyses of the 6-Storey Frame

SSI: Soil-Structure Interaction FF: Free Field

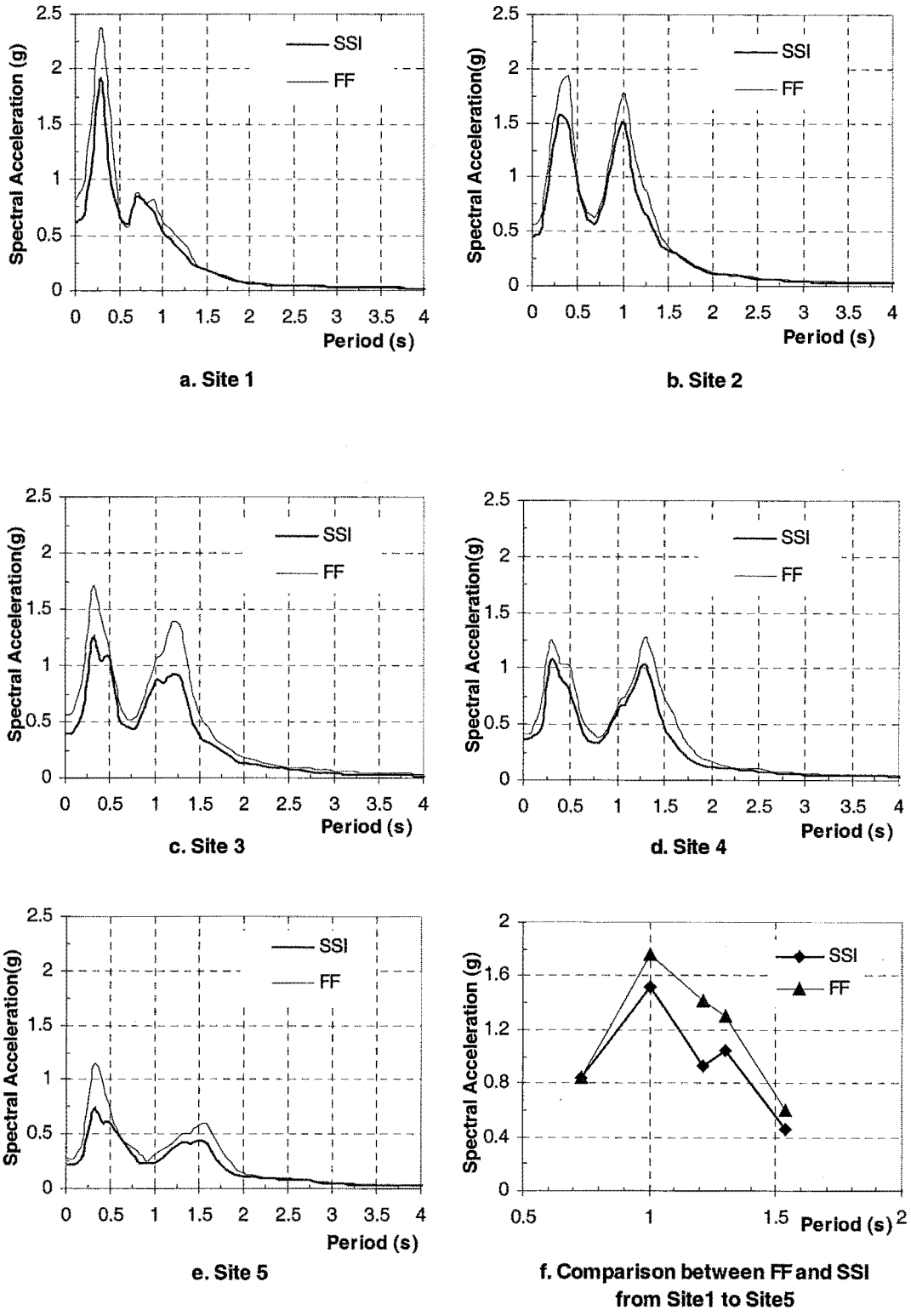

Figure 7.4 from a to e: Comparison of the Acceleration Spectra for the Free Field and Soil-Structure Interaction at Point O from Site1 to Site5 for the Linear Analyses of the 6-Storey Frame

f: Comparison of the Spectral Peak Acceleration at Longer Period

SSI: Soil-Structure Interaction FF: Free Field

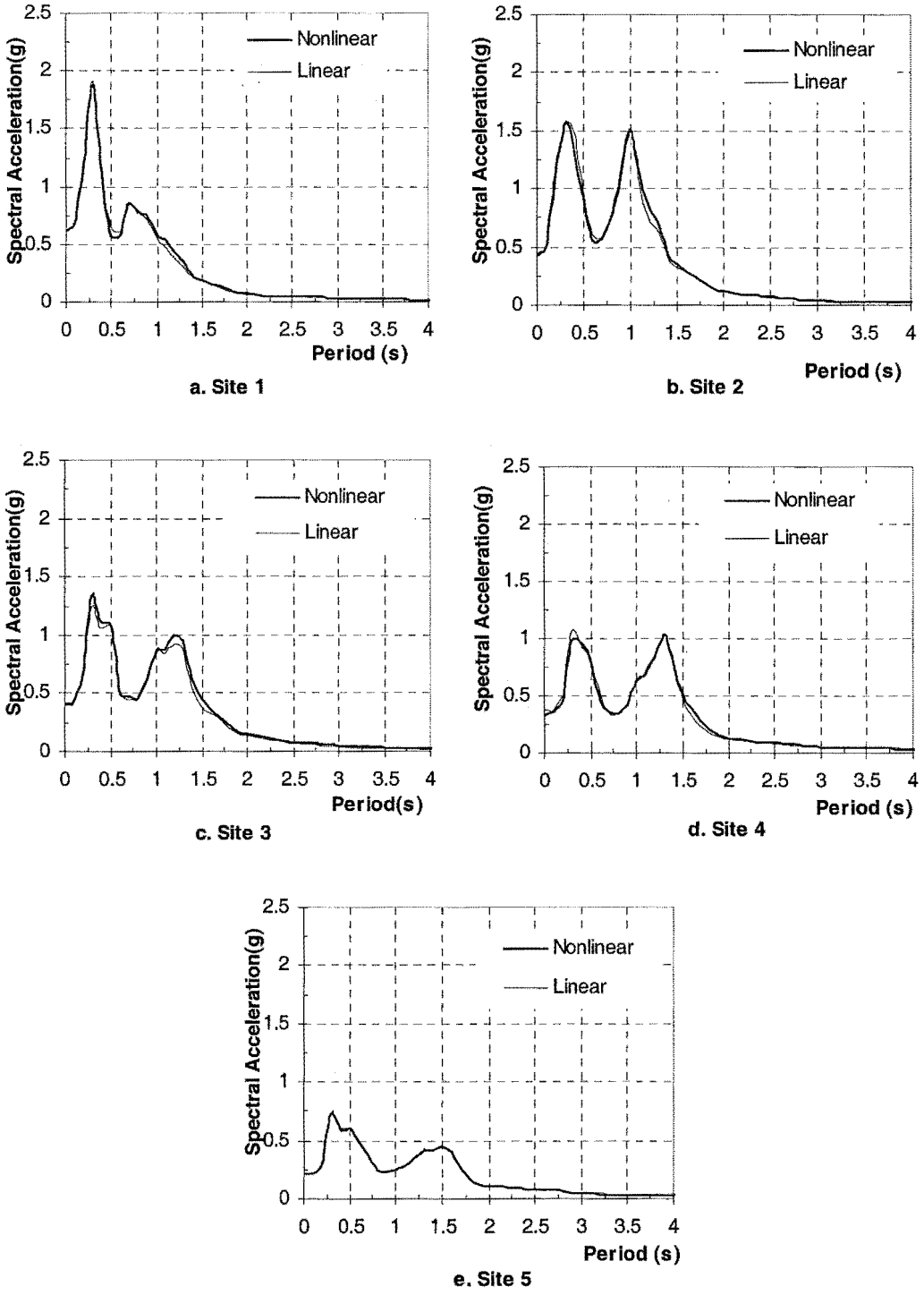

Figure 7.5 Comparison of the Acceleration Spectra of the Soil-Structure Interaction for the Linear and Nonlinear Analyses at Point O from Site1 to Site5 for the 6-Storey Frame

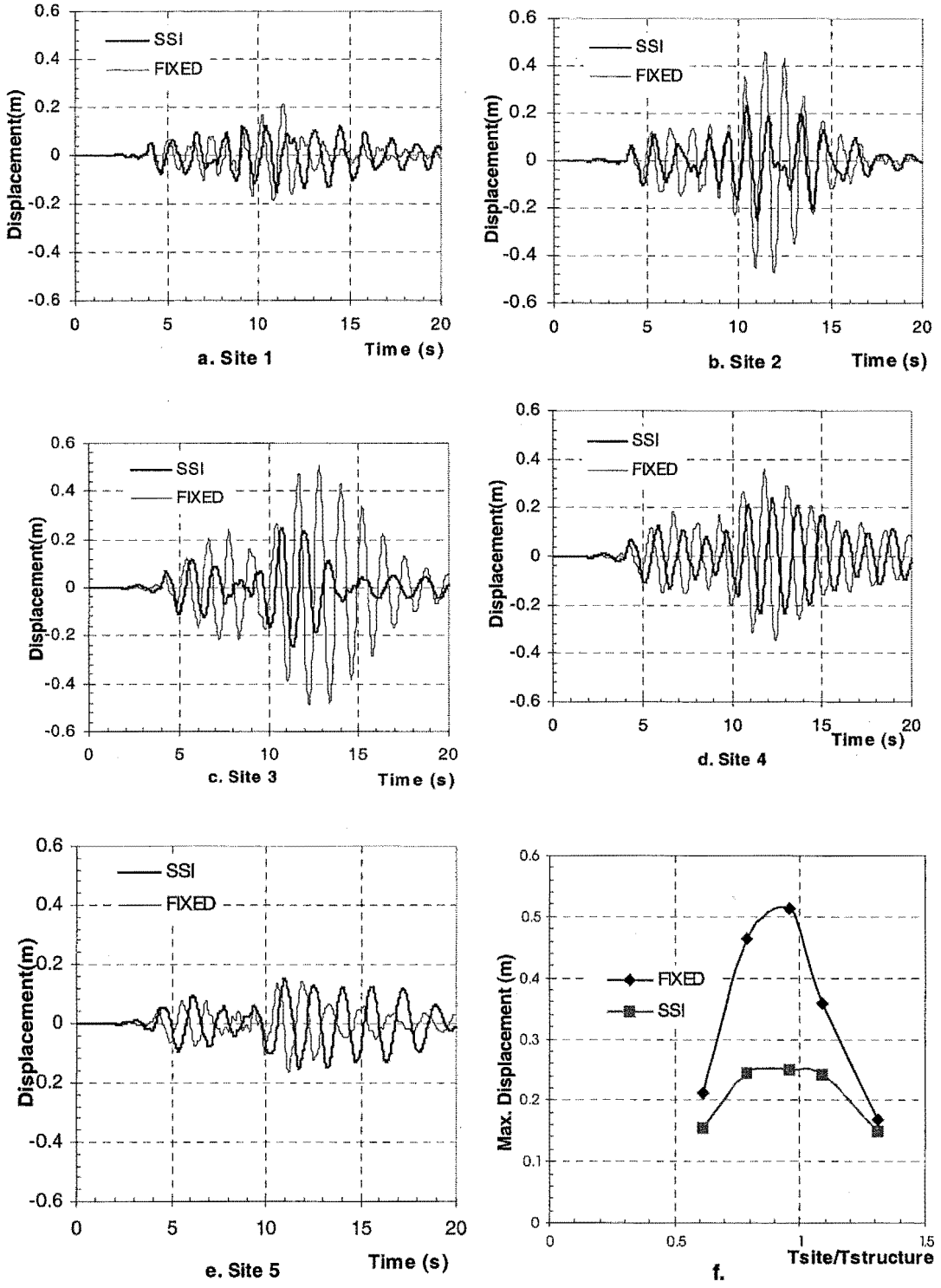

Figure 7.6 from a to e: Comparison of the Displacement Time Histories at the Top Floor for the Fixed-Base and Soil-Structure Interaction from Site1 to Site5 for the Linear Analyses of the 6-Storey Frame

f: Relationship between the Maximum Displacement at the Top Floor and Ratio of the Fundament periods

Fixed: Fixed-Base SSI: Soil-Structure Interaction

Table 7.2 Natural vibration period of Soil-Structure System

No	Site1	Site2	Site3	Site4	Site5
System Period T(s)	1.391	1.532	1.708	1.851	2.112

In order to display the effect of different sites on the structural response for the linear analysis, the relationship between the maximum displacement at the top floor and the ratio of the natural vibration periods for the fixed-base and soil-structure interaction cases is given in Fig.7.6f. This figure shows the effect of resonance from the fixed-base case on the structural response and the effect of the soil-structure interaction on the structural response. The reason for the above results is that for the fixed-base case there are two spectral peak accelerations on the ground surface (shown in Fig.7.4) and the longer period for the spectral peak acceleration is close to the natural vibration period of the structure so that resonance occurs. However, for the soil-structure interaction case the predominant period of the input motion is much less than the natural vibration period of the soil and structure system so that the effect of soil-structure interaction reduces displacements at the top floor.

The displacements at the top floor for the fixed-base and soil-structure interaction cases from the nonlinear analyses are given in Fig.7.7. The displacements at the top floor do not show resonance for the fixed-base case, which is different from the results from the linear analysis. The reason is due to the yielding of the structure so that the natural vibration period of the structure is lengthened. By comparing the maximum displacements at the top floor for the fixed-base and soil-structure interaction cases from the nonlinear analyses, only a slight difference can be seen.

The above discussions focus on the effect of soil-structure interaction on the maximum displacement and displacement time history at the top floor. In design, however, the inter-storey shear force is also a very important parameter. For the linear analyses, the ratio of the maximum inter-storey shear forces for the case of soil-

structure interaction to the case of fixed-base is shown in Fig.7.8. Soil-structure interaction greatly reduces the inter-storey shear force. A similar ratio as in Fig.7.8 for the maximum inter-storey shear force in the nonlinear analyses is shown in Fig.7.9. From site1 to site5, the maximum ratio of the inter-storey shear forces is close to 1.0, but average ratio is still less than 1.0. This illustrates the effect of soil-structure interaction on the inter-storey shear force for the nonlinear analysis.

The rocking of the foundation is investigated because it is an important parameter in considering soil-structure interaction. The rocking time histories from site1 to site5 for the linear analyses are shown in Fig.7.10. In order to display the effect of the natural vibration periods of the site and the structure on the rocking, the relationship between rocking and the ratio of the natural vibration periods is shown in Fig.7.11. It shows that when the natural vibration period of the site is close to the natural vibration period of the structure, the rocking attains its maximum value. When the ratio is much less than 1.0, the rocking will be very small. This result shows that the natural vibration periods of the site and the structure will control the effect of soil-structure interaction on the structural response.

Similar results from the nonlinear analyses are shown in Fig.7.12, which displays the same characteristics as in Fig.7.10. In order to display the effect of the natural vibration periods of the site and structure to the rocking for the nonlinear analyses, the relationship between the rocking and the ratio of the natural vibration periods is shown in Fig.7.13. By comparing Fig.7.11 and Fig.7.13, it can be seen that the yielding of the structure reduces the maximum rocking. The reason is that the yielding of the structure increases the equivalent structural damping so that the maximum amplitude of the rocking reduces.

7.2.2 The 12-Storey Frame

Following the same procedure as used in section 7.2.1, the first step was to investigate the effect of the structure on the ground acceleration response at point O. Then the effect of soil-structure interaction to structural response was carried out. The natural vibration period of the 12-storey frame is different from that of the 6-storey frame, so

a comparison between two structural responses is also carried out to illustrate the effect of the differences in the structural response.

7.2.2.1 The Effect of the Structure on the Ground Acceleration Response

The acceleration spectra for the free field and soil-structure interaction cases at point O using the linear analyses are shown in Fig.7.14. There are two peaks in these acceleration spectra and the spectral peak accelerations for the free field and soil-structure interaction cases show considerable difference at the period of 0.3 seconds. The spectral peak accelerations at longer periods are, however, closer than at the period of 0.3 seconds. By comparing Fig.7.4 (6-storey frame) and Fig.7.14 (12-storey frame), the two ground acceleration responses show a great difference. The comparison illustrates that the ground acceleration response at point O is affected by the structure.

The acceleration spectra of the ground acceleration responses at point O from the linear and nonlinear analyses are shown in Fig.7.15. As in Fig.7.5, there is only a slight difference in the spectra from the both analyses.

7.2.2.2 Evaluation of the Structural Response

For the 12-storey frame, the displacement time histories at the top floor for the fixed-base and soil-structure interaction cases from the linear analyses are shown in Fig.7.16. The maximum displacements for the two cases are nearly the same and their frequency contents are similar except for the result for site5. For site5 with the longer natural vibration period, the difference between the fixed-base and soil-structure interaction cases is very marked. The reason is most likely that as the natural vibration period of the site is close to the natural vibration period of the structure, the effect of soil-structure interaction on the displacement time history will be marked.

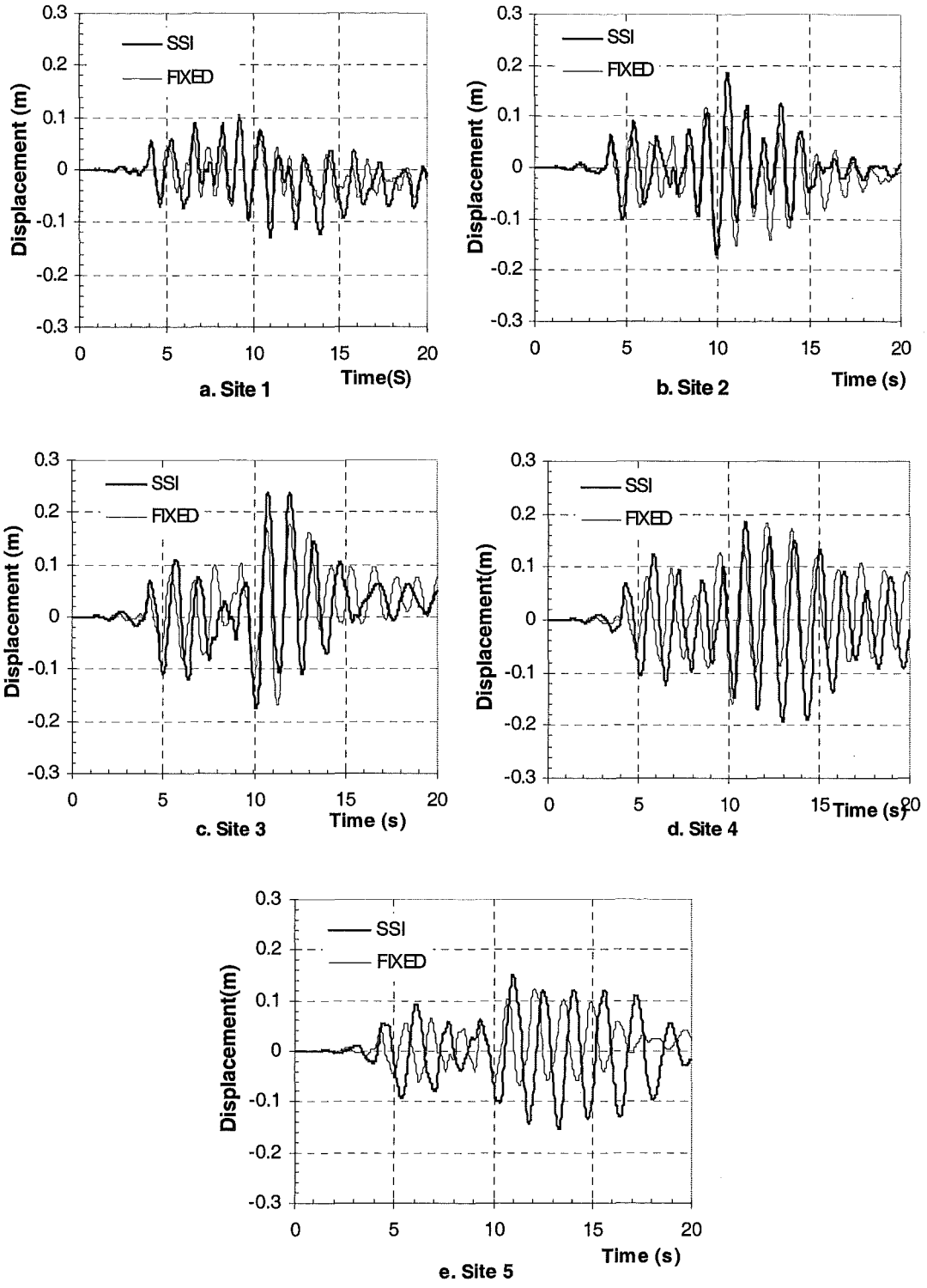

Figure 7.7 Comparison of the Displacement Time Histories at the Top Floor for the Fixed-Base and the Soil-Structure Interaction from Site1 to Site5 for the Nonlinear Analyses of the 6-Storey Frame

Fixed: Fixed-Base SSI: Soil-Structure Interaction

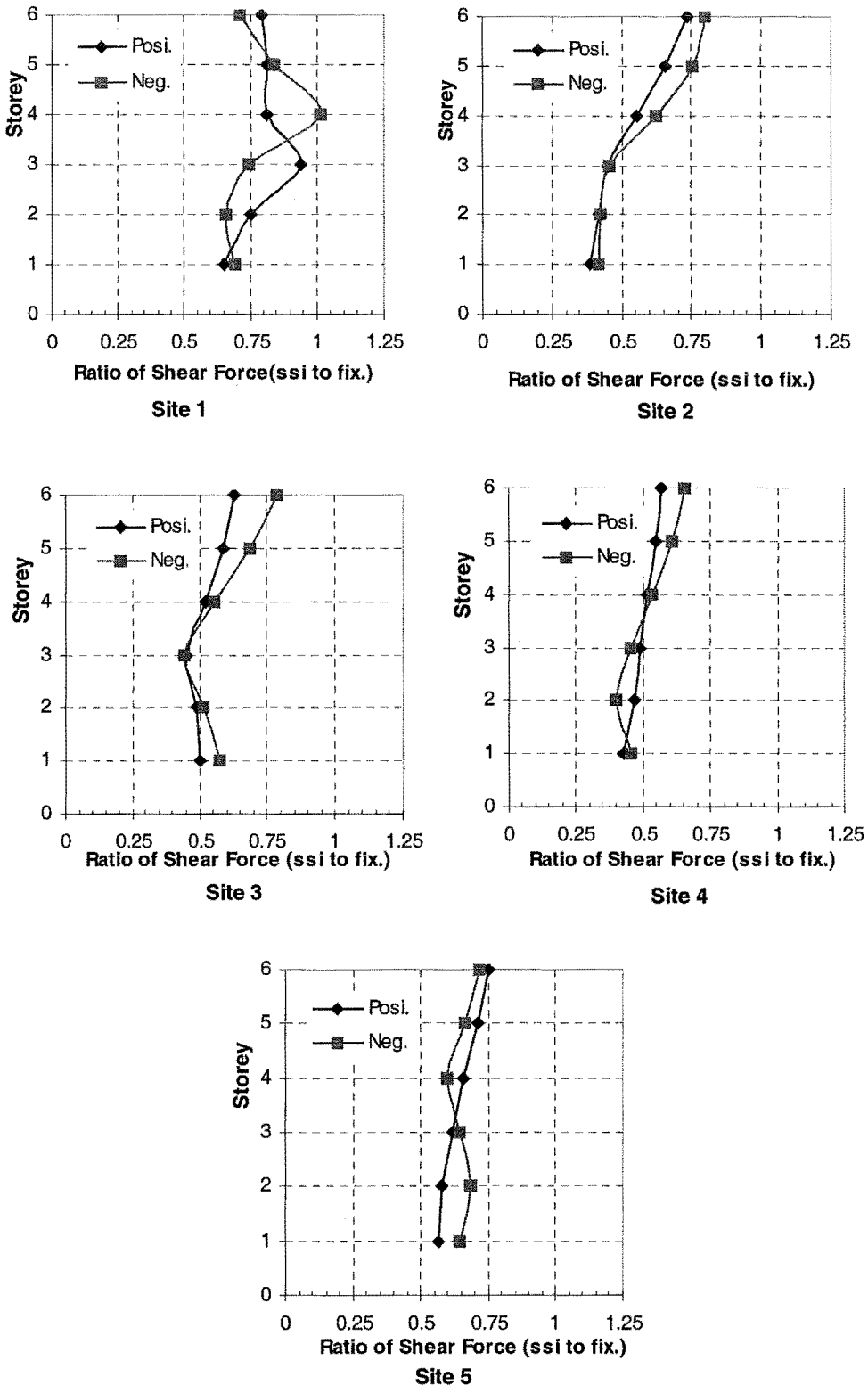

Figure 7.8 Ratio of the Inter-Storey Shear Forces of the Soil-Structure Interaction to the Fixed-Base from Site1 to Site5 for the Linear Analyses of the 6-Storey Frame

Posi: Position Shear Force Neg: Negative Shear Force

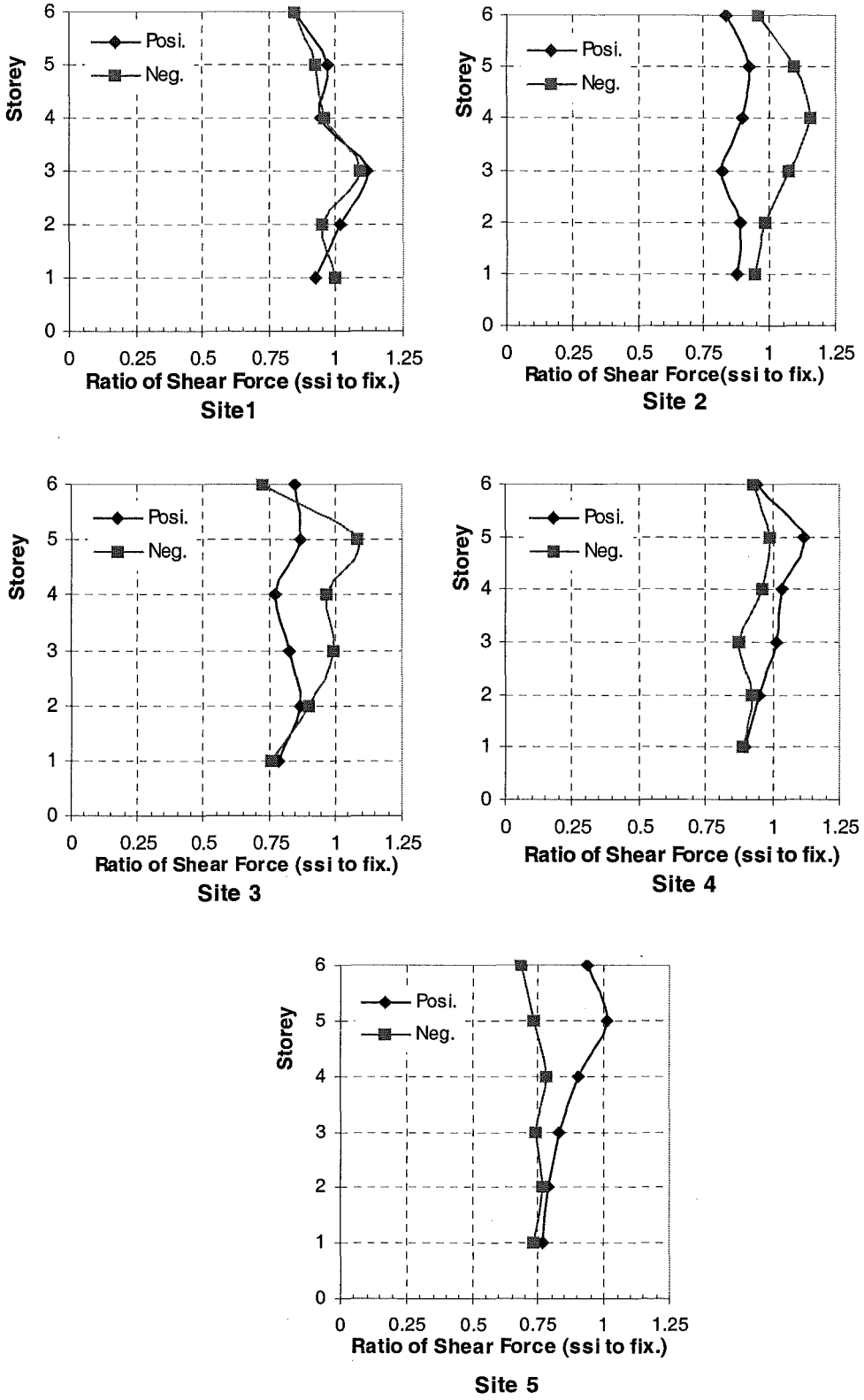

Figure 7.9 Ratio of the Inter-Storey Shear Forces of the Soil-Structure Interaction to the Fixed-Base from Site1 to Site5 for the Nonlinear Analyses of the 6-Storey Frame

Posi: Positive Shear Force Neg: Negative Shear Force

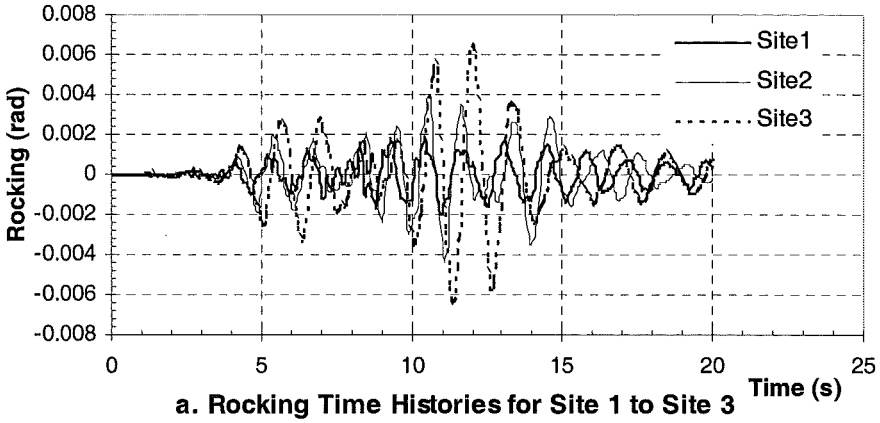

a. Rocking Time Histories for Site 1 to Site 3

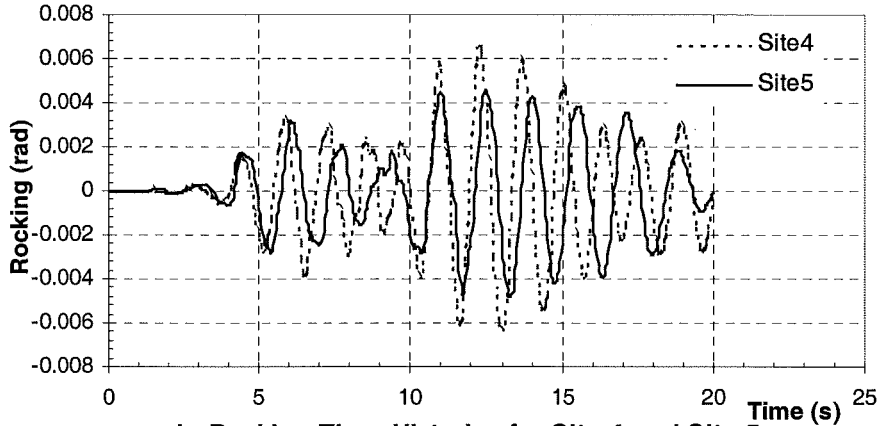

b. Rocking Time Histories for Site 4 and Site 5

Figure 7.10 The Rocking Time Histories from Site1 to Site5 for the Linear Analyses of the 6-Storey Frame

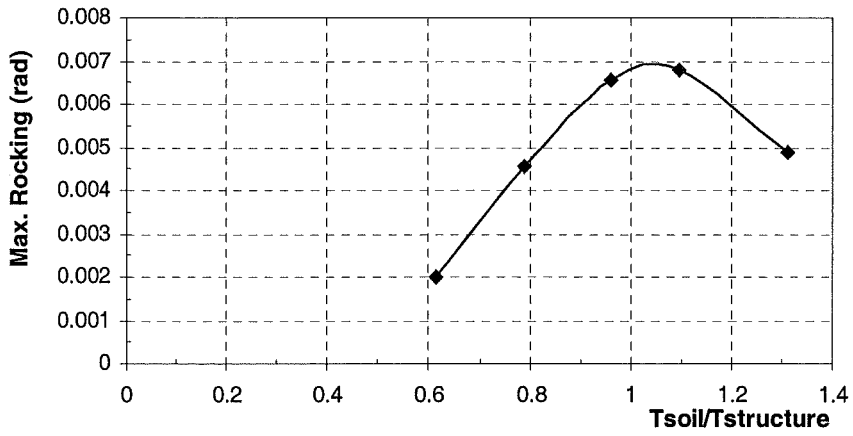

Figure 7.11 Relationship between the Maximum Rocking of the Natural Vibration Period of the Sites to the Structure for the Linear Analyses of the 6-Storey Frame

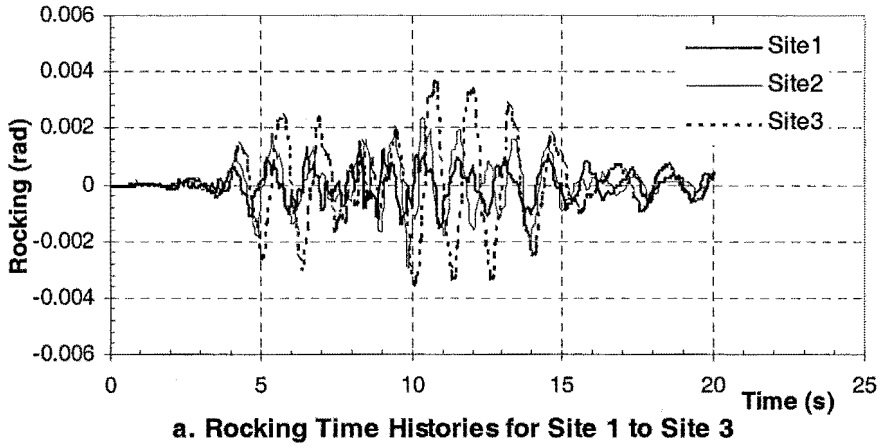

a. Rocking Time Histories for Site 1 to Site 3

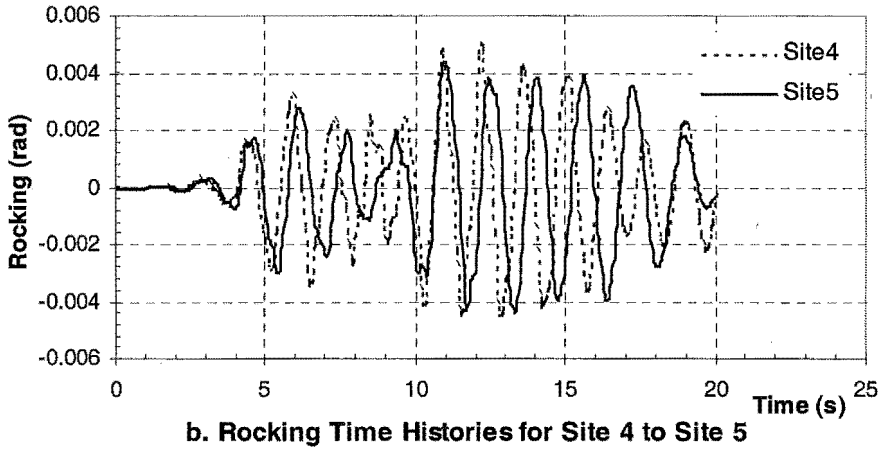

b. Rocking Time Histories for Site 4 to Site 5

Figure 7.12 The Rocking Time Histories from Site1 to Site5 for the Nonlinear Analyses of the 6-Storey Frame

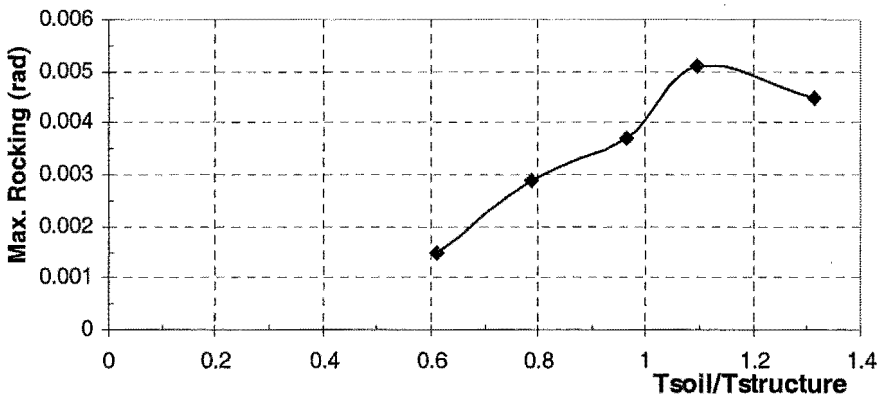

Figure 7.13 Relationship between the Maximum Rocking and Ratio of the Natural Vibration Period of the Sites to the Structure for the Nonlinear Analyses of the 6-Storey Frame

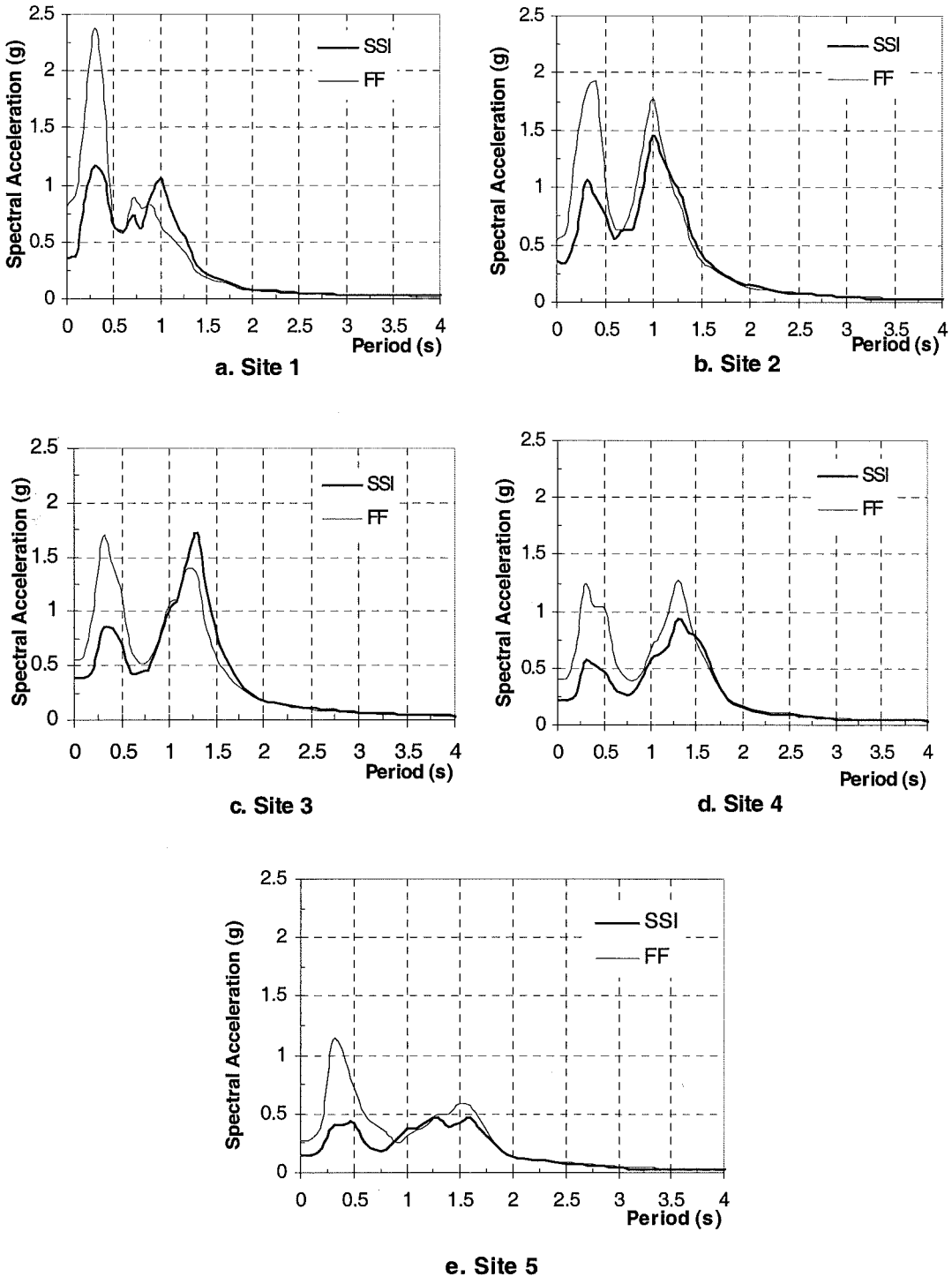

Figure 7.14 Comparison of the Acceleration Spectra for the Free Field and the Soil-Structure Interaction at Point O from Site1 to Site5 for the Linear Analyses of the 12-Storey Frame

SSI: Soil-Structure Interaction FF: Free Field

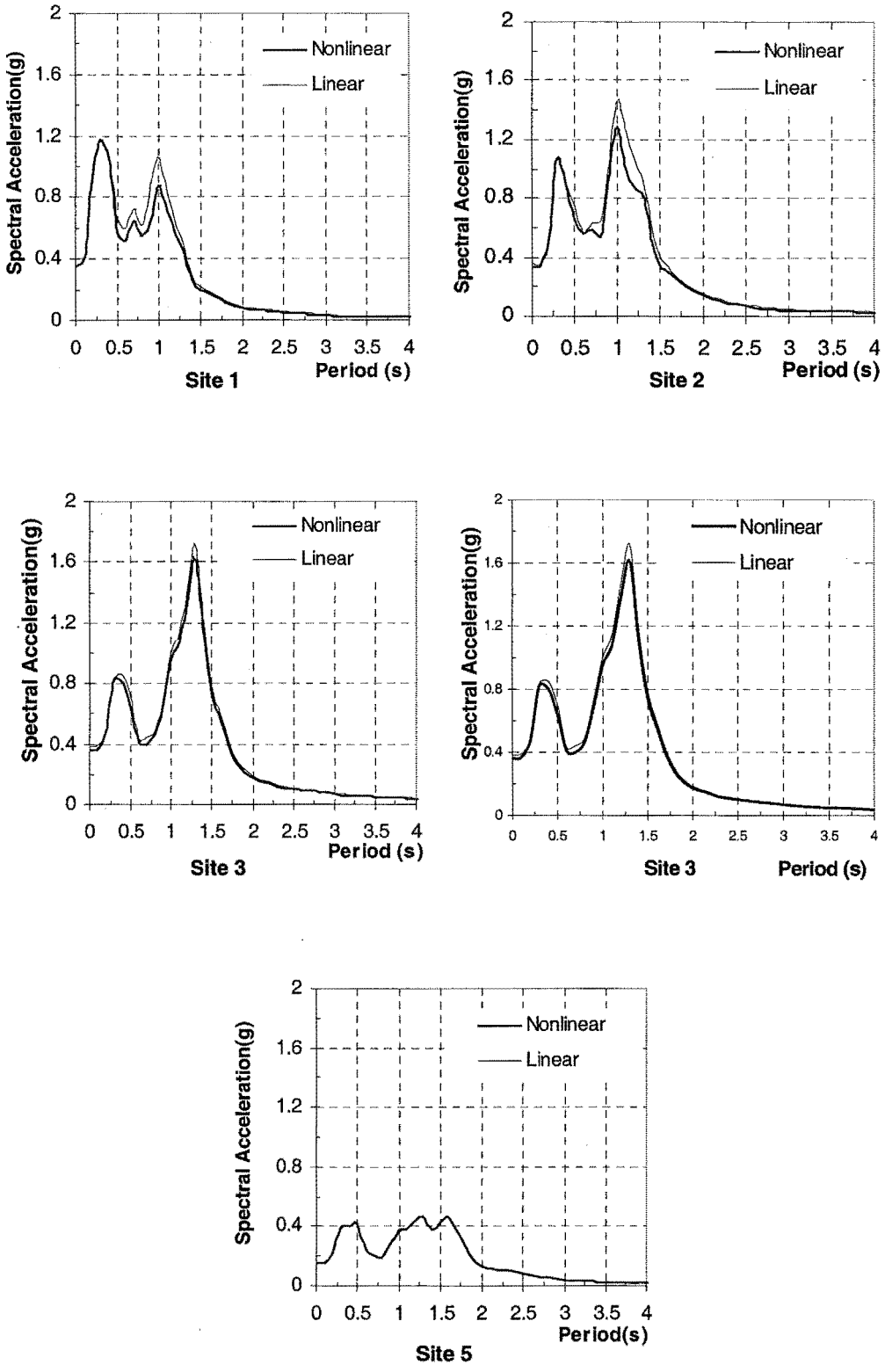

Figure 7.15 Comparison of the Acceleration Spectra of the Soil-Structure Interaction at Point O from Site1 to Site5 for the Linear and Nonlinear Analyses of the 12-Storey Frame

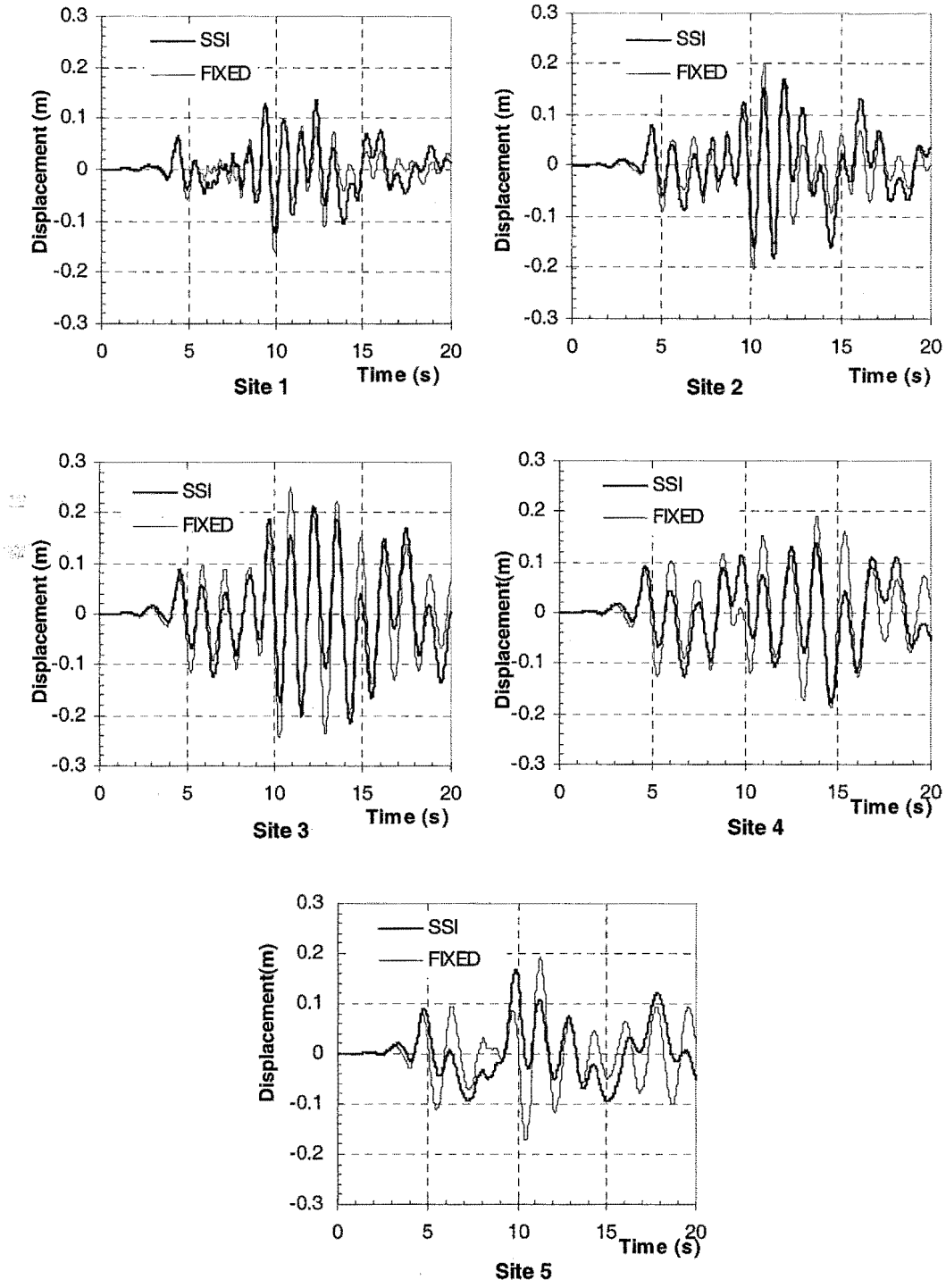

Figure 7.16 Comparison of the Displacement Time Histories at the Top Floor for the Fixed-Base and the Soil-Structure Interaction from the Linear Analyses of the 12-Storey Frame

SSI: Soil-Structure Interaction Fixed: Fixed-Base

The displacement time histories at the top floor for the fixed-base and soil-structure interaction cases from the nonlinear analyses are shown in Fig.7.17. The maximum displacements at the top floor are nearly the same for the two cases. The vibration frequency of the displacement shows a very slight difference.

For the 12-storey frame, the maximum displacements at the top floor from the linear and nonlinear analyses for the fixed-base and soil-structure interaction cases are nearly the same. The reason is that the natural free-vibration period of the structure is much longer than both the natural free-vibration period of the soil and the predominant period of the input motion from the basement rock. This indicator shows that the effect of the soil-structure interaction on the structural response is not very important.

The ratio of inter-storey shear forces from site1 to site5 for the linear analyses in Fig.7.18 shows different characteristics from the results of the 6-storey frame. At the lower floors, the ratio is greater than 1.0 and at higher floors the ratio is less than 1.0. The ratio of inter-storey shear forces from site1 to site5 for the nonlinear analyses shown in Fig.7.19 is generally less than 1.0. These results illustrate that the material nonlinearity of the structure reduces the structural response. The effect of high modes on the inter-storey shear forces is clear in Figs. 7.18 and 7.19.

The rocking time histories from the linear and nonlinear analyses are shown in Figs. 7.20 and 7.21. The maximum rocking at site3, site4 and site5 are nearly the same for the two analysis methods, but the rocking time histories are different.

By comparing the results from the 6-storey frame and 12-storey frame shown in Figs. 7.6 and 7.7 and Figs. 7.16 and 7.17, the soil-structure interaction for the 6-storey frame is seen to be more significant than for the 12-storey frame when subjected to the Loma Prieta earthquake. The result illustrates that the relationship between the predominant period of the input motion from the basement rock and the natural vibration periods of the site and structure will decide the effect of the soil-structure interaction on the structural response.

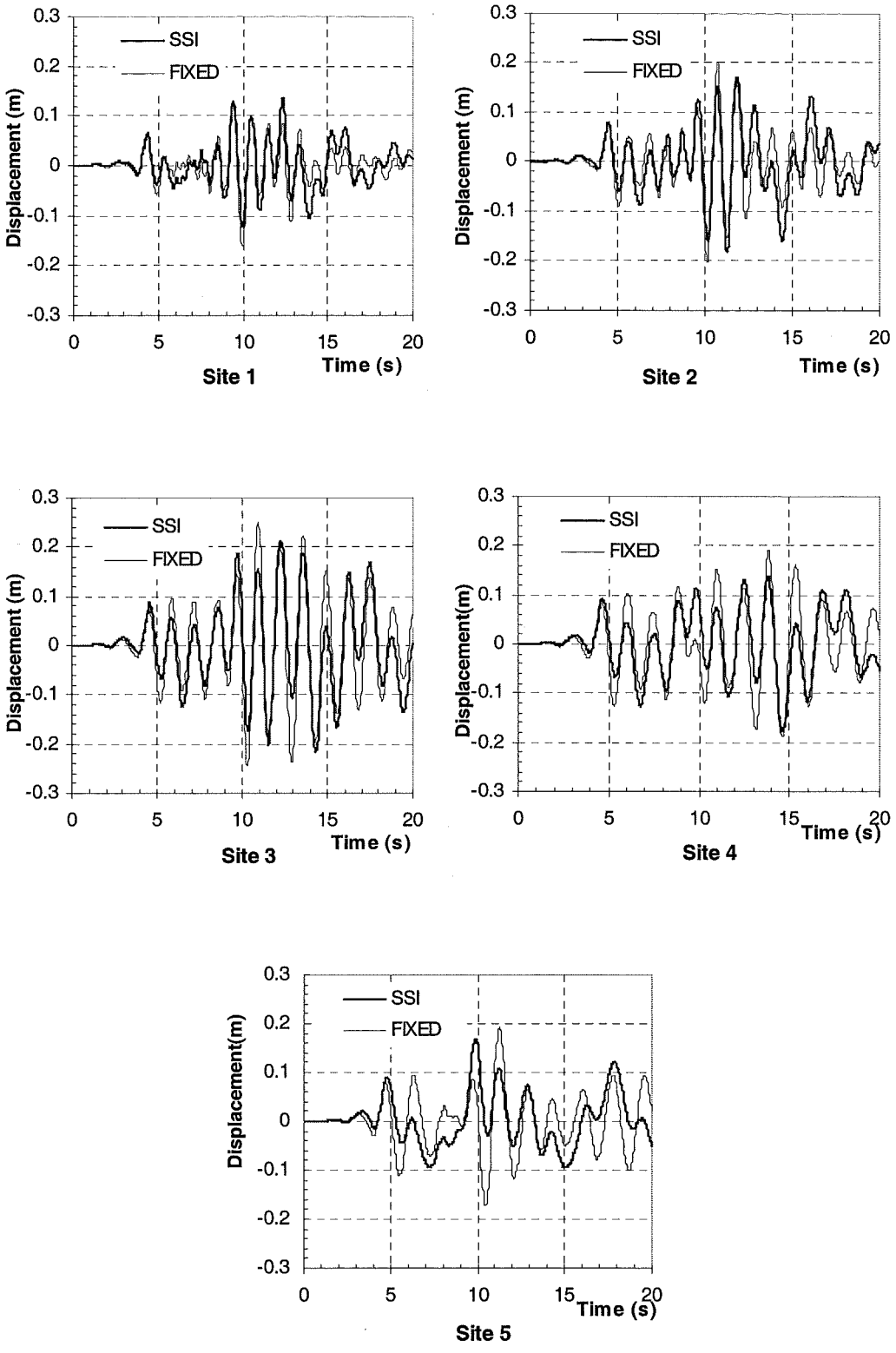

Figure 7.17 Comparison of the Displacement Time Histories at the Top Floor for the Fixed-Base and the Soil-Structure Interaction from the Nonlinear Analyses of the 12-Storey Frame

SSI: Soil-Structure Interaction FIXED: Fixed-Base

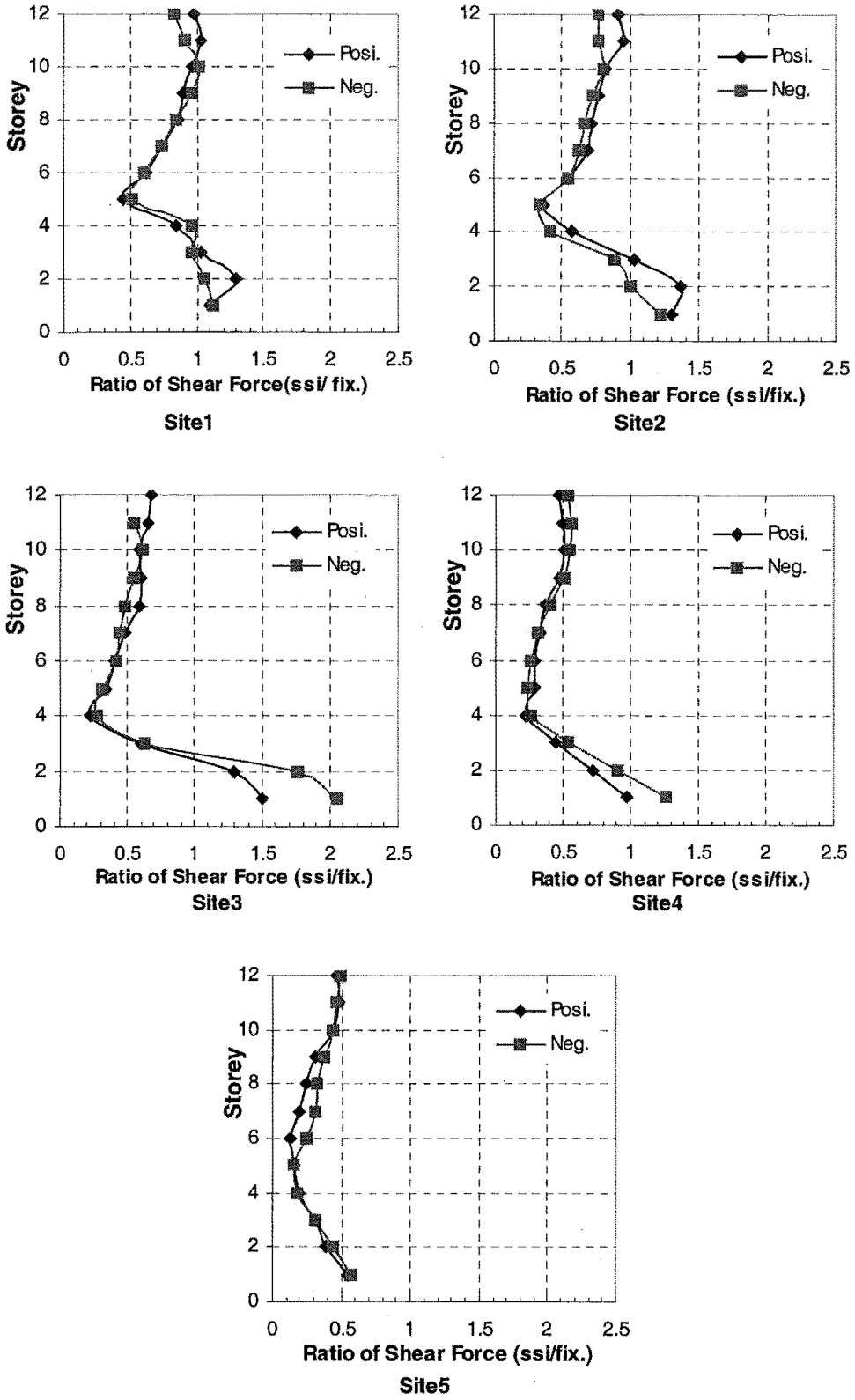

Figure 7.18 Ratio of the Inter-Storey Shear Forces of the Soil-Structure Interaction to the Fixed-Base from Site1 to Site5 for the Linear Analyses of the 12-Storey Frame

Posi: Positive Shear Force Neg: Negative Shear Force

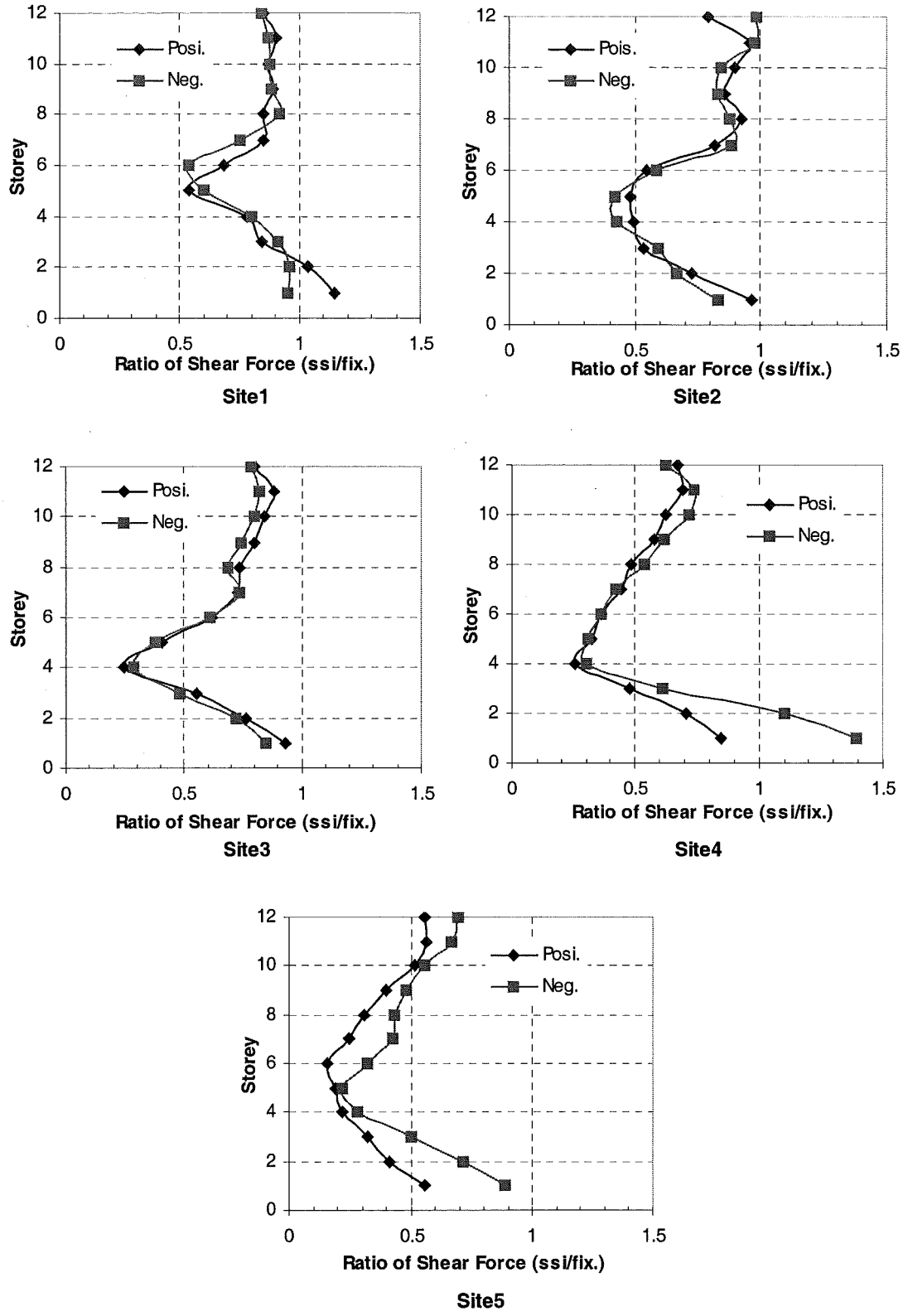

Figure 7.19 Ratio of the Inter-Storey Shear Forces of the Soil-Structure Interaction to the Fixed-Base from Site1 to Site5 for the Nonlinear Analyses of the 12-Storey Frame

Posi: Positive Shear Force Neg: Negative Shear Force

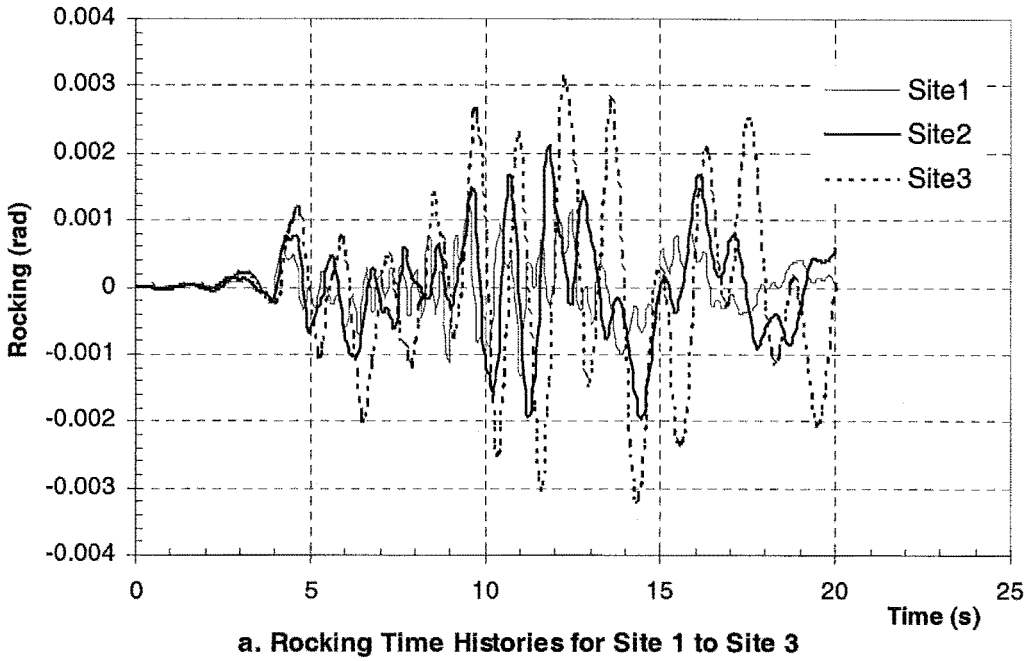

a. Rocking Time Histories for Site 1 to Site 3

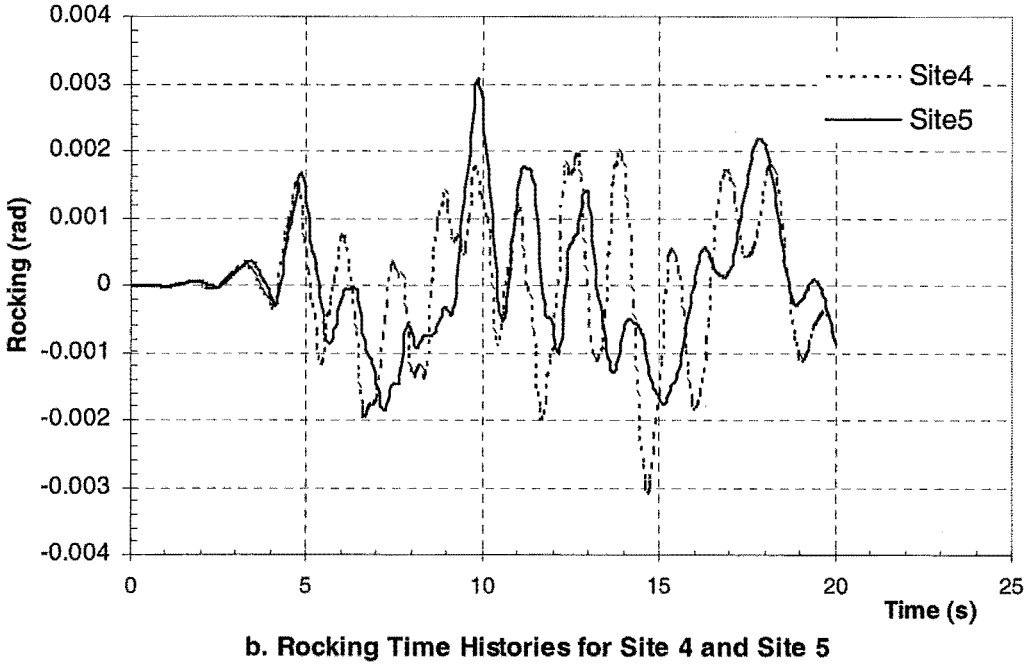

b. Rocking Time Histories for Site 4 and Site 5

Figure 7.20 The Rocking Time Histories from Site1 to Site5 for the Linear Analyses of the 12-Storey Frame

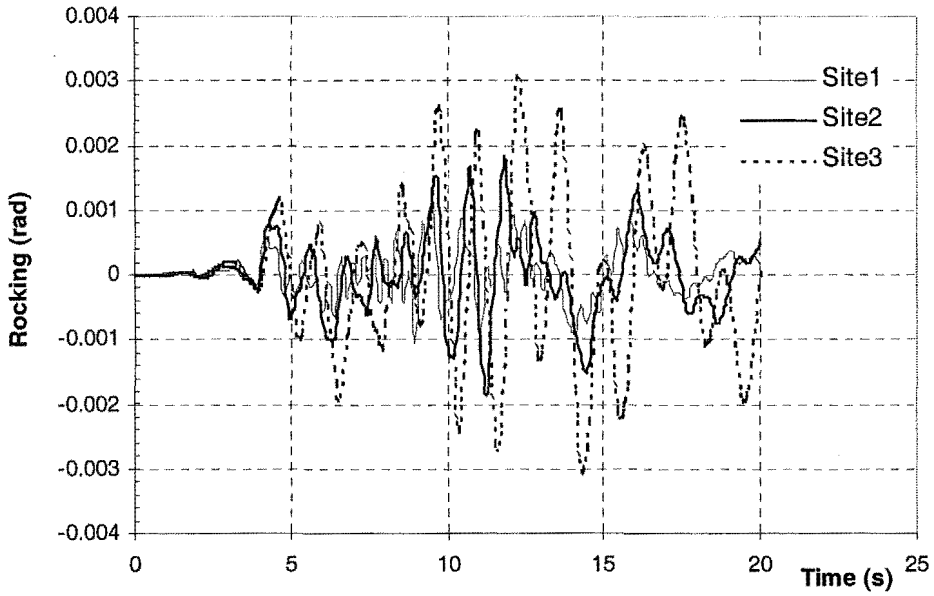

a. Rocking Time Histories for Site 1 to Site 3

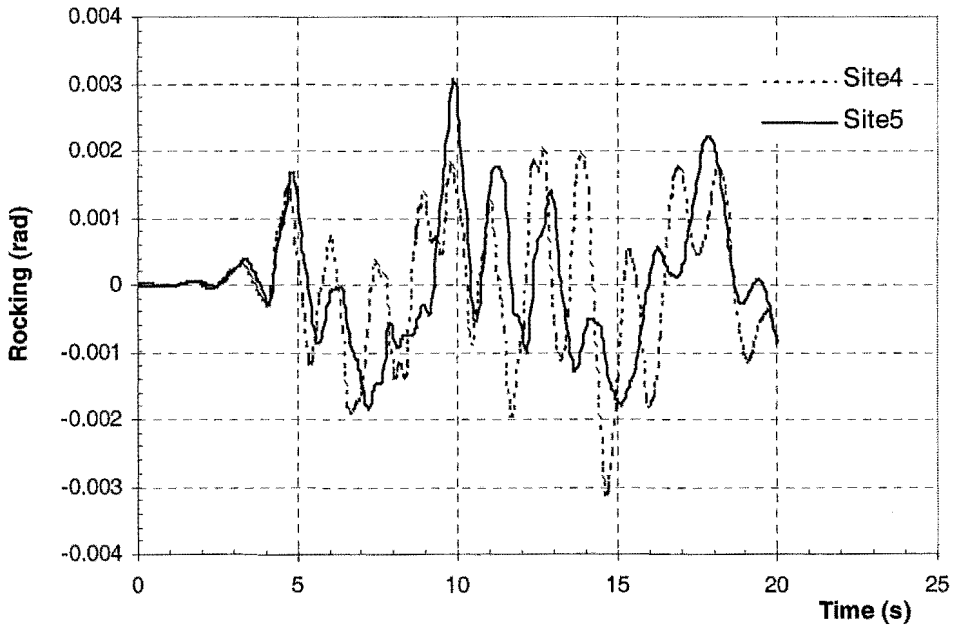

b. Rocking Time Histories for Site 4 to Site 5

Figure 7.21 The Rocking Time Histories from Site1 to Site5 for the Nonlinear Analyses of the 12-Storey Frame

7.3 The Mexico City Earthquake

The Mexico City earthquake of 19th September 1985 has had a great impact on the understanding of local site effects. Its main characteristics were small peak ground acceleration amplitude, narrow frequency range and long predominant period. Its influence on structures is investigated by considering the fixed-base and soil-structure interaction cases. The 6-storey and 12-storey frames are again used as the prototype structures in this investigation.

7.3.1 The 6-Storey Frame

The 6-storey frame employed is the same as in section 7.2.1. The steps of investigation are the same as was outlined in section 7.2.1.

7.3.1.1 The Effect of the Structure on the Ground Acceleration Response

In section 7.2.1.1, when the Loma Prieta earthquake of 19th October 1989 was used as an input motion from the basement rock to investigate the response of the 6-storey frame, the ground acceleration response at point O for the soil-structure interaction case is less than that for the free field case. When the Mexico City earthquake is used as an input motion from the basement rock, the acceleration spectra at point O for the free field and soil-structure interaction cases are shown in Fig.7.22. From the figure, it can be seen that at the natural vibration periods of the sites, the spectral accelerations at point O for the free field case are greater than or equal to those for the soil-structure interaction case. However, at the predominant period of the input motion, the spectral acceleration at point O for the free field case is less than that for the soil-structure interaction case. By comparing Fig.7.22 and Fig.7.4, these results can be easily explained as follows.

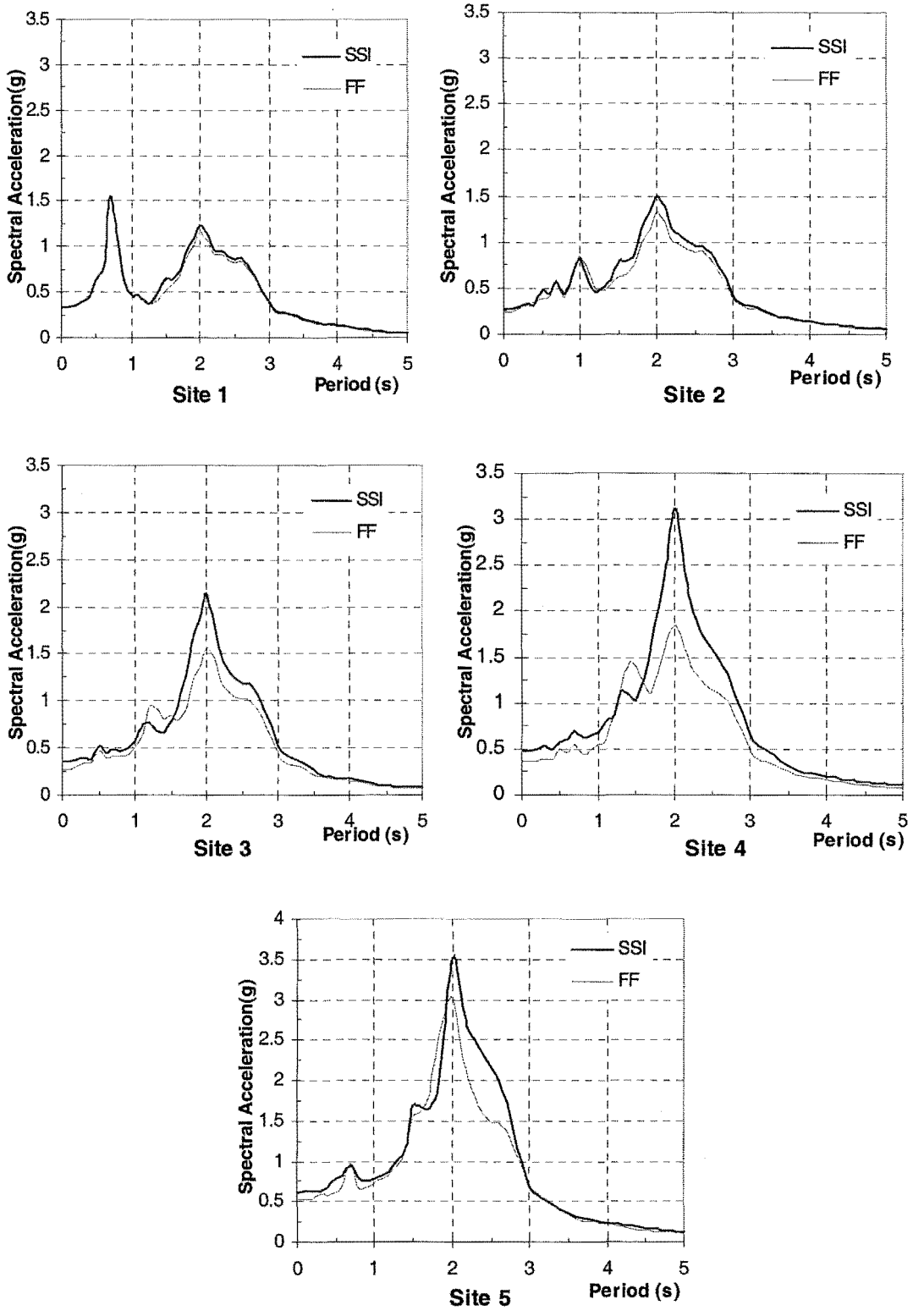

Figure 7.22 Comparison of the Acceleration Spectra between the Free Field and the Soil-Structure Interaction at Point O from Site1 to Site5 for the Linear Analyses

SSI: Soil-Structure Interaction FF: Free Field

The natural vibration periods of the sites and soil-structure systems are listed in Tables 7.1 and 7.2. The predominant period of the input motion is about 2.0s. These data show that the natural vibration periods of the soil-structure systems are close to the predominant period of the input motion, so at the predominant period of the input motion the spectral acceleration at point O for the free field case is less than that for the soil-structure interaction case. This result illustrates that the ground acceleration response at point O for the soil-structure interaction case is influenced by many factors, but the predominant period of an input motion, the natural vibration periods of a site and soil-structure system are the main factors.

When the structural model is nonlinear, the acceleration spectra at point O for the soil-structure interaction case from the linear and nonlinear analyses are shown in Fig.7.23. From the figure, it is seen that the spectral accelerations at point O from the linear analyses are greater than those from the nonlinear analyses. The reason is that due to the yielding of the structure, the natural vibration period of the soil-structure system is lengthened and moved away from the predominant period of the input motion.

7.3.1.2 Evaluation of the Structural Response

The same method is used as in section 7.2.1.2 to investigate the structural response for the fixed-base and soil-structure interaction cases. For the Mexico City earthquake, the displacement time histories at the top floor from site1 to site5 for the fixed-base and soil-structure interaction cases from the linear analyses are shown in Fig.7.24. For site1 to site3, the maximum displacements for the fixed-base case are greater than those for the soil-structure interaction case. For site4 and site5, however, the maximum displacements for the fixed-base case are less than those for the soil-structure interaction case. These characteristics are shown in Fig.7.24f. From this figure, it is seen that when T_{system}/T_{input} is greater than 0.92 for the soil-structure interaction case, the maximum displacement at the top floor increases significantly. For the fixed-base case, however, as T_{soil}/T_{input} increases, the maximum displacement only increases proportionally.

The displacement time histories at the top floor for the fixed-base and soil-structure interaction cases from the nonlinear analyses are shown in Fig.7.25. Although the maximum displacements for both cases are nearly the same, by comparing displacement time histories between both cases from site1 to site5, some differences can be seen. The first is that in the fixed-base case the structure clearly shows yielding, however in the soil-structure interaction case the structure does not clearly show yielding. The other difference is that although the maximum displacements are similar for both cases, their vibration time histories are different. In this case, the effect of the soil-structure interaction on the structural response shows different aspects of the structural response (normally the maximum displacement is used).

By comparing the displacement time histories in Figs. 7.25 and 7.7 under the Mexico City and the Loma Prieta earthquakes, the same characteristics can be found: the vibration amplitude of the displacement in the soil-structure interaction case is greater than that in the fixed-base case; also, the maximum displacements at the top floor from the nonlinear analyses are always equal to or less than those from the linear analysis.

In order to display the effect of soil-structure interaction on the inter-storey shear forces from the linear analyses, the ratio of inter-storey shear forces is used and shown in Fig.7.26. The inter-storey shear forces generated in the soil-structure interaction case are greater than those generated in the fixed-base case.

The ratio of inter-storey shear forces from the nonlinear analyses is shown in Fig.7.27 and indicates that the ratio is close to 1.0. These results are similar to those from the displacement analyses for the top floor, in which the maximum displacements for both cases are almost the same.

An important consideration in the study of soil-structure interaction is the rocking of the foundations. Rocking from the linear analyses is shown in Fig.7.28. From this figure, it is easy to see that for site1, site2 and site3, the rocking of the foundations is very small. However, for site4 and site5 the rocking of the foundations is much larger. In order to display the change of the maximum rocking of the foundations, the relationship between the maximum rocking and the ratio of the natural vibration

periods to the predominant period is plotted in Fig.7.29. From the figure, it is seen that when the natural vibration period of the system, $T_{system,}$ is close to the predominant period of the input motion, $T_{input,}$ the maximum rocking of the foundation increases. This result is similar to that shown in Fig.7.24f.

The rocking of the foundations from the nonlinear analyses is shown in Fig.7.30. When comparing Fig.7.30 with Fig.7.28, the vibration amplitudes of the rocking of the foundations in Fig.7.30 are considerably less than those in Fig.7.28. Fig.7.31 shows the change of the maximum rocking from the nonlinear analyses. It can be seen that no resonance occurs.

7.3.2 The 12-Storey Frame

The 12-storey frame is the same as was used in section 7.2.1.2. As in section 7.3.1, the effect of the structure on the ground acceleration response and the evaluation of the structural response will be investigated.

7.3.2.1 The Effect of the Structure on the Ground Acceleration Response

The acceleration spectra at point O for the free field and soil-structure interaction cases from the linear analyses are shown in Fig.7.32. For site1 and site2, the spectral accelerations for the free field case are slightly greater than those for the soil-structure interaction case. However, for site4 and site5, the spectral accelerations for the free field case are slightly less than those for the soil-structure interaction case.

The acceleration spectra from the linear and nonlinear analyses are shown in Fig.7.33. These indicate that there is little difference between the cases. This result illustrates that the structural material properties do not affect the ground acceleration response at point O.

7.3.2.2 Evaluation of the Structural Response

As in the earlier sections, the structural response is still described by the displacement at the top floor, the ratio of inter-storey shear forces and the rocking of the foundations. The displacement time histories at the top floor for the fixed-base and soil-structure interaction cases from the linear analyses are shown in Fig.7.34. From this figure, the maximum displacements at the top floor for site1 to site5 from the fixed-base case are greater than those from the soil-structure interaction case. For the fixed-base case, the maximum displacement increases quickly from site1 to site5. For the soil-structure interaction case, the difference of the maximum displacements from site1 to site5 is small. In order to explain the analytical results for the fixed-base case, it can be seen from Fig.7.32 that the spectral peak acceleration at the period of 2.0 seconds increases from site1 to site5 and these acceleration time histories have been used as the input motions of the fixed-base case. In this situation the structural resonance results in large displacements at the top floor. For the soil-structure interaction case, however, the natural vibration periods of the soil-structure systems for site1 to site5 listed in Table 7.3 are much greater than the predominant period of the input motion at the basement rock. Therefore, the displacement at the top floor for the soil-structure interaction case is much less than that for the fixed-base case.

Table 7.3 Natural vibration Periods of the Soil-Structure System

No.	Site1	Site2	Site3	Site4	Site5
System Period	3.28	3.759	4.306	4.727	5.466

The displacement time histories at the top floor for site1 to site5 from the nonlinear analyses are shown in Fig.7.35. When comparing Fig.7.35 with Fig.7.34, the difference between the maximum displacements at the top floor for the fixed-base and soil-structure interaction cases from the nonlinear analysis is less.

The above difference for the fixed-base case from site1 to site5 can be explained as follows: once the yielding of the structure occurs, its natural vibration period is lengthened. For different input motions due to the amplification of the sites, however, the period will increase by differing amounts. This results in the slight difference in the maximum displacements at the top floor from site1 to site5 for the fixed-base case.

The inter-storey shear force is an important index for assessing structural damage. Because the fixed-base case from the linear analysis is a special case (in that the predominant period of the input motion is close to the natural vibration period of the structure), its inter-storey shear force will not be discussed in this section. The ratio of the inter-storey shear forces from the nonlinear analyses is shown in Fig.7.36. The inter-storey shear forces for the fixed-base and soil-structure interaction cases are very close for site1 to site3. For site4 and site5, however, at the top of the structure the inter-storey shear force for the soil-structure interaction case is greater and at the lower part of the structure it is less. This result is different from that under the Loma Prieta earthquake that has a short predominant period. When compared with the results of the 6-storey frame from the nonlinear analyses in Fig.7.27, this result shows the effect of higher modes of the structure on the structural response.

The rocking of foundations from the linear analyses is shown in Fig.7.37. As the natural vibration period of the site is close to the predominant period of the input motion, the maximum rocking increases. The rocking from the nonlinear analyses is shown in Fig.7.38. When comparing the results shown in Fig.7.38 and in Fig.7.37, it can be noticed that the maximum rocking from the nonlinear analyses is smaller than that from the linear analyses. The result illustrates that the material nonlinearity of the structure has an influence on the response of the foundation. The reason can be explained as following: the hysteric damping in the structure dissipates more earthquake energy than only viscous damping in the linear elastic structure so that the response of the foundation is affected. By comparison with the results from the Loma prieta earthquake in Figs. 7.20 and 7.21, it can be seen that the input motions from the basement rock have a great influence on the response of the foundation in the case of the Mexico City earthquake.

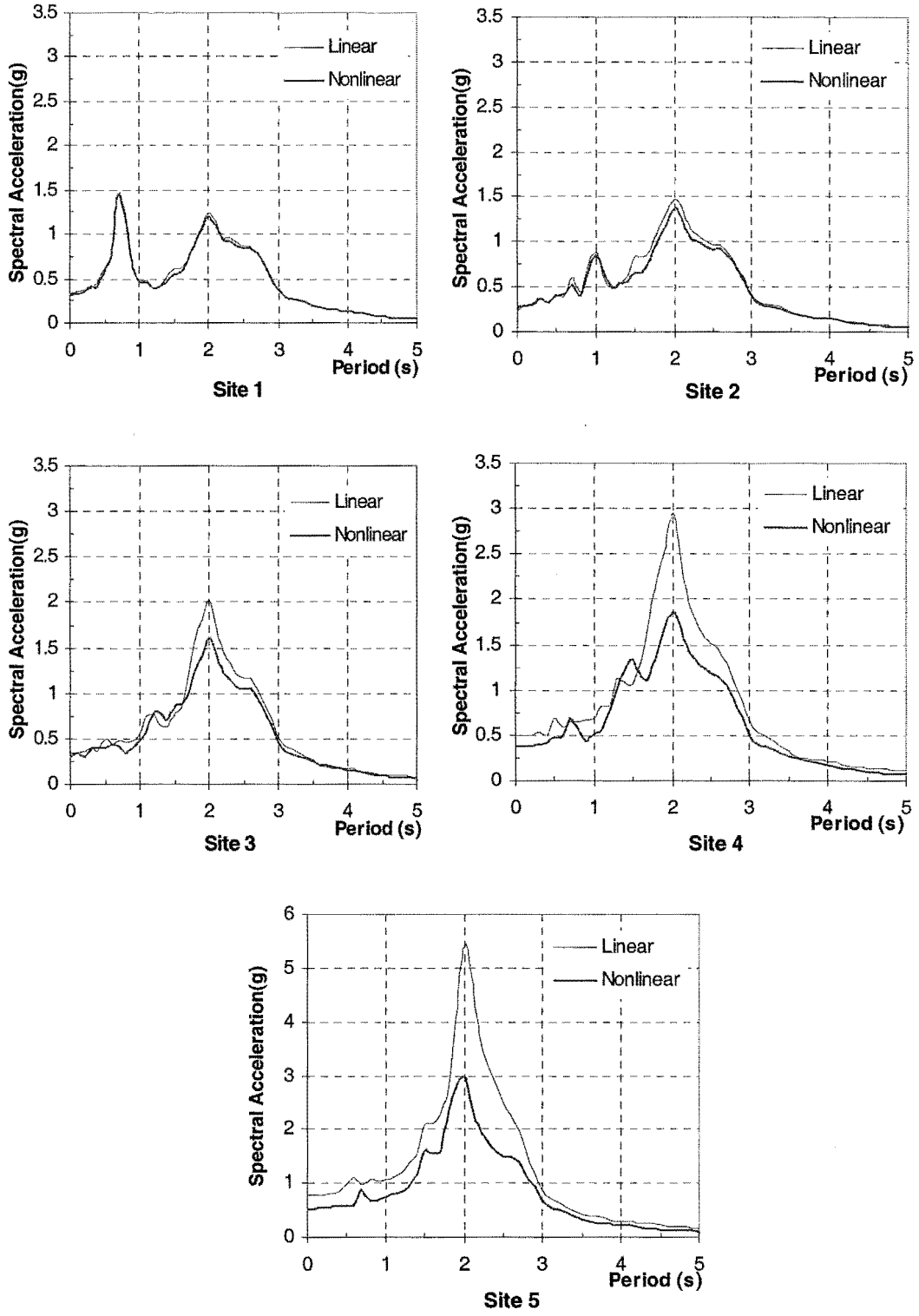

Figure 7.23 Comparison of the Acceleration Spectra of the Soil-Structure Interaction for the Linear and Nonlinear Analyses at Point O from Site1 to Site5 for the 6-Storey Frame

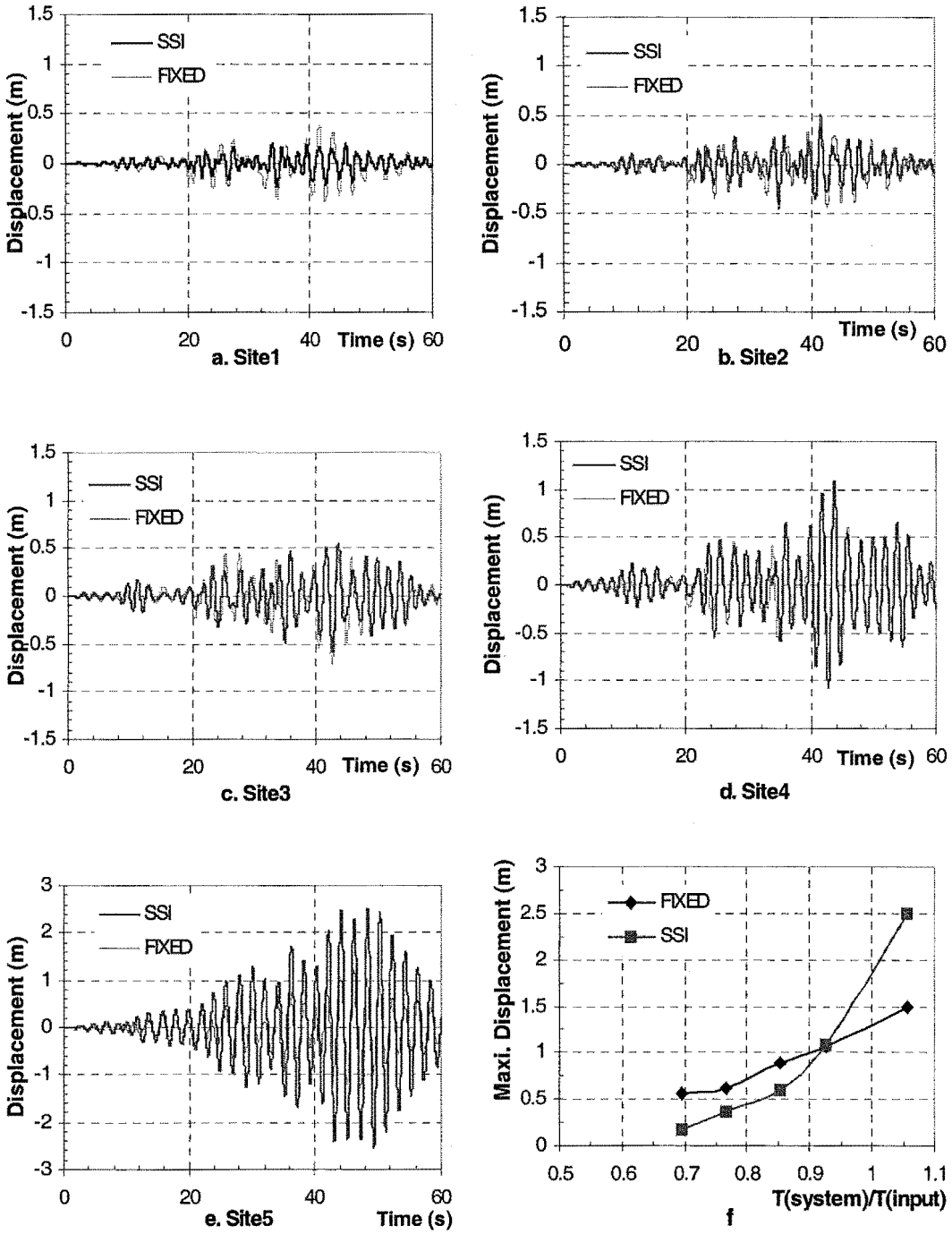

Figure 7.24 from a to e: Comparison of the Displacement Time Histories at the Top Floor for the Fixed-Base and the Soil-Structure Interaction from Site1 to Site5 for the Linear Analyses of the 6-Storey Frame

f: Relationship between the Maximum Displacement and the Ratio of the Fundamental Periods

SSI: Soil-Structure Interaction FIXED: Fixed-Base

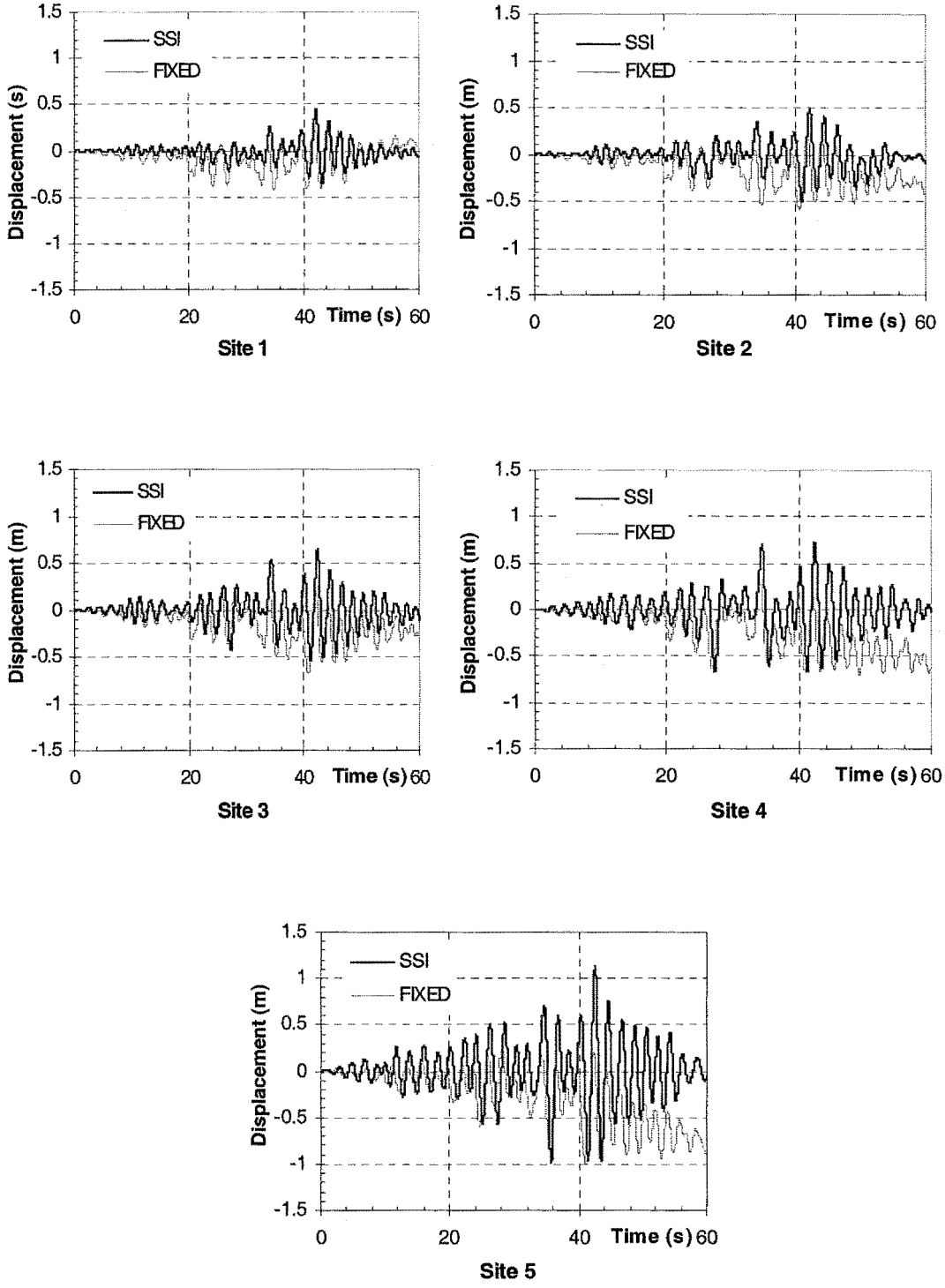

Figure 7.25 Comparison of the Displacement Time Histories at the Top Floor for the Fixed-Base and the Soil-Structure Interaction from Site1 to Site5 for the Nonlinear Analyses of the 6-Storey Frame

SSI: Soil-Structure Interaction FIXED: Fixed-Base

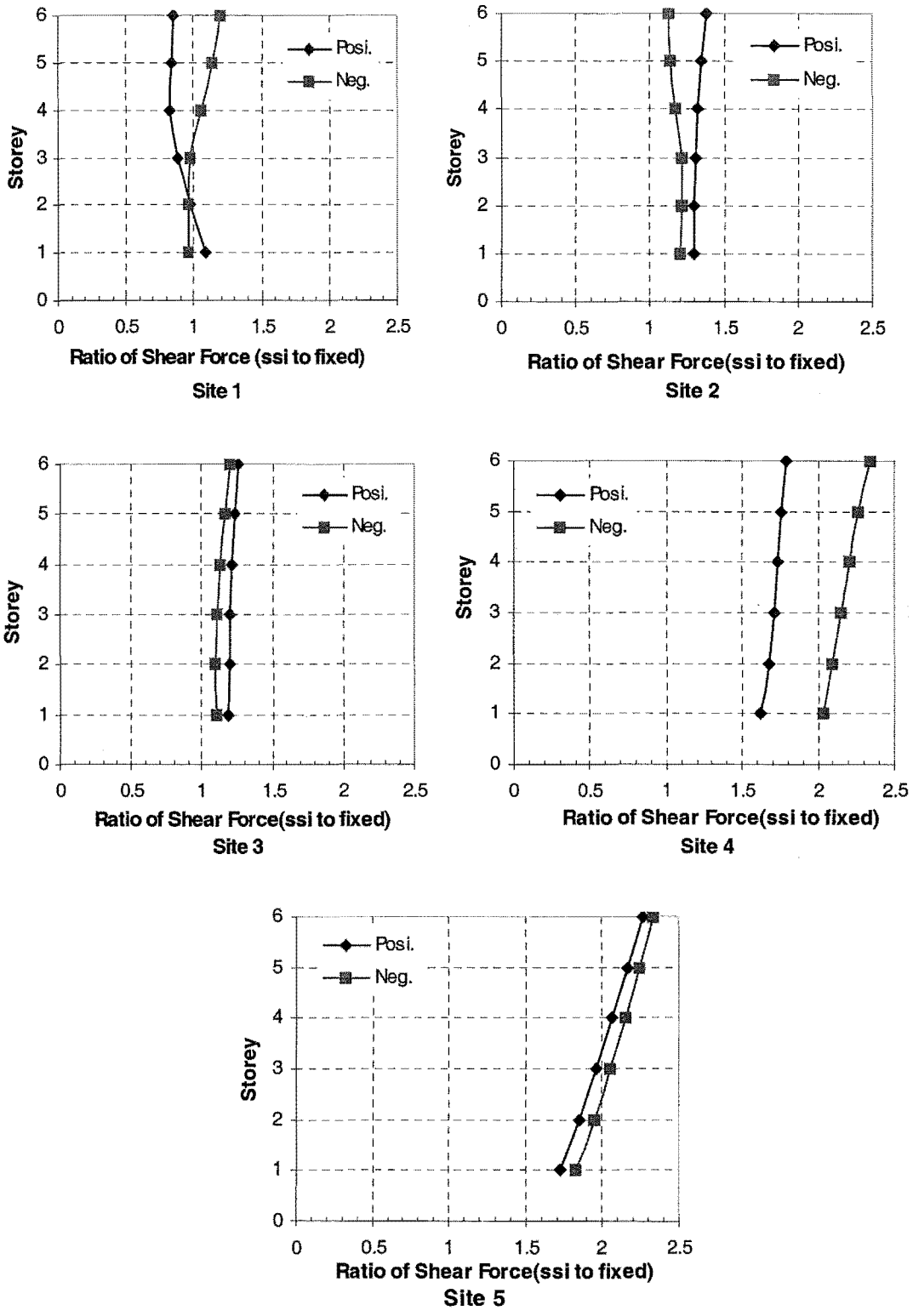

Figure 7.26 Ratio of the Inter-Storey Shear Forces of the Soil-Structure Interaction to the Fixed-Base from Site1 to Site5 for the Linear Analyses of the 6-Storey Frame

Posi: Positive Shear Force Neg: Negative ShearForce

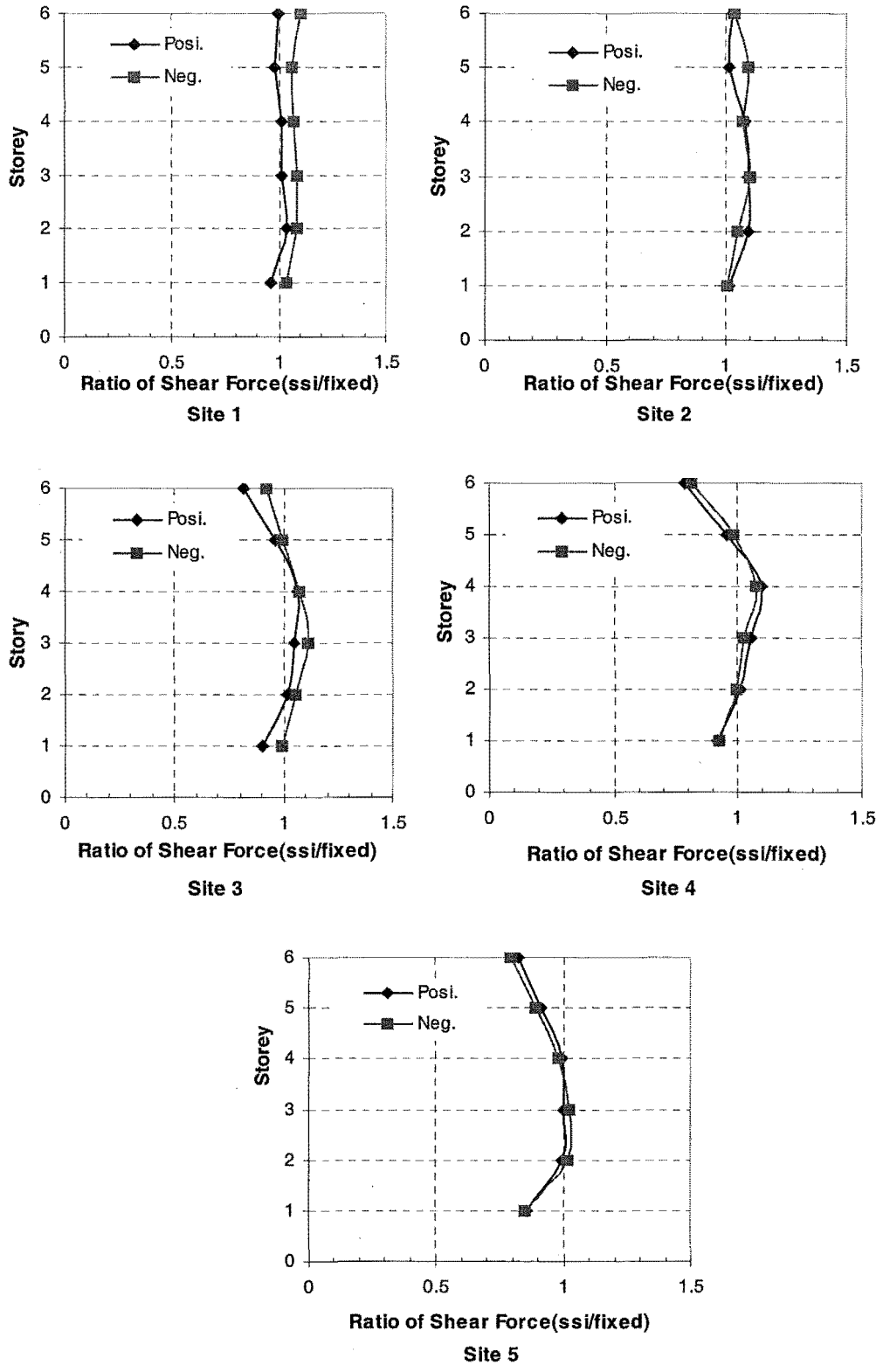

Figure 7.27 Ratio of the Inter-Storey Shear Forces of the Soil-Structure Interaction to the Fixed-Base from Site1 to Site5 for the Nonlinear Analyses of the 6-Storey Frame

Posi: Positive Shear Force Neg: Negative Shear Force

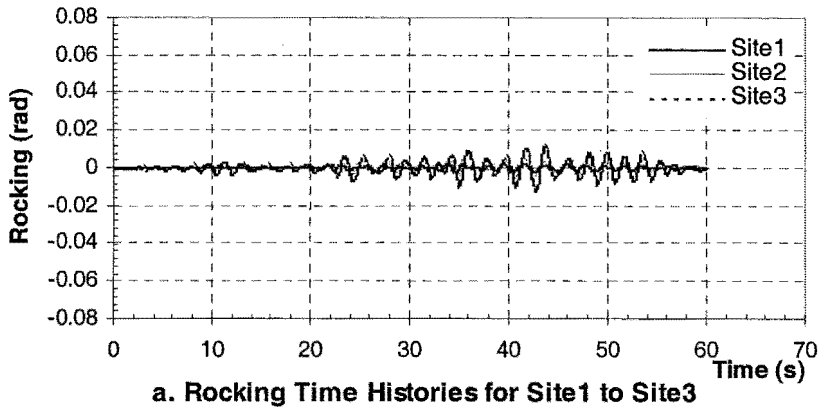

a. Rocking Time Histories for Site1 to Site3

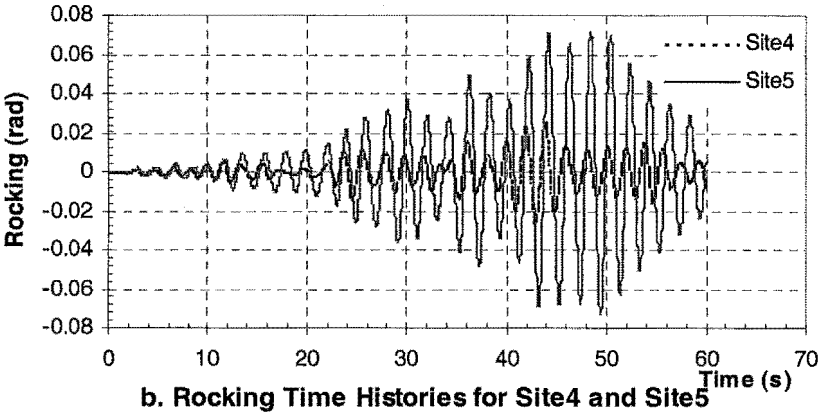

b. Rocking Time Histories for Site4 and Site5

Figure 7.28 The Rocking Time Histories from Site1 to Site5 for the Linear Analyses of the 6-Storey Frame

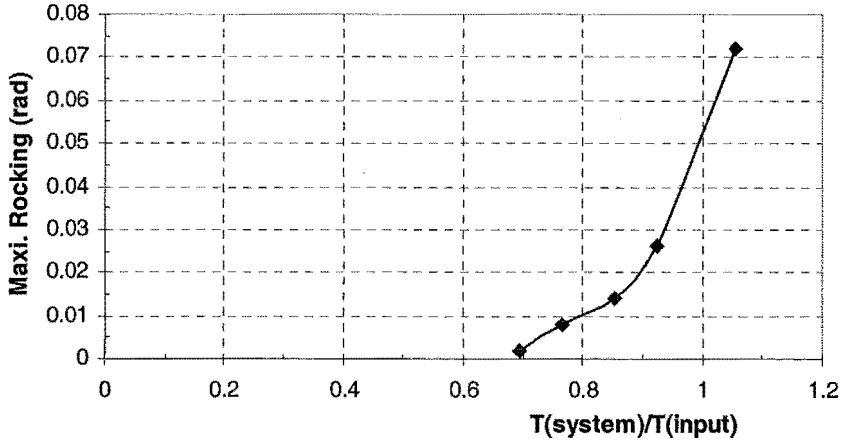

Figure 7.29 Ralationship between the Maximum Rocking and Ratio of the Natural Vibration Periods of the System to the Predominant Period for the Linear Analyses of the 6-Storey Frame

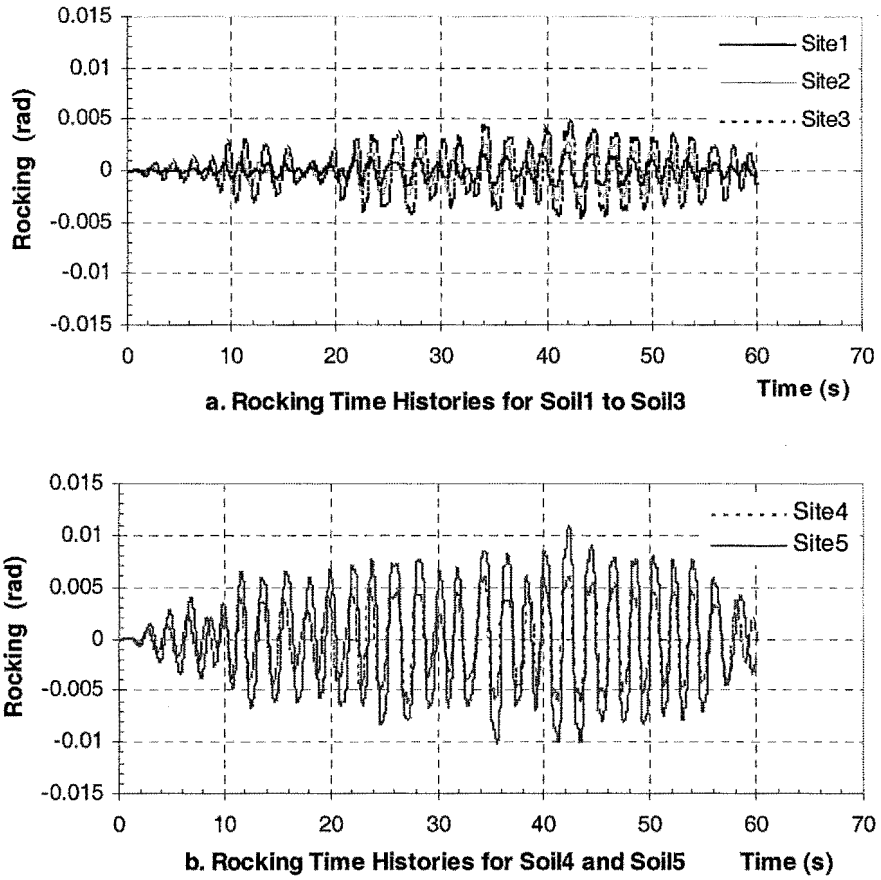

Figure 7.30 The Rocking Time Histories from Site1 to Site5 for the Nonlinear Analyses of the 6-Storey Frame

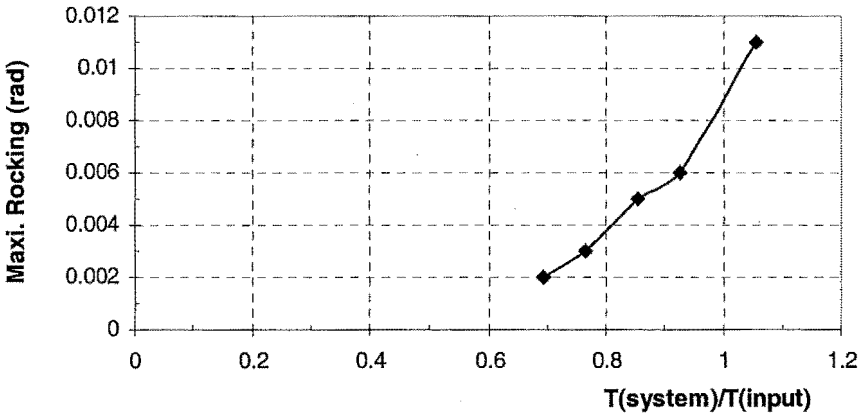

Figure 7.31 Ralationship between the Maximum Rocking and Ratio of the Natural Vibration Periods of the System to the Predominant Period for the Nonlinear Analyses of the 6-Storey Frame

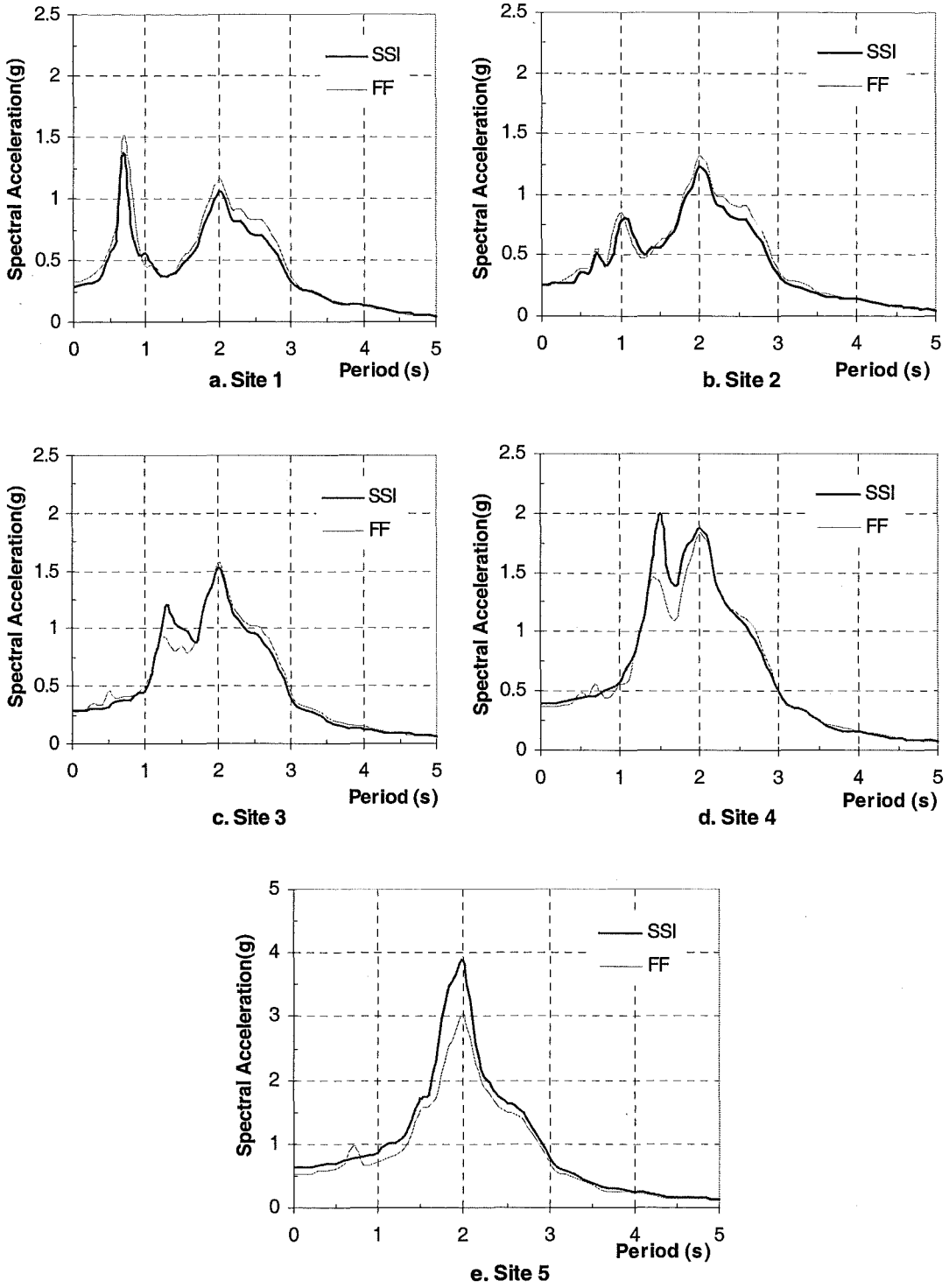

Figure 7.32 Comparison of the Acceleration Spectra for the Free Field and the Soil-Structure Interaction at Point O from Site1 to Site5 for the Linear Analyses of the 12-Storey Frame

SSI: Soil-Structure Interaction FF: Free Field

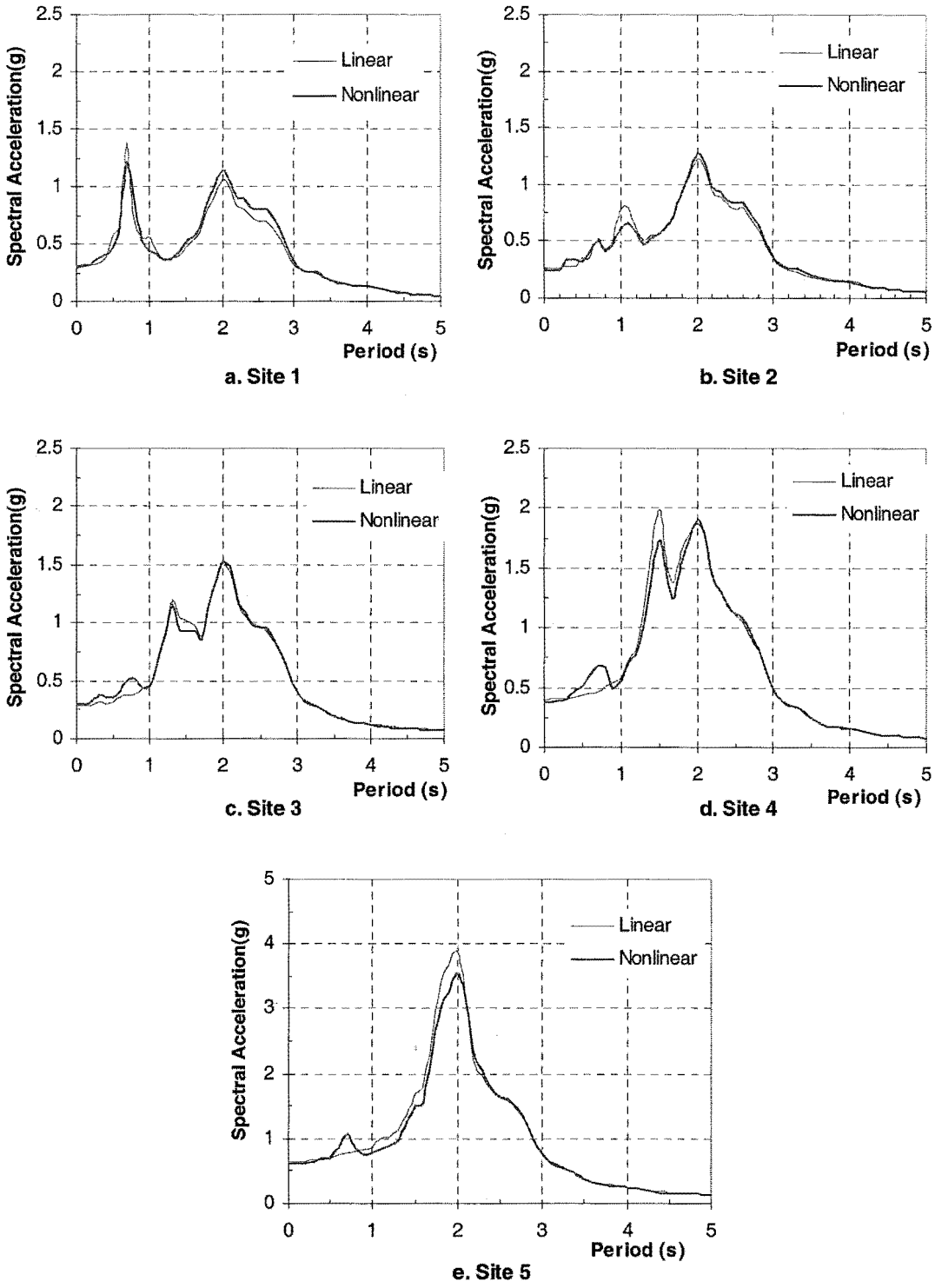

Figure 7.33 Comparison of the Acceleration Spectra of the Soil-Structure Interaction for the Linear and Nonlinear Analyses at Point O from Site1 to Site5 for the 12-Storey Frame

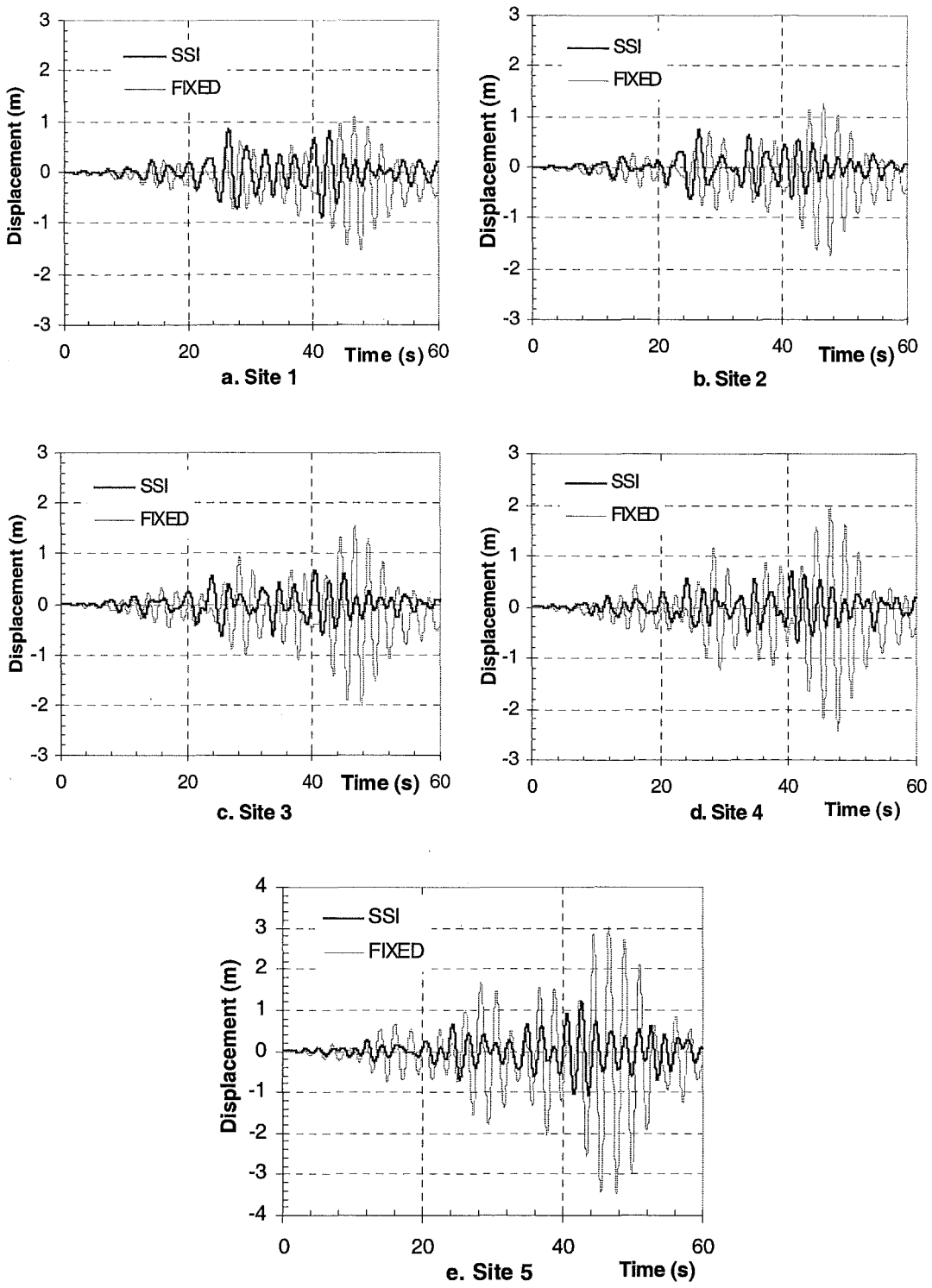

Figure 7.34 Comparison of the Displacement Time Histories at the Top Floor for the Fixed-Base and Soil-Structure Interaction from Site1 to Site5 for the Linear Analyses of the 12-Storey Frame

FIXED: Fixed-Base SSI: Soil-Structure Interaction

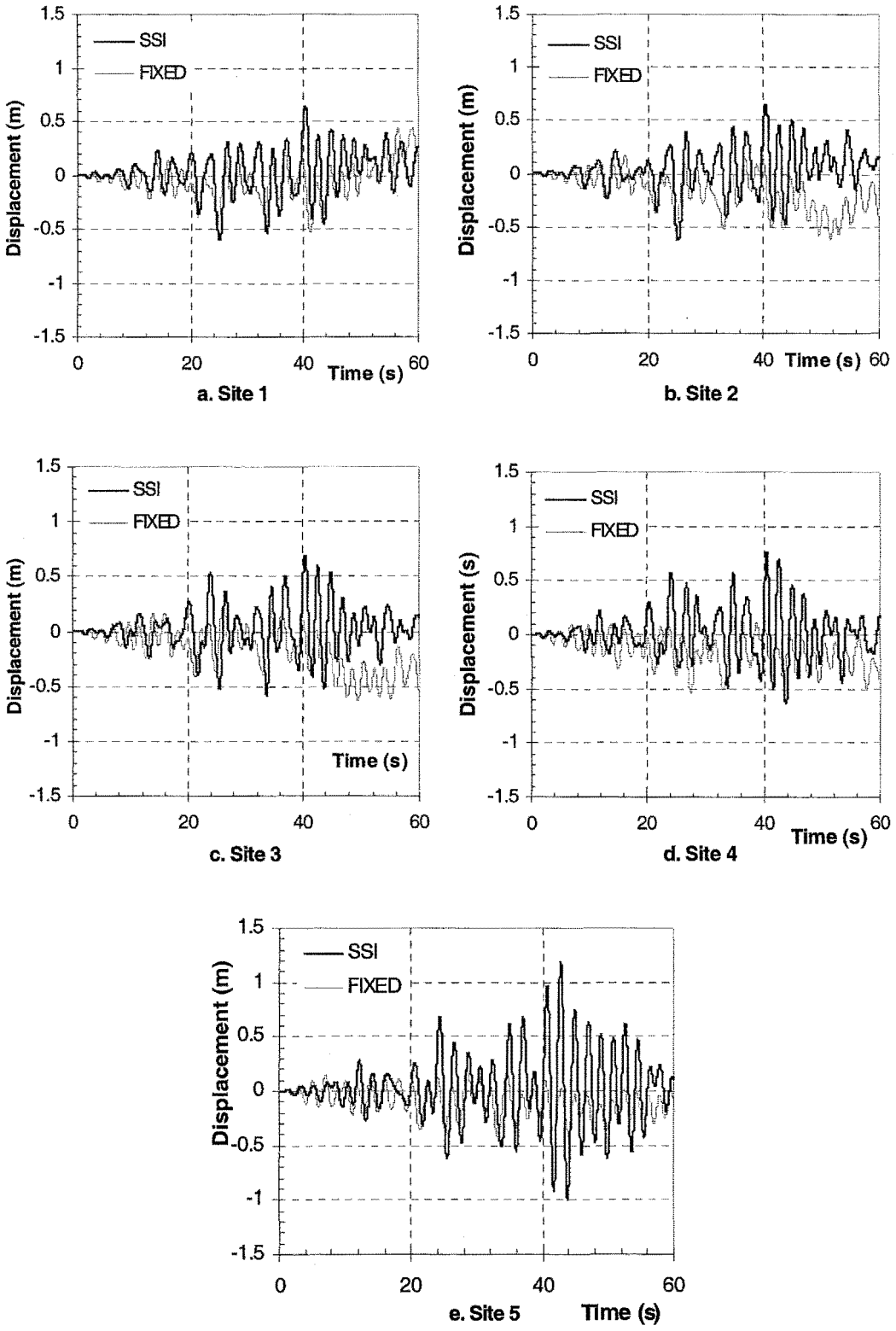

Figure 7.35 Comparison of the Displacement Time Histories at the Top Floor for the Fixed-Base and Soil-Structure Interaction from Site1 to Site5 for the Nonlinear Analyses of the 12-Storey Frame

FIXED: Fixed-Base SSI: Soil-Structure Interaction

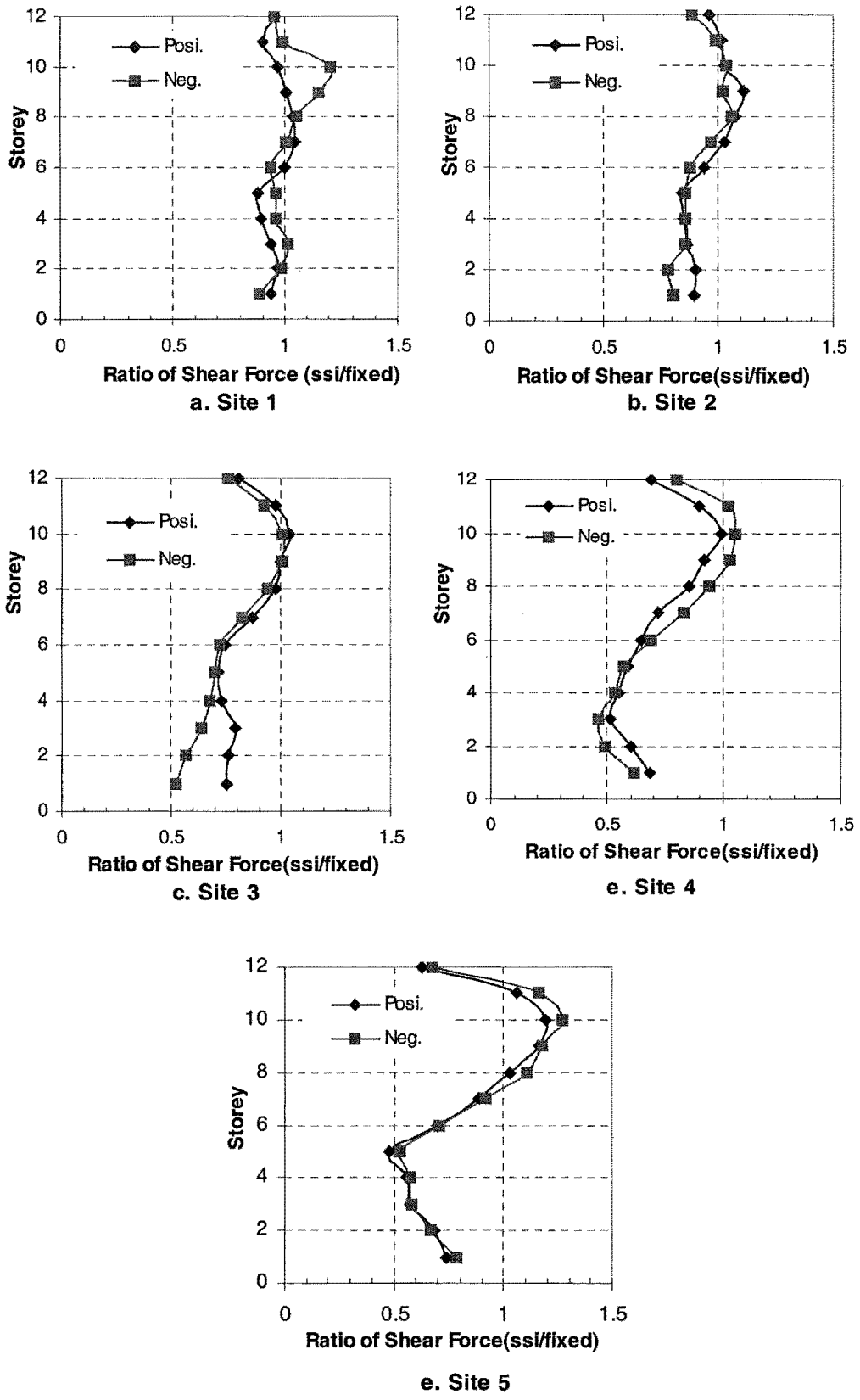

Figure 7.36 Ratio of the Inter-Storey Shear Forces of the Soil-Structure to the Fixed-Base from Site1 to Site5 for the Linear Analyses of the 12-Storey Frame

Posi: Positive Shear Force Neg: Negative Shear Force

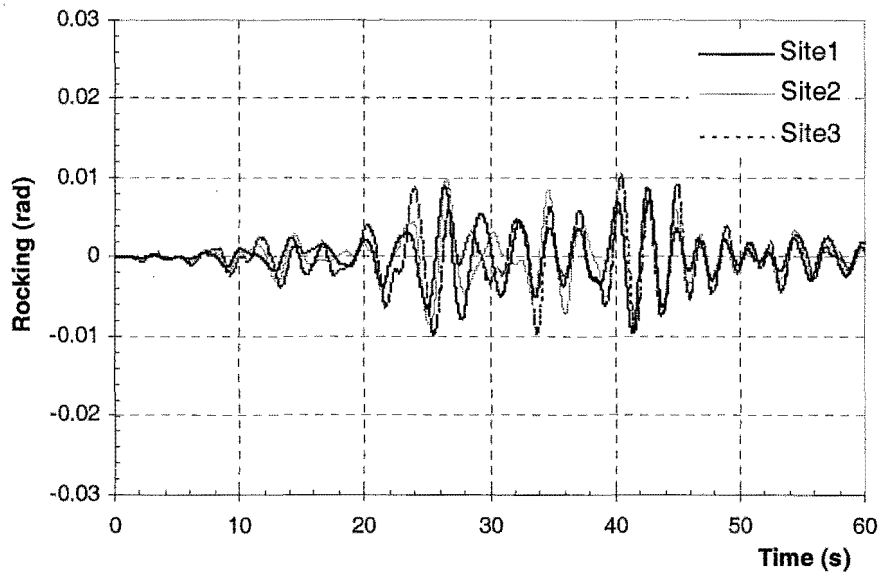

a. Rocking Time Histories for Site1 to Site3

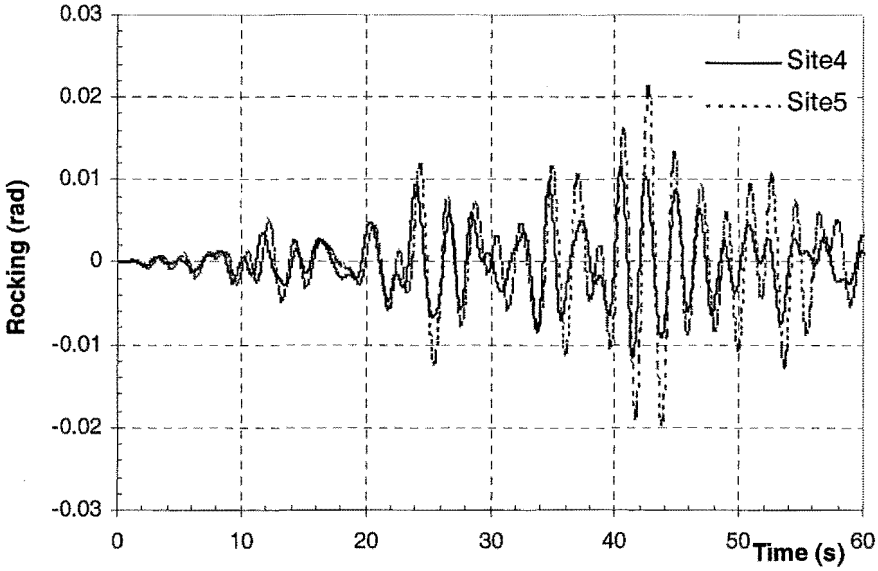

b. Rocking Time Histories for Site4 and Site5

Figure 7.37 Rocking Time Histories of the Foundation from Site1 to Site5 for the Linear Analyses of the 12-Storey Frame

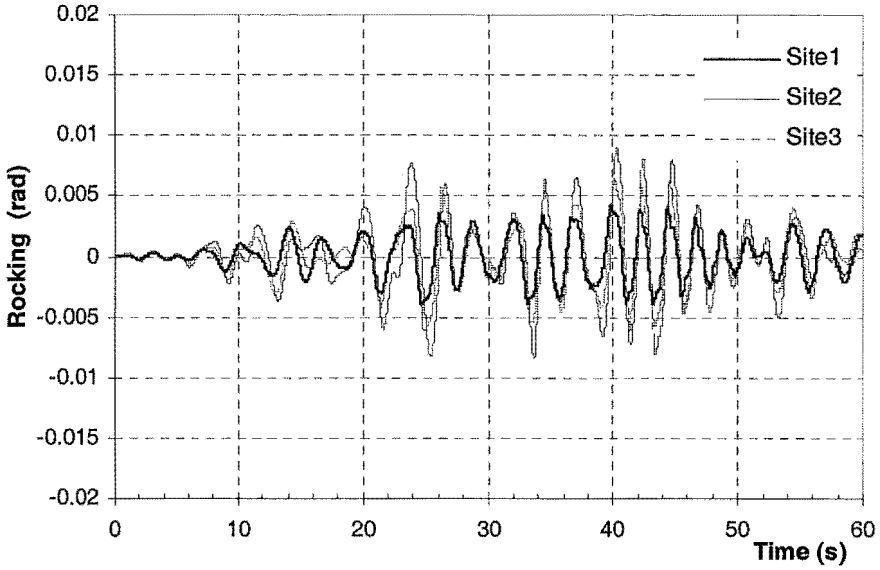

a. Rocking Time Histories for Site1 to Site3

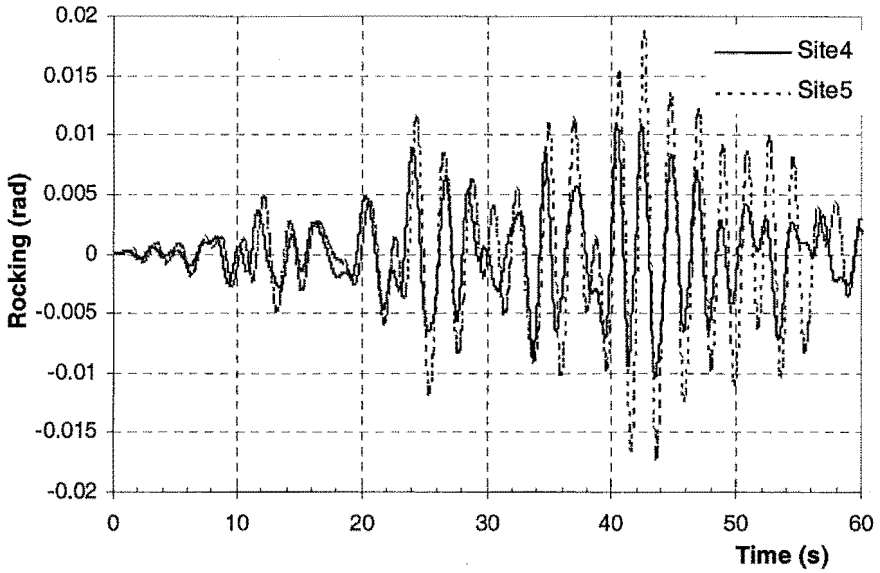

b. Rocking Time Histories for Site4 and Site5

Figure 7.38 Rocking Time Histories of the Foundation from Site1 to Site5 for the Nonlinear Analyses of the 12-Storey Frame

7.4 Summary

The effect of soil-structure interaction on the structural response is very important in structural design. Its effect, however, can be different depending on the site, structure and input motion. In order to display the effect of these factors on soil-structure interaction, five different sites, two earthquake records and two multi-storey frames were selected. Their natural periods of free-vibration are shown in Figs. 7.39a and b:

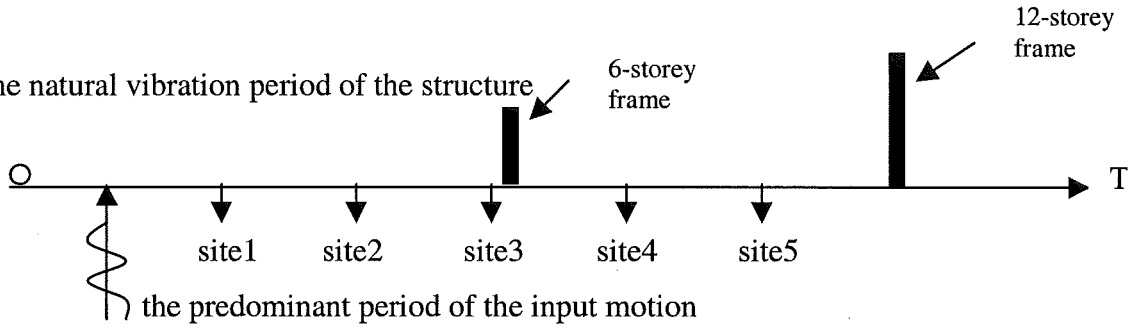

(a) comparison of periods between the predominant period of the Loma Prieta earthquake, the natural vibration period of free vibration of the 6-storey frame, the natural vibration period of the sites

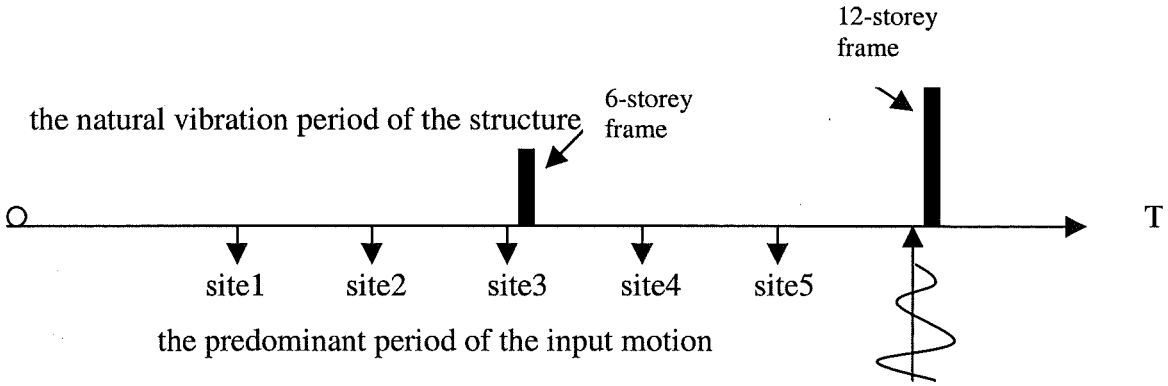

(b) comparison of periods of the Mexico City earthquake, the 6-storey frame, the 12-storey frame and the five different sites

Fig. 7.39 Relative position of periods for the predominant period of the input motion, the natural vibration period of the structure and the five different sites

From the above analyses, it is obvious that the effect of soil-structure interaction on the structural response is mainly controlled by the predominant period of an input motion from the basement rock and the natural vibration periods of both site and structure. The yielding of the structure also affects the structural response. Some effects of these factors to soil-structure interaction can be noted:

The first is the ground acceleration response at point O. Normally the spectral acceleration of the ground acceleration response at point O for a soil-structure interaction case is less than that for a free field, but when the natural vibration periods of the site or the predominant period of an input motion from the basement rock is equal to the natural vibration period of the structure, the spectral acceleration of the ground acceleration response at point O for the soil-structure interaction will be greater than that for the free field. This result illustrates that the structure has an effect on the ground acceleration response at point O. When the natural vibration period of the site differs significantly from the predominant period of the input motion, the spectral peak acceleration of the free field or ground acceleration response at point O will gradually reduce.

All cases investigated show that structural material non-linearity has little influence on the ground acceleration response at point O, except for the case of structural resonance.

The effect of soil-structure interaction on structural response is influenced by many parameters. Some results are listed in the following to show their influence. For the Jury 6-storey frame from the linear analysis, the maximum displacement at the top floor for the soil-structure interaction case is less than that for the fixed-base case under the Loma Prieta earthquake. However, under the Mexico City earthquake, the maximum displacement at the top floor for the soil-structure interaction case is greater than that for the fixed-base case. Similar results for the inter-storey shear force from the nonlinear analysis were observed. However, for the Loma Prieta earthquake and the Mexico City earthquake, the Jury 12-storey frame shows different responses as shown in Figs. 7.17 and 7.35 for the linear analysis. For the Loma Prieta earthquake, the maximum displacements at the top floor for the soil-structure interaction case and the fixed-base case are nearly the same. However, for the Mexico City earthquake,

results from the linear analysis for the fixed-base case are much greater than that for the soil-structure interaction case. The above results show that soil-structure interaction has a significant influence on structural response and is mainly controlled by the predominant period of the input motion and the natural vibration period of the site and structure. Therefore the effect of soil-structure interaction on the structural response is different for different sites, different structures and different earthquakes.

The effect of soil-structure interaction on the structural response is not only shown in the displacements on the top floor, but also shown in the inter-storey shear forces. Therefore, the inter-storey shear force is an important parameter to show the effect of soil-structure interaction.

Rocking of a foundation is an important factor in the effect of soil-structure interaction on the structural response. In this investigation, the rocking time history shows similar characteristics to the displacement time history at the top floor. This is to be expected because of the rigid body rocking mode of the structure and this is a direct correlation with the top floor displacement.

The yielding of the structure can change the structural response and reduce the effect of the structural resonance.

Chapter Eight

Investigation of Seismic Soil-Structure Interaction Using a Bounding Surface Soil Model

8.1 Introduction

In Chapter 7, the effect of soil-structure interaction on the structural response was investigated in detail by using a linear elastic soil model and some observations were made concerning those results. However, nonlinear soil behaviour has been observed in many earthquakes, for example: the Northridge earthquake of 1994 and the Kobe earthquake of 1995 and the results from laboratory tests as shown in Chapter 3 have confirmed that when the strain exceeds 10^{-4}, soil will show a nonlinear behaviour.

In order to show the effect of nonlinear soil properties on the structural response, the bounding surface model introduced in Chapter 3 is used to represent the soil behaviour in the near field. A linear elastic model is used to represent the behaviour of the structure. The 6-storey and 12-storey frames introduced in Chapter 7 are used again to investigate these structural responses. Their natural vibration periods are 1.14s and 2.24s. Element meshes of both the soil and structure are shown in Appendices 2 and 3. The Loma Prieta and the Mexico City earthquakes introduced in Chapters 6 and 7 are used as input motions from the basement rock. Their acceleration time histories and acceleration spectra have been shown in Figs. 6.1 and 7.2 respectively.

As discussed in Chapter 6, a strong bedrock shaking will tend to generate strong nonlinear soil behaviour. A weak bedrock shaking can be, however, approximated by a linear elastic analysis. In this investigation, a selected motion that is in between the above two states will be used, that is the acceleration time histories of the Loma Prieta and the Mexico City earthquakes scaled by a factor of 4. The results show the predominant periods are unchanged for these input motions.

Parameters used in the bounding surface model for this site are listed in Table 8.1. In order to determine the pre-consolidation pressure, the water table is assumed to lie at ground surface, the static earth pressure coefficient is 0.5 and a normal consolidated soil is considered. From the above assumptions, the pre-consolidation pressure and effective normal stresses at different Gauss integration points can be determined.

Table 8.1

λ	κ	N_c	N_e	R_c	A_c	T	C	H_c	H_e	ν	Void ratio
0.29	0.04	0.26	0.21	2.0	0.4	0.01	0.3	6.0	6.0	0.3	1.04

In the aforementioned models, the finite element method is employed to simulate the near field soil and the structure. The boundary element is used as a transmitting boundary to simulate the far field soil. An assumption for the linear and homogeneous far field domain is therefore introduced into the calculation. In this study, only a vertically propagating SH wave and a surface foundation are considered.

The purpose in this study is to investigate the effect of the nonlinear soil behaviour on the structural response, so a comparison between the linear and nonlinear soil-structure interaction analyses is carried out. The effects of the structure on the ground response for both the linear and nonlinear analyses are illustrated by acceleration spectra at the foundation level. The effects of both the linear and nonlinear soil models on the structural response are represented by the acceleration and displacement time histories at the top floor and the permanent settlement of the foundation.

8.2 The Scaled Loma Prieta Earthquake

The effect of the soil-structure interaction for the 6-storey and 12-storey frames is investigated when they are subjected to the scaled Loma Prieta earthquake. The first investigation is the effect of the structure on the ground response when the linear and nonlinear soil models are considered. The other investigations involve the effects of the linear and nonlinear soil models on the structural response. From Chapter 7, it was

found that the predominant period of the input motion from the basement rock and the natural vibration periods of the site and structure have an important influence on the response of structures. In this Chapter, the effect of these periods will be investigated again.

8.2.1 The Effect of the Structure on the Ground Response

Fig.8.1 shows the acceleration spectra at the foundation level for the 6-storey and 12-storey frames from the linear and nonlinear analyses.

By comparing these results from the linear and nonlinear analyses in Fig.8.1a, it is observed that the nonlinear analysis has an amplified spectral acceleration at the natural vibration period of the structure. When the natural period in Fig.8.1a exceeds about 0.75s, the spectral acceleration from the nonlinear analysis is larger than that from the linear analysis. This result shows that the nonlinear analysis reduces the acceleration vibration frequency of the soil-structure system when compared to the results from the linear analysis. From Fig.8.1a, it was also found that the spectral peak accelerations for the linear analysis is at about the predominant period of the input motion from the basement rock and the natural vibration period of the site. The spectral peak accelerations for the nonlinear analysis is, however, at the natural vibration period of the structure and the periods of the high modes of free vibration of the site.

By comparing the linear and nonlinear analyses in Fig.8.1b, when the period in the acceleration spectrum is over about 0.9s, the spectral acceleration from the nonlinear analysis is greater than that from the linear analysis, however when compared to Fig.8.1a, the difference is not large. The reason is that the natural vibration period of the 12-storey frame is 2.24s which is much longer than the predominant period of the input motion from the basement rock and the natural vibration period of the site for the nonlinear analysis.

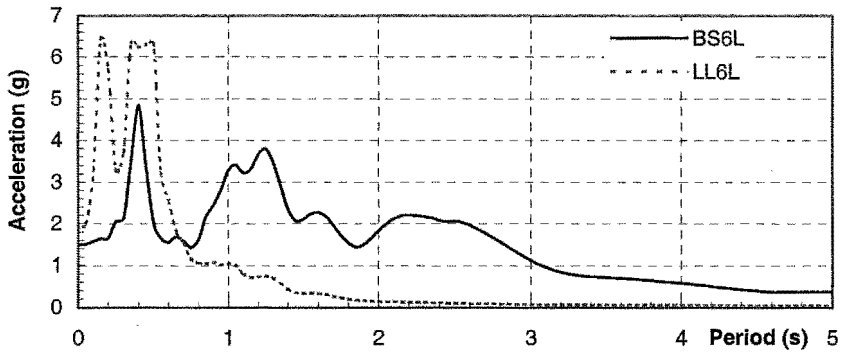

a. Comparison of Acceleration Spectra between the Linear and Nonlinear Analyses for the 6-Storey Frame

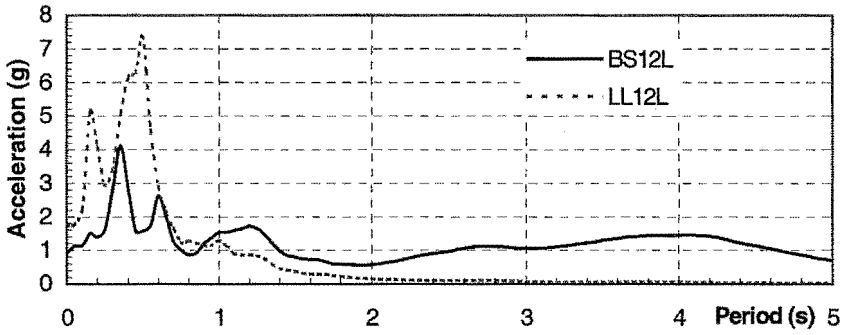

b. Comparison of Acceleration Spectra between the Linear and Nonlinear Analysis for the 12-Storey Frame

Figure 8.1 Comparison of Acceleration Spectra for the linear and Nonlinear Analyses at the Foundation Level for the 6-Storey and 12-Storey Frames under the Loma Prieta Earthquake

BS – bounding surface model; LL – linear elastic model

In order to illustrate the responses at the foundation level for the 6-storey and 12-storey frames from the linear and nonlinear analyses, the acceleration and displacement time histories are shown in Figs. 8.2 and 8.3. From these figures, it can be seen that the maximum displacements from the nonlinear analyses are greater than those from the linear analyses and the maximum accelerations from the nonlinear

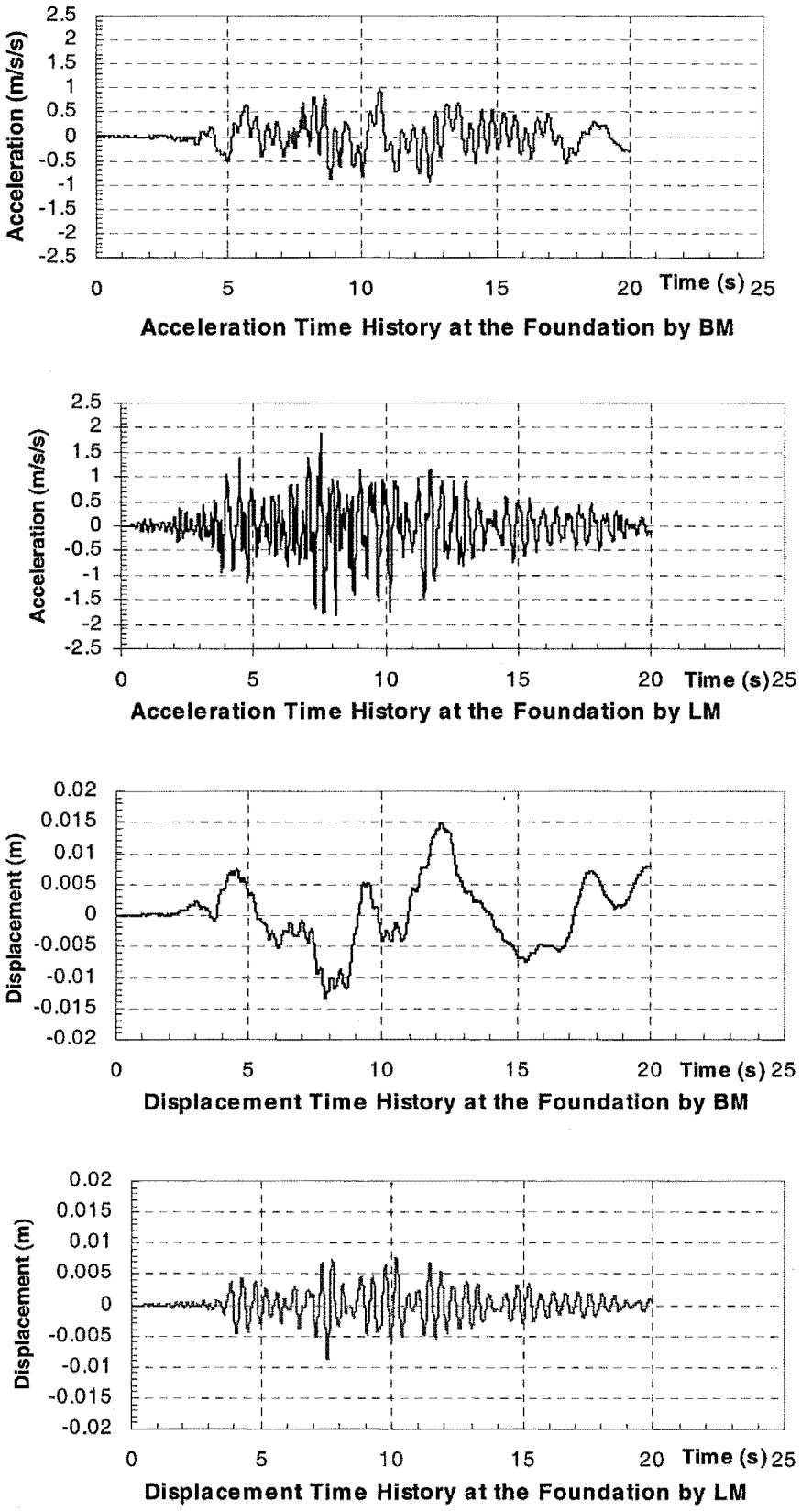

Figure 8.2 The Acceleration and Displacement Time Histories at the Foundation Level for the 6-Storey Frame under scaled Loma Prieta Earthquake

BM: Bounding Surface Soil Model LM: Linear Elastic Soil Model

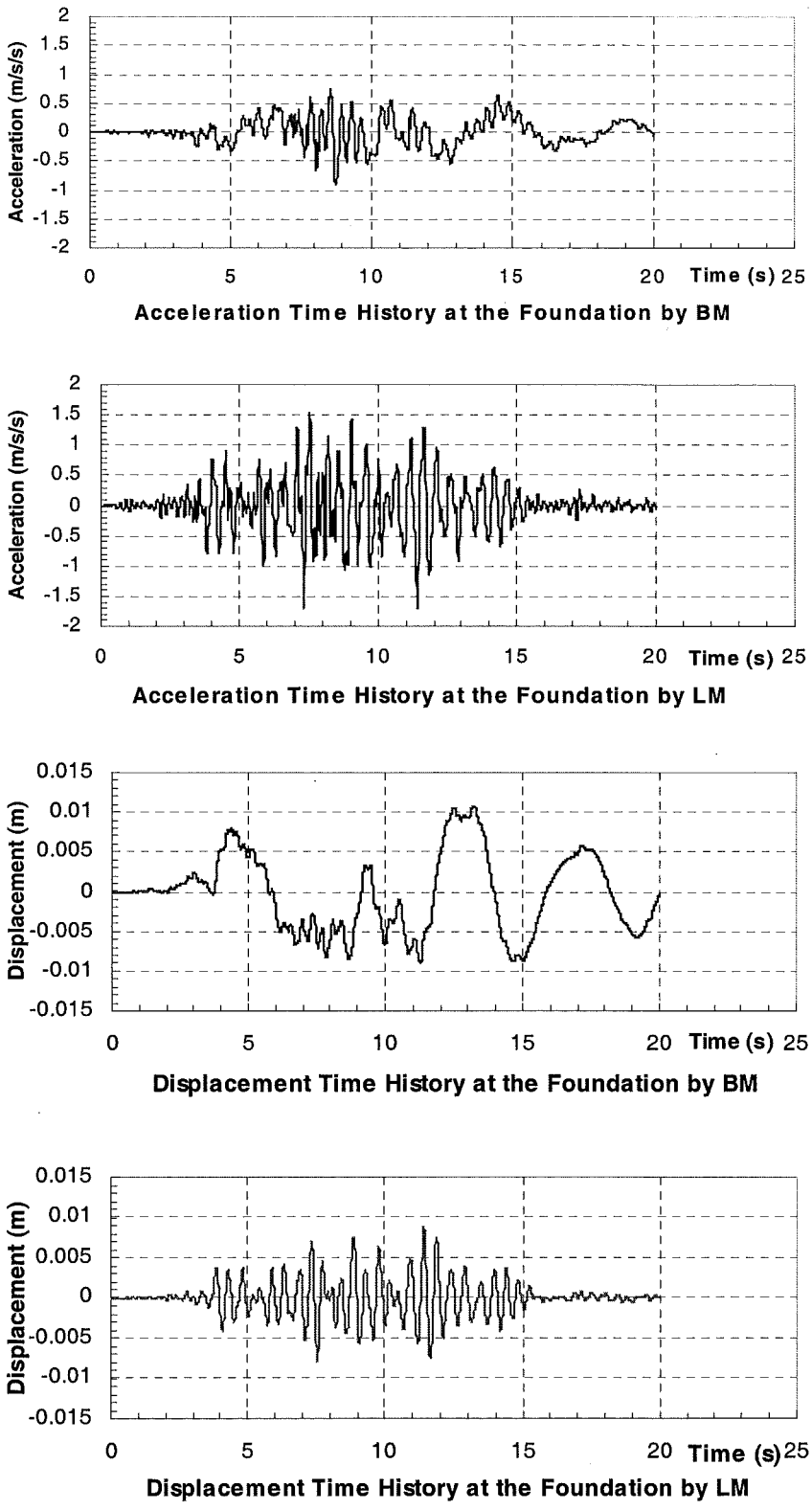

Figure 8.3 The Acceleration and Displacement Time Histories at the Foundation Level for the 12-Storey Frame under scaled Loma Prieta Earthquake
BM: Bounding Surface Soil Model LM: Linear Elastic Soil Model

analyses are less than those from the linear analyses. Figs. 8.2 and 8.3 also show that the acceleration vibration frequency from the nonlinear analyses is lower than that from the linear analyses. By comparing the results from Figs. 8.2 and 8.3 for the linear and nonlinear analyses, it is seen that the difference between the responses for the nonlinear and linear analyses is mainly due to the yielding of the soil.

8.2.2 The Effect of the Bounding Surface Soil Model on the Structural Response

The effect of the nonlinear soil model on the structural response is investigated in this section for two aspects. One aspect is the horizontal displacement and acceleration at the top floor. The other aspect is the permanent settlement of the foundation.

The horizontal displacement and acceleration time histories at the top of floor are shown in Figs. 8.4 and 8.5. For the 6-storey frame in Fig.8.4, the horizontal displacement time histories show a difference for vibration frequency and amplitude between the linear and nonlinear analyses. The maximum displacement and acceleration from the nonlinear analyses are less than those from the linear analyses and the vibration frequency for the nonlinear analyses is lower than that for the linear analyses. For the 12-storey frame in Fig.8.5, the horizontal displacement and acceleration time histories from the nonlinear analyses show that the vibration frequency is lower than the linear analyses, and the maximum displacement and acceleration are less than those from the linear analyses.

For the 6-storey frame in Fig.8.1, however, when the period is greater than 0.75s, the spectral acceleration for the nonlinear analyses is amplified at the foundation level, but its effect on the structural response is not clear from Fig.8.4. This result is different from Fig.6.8 in Chapter 6, where the free field response for the nonlinear analysis was used as the input motion for the fixed-base 6-storey frame. There, the effect of soil-structure interaction on the structural response depends on both the predominant period of the input motion on the ground surface and the natural vibration period of the structure. When the soil model is nonlinear and the effect of the soil-structure interaction on the structural response is considered, the above two

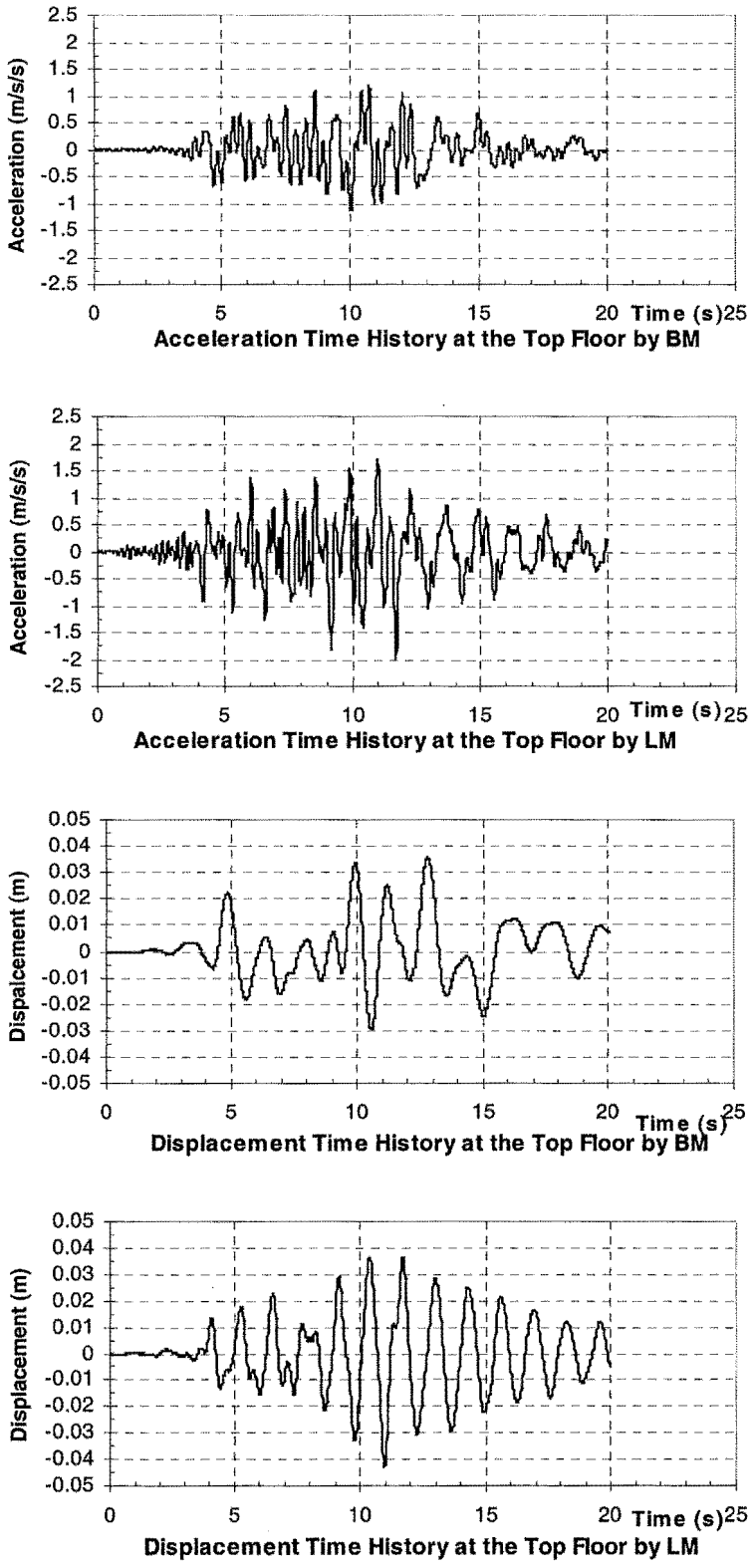

Figure 8.4 The Acceleration and Displacement Time Histories at the top floor for the 6-Storey Frame under scaled Loma Prieta Earthquake

BM: Bounding Surface Soil Model LM: Linear Elastic Soil Model

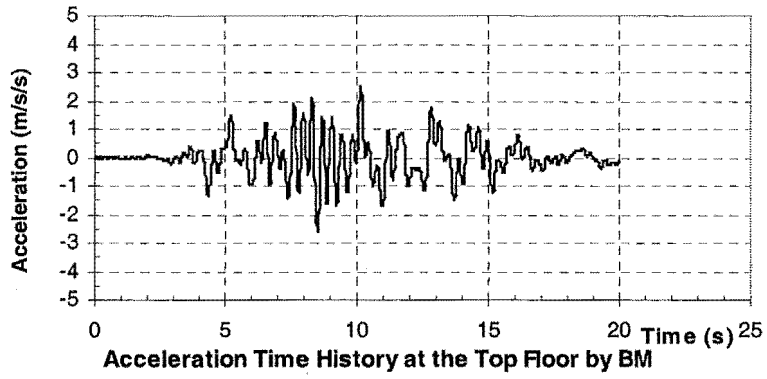

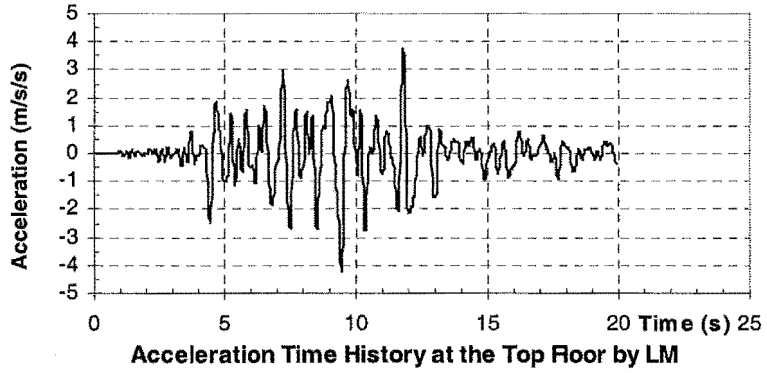

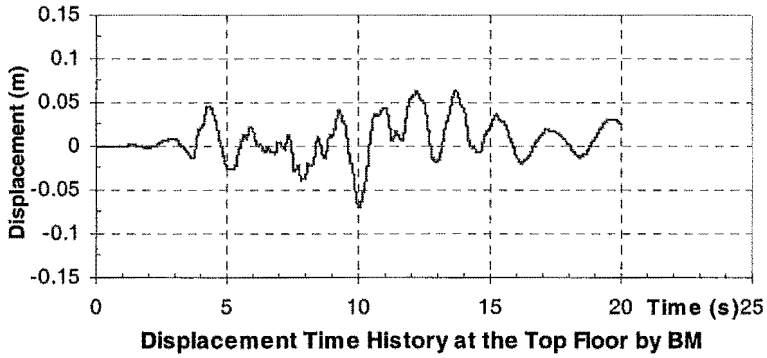

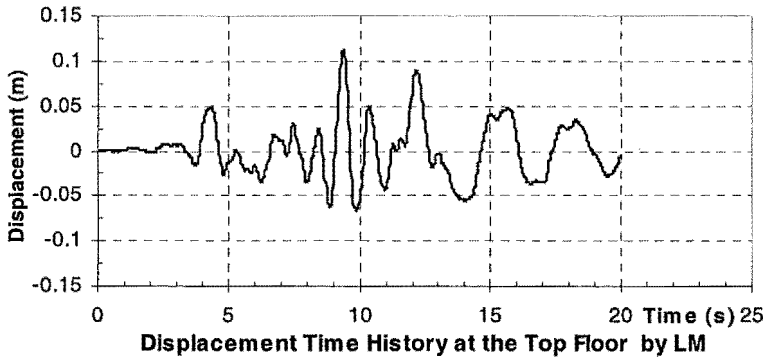

Figure 8.5 The Acceleration and Displacement Time Histories at the top floor for the 12-Storey Frame under scaled Loma Prieta Earthquake

BM: Bounding Surface Soil Model LM: Linear Elastic Soil Model

periods will be not sufficient to explain the difference between the linear and nonlinear analyses.

When a linear soil model is used to analyse the effect of soil-structure interaction, the permanent settlement of the foundation does not occur. This contradicts the observations from many earthquakes where such a settlement has been evident. Although unloading results in swelling, some permanent deformation will still remain. When soil-structure interaction is considered in the analysis of the structural response, the permanent deformation of the soil will generate a permanent settlement of the foundation. This settlement is very important to realising the effect of an earthquake on structural response.

The permanent settlement time history of the foundation is shown in Fig.8.6 for the 6-storey frame in the nonlinear analysis. From Fig.8.6, the rate of settlement is very small during the first 5 seconds, between 5 seconds to 15 seconds which is the period of strong shaking the rate of settlement increases rapidly, but after 15 seconds the

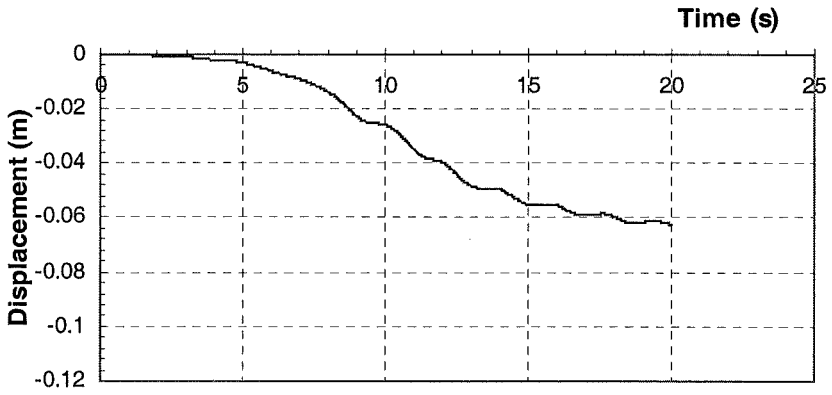

Figure 8.6 The Permanent Settlement Time History of the Foundation for the 6-Storey Frame

rate of settlement decreases markedly. It also shows that the vertical vibration amplitude of the foundation is very small.

For the 12-storey frame, the response is different from that of the 6-storey frame for the linear elastic soil model shown in Chapter 7. When the nonlinear soil model is

used, the permanent settlement time history of the foundation for the 12-storey frame is as plotted in Fig.8.7.

By comparison with Fig.8.6, both permanent settlement time histories show similar trends, but the maximum permanent settlement of the foundation for the 12-storey frame is larger than that for the 6-storey frame. On the other hand, the vibration frequency in the vertical direction for the 12-storey frame is lower than that for the 6-storey frame.

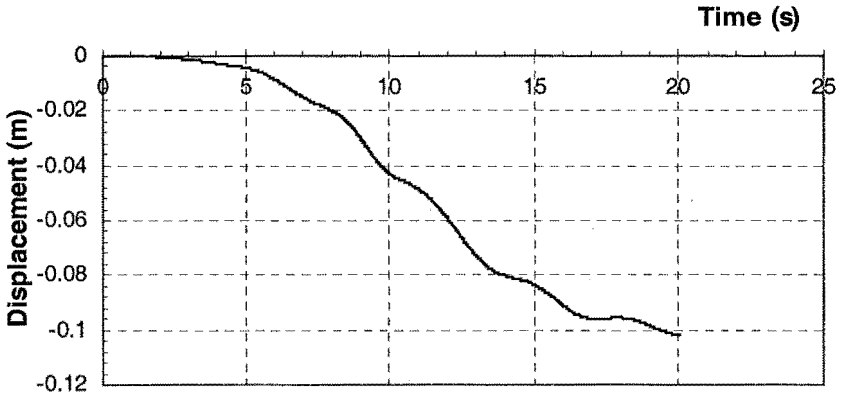

Figure 8.7 The Permanent Settlement Time History of the Foundation for the 12-Storey Frame under the Loma Prieta Earthquake

8.3 The Scaled Mexico City Earthquake

The effect of the Mexico City earthquake on the structural response has been investigated in Chapter 7 using a linear soil model. In this section, the scaled Mexico City earthquake is used as an input motion from the basement rock. The bounding surface model is used to represent the soil behaviour and to investigate the effect of the structure on the ground response and the effect of soil models on the structural response.

8.3.1 The Effect of the Structure on the Ground Response

In Chapter 7, the linear elastic soil model was used to represent the soil behaviour in order to carry out the soil-structure interaction analysis under the Mexico City

earthquake. That investigation showed that the effect of the structure on the ground response differs from that using the Loma Prieta earthquake. Fig.8.8 shows the acceleration spectra of the 6-storey and 12-storey frames at the foundation level using the linear and nonlinear analyses.

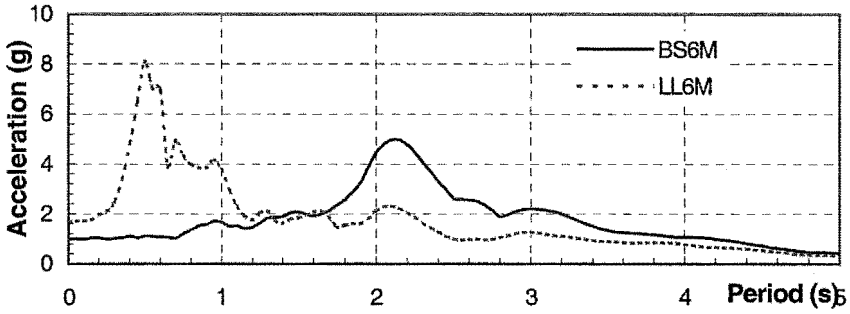

a. Comparison of Acceleration Spectra between the linear and Nonlinear Analyses for the 6-Storey Frame

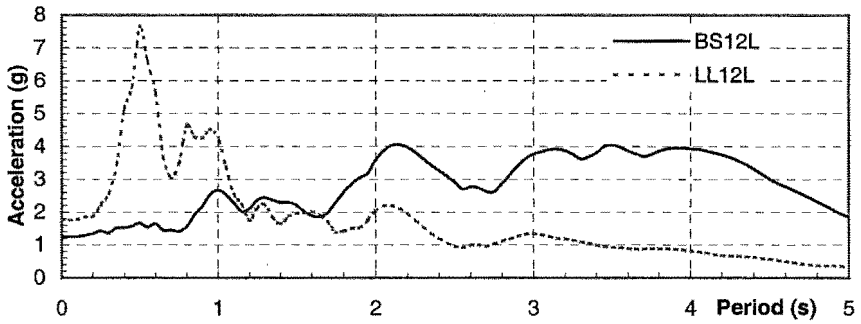

b. Comparison of Acceleration Spectra between the Linear and Nonlinear Analyses for the 12-Storey Frame

Figure 8.8 Comparison of Acceleration Spectra between the Linear and Nonlinear Analyses at the Basement for the 6-Storey and 12-Storey Frames
BS-Bounding Surface Model LL-Linear Elastic Model

The 6-storey frame in Fig.8.8a shows a great difference between the acceleration spectra for the linear and nonlinear analyses. For the linear analyses, the spectral peak acceleration occurs at about 0.5s. However, for the nonlinear analysis, the spectral peak acceleration is at about 2.1s. This difference shows that the yielding of the soil in the nonlinear analysis lengthens the natural vibration period of the site, thus the spectral acceleration at the predominant period of the input motion from the basement rock is amplified. For the 12-storey frame in Fig.8.8b, the acceleration spectra show characteristics different from those for the 6-storey frame. The spectral acceleration for the nonlinear analyses is amplified at periods greater than 1.7s when compared

with the linear analysis. The reason for this difference is that the predominant period of the input motion is close to the natural vibration period of the structure and the yielding of soil lengthens the natural vibration period of the site. By comparing Figs. 8.8 and Fig.8.1, it can be seen that for the nonlinear analyses the predominant period of the input motion also has a great effect on the ground response.

In order to display characteristics of the acceleration and displacement at the foundation level, their time histories are shown in Figs. 8.9 and 8.10. For the 6-storey frame in Fig.8.9, the vibration frequency for the nonlinear analysis is much lower than that for the linear analysis, and the maximum acceleration for the nonlinear analysis is less than in the linear analysis. However, the maximum displacement for the nonlinear analysis is greater than that from the linear analysis. For the 12-storey frame in Fig.8.10, these response characteristics are the same as those for the 6-storey frame, but the maximum displacements for the linear and nonlinear analyses are closer. This illustrates that the natural vibration period of the structure in the nonlinear analysis has a great influence on the ground response.

By comparing Figs. 8.9 and 8.10 with Figs. 8.2 and 8.3 for the linear analysis, the vibration frequency of the acceleration at the foundation level for the 12-storey frame is higher than that for the 6-storey frame. However, in the nonlinear analysis, the vibration frequency at the foundation level for the 12-storey frame does not appear to be higher than that for the 6-storey frame. The reason is that the yielding of the soil reduces the stiffness of the soil-structure system. Therefore, when a nonlinear soil model is used to analyse the effect of soil-structure interaction on the structural response, the nonlinear soil behaviour changes the structural response.

8.3.2 The Effect of the Bounding Surface Soil Model on the Structural Response

The acceleration and displacement time histories at the top floor for the 6-storey and 12-storey frames under the scaled Mexico City earthquake are shown in Figs. 8.11 and 8.12. For the 6-storey frame in Fig.8.11, the vibration frequency of the frame for the nonlinear analyses is lower than that for the linear analysis, but the maximum

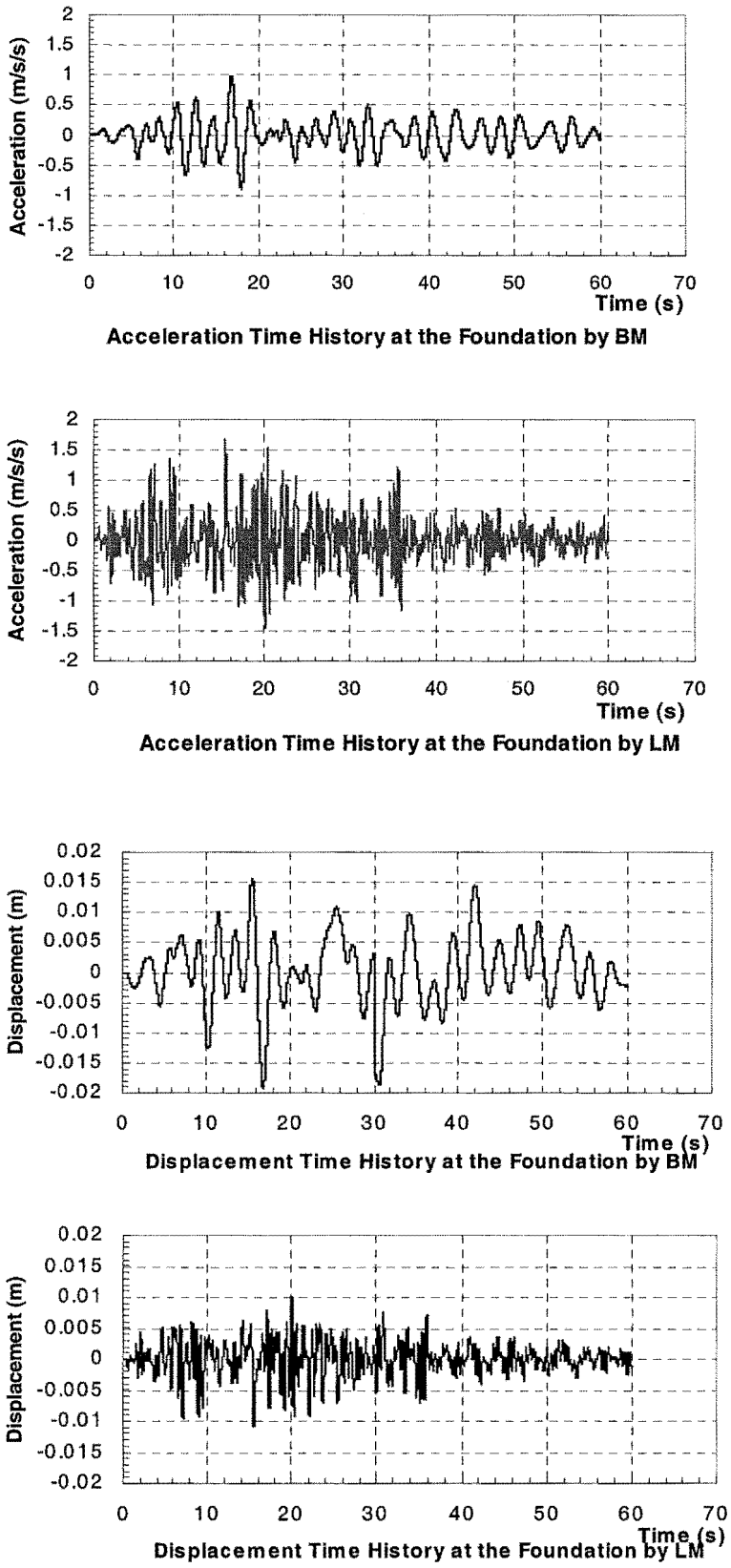

Figure 8.9 The Acceleration and Displacement Time Histories at the Foundation Level for 6-Storey Frame under scaled Mexico City Earthquake

BM: Bounding Surface Soil Model LM: Linear Elastic Soil Model

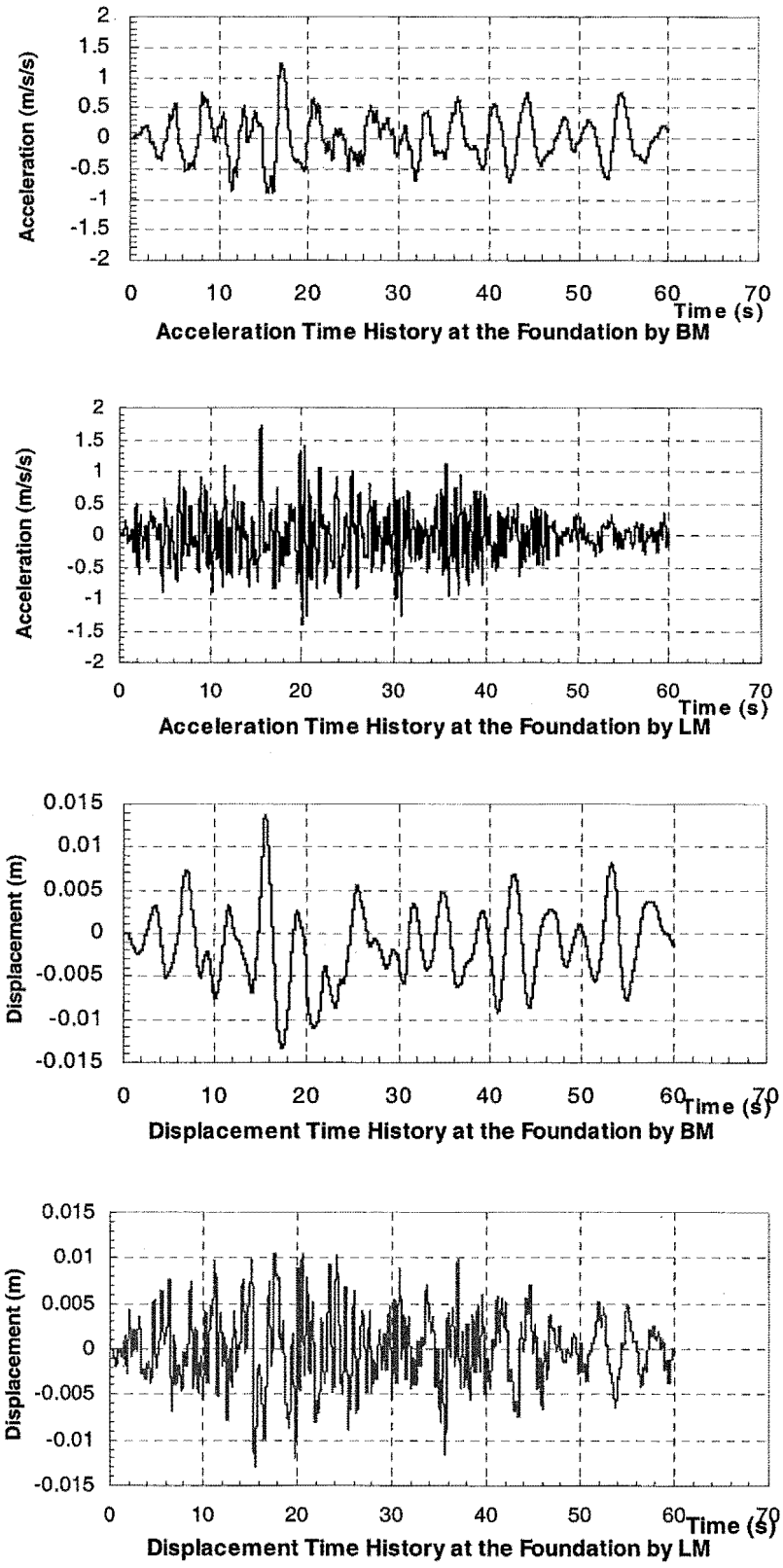

Figure 8.10 The Acceleration and Displacement Time histories at the Foundation Level for 12-Storey Frame under Scaled Mexico City Erathquake

BM: Bounding Surface Soil Model LM: Linear Elastic Soil Model

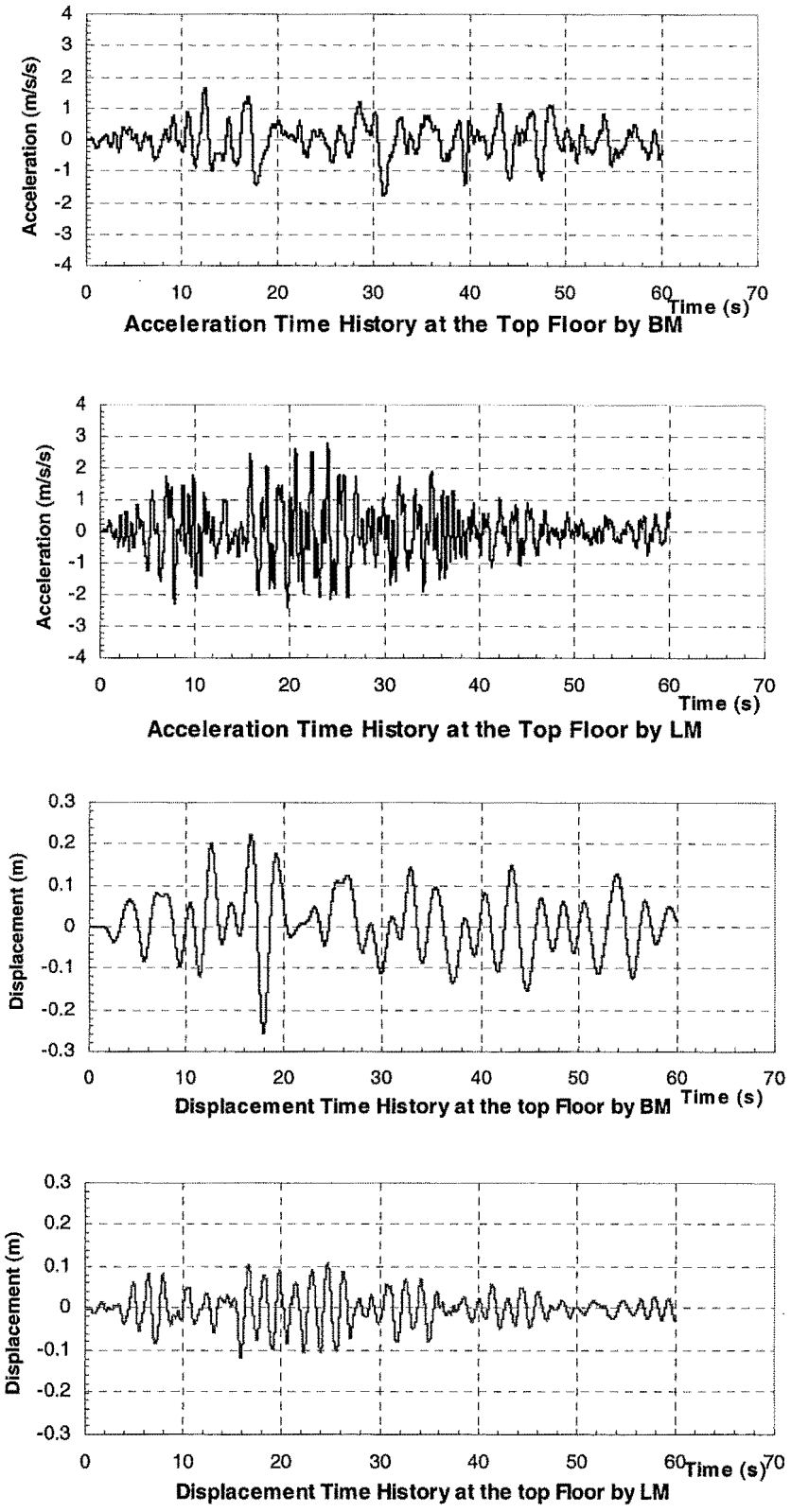

Figure 8.11 The Acceleration and Displacement Time Histories at the Top Floor for the 6-Storey Frame under Scaled Mexico City earthquake

BM: Bounding Surface Soil Model LM: Linear Elastic Soil Model

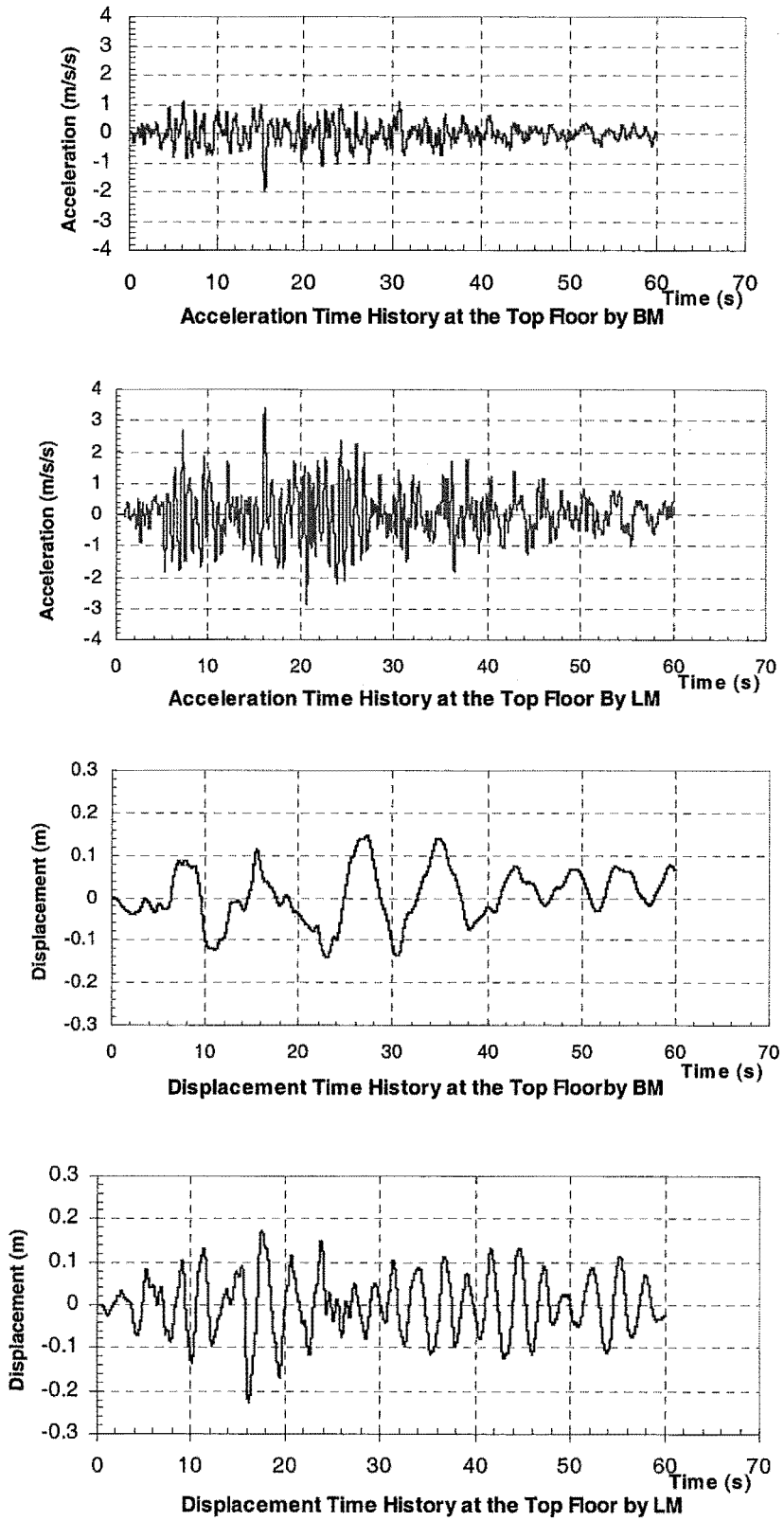

Figure 8.12 The Acceleration and Displacement Time Histories at the Top Floor for the 12-Storey Frame under Scaled Mexico City Earthquake

BM: Bounding Surface Soil Model LM: Linear Elastic Soil Model

displacement at the top of floor for the nonlinear analysis is greater than that for the linear analysis. For the 12-storey frame in Fig.8.12, the vibration frequency of the frame from the nonlinear analysis is lower than that from the linear analysis, however the maximum displacement at the top of floor from the nonlinear analysis is less than that from the linear analysis. These results show that the effect of the soil-structure interaction on the structural response for the nonlinear soil model is different from those for the linear elastic soil model.

In comparing Fig.8.11 with Fig.8.4 for the nonlinear analysis, the acceleration vibration frequency of the 6-storey frame under the scaled Loma Prieta earthquake is higher than that under the scaled Mexico City earthquake. However the maximum displacement at the top of floor under the scaled Loma Prieta earthquake is much less than that under the scaled Mexico City earthquake. From the scaled Loma Prieta earthquake, the maximum displacement at the top floor for the nonlinear analysis is less than the linear analysis, however from the scaled Mexico City earthquake, the maximum displacement at the top floor for the nonlinear analysis is greater than the linear analysis. The reason is that the vibration period of the soil-structure system due to the soil yielding is close to the predominant period of the input motion from the basement rock.

In comparing Fig.8.12 and Fig.8.5, both results show similar characteristics. The maximum accelerations and displacements at the top floor of the structure for the nonlinear analysis are smaller than those for the linear analysis.

The above analyses concern mainly the acceleration and displacement time histories. The following sections will investigate the permanent settlement of the foundation.

The permanent settlement time history of the foundation for the 6-storey frame is shown in Fig.8.13. The permanent settlement of the foundation gradually increases as the vibration duration increases. By comparing Fig.8.13 and Fig.8.6, both permanent settlement time histories have similar characteristics, but under the scaled Mexico City earthquake the permanent settlement of the foundation for the 6-storey frame is larger than for the scaled Loma Prieta earthquake. Fig.8.14 shows the permanent settlement time history of the foundation for the 12-storey frame. By comparing

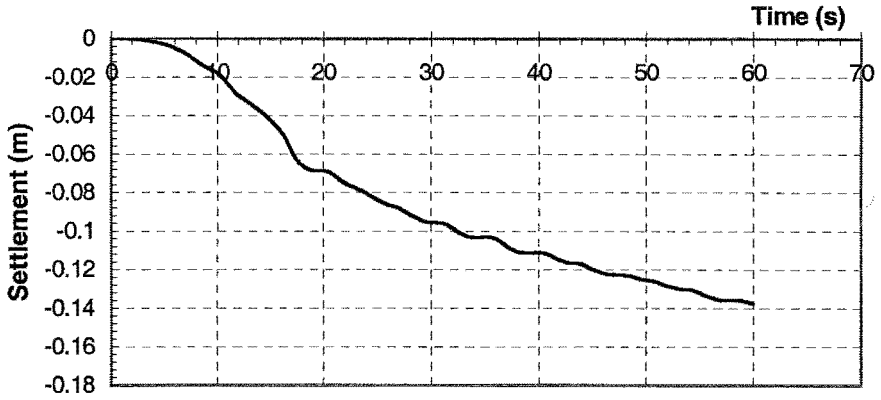

Figure 8.13 The Permanent Settlement of the Foundation for the 6-Storey Frame

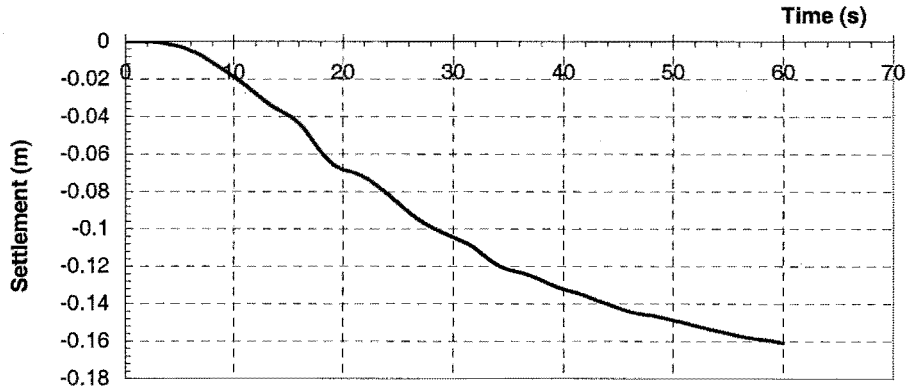

Figure 8.14 The Permanent Settlement of the Foundation for the 12-Storey Frame

Fig.8.14 and Fig.8.13, the permanent settlement of the foundation for the 12-storey frame is larger than the 6-storey frame, but the vibration frequency for the 6-storey is greater than that for the 12-storey frame.

8.4 Summary

In this Chapter, a nonlinear soil model is used to represent soil behaviour and a linear model is used to represent structural behaviour. Due to the yielding of the soil in the nonlinear analysis, the natural vibration period of the site is lengthened so that the effects of the soil-structure interaction on the structural response for the linear elastic and nonlinear soil models are different. Normally the soil yielding can reduce the structural response.

In comparing acceleration spectra at the foundation level of the linear and nonlinear analyses, the spectral peaks are at different periods for both analyses. This difference generates different structural responses.

The permanent settlement of a foundation is an important factor in the structural safety evauation. From these analyses, it can be noted that the permanent settlement of the foundation has accumulative characteristics. As the duration of the vibration increases, the settlement increases. When a soil-structure system is subjected to different earthquakes, the maximum settlements are different.

Chapter Nine

Conclusions and Recommendations for Further Research

9.1 Conclusions

The study of the effect of seismic soil-structure interaction on the structural response of framed structure by using linear elastic and bounding surface soil models has been carried out in this research. Some conclusions from this research are helpful for understanding the effects of the soil-structure interaction on the structural response and improving the seismic structural design. While the use of spring and dashpot model to represent soil behaviour is becoming the trend for modelling soil-structure interaction, the finite element analysis models and boundary element models in this research have shown a significant influence of soil yielding on the structural response, an effect that is difficult to represent in the simple spring and dashpot models.

The bounding surface soil model based on plasticity theory and the characteristics of several numerical integration methods have been introduced in Chapter Three. The numerical implementation for the bounding surface model shows that the method used in this implementation can reduce the calculation error. The result predicted by the model for a test problem shows that this soil model can reflects the nonlinear loading and unloading properties of the soil. By comparing the characteristics of these numerical integration methods, the α method of time step integration was chosen and used in the program SSINAP2D. In order to speed up convergence and keep numerical error in a tolerable range, a predictor-corrector algorithm was used in the program. The results predicted by RUAUMOKO for the 6-storey frame are very similar to the results predicted by SSINAP2D.

A direct boundary element method in the time domain has been introduced in Chapter four. The fundamental singular solutions for two-dimensional analysis, which are used directly in the numerical implementation, were given in details. The numerical treatment in the time domain for the two-dimensional analysis was obtained by the

constant and linear time variations and expressions for some complex functions were given in detail. A numerical example shows that this method provides a comparable result with other solutions in the published literatures.

A method for coupling the boundary elements and the finite elements in the time domain based on a simplified implementation procedure has been proposed in Chapter Five and a detailed mathematical procedure has been given. In this method, existing boundary element and finite element packages only need to be revised slightly to incorporate the two models. A flowchart given in this Chapter can be used as the basis for a linear or a nonlinear analysis program.

Nonlinear site amplification analyses using the bounding surface soil model were carried out in Chapter Six. The acceleration spectra obtained for the nonlinear site amplification analyses are different from those from the linear site amplification analyses. The nonlinear site amplification analyses amplify the spectral accelerations at the longer natural periods when compared with those from the linear site analyses. In the present design spectrum, the effect of the nonlinear site amplification on the structural response is not considered. While the peak ground acceleration (PGA) is affected by the maximum input acceleration from the basement rock, this analysis shows that peak ground acceleration is affected also by the input acceleration time history.

The effect of soil-structure interaction on the structural response has been carried out in Chapter Seven. The effect of the soil-structure interaction on the structural response is affected not only by the properties of the soil and structure but also by the input motion from the basement rock. Therefore the effect of the soil-structure interaction is important not only for a stiff structure but also for a flexible structure. However the effect of the soil-structure interaction for the flexible structure shows different characteristics from the effects of the soil-structure interaction on the stiff structure due to the effect of higher modes of vibration. Generally, when the following two cases occur, the soil-structure interaction can reduce the structural response. One case is when the predominant period of the input motion from the basement rock is less than the fundamental natural vibration periods of both the site and the structure. The other case is when the predominant period of the input motion is greater than the

fundamental natural vibration period of the soil and less than that of the structure. However, when the predominant period of the input motion from the basement rock is greater than the natural vibration periods of both the site and the structure, neglecting soil-structure interaction in a seismic analysis could lead an unsafe design.

The effect of the soil-structure interaction on the structural response when using the bounding surface soil model has been investigated in Chapter Eight. The yielding of the soil changes the natural vibration period of the soil-structure system so that the solution is more complex. This investigation shows that the nonlinear behaviour of the soil could reduce the structural response. The effect of the input motion from the basement rock on the soil-structure interaction also has an important influence on the structural response.

In the following sections, some detailed conclusions from both the local site amplification and seismic soil-structure interactions when using the linear elastic and bounding surface soil models are given.

9.1.1 Conclusions for Local Site Amplification and its Effect on Structural Response (in Chapter Six)

Three sets of soil parameters were used in this research to represent three different soft clay sites when the Loma Prieta, the El-Centro and the Parkfield earthquakes were used as input motions at the basement rock.

When subjected to a strong motion, the natural vibration period of the soft clay site represented by the bounding surface soil model is lengthened due to the yielding of the soil. Therefore for a soft clay site under a strong motion, the ground acceleration response will influence those structures with longer natural vibration periods. This is different to the results obtained from the linear elastic analysis where the natural vibration period of the site has an influence on the structural response.

The peak ground accelerations or the peak ground spectral accelerations obtained from the bounding surface soil model are lower than those from the linear elastic

analyses due to the hysteric and viscous damping of the soil, which was obtained by using hysteric model.

The site amplification or attenuation of the seismic wave motion shown from the nonlinear analysis depends on not only the maximum acceleration of the input motion from the basement rock, but also the input motion time history. When the maximum input acceleration reaches about 0.4g, the peak ground acceleration at the surface reaches about 0.4g according to the nonlinear analyses. This result is similar to site investigation results (Idress, 1990). However, in some cases, such as with the Parkfield earthquake, the result from the analysis using the bounding surface soil model shows the nonlinear amplification of the site.

For the ground acceleration response, the results for both the linear elastic and bounding surface soil models show a difference at the ground surface, but when comparing the results at depth greater than about 20m, the difference of the results from both the linear elastic and bounding surface soil models is negligible. This depth, though not an exact boundary, is helpful as a reference point.

When subjected to a strong input motion, the frequency content of the ground acceleration response from the linear elastic soil model is similar to the frequency content of the input motion from the basement rock, but the acceleration on the ground surface is amplified by the site.

Under a weak input motion, the effect of yielding of the soil is not evident, so that both results for the maximum acceleration and the frequency on the ground surface from both the linear elastic and bounding surface soil models are similar. Therefore when subjected to a weak input motion, a linear elastic analysis for these soft clay sites gives a satisfaction approximation to the response on the ground surface.

For the above cases, the fixed-base structural responses were investigated when the acceleration time histories at the ground surface from both the linear elastic and bounding surface soil model were used as the input motions for the 6-storey frame. These investigations show that the structural responses from the bounding surface soil model are different from those from the linear elastic analyses. This is because the

yielding of the soil amplifies the longer period part of the input motion in the acceleration spectrum.

9.1.2 Conclusions for Soil-Structure Interaction When Using a Linear Elastic Soil Model (in Chapter Seven)

The effects of soil-structure interaction on the structural response were investigated when using the linear elastic soil model for the 6- and 12-storey frames, the Loma Prieta and the Mexico City earthquakes and five sets of soil parameters, each with a different natural vibration period. In order to consider the effects of the soil-structure interaction on the structural response, the input motion for the fixed-base frame analysis is obtained from the acceleration response at the foundation level for the soil-structure interaction analysis. This method is different from that using the free field response as the input ground motion for the fixed-base frames.

The soil-structure interaction reduces the inter-storey shear force in the frame noticeably when the structural response is controlled by the lower modes of the structures such as in the case of the 6-storey frame. When higher modes of free-vibration of the structure influence the structural responses such as in the case of the 12-storey frame, the effect of the soil-structure interaction on the inter-storey shear forces becomes complex.

The soil-structure interaction can reduces the maximum displacement at the top floor such as occurred for the 6-storey frame. The reason is that the soil-structure interaction lengthens the natural vibration period of the frame and generates the effective damping in the soil-structure system.

The soil-structure interaction significantly reduces the inelastic displacement at the top floor due to the rocking of the foundation such as was shown for the 12-storey frame. In this procedure, the cyclic vibration amplitude of the displacement at the top floor is different from that for the fixed case due to the displacement at the roof caused by the rigid body rocking at the foundation.

The soil-structure interaction is not only influenced by the soil, but also by the structural behaviour. From the research results, the nonlinear structural behaviour reduces the rocking of the foundation. This may be due to the hysteric damping in the structure dissipating more energy.

The ground acceleration response at the foundation level when considering the soil-structure interaction is different from that from a free field analysis. In most of the cases investigated, the maximum acceleration response from the free field analysis is greater than that from the soil-structure interaction analysis. However, in some specific cases such as when resonance occurs, the maximum acceleration response from the free field analysis is less than that from the soil-structure interaction analysis. Therefore when the response from the free field analysis is used as the input motion in fixed-base or spring-dashpot-frame analyses, suitable scaling of the input motion may be necessary.

From this investigation, the input motion from the basement rock has a significant influence on the soil-structure interaction. Different input motions from the basement rock generate different effects on the soil-structure interaction such as that seen in the 6- and 12-storey frames under the Loma Prieta and the Mexico City earthquakes. The effect of the input motion from the basement rock on the soil-structure interaction can be determined approximately by the predominant period of the input motion from the basement rock and the natural vibration period of the soil-structure system. This is different from the traditional approach, in which the effect of only the soil and the structure are considered. From the viewpoint of the soil-structure and input motion system, the effect of the soil-structure interaction on the structural response is important.

9.1.3 **Conclusions for Soil-Structure Interaction When Using a Bounding Surface Soil Model (in Chapter 8)**

The 6- and 12-storey frames were investigated by using the bounding surface soil model when a site is subjected to scaled Loma Prieta and scaled Mexico City

earthquakes and the results from these analyses are compared with the analysis using a linear elastic soil model.

The soil-structure interaction using the bounding surface soil model reduce the structural response due to the hysteretic damping. These results are similar to those of Trifunac and Todorovska (1999). However, the nonlinear soil behaviour does not show the passive vibration isolation proposed by Trifunac and Todorovska (1998). In the soil-structure interaction analyses using the bounding surface soil model, the stiffness of the soil changes with the changes in stress levels so that the natural vibration frequencies of the soil-structure system also changes. Therefore it is very difficult to estimate the effect of the non-linearity on the natural vibration period of the soil-structure system.

The acceleration response at the foundation level using the bounding surface soil model is different from that obtained using the linear elastic soil model in terms of the vibration frequency and amplitude. The analyses using the bounding surface soil model amplify the acceleration response in the longer natural periods of the acceleration spectra, but reduce the maximum vibration amplitude of the acceleration. It is clear that this acceleration spectrum is very different from the design spectrum used in design codes. When compared with present design spectrum in NZ4203, the acceleration spectrum obtained using the bounding surface model will affect those structures with longer natural vibration period.

The permanent settlements of the foundations from the 6- and 12-storey frame analyses show that the displacement is accumulative. The settlement is mainly caused by the inelastic vertical deformation of the soil under the structural weight and the rocking of the foundation. This effect is similar to the "shake-down" effect in beam members in plastic structural mechanics.

For a soft clay site and strong bedrock shaking, present spring and dashpot models or linear elastic soil models can not show the nonlinear behaviour of the soil so that the effect of the soil yielding on the structural response is not shown by these models. The bounding surface soil model used in the analyses, however, overcomes this

disadvantage and shows the same results with those from site investigations (Trifunac and Todorovska, 1999)

The acceleration spectrum at the level of a foundation for a soft clay site using the bounding surface soil model shows that the accelerations at the longer natural periods are amplified and shows the effect of the presence of the structure on the ground surface response. If the free field response is used as the input motion for a spring and dashpot model, the effect of both the soil non-linearity and the presence of the structure on the ground surface response cannot be contained in the input motion.

The direct boundary element method in the time domain representing the far field for a nonlinear analysis avoids the use of the Fast Fourier Transform which has to be used if the boundary element method in the frequency domain is used to represent the far field. When nonlinear soil-structure interaction analysis using the finite element method is carried out, the integration direct boundary element in the time domain can save a large amount of computation and also automatically meets the radiation condition.

9.2 Recommendations for Further Research

Further research needs to be carried out by theoretical and experimental means to explain some of the results and findings that have been introduced.

1 Nonlinear local site amplification and the effect of soil-structure interaction on the structural response have been investigated. However, this investigation was carried out only for a clay soil and for a depth of deposit of 30m. Generally, deposit depths are often of the range of 0 to 40m. Therefore the effect of different deposit depths should be investigated further. For a real site, there is often a variation of soil properties with depth, therefore this effect also needs further investigation.

2 In this research, only simple 6- and 12-storey frames were investigated. Different frames have different natural vibration periods and soil-structure interaction will have different effects on the structural response. A wider range of investigations are necessary for different types of framed structures.

3 Soil is a multi-pore medium. When the soil is saturated, the interaction between the multi-pore medium and water can be very important. If this medium-pore water interaction could be considered in a computer analysis, the reliability of results from the soil-structure interaction analyses will then be higher.

4 The boundary element method in the time domain proposed in this research can be used to represent the far field and the method is also easily implemented into a nonlinear analysis, but it is suitable only for a homogenous far domain. However, layered soils are usually found in practice. Therefore, if this method is to be used in a layered soil, compatibility and equilibrium conditions at the interfaces between the different layers must be considered. This could be done by using a multi-domain boundary element solution. This development will require further investigation.

5 In this research, the effect of soil-structure interaction on the structural response were investigated based on the linear elastic soil model and linear elastic structural model, linear elastic soil model and nonlinear structural model, and nonlinear soil model and linear elastic structural model. A nonlinear soil model and nonlinear structural model case must be investigated to obtain the full understanding of the significance of the soil-structure interaction.

6 The analyses performed in this thesis covered only two-dimensional models of the soil and the structure. The analyses must be extended to three-dimensions to ensure that problems with the three-dimensional nature of real soil-structure interaction are understood.

REFERENCES

1. **ABOUSEEDA H, DAKOULAS P,** *Non-Linear Dynamic Earth Dam-Foundation Interaction Using A BE-FE Method*, Earthquake Engineering and Structural Dynamics, Vol.27, pp.917-936, 1998

2. **AHMAD S, BANERJEE P.K**, *Multi-Domain BEM for Two-Dimensional Problems of Elastodynamics*, Int. J. for Numerical Methods in Engineering, Vol.26, pp.899-911, 1988

3. **ANANDARAJAH A, RASHIDI H, ARULANANDAN**, *Elasto-Plastic Finite Element Analysis of a Soil-Structure System under Earthquake Excitations*, Computers and Geotechnics, Vol.17, pp.301-325, 1995

4. **ANDERSON D. G, RICHART F. E**, *Effects of Shearing on Shear Modulus of Clays*, Journal of Geotechnical Engineering Division, GT9, Vol.102, pp. 975-987, 1976

5. **ANTES H,** *A Boundary Element Procedure for Transient Wave Propagation in Two-dimensional Isotropic Elastic Media*, Finite Elements Modelling, Vol.1, pp.313-322, 1985

6. **ARULANANDAN K, MURALEETHARAN K. K, YOGACHANDRAN C**, *Seismic Response of Soil deposits in San Francisco Marina District*, J. of Geotechnical and Geoenvironmental Engineering, Vol.121, pp.965, 1997

7. **BATH K. J, WILSON E. L**, *Numerical Method in Finite Element Analysis*, Prentice-Hall, Inc., Englewood Cliffs, New Jersey, 1976

8. **BEER G, MEEK J. L,** *The Coupling of Boundary and Finite Element Methods for Infinite Domain Problems in Elasto-plasticity*, Int. Conference on BEM 3rd, Irvine, CA, 1981

9. **BORJA R. I, WU W. H,** *Vibration of Foundations on Incompressible Soils on Elastic Region*, Journal of Geotechnical Engineering, No.9, Vol.120, pp.1570-1591, 1994

10. **BOUCHON M, AKI K,** *Discrete Wave Number Representation of Seismic-Source Wave Fields*, Bull. Seism. Soc. Am.,

11. **BREBBIA C. A, TELLS J.C. F, WROBEL L. C**, *Boundary Element techniques*, Berlin, Heidelberg, New York, Springer, 1984

12. **BREBBIA C. A, GEORGIOU P**, *Combination of Boundary and Finite Elements in Elastostatics*, Appl. Math. Modelling, Vol.3, pp. 212-220, 1979

13. **CARR, A. J**, *RUAUMOKO – Inelastic Dynamic Analysis Program*, Department of Civil Engineering, University of Canterbury, 1998

14. **CHANG C. Y, POWER M. S, TANG Y. K, MOK C. M**, *Evidence of nonlinear soil response during a moderate earthquake*, 12 World Conference of Soil Mechanics and Foundation Engineering, pp.1927-1930, 1990

15. **CHEN W. F, MIZUNO E**, *Nonlinear Analysis in Soil Mechanics: Theory and Implementation*, Developments in Geotechnical Engineerings, Elsevier Science Publishers B. V., 1990

16. **CLOUGH RAY W, PENSIEN JOSEPH,** *Dynamics of Structures*, McGraw-Hill, Inc, 1993

17. **COOK R. D,** *Concepts and Applications of Finite Element Analysis*, John Wiley & Sons, 1990

18. **DAFALIAS Y. F, HERRMAN L.R,** *Bounding Surface Formulation of Soil Plasticity*, Soil Mechanics – Transient and Cyclic Loads, Editors: Pande G. N, Zienkiewicz O. C, John Wiley and Sons, New York, pp.253-286, 1982

19. **DAFALIAS Y. F, HERRMANN L.R**, *Bounding Surface Plasticity: Application to Isotropic Cohesive Soils*, Journal of Engineering Mechanics, Vol.112, pp. 1263-1291, 1986

20. **DAFALIAS Y.F, POPOV E. P**, *Plastic Internal Variables Formalism of Cyclic Plasticity*, Journal of Applied Mechanics, Vol.43, pp. 645-651, 1976

21. **DANIEL RESENDIZ, VELESOS A. S**, *Soil-Structure Interaction in Mexico City during the 1985 Earthquakes*, The Mexico Earthquakes-1985, edited by Michael A. Cassaro and Enrique Martinez Romero, pp.193-203, published by American Society of Civil Engineering, 1987

22. **DESAI C. S, SIRIWARDANE H. J**, *Constitutive Laws for Engineering Materials with Emphasis on Geologic Materials*, Prentice-Hall, Englewood Cliffs, 1984

23. **DOWRICK D. J**, *Earthquake Resistant Design – for Engineers and Architects*, Second Edition, John Wiley & Sons, Ltd, 1987

24. **ERINGEN A. C, SUHUBI E. S**, *Elastodynamics*, Academic Press, New York, 1975

25. **ESTORFF O. U, PRABUCKI**, *Dynamic Response in the Time Domain by Coupled Boundary and Finite Elements*, Computational Mechanics, Vol.6, pp.35-46, 1990

26. **FENG Y. T, OWEN D.R. J**, *Iterative Solution of Coupled FE/BE Discretizations for Plate-Foundation Interaction Problems*, Int. J. Numerical Methods in Engineering, Vol.39, pp.1889-1901, 1996

27. **FINN W. D. LIAM, LEE K. W, MARTIN G. R**, *An effective stress model for liquefaction*, J. of the Geotechnical Engineering Division, ASCE, Vol.103, No. GT6, pp.517-533, 1976

28. **FINN W. D. LIAM**, *Dynamic effective stress response of soil structures: Theory and centrifuge model studies*, Fifth International Conference on Numerical Methods in Geomechanics, Nagoya, pp.35-46, 1-5 April 1985

29. **FUKUTAKE K, SUKI A, SATO M, SHAMOTO Y**, *Analysis of Saturated Dense Sand-Structure System and Compression with Results from Shaking Table Test*, Earthquake Engineering and Structural Dynamics, Vol.19, pp.977-992, 1990

30. **GANEV T, YAMAZAKI F,ISHIZAK H, KITAZAWA M,** *Response Analysis of the HIGHESHI-KOBE bridge and Surrounding Soil in the 1995 HYOGOKEN-NANBU earthquake*, Earthquake Engineering and Structural Dynamics, Vol.27, pp.557-576, 1998

31. **GERADIN M, IDELSOHN S, HOGGE M**, *Computational Strategies for the Solution of Large Nonlinear Problems via Quasi-Newton Methods*, Computers and Structures, Vol.13, pp.73-81, 1981

32. **GRAHAM C. J**, *Nonlinear Soil Modelling*, Report No. 294, School of Engineering, University of Auckland, March 1982

33. **HADJIAN A. H, LUCO J. E, TSAI N. C,** *Soil-Structure Interaction: Continuum or Finite Element?*, Nuclear Engineering and Design, Vol.31, pp.151-167, 1974

34. **HENRY D. P, BANERJEE P. K**, *A Variable Stiffness Type Boundary Element Formulation for Axisymmetric Elasto-Plastic Media*, Int. J. Numer. Methods Eng., Vol.26, pp.1005-1027, 1988

35. **HENRY D. P, BANERJEE P. K, A** *Variable Stiffness Type Boundary Element Formulation for Axisymmetric Elato-plastic Media*, Int. J. for Numerical Methods in Engineering, Vol. 26, pp.1005-1027, 1988

36. **HERRMANN L. R, KALIAKIN V, SHEN C. K, MISH K. D, ZHU Z. Y,** *Numerical Implementation of Plasticity Model for Cohesive Soils*, Journal of Engineering Mechanics, No.4, Vol.113, pp.500-519, 1987

37. **HILBER H. M, HUGHES T. J. R, TAYLOR R. L**, *Improved Numerical Dissipation for Time Integration Algorithms in Structural Dynamics*, EESD, Vol.5, pp.283-292, 1977

38. **HINTON E, OWEN D. R. J**, *Finite Element Programming*, Academic Press, 1977

39. **IDRISS I. M**, *Response of Soft Soil Sites During Earthquakes*, in J. M. Duncan, ed., Proceedings, H. Bolton Seed Memorial Symposium, BiTech Publishers, Vancouver, British Columbia, Vol.2, pp.273-289, 1990

40. **JOYNER W. B**, *A Method for Calculating Nonlinear Seismic Response in Two Dimensions*, BSSA Vol.65, pp.1337, 1975

41. **KARABALIS D. L, BESKOS D. E**, *Dynamic Response of 3-D Flexible Foundations by Time Domain BEM and FEM*, Soil Dynamics and Earthquake Engineering, Vol.4, pp.91-101, 1985

42. **KREIG R. D, A** *Practical Two-Dimensional Plasticity Model*, Journal of Applied Mechanics, Vol.42, pp.641-646, 1975

43. **KOBAYASHI S, MORI K,** *Three-Dimensional Dynamic Analysis of Soil-Structure Interactions By Boundary Integral Equation-Finite Element Combined Method*, Shaw R. P., et al (eds): Innovative Numerical Methods in Engineering, pp.613-618, Berlin, Heidelberg, New York: Springer, 1986

44. **LACY S. J, PROVEST J. H**, *Nonlinear Seismic Response Analysis of Earth Dams*, Soil Dynamics and Earthquake Engineering, No.1, Vol.6, pp.48-63, 1987

45. **LACHAT J. C, WATSON J. O**, *Effective Numerical Treatment of Boundary Integral Equations: A Formulation for Three-Dimensional Elatostatics*, Int. J. for Numerical Methods in Engineering, Vol.10, pp.911-1005, 1976

46. **LARKIN T. J**, *The Propagation of Seismic Waves through Nonlinear Soil Media*, PhD. Thesis, University of Auckland, New Zealand, 1976

47. **LARKIN T. J**, *Densor-A Computer Program for Seismic Response Analysis of Nonlinear Horizontal Soil Layers*, Norwegian Geotechnical Institute, Internal Report No. 51508-6, 1978

48. **LI H B, HAM G. M, MANG H. A, TORZICKY P,** *A New Method for the Coupling of Finite Element and Boundary Element Discretized Subdomains of Elastic Bodies*, Comp. Meth. in Appl. Mech. Engng. Vol.54, pp.161-185

49. **LI X. S, SHEN C. K, WANG Z. L**, *Fully Coupled Inelastic Site Response Analysis for 1986 Lotung Earthquake*, J. of Geotechnical and Geoenvironmental Engineering, Vol.124, pp.560-573, 1998

50. **LIU W. K, BELYTSCHKO T**. *Mixed-Time Implicit-Explicit Finite Elements for Transient Analysis*, Computer and Structures, Vol.15, pp. 445-450, 1982

51. *Loma Prieta Earthquake, October 17, 1989, Preliminary Reconnaissance Report*, Earthquake Engineering Research Institute, 1989

52. **LUCO J.E, WONG H. L**, *Response of structures to nonvertically incident seismic waves*, Department of Applied mechanics and Engineering Sciences, University of Califonia, San Diego, 1979

53. **LYSMER J, RICHARD F. E**, *Dynamic Response of Footings to Vertical Loading* , Journal of the Soil Mechanics and Foundations Division, SM1, Vol,92, pp. , 1969

54. **LYSMER J, UDAKA T, SEED H. B, HWANG R**, *LUSH-A Computer Program for Complex Response Analysis of Soil-Structure System*, Earthquake Engineering Research Center, Report No. EERC 74-4, University of California, Berkeley, 1974

55. **MANOLIS G. D,** *A Comparative Study on three Boundary Element Method Approaches to Problems in Elastodynamics*, Int. J. for Numerical Methods in Engineering, Vol.19, pp.73-91, 1983

56. **MANOLIS G. D, BESKOS D. E,** Boundary Element Methods in Elastodynamics, London, 1989

57. **MARSH E. J**, *Two Dimensional Nonlinear Seismic Ground Response Studies*, Department of Civil Engineering, University of Auckland, Report No. 536, July, 1992

58. **MARTIN G. R, FINN W. D. LIAM, SEED H. B**, *Fundamental of liquefaction under cyclic loading*, J. of the Geotechnical Engineering Division, ASCE, Vol.101, No. GT5, pp.423-438, 1975

59. **MASING G**, *Eigenspannungen und verfestigung beim messing*, Proceedings of the 2nd International Congress of Applied Mechanics, Zurich, Switzerland, 1926

60. **MITA A, YOSHIDA K, KUMAGAI S, SHIOYA K,** *Soil-Structure Interaction Experiment Using Impulse Response*, Earthquake Engineering and Structural Dynamics, Vol.18, pp.727-744, 1989

61. **MOROZ Z**, *On the Description of Anisotropic Work Hardening*, J. Mech. Phys. Solids, Vol.15, pp.163-175, 1967

62. **MOROZ Z, NORRIS AND ZIENKIEWICZ**, *Application of an Anisotropic hardening Model in an Analysis of Elasto-Plastic Deformation of Soils*, Geotechnique, Vol.29, pp.1-34, 1979

63. **MURALEETHARAN K. K, MISH K. D, ARULANANDAN K,** *A Fully Coupled Non-Linear Dynamic Analysis Procedure and Its Verification Using Centrifuge Test Results*, Int. J. for Numerical and Analytical Methods in Geomechanics, Vol.18, pp.305-325, 1994

64. **NAYLOR D. J**, *Stresses in Nearly Incompressible Materials by Finite Elements with Application to Calculation of Excess Pore Water Pressures*, Int. J. for Numerical Methods in Engineering, Vol.8, pp.443-460, 1974

65. **NEWMARK N. M, HALL W. J**, *Earthquake Spectra and Design*, Earthquake Engineering Research Institute, 1982

66. **NIWA Y, KOBAYASHI S, FUKUI T**, *Application of Integral Equation Method to Some Geomechanical Problems*, Numerical methods in Geomechnics, New York, pp.120-131, 1976

67. **OWEN D. R. J, HINTON E,** *Finite Elements in Plasticity: Theory and Practice*, Pineridge Press, Swansea, 1980

68. **PANDE G. N, PIETRUSZCZAK S**, *A Critical Look at Constitutive Models for Soils,* Geomechanical Modelling in Engineering Practice, Edited by Punger R., Studer J. A, Balkema A. A, Boston, pp.369-395, 1986

69. **PAULAY T, PRIESTLEY M. N. J**, *Seismic design of reinforced concrete and masonry buildings*, Wiley, 1992

70. **PENDER M**, *Earthquake Soil-Structure Interaction, Spring and Dashpot Models, and Real Soil Behaviour*, Bulletin of the New Zealand National Society for Earthquake Engineering, No.4, Vol.16, pp.320-330, 1983

71. **PREVOST J. H**, *Mathematical Modelling of Monotonic and Cyclic Undrained Clay Behavior*, Int. J. for Numerical Analytical Methods in Geomechanics, Vol.1, pp.195-216, 1977

72. **PREVOST J. H**, *Nonlinear Transient Phenomena in Saturated Porous Media*, Comput. Methods Appl. Mech. Eng., Vol.30, pp.3-18, 1982

73. *Preliminary Report on the Principal Geotechnical Aspect of the October 17, 1989 Loma Prieta Earthquake*, Preliminary Findings from Field Investigations and Associated Studies Performated by Teams, Earthquake Engineering Research Center, Report No. UCB/EERC-90/05, April 1990

74. **QUAAS R, MENU E,** *Strong Motion Arrays and Characteristics*, The Mexico Earthquakes-1985, edited by Michael A. Cassaro and Enrigue Martinez Romero, published by the American Society of Civil Engineers, 1987

75. **RICHARD F. E, WHITMAN R. V**, *Comparison of Footing Vibration Tests with Theory*, Journal of the Soil Mechanics and Foundations Division, SM6, Vol,93, pp.143-167, 1967

76. **ROMO M. P**, *Clay Behaviour, Ground Response and Soil-Structure Interaction Studies in Mexico City*, Third International Conference on Recent Advances in Geotechnical Earthquake Engineering and Soil Dynamics, St. Louis, Vol. 2, pp.1039-1051, 1995

77. **SANGREY D. A, HENKEL D. J, ESPIG N. I,** *The Effective Stress Response of a Saturated Clay Soil to Repeated Loading*, Canadian Geotechnical Journal, No.3, Vol.6, pp. 241-252, 1969

78. **SCHNABLE P. B, LYSMER J, SEED H. B**, *SHAKE-A Computer Program for Earthquake Response Analysis of Horizontally Layered Sites*, Earthquake Engineering Research Center, Report No. EERC 72-12, University of California, Berkeley, December

79. **SEED H. B, ROMO M. P, JOSEPH SUN, JAIME A. AND LYSMER J.**, *Relationships between Soil Conditions and Earthquake Ground Motions in Mexico City in the Earthquake of Sept. 19, 1985*, Earthquake Engineering Research Center, Report No. UCB/EERC-87/15, October 1987

80. **SEED H. B, LYSMER, J, HWANG, R**, *Soil-Structure Interaction Analysis for Seismic Response*, Journal of Geotechnical Engineering Division, GT5, Vol.10, pp.439-457, 1975

81. **SEED H. B, IDRISS I. M**, *Influence of Soil Conditions during Earthquakes*, Journal of Soil Mechanics and Foundations Division, SM1, Vol.95, pp.99-137, 1969

82. **SEED H. B, LYSMER J, HWANG R,** *Soil-Structure Interaction Analyses for Seismic Response,* J. of the Geotechnical Engineering Division, Vol.101, pp.439-458, 1975

83. **SEED H. B, ROMO M. P, JAIME A, LYSMER J,** *Relationships between Soil Conditions and Earthquake Ground Motions in Mexico City in the Earthquake of Sept. 19, 1985*, Earthquake Engineering Research Center, Report No. UCB/EERC-87/15, October 1987

84. *Seismological and Engineering Aspects of the 1995 HYOGOKEN-NANBU (Kobe) Earthquake*, Earthquake Engineering Research Center, Report No. UCB/EERC-95/10, November 1995.

85. **SPYRAKOS C.C, BESKOS D.E**, *Dynamic Response of Flexible Strip Foundations by Boundary and Finite Elements*, Soil Dynamics and Earthquake Engineering, Vol.5, pp.84-96, 1986

86. **STEWART J. P, BRAY J. D, SEED R. B AND SITAR N,** *Preliminary Report on the Principal Geotechnical Aspects of the January 17, 1994 Northridge Earthquake*, Earthquake Engineering Research Center, Report No. UCB/EERC-94/08, June 1994

87. **STROUD A. H, SECREST D**, *Gaussian Guadrature Formulas*, Englewood Cliffs: Prentice-Hall, 1966

88. **SUN J. I, GOLESORKHI R, SEED H. B**, *Dynamic Moduli and Damping Ratio for Cohesive Soils*, Earthquake Engineering Research Center, Report, No. UCB/EERC-88/15, 1988

89. **SWOBODA G, MERTZ W, BEER G**, *Rheological Analysis of Tunnel Excavations by Means of Coupled Finite Element(FEM)-Boundary Element(BEM)* Analysis, Int. J. for Numerical and Analytical Method in Geomechanics, Vol.11, pp.115-129, 1987

90. **TAKAJI KOKUSHO AND MASALLI MATSUMOTO,** *Nonlinearity in Site Amplification and Soil Properties during the 1995 Hyogoken-Nambu Earthquake*,

Special Issue on Geotechnical Aspects of the January 17, 1995 Hyogoken-Nambu Earthquake, No.2

91. **TAYLOR P. W, LARKIN T. J**, *Seismic Soil Response of Nonlinear Soil Media*, Proc. American Society of Civil Engineers, Geotechnical Division, Vol.104, pp.369, 1978

92. **TRIFUNAC M. D, TODOROVSKA M. I**, *Reduction of Structural Damage by Nonlinear Soil Response*, Proc. American Society of Civil Engineers, Structural Division, Vol.125, pp.89,1999

93. **TRIFUNAC M. D, TODOROVSKA M. I,** *Nonlinear Soil Response as a Natural Passive Isolation Mechanism-the 1994 Northridge, California, Earthquake*, Soil Dynamics and Earthquake Engineering, vol.17, pp.41, 1998

94. **UANG C. M, BERTERO V. V**, *Use of Energy as a Design Criterion in Earthquake-Resistant Design*, Earthquake Engineering Research Center, Report No. UCB/EERC-88/18, Nov. 1988

95. **VALLABHAN C. V. G,** *Coupling of BEM/FEM Technology: An Overview*, Proceeds of the 3rd Boundary Element Technology Conference, BETECH 87, Rio de Janeiro, 1987

96. **VELESOS A. S, VERBIC B**, *Vibration of Viscoelastic Foundations*, Earthquake Engineering and Structural Dynamics, Vol.2, pp.87-102, 1973

97. **VELESOS A. S, VERBIC B**, *Basic Response Functions for Elastic Foundation*, Journal of Engineering Mechanics, EM2, Vol.100, pp.189-202, 1974

98. **WOLF J. P, DARBRE G. R**, *Danamic-Stiffness Matrix of Soil by the Boundary-Element Method: Conceptional Aspects*, Earthquake Engineering and Structural Dynamics, Vol.12, pp.385-400, 1984

99. **WOLF J. P, DARBRE G. R**, *Danamic-Stiffness Matrix of Soil by the Boundary-Element Method: Embedded Foundation*, Earthquake Engineering and Structural Dynamics, Vol.12, pp.401-416, 1984

100 **WOLF J. P,** *Dynamic Soil-Structure Interaction*, Prentice Hall, 1985

101 **WOLF J. P,** *Soil-Structure Interaction Analysis in Time Domain*, Prentice Hall, Englewood Cliffs, New Jersey, 1988

102 **WOLF J. P**, *Foundation Vibration Analysis Using Simple Physical Models*, Englewood Cliffs, New York: PTR Prentice Hall, 1994

103 **ZHAO X. Q,** *Seismic Soil-Structure Interaction*, A Thesis Submitted in Partial Fulfilment of the Requirements for the Degree of Doctor of Philosophy at the University of Canterbury, 1989

104 **ZHAO J. X, CARR A. J, and MOSS P. J**, *Caculating the Dynamic Stiffness Matrix of 2-D Foundations by Discrete Wave Number Indirect Boundary Element Methods*, Earthquake Engineering and Structural Dynamics, Vol.26, pp.115-134, 1997

105 **ZHAO J. X,** *Vertical Soil-Structure Interaction of the Gisborne Post Office Building,* Pacific Conference on Earthquake Engineering, Australia, pp.227-236, 1995.

106 **ZIENKIEWICZ O. C**, *The Finite Element Method*, 3rd edited, McGraw-Hill, London, 1977

107 **ZIENKIEWICZ O. C, KELLY D. M, BETTS P**, *The Coupling of the Finite Element Method and Boundary Solution Procedures*. Int. J. for Numerical Methods in Engineering, Vol.11, pp.355-376, 1977

Appendix One

$$G_{ij1}^{N-n+1}=\frac{1}{2\pi\rho}[\frac{H(\alpha_1-1)}{c_1^2}\{\frac{T}{\Delta T}\left[\frac{\delta_{ij}}{2}\left\{\cosh^{-1}(\alpha_1)-\alpha_1\beta_1\right\}+r_{,i}r_{,j}\alpha_1\beta_1\right]$$
$$+\frac{r}{c_1\Delta T}\left[\frac{\delta_{ij}}{3}\beta_1^3-r_{,i}r_{,j}\left(\frac{2}{3}\beta_1^3+\beta_1\right)\right]\}$$
$$+\frac{H(\alpha_2-1)}{c_2^2}\{\frac{T}{\Delta T}\left[\left\{\cosh^{-1}(\alpha_2)+\alpha_2\beta_2\right\}-r_{,i}r_{,j}\alpha_2\beta_2\right]$$
$$+\frac{r}{c_2\Delta T}\left[-\frac{\delta_{ij}}{3}\left(\beta_2^3+3\beta_2\right)+r_{,i}r_{,j}\left(\frac{2}{3}\beta_2^3+\beta_2\right)\right]\}]_{z=(N-n)\Delta T}^{z=(N-n+1)\Delta T}$$

$$G_{ij2}^{N-n+1}=\frac{1}{2\pi\rho}[\frac{H(\alpha_1-1)}{c_1^2}\{(1-T/\Delta T)\left[\frac{\delta_{ij}}{2}\left\{\cosh^{-1}(\alpha_1)-\alpha_1\beta_1\right\}+r_{,i}r_{,j}\alpha_1\beta_1\right]$$
$$-\frac{r}{c_1\Delta T}\left[\frac{\delta_{ij}}{3}\beta_1^3-r_{,i}r_{,j}\left(\frac{2}{3}\beta_1^3+\beta_1\right)\right]\}$$
$$+\frac{H(\alpha_2-1)}{c_2^2}\{(1-T/\Delta T)\left[\left\{\cosh^{-1}(\alpha_2)+\alpha_2\beta_2\right\}-r_{,i}r_{,j}\alpha_2\beta_2\right]$$
$$-\frac{r}{c_2\Delta T}\left[-\frac{\delta_{ij}}{3}\left(\beta_2^3+3\beta_2\right)+r_{,i}r_{,j}\left(\frac{2}{3}\beta_2^3+\beta_2\right)\right]\}]_{z=(N-n)\Delta T}^{z=(N-n+1)\Delta T}$$

$$F_{ij1}^{N-n+1}=\frac{\mu}{2\pi\rho r}[\frac{H(\alpha_1-1)}{c_1^2}\{\frac{T}{\Delta T}\left[-\frac{\alpha_1}{\beta_1}(A_1)+2\alpha_1\beta_1(A_2)\right]$$
$$+\frac{r}{c_1\Delta T}\left[\frac{1}{\beta_1}(A_1)-2(A_2)\left(\frac{2}{3}\beta_1^3+\beta_1\right)\right]\}$$
$$+\frac{H(\alpha_2-1)}{c_2^2}\{\frac{T}{\Delta T}\left[\frac{\alpha_2}{\beta_2}(A_3)-2\alpha_2\beta_2(A_2)\right]$$
$$+\frac{r}{c_2\Delta T}\left[-\frac{1}{\beta_2}(A_3)+2(A_2)\left(\frac{2}{3}\beta_2^3+\beta_2\right)\right]\}]_{z=(N-n)\Delta T}^{z=(N-n+1)\Delta T}$$

$$F_{ij2}^{N-n+1}=\frac{\mu}{2\pi\rho r}[\frac{H(\alpha_1-1)}{c_1^2}\{(1-T/\Delta T)\left[-\frac{\alpha_1}{\beta_1}(A_1)+2\alpha_1\beta_1(A_2)\right]$$
$$-\frac{r}{c_1\Delta T}\left[\frac{1}{\beta_1}(A_1)-2(A_2)\left(\frac{2}{3}\beta_1^3+\beta_1\right)\right]\}$$

$$+\frac{H(\alpha_2-1)}{c_2^2}\{(1-T/\Delta T)\left[\frac{\alpha_2}{\beta_2}(A_3)-2\alpha_2\beta_2(A_2)\right]$$

$$-\frac{r}{c_2\Delta T}\left[-\frac{1}{\beta_2}(A_3)=2(A_2)\left(\frac{2}{3}\beta_2^3+\beta_2\right)\right]\}]_{z=(N-n)\Delta T}^{z=(N-n+1)\Delta T}$$

Appendix Two

Mesh of the Finite Element of Soil-Structure Interaction for the 6-Storey Frame

Elastic Modulus of the Structure $E = 2.5\times10^7\ kP_a$

Shear Modulus of the Structure $G = 1.04\times10^7\ kP_a$

Bi-linear Factor $RA = 0.025$

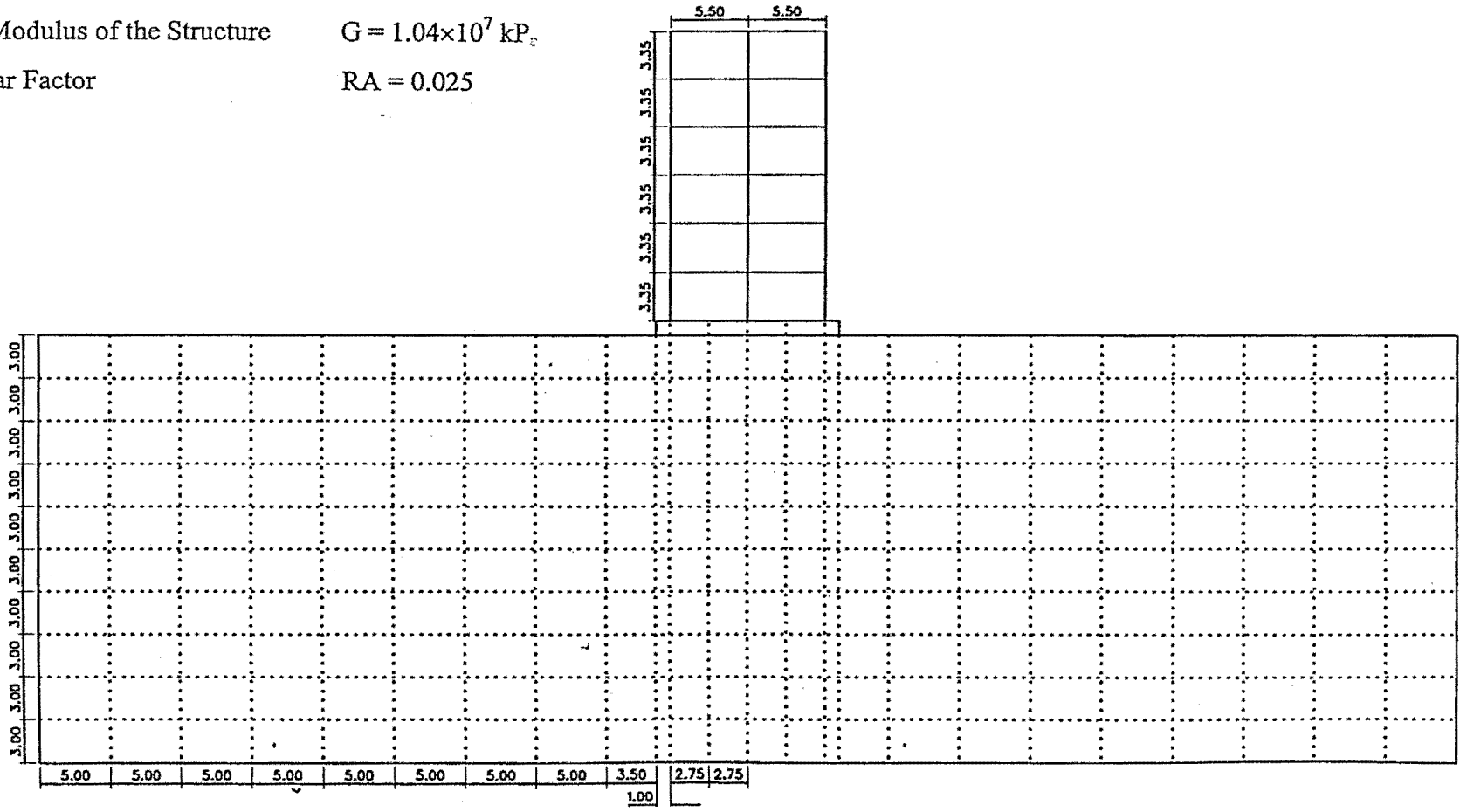

Appendix Three

Mesh of the Finite Element of Soil-Structure Interaction for the 12-Storey Frame

Elastic Modulus of the Structure $E = 2.5\times10^7\ kP_a$

Shear Modulus of the Structure $G = 1.04\times10^7\ kP_a$

Bi-linear Factor $RA = 0.025$

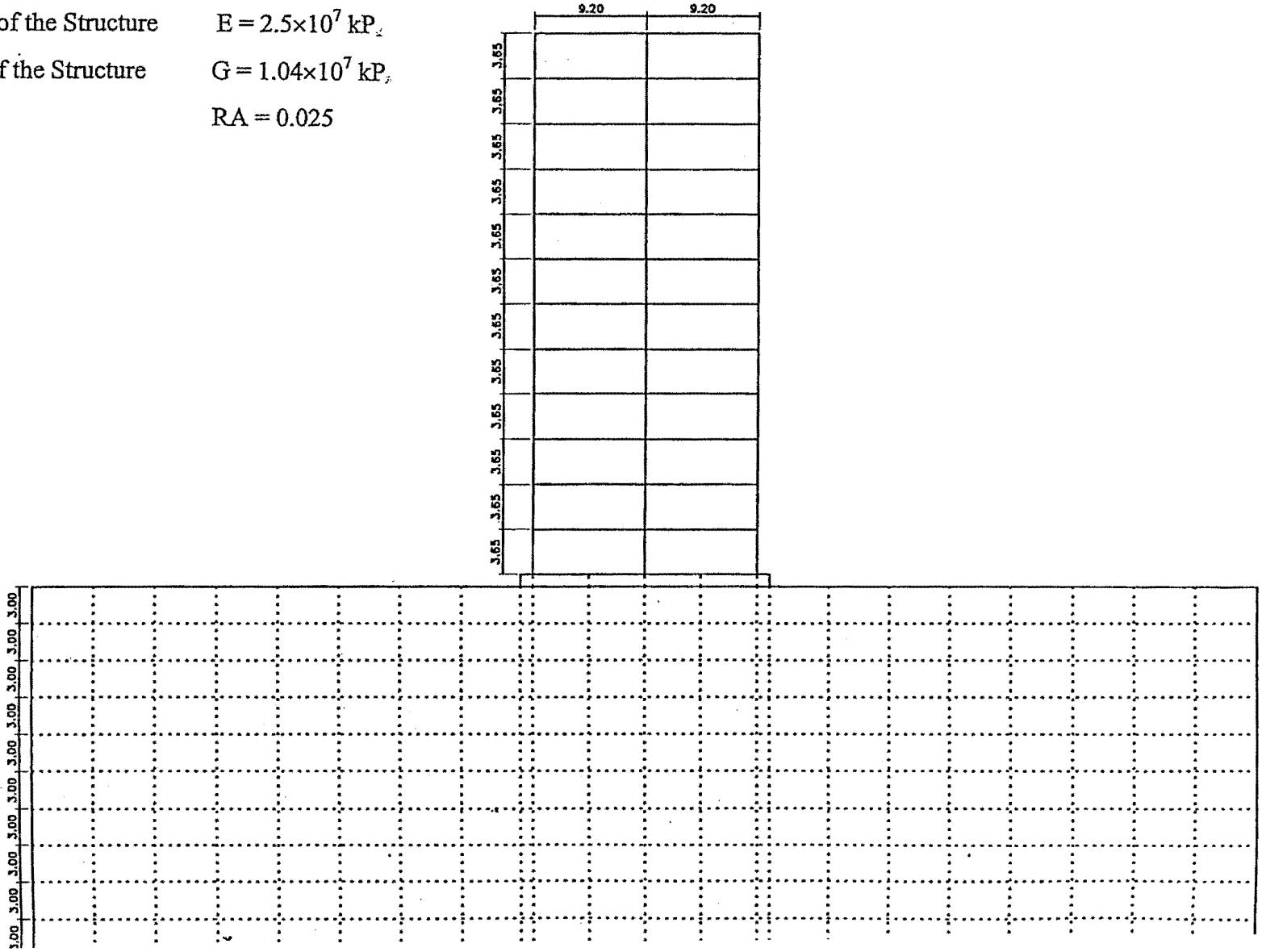

Appendix Four

Members with different properties in the 6 and 12-Storey frames are listed as following

E: Elastic Modulus of member material
G: Shear Modulus of member material
A: Cross-section area of the member section
AS: Effective shear area of the member section
I: Moment of inertia of section
RA: Bi-linear factor
H: Plastic Hinge Length
M_{yi} : Positive or negative yield moment at end i

The 6-Storey Frame

Member Type	E	G	A	AS	I	RA	H	M_{yi+}	M_{yi-}	M_{y2+}	M_{y2-}
*1	2.5e7	1.04e7	0.1688	0.1688	2.813E-3	0.025	0.35	435.0	519.0	423.0	197.0
2	2.5e7	1.04e7	0.1688	0.1688	2.813E-3						
3	2.5e7	1.04e7	0.1519	0.1519	2.050E-3						
4	2.5e7	1.04e7	0.1519	0.1519	2.050E-3						
*5	2.5e7	1.04e7	0.2269	0.2269	6.100E-3	0.025	0.385	645.0	775.0	635.0	300.0
6	2.5e7	1.04e7	0.2269	0.2269	6.100E-3						
7	2.5e7	1.04e7	0.1875	0.1875	4.167E-3						
8	2.5e7	1.04e7	0.1875	0.1875	4.167E-3						
9	2.5e7	1.04e7	0.1050	0.1050	3.150E-3	0.025	0.42	262.0	-262.0	232.0	-232.0
10	2.5e7	1.04e7	0.0963	0.0963	2.426E-3	0.025	0.385	173.0	-184.0	155.0	-155.0
11	2.5e7	1.04e7	0.0963	0.0963	2.426E-3	0.025	0.385	115.0	-131.0	119.0	-115.0
12	2.5e7	1.04e7	0.0963	0.0963	2.426E-3	0.025	0.385	115.0	-115.0	115.0	-115.0
13	2.5e7	1.04e7	0.1050	0.1050	3.150E-3	0.025	0.42	232.0	-232.0	262.0	-262.0
14	2.5e7	1.04e7	0.0963	0.0963	2.426E-3	0.025	0.385	155.0	-155.0	184.0	-173.0
15	2.5e7	1.04e7	0.0963	0.0963	2.426E-3	0.025	0.385	115.0	-119.0	131.0	-115.0
16	2.5e7	1.04e7	0.0963	0.0963	2.426E-3	0.025	0.385	115.0	-115.0	115.0	-115.0

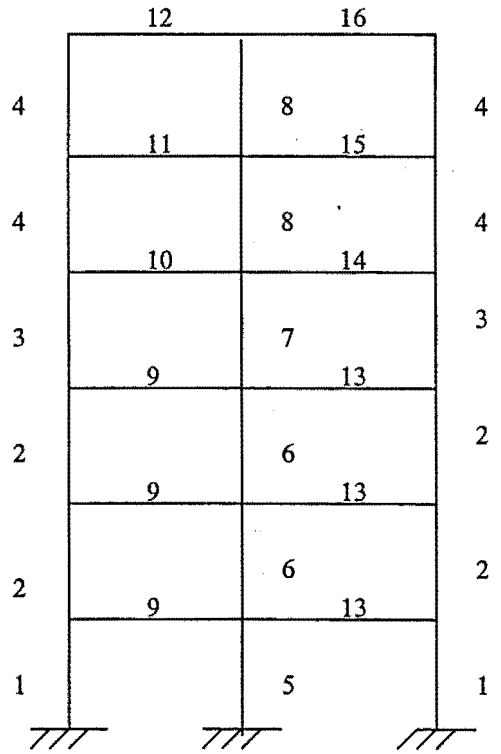

The 12-Storey Frame

Member Type	E	G	A	AS	I	RA	H	M_{y1+}	M_{y1-}	M_{y2+}	M_{y2-}
*1	2.5E7	1.04E7	0.2906	0.2906	0.01455	0.025	0.543	1338.0	1531.0	1263.0	665.0
2	2.5E7	1.04E7	0.2906	0.2906	0.01455						
3	2.5E7	1.04E7	0.2813	0.2813	0.01318						
4	2.5E7	1.04E7	0.2813	0.2813	0.01318						
5	2.5E7	1.04E7	0.2438	0.2438	0.00855						
6	2.5E7	1.04E7	0.2438	0.2438	0.00855						
*7	2.5E7	1.04E7	0.4800	0.4800	0.0256	0.025	0.543	1986.0	1986.0	2450.0	2038.0
8	2.5E7	1.04E7	0.4800	0.4800	0.0256						
9	2.5E7	1.04E7	0.3942	0.3942	0.01727						
10	2.5E7	1.04E7	0.3942	0.3942	0.01727						
11	2.5E7	1.04E7	0.3417	0.3417	0.01297						
12	2.5E7	1.04E7	0.3417	0.3417	0.01297						
13	2.5E7	1.04E7	0.1800	0.1800	0.02382	0.025	0.63	976.0	-976.0	893.0	-893.0
14	2.5E7	1.04E7	0.1800	0.1800	0.02382	0.025	0.63	1142.0	-1142.0	1047.0	-1047.0
15	2.5E7	1.04E7	0.1800	0.1800	0.02382	0.025	0.63	988.0	-988.0	887.0	-887.0
16	2.5E7	1.04E7	0.1700	0.1700	0.02017	0.025	0.595	762.0	-833.0	714.0	-714.0
17	2.5E7	1.04E7	0.1600	0.1600	0.01689	0.025	0.56	559.0	-631.0	547.0	-464.0
18	2.5E7	1.04E7	0.1600	0.1600	0.01689	0.025	0.56	307.0	-369.0	381.0	-307.0
19	2.5E7	1.04E7	0.1600	0.1600	0.01689	0.025	0.56	307.0	-307.0	307.0	-307.0
20	2.5E7	1.04E7	0.1800	0.1800	0.02382	0.025	0.63	893.0	-893.0	976.0	-976.0
21	2.5E7	1.04E7	0.1800	0.1800	0.02382	0.025	0.63	1047.0	-1047.0	1142.0	-1142.0
22	2.5E7	1.04E7	0.1800	0.1800	0.02382	0.025	0.56	887.0	-887.0	988.0	-988.0
23	2.5E7	1.04E7	0.1700	0.1700	0.02017	0.025	0.595	714.0	-714.0	833.0	-762.0
24	2.5E7	1.04E7	0.1600	0.1600	0.01689	0.025	0.56	464.0	-547.0	631.0	-559.0
25	2.5E7	1.04E7	0.1600	0.1600	0.01689	0.025	0.56	307.0	-381.0	369.0	-307.0
26	2.5E7	1.04E7	0.1600	0.1600	0.01689	0.025	0.56	307.0	-307.0	307.0	-307.0

Note: symbol * denotes the beam-column frame member, where

M_B : Yield moment at B
M_{1B} : Yield moment at P=(2/3)*P_B
M_{2B} : Yield moment at P=(1/3)*P_B
M_0 : Yield moment at P=0.0

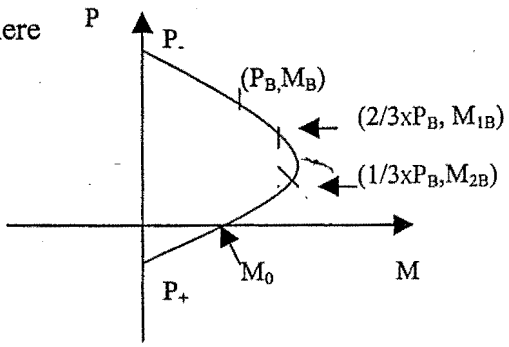

Axial compression and tension yield forces for 6- and 12-storey frames

6-storey frame				12-storey frame			
Member Type	P-	P+	P_B	Member Type	P-	P+	P_B
1	-6290.0	934.0	-3690.0	1	-11152.0	1930.0	-6075.0
5	-8454.0	1255.0	-5010.0	7	-17888.0	2656.0	-10920.0

Detailed explanation is given by Carr (1998)

The following figure of the 12-storey frame shows that frame member type are applied to different members of the frame.